Scuola di Dottorato in Ingegneria Civile e Architettura
Dottorato in Ingegneria Strutturale e Geotecnica

3D beam-column finite elements under tri-axial stress-strain states: non-uniform shear stress distribution and warping

Paolo Di Re

XXIX Ciclo - A.A. 2015/2016

Dipartimento di Ingegneria
Strutturale e Geotecnica

Sapienza
Università di Roma

SAPIENZA
UNIVERSITÀ DI ROMA

Faculty of Civil and Industrial Engineering
Department of Structural and Geotechnical Engineering

PhD Thesis in Structural Engineering

3D beam-column finite elements under tri-axial stress-strain states: non-uniform shear stress distribution and warping

PhD Candidate:
Paolo Di Re

Advisors:
Prof. Daniela Addessi

Co-Advisor:
Prof. Filip C. Filippou
(UC Berkeley)

Rome, February 2017

Abstract

In many engineering structures, the effects of shear and torsional loads are an important aspect of both the analysis and the design process. These effects are usually neglected in typical framed structures. However, in some relevant cases, such as bridges, shear walls or thin-walled frames, it is essential to account for the shear and torsional loads and their interaction with the other loading conditions to correctly reproduce the structural response.

In this framework, the main task is to accurately describe the nonlinear structural response in terms of global behavior and local stress-strain distributions, reproducing the coupling of the stress components and its influence on the global response. This results even more important in large scale structures made of cementitious and/or innovative composite materials, widely adopted in nowadays professional practice. Indeed, these structures usually show degrading mechanisms and softening behavior. Hence, they require sophisticated computational models and ad hoc analysis strategies to predict the structure capacity under severe loading conditions.

A standard approach to analyze these structures is the adoption of beam-column finite element (FE) models, which are often preferred with respect to two-dimensional (2D) plate/shell or three-dimensional (3D) FEs, because of their efficiency and low computational cost. However, most beam-column FE formulations are based on the classical Euler-Bernoulli or Timoshenko theory, assuming the cross-sections to remain plane during the loading process. This assumption requires specific corrective measures, when the shear and torsion and the related warping effects are pronounced.

This work discusses the simulation of RC members with a 3D 2-node beam FE that includes warping effects. The FE formulation in [1] is extended to allow the description of structural members with softening material behavior. The governing equations are derived from a four-field Hu-Washizu variational principle, with independent interpolation of the warping displacement field from the rigid section displacements, the generalized section deformations and the material stress fields. In particular, the warping of the cross-section is described by interpolating the out-of-plane displacement with the addition of a variable number of local degrees of freedom to those commonly used

for the beam FE. The global nonlinear response and the local distributions of strains and stresses are described introducing a fiber cross-section discretization. Hence, the coupling of axial, flexural, shear and torsional effects in terms of material response is automatically taken into account.

Focusing on RC structures, the damaging mechanisms of the concrete material is described by adopting a new 3D nonlinear constitutive relationship with plasticity and damage. This is an enhanced version of that proposed in [2] and introduces the description of the unilateral effects typically appearing in concrete-like materials, due to the crack opening and closure. A Drucker-Prager type plastic model is coupled with a two-parameter isotropic damage model, where two scalar variables are used to describe the damage in tension and compression, respectively.

The localization problems and the related mesh-dependency, due to the softening material behavior, are controlled through a regularization technique based on a properly modified nonlocal integral procedure. For beam-column FEs, the nonlocal strain measures are evaluated performing the integration of the local generalized section deformations along the element axis, whereas for 2D FEs the nonlocal integration is performed considering the generalized membrane/plate deformations.

The proposed model is implemented and validated through some correlation studies. These consider the numerical analysis of a series of plain concrete and RC beams subjected to torsional loads and of two RC shear walls. The results are compared with experimental measurements and with those of standard FE beam models.

Acknowledgements

Prima tra tutti, ringrazio la mia relatrice, la Prof. Addessi, per avermi guidato in questi che sono stati gli anni più intensi e più importanti del mio percorso di studi. Gran parte del merito per i traguardi raggiunti lo devo a lei, alla sua grande dedizione e alla sua fiducia nei miei confronti.

Ringrazio, poi, il Prof. Ciampi, per il suo supporto sia scientifico che morale e la sua significativa disponibilità. Lui mi ha trasmesso la passione per questa materia ed è sempre stato per me un punto di riferimento e una fonte di ispirazione.

I also thank Prof. Filippou to have accepted me at the UC Berkeley and treated me as a son, significantly influencing both my work and my education. The fifteen months spent in California have been the best and most exciting of my life and I have to thank him as well as Prof. Addessi and Prof. Ciampi for this opportunity.

Ringrazio anche il mio compagno di avventura (o forse dovrei direi di disavventura) Nicolò Vaiana, per la sua sincera e disinteressata amicizia e per aver reso la mia permanenza negli Stati Uniti decisamente più allegra e meno faticosa.

Infine, ringrazio tutta la mia famiglia, i miei genitori, mio fratello, mia zia e mia nonna, per essere sempre stati presenti in questi anni ed avermi aiutato nei momenti più difficili, e ringrazio Ilenia, per aver condiviso le mie gioie e le mie ansie ed avermi spinto a credere sempre più in me stesso, così come ringrazio tutti i miei amici, in particolare Laura e Attilio.

Contents

List of Figures

List of Tables

Chapter 1

Introduction, literature review and objectives

1.1 General

Beam-column finite elements (FE) are widely used to describe the inelastic response of structural members in large scale simulations, because of the optimal balance between accuracy and computational efficiency they offer.

Among the different beam FE models, force-based and mixed formulations have proven superior capacities with respect to the classical displacement-based models under large inelastic, cyclic deformations, although the slight increase in computational cost for the element state determination.

In this framework, many researchers focused their efforts on the development of efficient, discrete fiber cross-section model to effectively capture the multi-axial coupling of the beam stress resultants under general constitutive material relations. While classical Euler-Bernoulli beam formulations assume that plane sections remain plane and normal to the axis and are unable to capture the effect of shear and torsion, recent studies have proposed enhanced models accounting for these effects. Nonetheless, the existing models do not appear to give a complete and realistic representation of the cross-section warping with the resulting shear stresses and strains and they fail in reproducing accurately the interaction of the shear and normal stresses along the beam axis, the local response near the boundaries and the shear lag phenomenon.

This issues result more relevant when dealing with damaging materials, such as concrete or innovative fiber reinforced composites. Indeed, nowadays the numerical simulation of plain and reinforced concrete (RC) structures under severe loading conditions is still a challenging problem, given the complex phenomena characterizing their mechanical behavior.

This chapter provides an introductive and general overview of the topics discussed in this dissertation and of the motivations that have driven to the presented work. This overview starts with a discussion of advantages and disadvantages of beam-column FEs in numerical structural analyses, illustrating the benefits of mixed and force-based models with respect to displacement based ones and presenting the literature review of existing beam-column FEs able to account for shear and torsional effects. Then, it presents a short description of the most common materials used in engineering structures, i.e. steel and concrete, focusing on their mechanical properties and presenting the literature review of existing plastic-damage material models. The chapter concludes with the objectives of the work and its main outline.

1.2 Beam-column FEs for structural analysis

In large scale numerical simulations, beam-column FEs are often preferred over 2D and three-dimensional 3D FEs, such as shell and solids, because they require significantly lower computational costs, yet providing sufficiently accurate solutions. In fact, although all real structural elements are 3D, many of them are sufficiently slender to be represented by 1D models. Classical beam theories describe the behavior of a 3D element by representing it as a collection of cross-sections orthogonal to a straight (or a curved) segment, usually indicated as element axis. By imposing specific hypotheses on the static and kinematic description, these theories condense all the mechanical information of the cross-sections in the reference axis and describe the element response through the resulting 1D model (Fig. 1.1). Considering this assumption, the mechan-

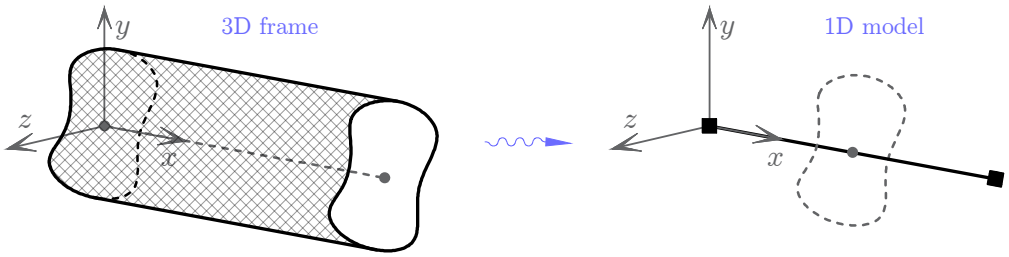

Figure 1.1: 3D frame as a 1D beam-column element.

ical response of frames and columns can be described considering the effects due to the four basic actions: axial forces, bending moments, shear forces and torsional moments (Fig. 1.2). Under linear elastic material responses, these effects can be studied separately and later superimposed to obtain the total response of the frame. This approach constitutes the fundamental idea of the De Saint Venant beam theory [3–7], where the definition of appropriate boundary conditions provides very accurate solu-

tions for linear elastic beams. Under nonlinear material responses, the superimposition of the effects due to the four basic actions can not be applied and other theories are preferred for the definition of numerical FE element models.

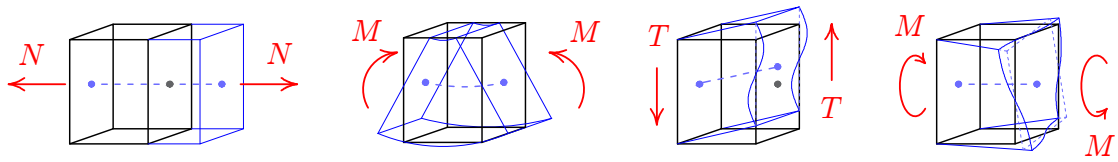

(*a*) Axial (*b*) Bending (*c*) Shear (*d*) Torsion

Figure 1.2: Basic force/deformation behaviors of a rectangular prismatic beam represented as deformed shape of a general beam portion.

The simplest beam theory for the formulation of FE models is known as Euler-Bernoulli beam theory, which assumes that plane cross-sections remain plane under deformation and orthogonal to the element axis. As shown in Fig. 1.2, under shear actions, the general cross-section undergoes warping deformations and its plane is no longer orthogonal to the element axis. Warping deformations arise under torsional actions as well, although the orientation of the cross-section plane with respect to axis does not change. Hence, the Euler-Bernoulli beam theory only accounts for the axial/flexural behavior of the beam, totally neglecting the effects of shear and torsional loads. Several theories and numerical models have been proposed in the last decades to overcome this limitation, many of which are based on the classical first-order shear theory known as Timoshenko beam theory [8]. A description of both the Euler-Bernoulli and the Timoshenko beam theories is given in Sec. 3.2 within the framework of force-based numerical models and the literature review on the most important beam-column FEs accounting for shear and torsion is presented in the following section.

Regardless of the adopted beam theory, beam-column numerical models consist in the discretization of each member of the structure through one or more FEs, where the nodal variables are considered as global degrees of freedom (DOF) and from them the mechanical fields (displacments, strains and stresses) are interpolated along the axis to determine the contribution of each element. Hence, beam-column FEs are usually classified as: displacement-based, force-based and mixed formulations. In displacement-based FEs, the global element variables are the nodal displacements; these are interpolated over the element length by means of appropriate shape functions (usually defined on polynomial basis) and the resulting displacement fields are used to evaluate the response inside the element volume. In force-based FEs, the internal response of the element is evaluated starting from the stress fields that are interpolated along the element length by imposing the equilibrium with the nodal forces. Mixed FEs are a

combination of these two approaches, that is they are derived by independently interpolating the stresses and the displacements, i.e. two-field mixed FE, or the stresses, the displacements and the strains, i.e. three-field mixed FEs. Additional fields can be considered and interpolated as well, to obtained enhanced multi-field formulation, as done for the model described in Sec. 3.4.

The standard 2-node displacement-based Euler-Bernoulli FE interpolates the nodal displacements with linear Lagrange polynomials for the axial components and cubic Hermite polynomials for the flexural/bending ones. As result, the strain and stress variations over the element axis for the axial and the flexural components are constant and linear, respectively. This condition is in general not sufficient to describe the response of beams under nonlinear material response, as the stresses and the strains often concentrate in small parts of the element and exhibit sharp variation along the axis. Although higher order elements can be defined [9], the displacement interpolation usually requires fine discretizations of each structural members, thus, increasing the overall computational cost. By contrast, by adopting force-based or mixed FEs, one element per member usually suffices to obtain very accurate solutions, because the strain/stress variations over the element length are defined through the equilibrium and the constitutive equations and in general they are exactly evaluated for any loading condition [10–14].

However, material nonlinearities can be treated in different ways when defining beam-column FEs. Indeed, nonlinear beam-column models are usually divided in two categories: models with lumped nonlinearities and models with distributed nonlinearities. A detailed summary of the earlier proposals of such models is provided by Spacone [15]. Formulations belonging to the first category identify specific cross-section of the element or specific portions along the element axis where the strains and the stresses assume their maximum values (usually at the ends) and concentrate the inelastic behavior of the beam in these zones. These models are usually referred to as plastic hinge models and their first proposals date back to the pioneering works by Clough et al. [16, 17] and Giberson [18]. Among them, formulations known as zero-length plastic hinge models, like the just mentioned ones, consider a linear elastic element with zero-length nonlinear springs concentrated at the ends that simulate the nonlinear behavior of the end cross-sections in terms of generalized section forces and deformations. In particular, the nonlinear springs can describe only the nonlinear moment-rotation relation, assuming the axial behavior of the cross-section as linear and defining what is known as one component models, or they can describe both the nonlinear moment-rotation relation and the nonlinear axial force-elongation relation, defining what is known as two-component models. For the latter case, many enhanced elements have

been proposed, usually describing the axial/flexural interaction under monotonic and cyclic loads through the definition of equivalent yield surfaces and flow rules, according to the classical plasticity theory, to describe the evolution of the generalized section forces. Among them it is worth mentioning the recent works by Liu et al. [19] and by Kostic et al. [20]. Finite-length plastic hinge models have been proposed as well, in terms of generalized cross-section constitutive laws [21, 22] or through the definition of a fiber model discretization of the cross-section [23, 24].

Formulations belonging to the second category consider that material inelastic behaviors can occur in any part of the element, i.e. they are smeared along the beam axis. Hence, they usually take advantage of a numerical integration rule along the element, defining a discrete number of quadrature cross-sections with nonlinear constitutive laws, to directly integrate the element response (Sec. 4.2). Among these models, those considering a fiber cross-section discretization (Sec. 5.3) have shown high efficiency and accuracy [25–29]. Indeed, the quadrature cross-sectional response derives from the numerical integration of the material longitudinal fibers composing the element, which leads to two main advantages: (1) they do not require the definition of nonlinear constitutive relations in terms of cross-section resultants, because the constitutive laws are defined at the fiber material level; (2) they allow to easily account for the interaction between the different stress components.

1.3 Existing 1D FEs for shear and torsion

Shear and torsional effects are usually neglected in the analysis of framed structure, as these have a reduced influence on the overall mechanical behavior with respect to the axial and flexural actions. Thus, Euler-Bernoulli FEs are frequently used in spite of more complex numerical models. However, in many structural applications, shear and torsional deformations become relevant to correctly describe the response and the adoption of formulations able to account for these effects is mandatory. For instance, in steel structures shear forces control the response of the short elements that resist to the horizontal loads in eccentrically braced frames (shear links) [30], whereas torsional forces significantly influence the behavior of thin-walled beams, especially when buckling phenomena take place. Indeed, because of the relevant cross-section out-of-plane deformations occurring in the latter case, flexural/torsional buckling behaviors often depend on the warping effects arising at the element boundaries and on the way beams converging in the same structural node interact with each other [31–34]. In concrete and RC structures, shear forces can not be neglected in the analysis of non-slender elements [35], such as shear walls [36] or squat bridge piers [37], whereas torsional forces

in all cases can yield relevant tensile strains and stresses, thus reducing the element capacity [38]. Moreover, structural members with applied warping constraints at the boundaries, such as bridge girders, can be subjected to relevant shear-lag phenomena, strongly influencing their elastic and inelastic behavior [39, 40]. Bairán [41] provides an accurate overview of the resistance mechanisms of RC elements under shear and torsion: friction and aggregate interlock, dowel action of longitudinal reinforcements, the truss mechanisms by Ritter and Morsch, etc., which are nowadays considered in many design codes, e.g. the Eurocode [42]. In addition, Bairán presents a detailed review of existing beam models accounting for shear, mainly focusing on smeared crack approaches for the material modeling [43].

As mentioned, the easiest models to describe the shear stress/strain evolution in beam-column element are based on the Timoshenko theory [8], which does not force the cross-sections to remain orthogonal to the element axis, unlike the Euler-Bernoulli theory, but it however assumes them to remain plane during the loading process. Because of this assumption, only constant shear strain distributions can be considered under shear actions (linear under torsional actions, see Sec. 3.2) and, thus, specific corrective measures are required to capture the correct behavior of the element. To address this issue, 2D plate/shell or 3D FEs are often used, but these require very high computational burden, although leading to accurate predictions of the structural responses.

Several Timoshenko beam-column FEs have been proposed, assuming constant shear over the cross-section. The standard 2-node displacement-based model with linear interpolation of the cross-section transversal displacements and rotations [44] exhibits shear locking issues, as opposed to the force-based and mixed models, which are free from locking and which show relevantly higher performances, particularly for inelastic material responses [14, 45]. However, many authors have presented enhanced displacement-based FEs that overcome the shear locking, either adopting a reduced integration approach [46] or introducing additional nodal DOFs to perform independent interpolations of the transversal displacements and rotations [47, 48].

By extending the standard Timoshenko model and by accounting for the warping deformation of the cross-sections, Bairán [41] has proposed a generalized beam model that describes non-uniform shear strain/stress distributions through an enhanced cross-section model, ensuring the equilibrium conditions between the fibers composing the element. The model adopts an accurate 3D material model to describe the brittle behavior of concrete and a 1D model to represent the transversal reinforcements, which are numerically described as embedded in the element volume. Some refinements of this first proposal have been later presented by Bairán himself and other authors [49, 50],

who studied the response of RC beams with several cross-section shapes under general monotonic loads.

Saritas [51] and Le Corvec [1] have also worked on this topic, proposing enhanced models to describe the effects of shear and torsion in structural frames and have provided a detailed literature review on beam-column FE models developed until the earliest 2000s. Saritas has proposed a 2-node force-based Timoshenko FE based on an enhanced kinematic description. The model assumes a fixed pattern for the shear strains over the cross-section due to the shear forces, evaluated under linear elastic conditions. The general 3D version of this model, also including the torsional effects, is discussed in Sec. 3.3.

Other formulations based on either shear strain or shear stress fixed pattern descriptions have been proposed for both shear and torsional actions, among which it is worth mentioning the contributions in [52–54]. However, because of their assumption, all of them lack in correctly representing the inelastic evolution of the material state during the loading process, as it is shown for the Saritas' model in Sec. 6.4.

By contrast, Le Corvec has proposed a 2-node mixed FE that accounts for the warping of the cross-sections by introducing a specific displacement field, in addition to the standard ones due to the rigid body motions. The model interpolates this warping field over the element volume, adopting a standard approach based on the definition of independent shape functions and introducing a specific number of additional DOFs. Thus, the warping displacement pattern over each element cross-section and the resulting shear stress/strain distribution are treated as element unknowns and are constantly updated during the loading process by imposing specific equilibrium conditions. Moreover, the additional DOFs can be used to apply warping constraints at boundaries and, thus, to account for shear-lag phenomena. Le Corvec has used this model to study the response of 3D steel beams and has demonstrated its high numerical performances and modeling flexibility. Hence, this is chosen as starting point for the model proposed in this work (Sec. 3.4).

Besides the beam-column FEs already mentioned and leaving out the models reviewed in [1, 41, 51], other very recent proposals based on sophisticated interpolatory approaches are worth to be considered. Ferradi et al. [40, 55] and Vieira et al. [56, 57] have described the cross-section out-of-plane displacements through the composition of independent warping modes, evaluated by imposing equilibrium conditions and adopted as independent warping interpolation functions. A similar approach has been proposed by Dikaros et al. [58, 59], who considered four independent warping functions in each spatial direction for the shear actions and two warping functions for the torsional actions; each of them is associated to a specific parameter, which is evaluated during the

loading process by exploiting the longitudinal equilibrium equations.

Finally, Genoese et al. [33, 60] has defined a mixed beam model based on the De Saint Venant beam theory, where the standard shear and torsion warping functions are integrated with an accurate description of the stress fields. The latter are evaluated as the sum of the exact De Saint Venant contribution and some further terms due to variable warping and are introduced in a Hellinger-Reissner functional to obtain a Ritz-Galerkin approximation of the model in terms of generalized cross-section quantities.

1.4 Common materials for engineering structures

Despite other common materials, like masonry and wood, and many innovative materials, like polymers or composites, new civil engineering structures are mostly realized with steel and/or concrete members, because of the good balance these materials offer between mechanical properties and economic costs. Hence, in the last decades, many efforts have been dedicated to study the behavior of both structural steel and concrete, mainly aiming to (1) understand the phenomenological processes characterizing their mechanical responses, (2) develop efficient numerical models to reproduce these responses in structural analyses and (3) improve the material performances, in terms for instance of strength and ductility. Indeed, a wide bibliography is available on the topic, among which it is worth mentioning some fundamental reference books [61–63].

As for many metals and alloys, the mechanical behavior of the steel is basically related to the way the material is composed at the microscopic scale, that is by a crystalline lattice with randomly distributed imperfections, such as dislocations. Small levels of stresses in the material only produce a reversible movement of the singular atoms composing the lattice, resulting in elastic macroscopic deformations. By contrast, high levels of stresses produce a permanent movement of the dislocations inside the lattice, due to the change in the arrangement of its crystalline planes, which possess a low resistance to shear. This results in a macroscopic growth of plastic strains with consequent energy dissipation.

A typical stress-strain curve resulting from an uni-axial test on a steel element (e.g. a reinforcing bar) usually shows an initial elastic branch, corresponding to the reversible deformation of the material, and a subsequent nonlinear plastic one, corresponding to the formation of permanent strains and starting when the stress exceeds the elastic limit σ_y (Fig. 1.3*a*). Moreover, the plastic branch is often characterized by strain-hardening phenomena, i.e. the increase of the material strength produced by the plastic strain growth. In fact, when dislocations are forced to move, they accumulate in some areas of the crystalline lattice and produce an increase of the material stiffness

and strength. The strain-hardening phenomena lead to two fundamental macroscopic effects, which need to be accounted for during the numerical analyses. The first one is usually reproduced in numerical models through the kinematic hardening. It consists in the increase of the material strength observable in monotonic loading conditions and often causing of the *Bauschinger effect*, that is the decrease of the yielding stress in compression, when the material accumulate plastic strains in tension, and vice versa (Fig. 1.3*a*). The second macroscopic effect, instead, is usually reproduced in numerical models through the isotropic hardening and consists in the increase of the yielding stress, for both tension and compression, due to subsequent loading/unloading beyond the elastic limit (Fig. 1.3*b*).

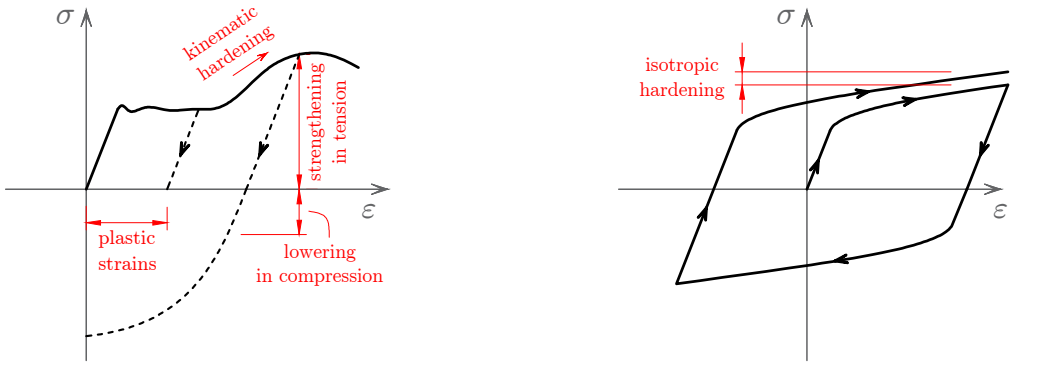

(*a*) Uni-axial stress-strain curve with kinematic hardening.

(*b*) Uni-axial stress-strain curve with isotropic hardening.

Figure 1.3: Schematic representation of typical responses for steel materials.

Finally, another phenomenon characterizes the mechanical response of steel materials. This is the material failure, represented by the progressive break of the intermolecular bonds connecting the crystalline planes and by their physical separation. The steel failure can be caused by high strain levels or by the combined effects of fatigue and, as for reinforcing bars, local instability under cyclic actions. However, this phenomenon is often neglected in the numerical simulations and is only considered in specific structural problems.

Unlike steel materials, showing such a ductile behavior, the mechanical response of concrete materials is influenced by more complex phenomena and, in general, it presents a brittle behavior. Indeed, as concrete is an heterogeneous composite with differently sized aggregate particles embedded in a cement paste, its response mostly depends on the interface bond between the mortar and the aggregates. The microcracks propagation along these interfaces causes the low strength in tension and nonlinear behavior in compression at low stress levels. The creation and growth of microcracks or microvoids and the collapse of the microporous structure is usually referred as *damage*

[64] and translates into a loss of stiffness and strength of the material.

A typical uni-axial stress-strain curve in tension (Fig. 1.4*a*) shows an initial elastic branch up to a level of stress that is usually $10 \div 12$ times smaller than the material peak compressive strength. Above this level the interface microcracks start to grow and usually one of them (or in any case very few of them) propagates very quickly in direction orthogonal to the applied load, leading to an abrupt failure of the material (softening behavior).

As opposed, in compression the material is more ductile. The stress-strain curve in this case (Fig. 1.4*a*) shows a linear elastic behavior up to almost the 30% of the peak compressive strength, because the level of stress does not suffice to generate microcraks propagation. For higher stresses, instead, the material softens, but it still shows a hardening response. In this phase, the transverse tensile strains due to the Poisson effect generate cracks nucleating in the direction parallel to the applied load and, when the maximum strength is reached, the material starts failing, exhibiting a quick and brittle loss of resistance.

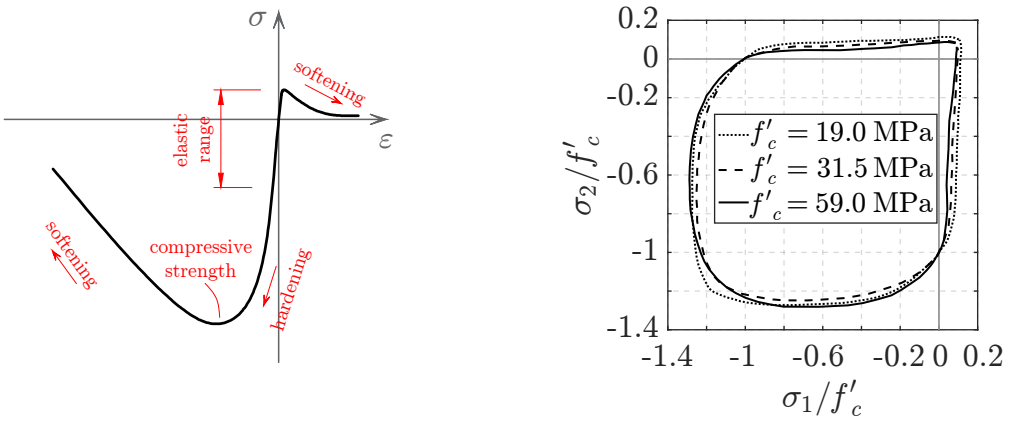

(***a***) Uni-axial stress-strain curve in tension and compression.

(***b***) Bi-axial failure envelope by Kupfer.

Figure 1.4: Typical mechanical monotonic response of concrete materials.

As the damage in compression is mainly produced by the transversal expansion of the material, the application of a confinement pressure in this direction can significantly increase the compressive strength. Indeed, several studies on the concrete behavior under bi-axial compression have shown that the maximum compressive strength can be increased up to $20 \div 25\%$ with respect to the uni-axial case and much higher levels of resistance can be obtained for tri-axial compressive stress states [65]. For example, Fig. 1.4*b* shows the bi-axial failure envelope as results from the experimental studies by Kupfer et al. [66] on three different types of concrete with an unconfined uni-axial compressive strength of 19.0 MPa, 31.5 MPa and 59.0 MPa.

The mechanical behavior under cyclic loads is also important. From a computational point of view it is characterized by two phenomena, that need to be taken into account in numerical simulations. The first one is the unilateral effects between tension and compression. Considering a material element volume subjected to tensile stresses, each time a crack opens, the element exhibits stiffness lowering, because the stress transmission between the two facing surfaces defining the crack is no longer possible. When the load is reversed in compression and the contact between the two surfaces is restored, part or all the stiffness lost in the tensile phase is recovered, that is the damage created in tension usually does not affect the compressive behavior of the material. By contrast, when the material is damaged in compression, the loss of stiffness is not recovered when reloaded in tension, i.e. the damage created in compression also affects the tensile response of the material. A schematic representation of this phenomenon is shown in Fig. 1.5*a*.

The second relevant aspect is the the growth of plastic strains. Indeed, despite concrete is mainly a brittle material, plastic strains occur upon unloading and reloading, in both tension and compression. For instance, Fig. 1.5*b* shows the experimental results by Karsan and Jirsa [67] on the uni-axial cyclic behavior in compression of a concrete specimen. In numerical models, the presence of plastic strains is modeled through the coupling of damage and elasto-plastic models.

These mechanical phenomena also characterize the response of masonry and composite materials. Hence, in structural simulations their behavior is numerically described through damage formulations that are similar to those adopted for concrete.

The following discussion limits to a literature review on the most consolidate three-dimensional (3D) material models for standard concrete, focusing on continuum damage and plastic-damage formulations.

1.5 Existing 3D damage and plastic-damage material models for concrete

In last decades, many constitutive models have been developed to reproduce the behavior of damaging materials, following different approaches. The most accurate way for describing the evolution of cracking phenomena is the adoption of FE models with embedded discontinuities, i.e. models that represent the discontinuities due to the crack opening in terms of displacement [68] and/or strains and stresses [69] discontinuities. These are based on the fracture mechanics theory and on the studies on brittle materials started by Griffith [70] in 1921. They usually refers to the definition of cohesive-zone models [71]. Despite their accuracy, embedded discontinuity models

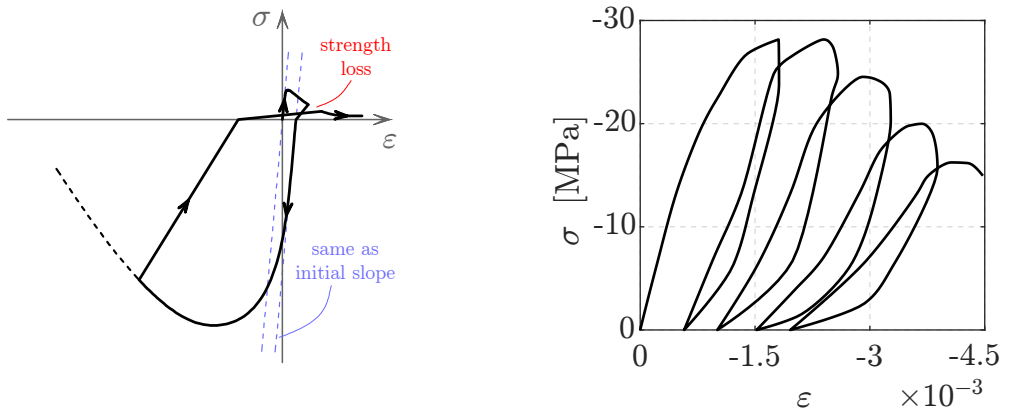

(*a*) Schematic uni-axial stress-strain curve - Unilateral effects.

(*b*) Experimental outcomes in compression by Karsan and Jirsa.

Figure 1.5: Typical mechanical cyclic response of concrete materials.

are very onerous and not suitable for large scale structure analysis. An accurate review of these models can be found in [72] and it is not pursued in this work.

A different approach considers the adoption of nonlinear models based on elasticity theory. These models do not represent the cracks as embedded in the material, but they only take into account the damaging effects by defining a nonlinear elastic constitutive relation that aims to reproduce the mechanical behavior of the material [73], usually starting from empirical considerations. Because of their simplicity, this kind of models has been extensively adopted within beam-column FE formulations, especially equivalent one-dimensional (1D) strain models, that are perfectly suitable for Euler-Bernoulli beam formulations (see Sec. 3.2). Indeed, some robust and consolidate proposals, such as [74, 75] are nowadays commonly used in both research and professional applications. However, the FE formulation considered in this work requires the adoption of 3D constitutive relations, as discussed in the following sections and in Chap. 3. Hence, 1D material models are not taken into account in this review. Bi-dimensional (2D) and 3D elastic nonlinear relations have been proposed as well, even though they consider more complex assumptions. Very performing formulations of this family belong to the class of the smeared cracks approaches. In these models, cracked concrete is simulated as a continuous medium with anisotropic characteristics that depend on the crack orientations and on their evolution during the loading process. A detailed review on smeared crack approaches is provided by Bairán [41], starting from the pioneering works on the Modified Compression Field Theory by Vecchio and Collins [76]. Similar advanced constitutive models, belonging to the class of the anisotropic damage formulations, are known as microplane models [77]. These allow to consider preferential directions along which the material stiffness degrades more than others, usually defining differ-

ent damage variables to independently modify the component of the elastic stiffness tensor [72].

Many attempts of defining simple but accurate 3D formulations have been made through nonlinear models based on damage mechanics, thus referred to as damage models. In this formulations, linear elastic constitutive relations are in general modified by introducing some scalar variables that are used to reduce the material stiffness and strength and, thus, representing the softening behavior of the concrete (see Sec. 2.3). One of the first proposals of damage models dates back to the works by Mazars [78] and Lemaitre [79]. In 1986 Mazars introduced an isotropic damage model based on the definition of two damage variables D_t and D_c, independently describing the material degradation under tensile and compressive stresses. The combination of the two damage variables provides the total damage parameter D, used to describe the initial elastic stiffness degradation, and results from the definition of two weighting coefficients α_t and α_c, linked to the tensile and the compressive stresses, that is:

$$D = \alpha_t D_t + \alpha_c D_c \tag{1.1}$$

The model is only suitable for monotonic loading simulations and it does not account for the residual plastic strains experimentally observed in concrete after unloading. However, many refinements of the original formulation have been proposed during the years [64, 80], until the latest one by Mazars et al. [81] in 2014, which allows for cyclic and dynamic loading simulations, yet neglecting the plastic phenomena. In this case, one damage variable D is defined, but this is evaluated from the combination of two thermodynamic variables Y_t and Y_c (see also Sec. 2.3):

$$Y = r\,Y_t + (1 - r)Y_c \tag{1.2}$$

In Eq. (1.2), r is a weighting factor to identify the tensile/compressive state and evaluated from the principal effective stress. Its definition has been proposed for the first time by Lee and Fenves [82], as discussed later.

Almost simultaneously to Mazars, in 1985 Lemaitre proposed the first damage model coupled with a Von Mises plasticity criterion to describe the plastic strain growth in the material, but considering only one damage parameter to represent the material stiffness degradation. Although Lemaitre underlined the relevant role of the plastic strains in the nonlinear cyclic response of concrete, the adoption of the Von Mises criterion and the definition of one damage parameter represent a drawback of the model, as the description of the non-symmetric behavior in tension and compression results inaccurate.

The adoption of other plasticity theories for the definition of plastic-damage formulations have been extensively investigated [83]. Indeed, non-symmetric plastic formulations are usually preferred over the classical Von Mises and J2 plasticity [63], which are widely used to represent steel materials. The easiest extension of the J2 model to consider the non-symmetric behavior in tension and compression is known as Drucker-Prager plasticity [84], which is described in Sec. 2.2 and is adopted for the plastic-damage model proposed in Sec. 2.4. This represents the 3D generalization of the Mohr-Coulomb criterion, usually adopted for soils and considering higher resisting stresses under compression and lower resisting stresses under tension.

Lubliner et al. [85] have proposed an enhanced yield criterion, known as Barcelona model, and have adopted it in a one-parameter damage model, later modified by Lee and Fenves [82] to define a two-parameter plastic-damage formulation. In their model, Lee and Fenves have proposed a specific way to combine the tensile and the compressive damaging responses, based on the evaluation of the weighting factor r, later on considered by Mazars [81] (Eq. (1.2)). In [82] the factor r is adopted to combine the principal plastic strains, used to evaluate the damage variable, and resulting as:

$$\dot{\boldsymbol{\varepsilon}}^p = \delta_t \, r \, \dot{\boldsymbol{\varepsilon}}^p_{max} + \delta_c \, (1 - r) \dot{\boldsymbol{\varepsilon}}^p_{min} \tag{1.3}$$

Eq. (1.3) allows a correct representation of the unilateral damage recovering upon load reversal.

Comi and Perego [86] have considered two scalar damage variables, D_t and D_c, and have used them to directly modify the total stress tensor $\boldsymbol{\sigma}$. They have proposed a specific combination of the tensile and the compressive stresses, resulting as follows:

$$\boldsymbol{\sigma} = 2\mu(1 - D_t)(1 - D_c)\boldsymbol{\epsilon} + K \, (1 - D_t)(1 - D_c)\boldsymbol{\varepsilon}^+ + K \, (1 - D_c)\boldsymbol{\varepsilon}^- \tag{1.4}$$

where μ and K are the initial undamaged shear and bulk moduli, respectively, $\boldsymbol{\epsilon}$ is the deviatoric part of the strain tensor $\boldsymbol{\varepsilon}$ and $\boldsymbol{\varepsilon}^{+/-} = trace^{+/-}(\boldsymbol{\varepsilon}) \, \mathbf{I}$ are its hydrostatic positive/negative parts. In other words, they use (1) a combination of both the tensile and the compressive damage variables to modify the deviatoric part of the stress tensor associated to the shear effects, (2) the same combination to modify the hydrostatic tensile part of the stress tensor and (3) the compressive damage variable to modify the hydrostatic compressive part. In this way, the shear component are influenced by both the tensile and the compressive damage, the pure compressive behavior is influenced by the compressive damage, to represent the unilateral effects, and the pure tensile behavior is influenced by the tensile damage as well as by the compressive damage produced under previous compressive states of the loading history.

A different model, but presenting similar features, has been proposed by Faria and Oliver [87], who have defined two distinct damage variables, d^+ and d^-, as well and have used them to compute the damaged stresses from the positive and negative part of the effective stress tensor, $\bar{\boldsymbol{\sigma}}^+$ and $\bar{\boldsymbol{\sigma}}^-$, i.e.:

$$\boldsymbol{\sigma} = (1 - d^+)\bar{\boldsymbol{\sigma}}^+ + (1 - d^-)\bar{\boldsymbol{\sigma}}^- \tag{1.5}$$

In this case $\bar{\boldsymbol{\sigma}}^+$ and $\bar{\boldsymbol{\sigma}}^-$ are simply defined considering the sign of the principal effective stresses.

Finally, Addessi et al. [2] have proposed a one-parameter plastic-damage model, which is modified in this work to formulate the constitutive relationship proposed in Sec. 2.4. In [2], the damage variable D is evaluated from the combination of two equivalent strain measures, Y_t and Y_c, describing the tensile and the compressive behavior, respectively, i.e.:

$$Y = \frac{Y_t}{Y_{0t}} + \frac{Y_c}{Y_{0c}} \tag{1.6}$$

Y_{0t} and Y_{0c} being the initial damage thresholds. Moreover, the damage evolution law depends on two material parameters, a and K, which are also obtained from specific combinations of the tensile and the compressive ones, $a_{t/c}$ and $K_{t/c}$, on the basis of appropriate weighting coefficients, $\alpha_{t/c}$, i.e.:

$$a = \alpha_t\, a_t + \alpha_c\, a_c \qquad \text{and} \qquad K = \alpha_t \frac{K_t}{Y_{0t}} + \alpha_c \frac{K_c}{Y_{0c}} \tag{1.7}$$

Even though the model considers a non-symmetric plastic criterion, its main drawback is related to the assumption in Eq. (1.6), which does not allow to represent the unilateral effects between tension and compression under cyclic loading. The formulation proposed in Sec. 2.4 overcomes this issue, proposing a different approach to combine the tensile and the compressive degrading effects.

1.6 Objectives

The present work focuses on the study of the cross-section warping effects in RC frames subjected to relevant shear and torsional loads. Its main goal is the definition of efficient tools for the numerical description of the non-uniform shear stress/strain distributions due to the warping and their interaction with the damaging phenomena typical of concrete-like materials. In particular, the objectives of the work are:

1. The extension of the beam-column finite element formulation proposed by Le Corvec [1] to the analysis of RC structures. This is accomplished through two

fundamental tasks: the definition of a material constitutive law, which is able to correctly represent the concrete behavior under any kind of stress/strain state; the introduction of an efficient regularization technique to prevent the damage/strain localization and mesh sensitivity issues. For the first task, the idea is to define and implement a new 3D plastic-damage model on the basis of the one proposed in [2] and to develop an optimized procedure for condensing out the stress components that are irrelevant for the beam formulation. For the second task, instead, an integral nonlocal formulation is applied to the adopted beam-column FE.

2. The extension of the beam-column finite element formulation proposed by Le Corvec to the adoption of new kinds of interpolation functions for the description of the warping displacements over the element cross-section. In particular, the adoption of Hermite polynomials is explored, aiming to reduce the total number of additional warping DOFs introduced in the numerical model, but preserving the accuracy of the solution. Moreover, a new procedure to remove the cross-section rigid body motion from the warping displacement field is investigated.

3. The formulation of a new a consistent nonlinear solution algorithm for finite element proposed in [1]. In particular, the idea is to define a non-iterative solution scheme, more suitable for the analysis of nonlinear softening behavior and numerically more efficient, as opposed to the original iterative proposal.

Adopting the beam-column FE formulation, with the above enhancements, this study aims to investigate the relevance of correctly representing the material shear stress/strain distributions inside the element volume, when dealing with the analysis of RC frames, and to analyze the influence of the boundary effects, that is the introduction of warping constraints and the related shear-lag effects. To this end, a fiber discretization of the element cross-sections is considered, to capture the multi-axial coupling of axial, shear, flexural and torsional components.

1.7 Work outline

The dissertation is organized as follows: after this introductive chapter, Chap. 2 describes the proposed 3D plastic-damage constitutive model, with a preliminary description of two elasto-plastic models (the J2 and the Drucker-Prager plasticity) and of classical damage models. Chap. 3 presents the beam-column formulation and discusses the refinements for the warping displacement interpolation and the variational formulation; an overview of the standard Euler-Bernoulli and the standard Timoshenko beam models is also given, together with the description of the enhanced model by

Saritas [51], extended to the 3D case. Chap. 4 analyzes the classical regularization techniques for force-based and mixed beam-column FEs and illustrates the adopted approach based on a nonlocal formulation. Chap. 5 examines all the FE computational aspects, starting from the description of the non-iterative solution algorithm for the beam-column Element State Determination, moving to the description of the Section State Determination and of the fiber section discretization and concluding with the description of the proposed plastic-damage material model linearized solution procedure; this chapter also presents the proposed nonlinear static condensation approach. Finally, Chap. 6 illustrates the correlation studies performed to validate the proposed numerical models and investigates their computational abilities, with the overall concluding remarks presented in Chap. 7.

Chapter 2

3D material constitutive model

2.1 Introduction

Metal materials and cementitious materials are the most adopted for engineering civil structures.

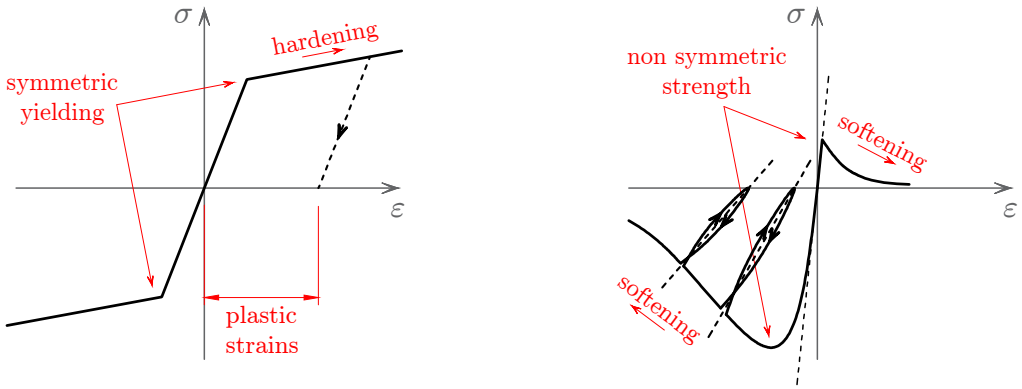

(*a*) Ductile elasto-plastic behavior.

(*b*) Fragile damage behavior.

Figure 2.1: Schematic representation of ductile and fragile material response.

Metals, like structural steel and aluminum, are homogeneous materials exhibiting a ductile mechanical behavior. From a numerical point of view, the description of their response is relatively simple and it is usually performed through elasto-plastic constitutive models. In fact, their behavior under severe loading conditions presents few key aspects (Fig. 2.1*a*): *symmetric response*, that is equal nonlinear behavior in tension and compression; *strain hardening*, that is positive material stiffness after yielding; *residual plastic strains*, that is inelastic residual deformations occurring after the loading removal. By contrast, cementitious materials, like concrete and masonry, are heterogeneous materials exhibiting a fragile mechanical behavior. Their numerical

simulation is more complex and requires the adoption of models able to account for the damaging effects. The damage is the onset and growth of micro- and macro-cracks, which produce a reduction in stiffness and strength of the material, up to the collapse of the structure. In particular, the effects of damage generally implies (Fig. 2.1*b*): *non symmetric behavior*, that is tensile strength lower then the compressive strength; *strain softening*, that is negative material stiffness in the inelastic branch of the response; *damage irreversibility*, that is the reduction in strength and stiffness due to the damage can not be recovered.

To simplify the description of these complex properties, damage models are usually formulated without describing the heterogeneity of the material and its microscopic behavior, but referring to a representative volume element, which describes all the material properties by homogenized variables. In other words, traditional stress-strain constitutive relations are used to model the material response, with the inclusion of internal variables that represent the degrading effects occurring during the loading.

However, as for metals, inelastic deformations may occur for brittle material as well, due to inter-granular displacements. Hence, the more advanced formulations for concrete-like materials use to combine damage models with elasto-plastic models, to account for both the degrading effects and the plastic strain growth. These are thus defined plastic-damage models.

This chapter describes a new 3D plastic-damage material model developed to reproduce the behavior of concrete-like materials under complex tri-axial stress state. The following two sections give an introduction of the main criteria that are the basis of the proposed model. In particular, Sec. 2.2 summarizes the fundamental equations of the standard J2 and Drucker-Prager plasticity; the latter is incorporated in the proposed model to describe the evolution of the plastic strains during the damaging process. Sec. 2.3, instead, presents the basic concepts for the definition of a general damage model, giving some classical examples from the literature. Finally, Sec. 2.4 describes the model developed in this work. The entire discussion refers to the Voigt notation of the Cauchy stress and total strain tensors, which are here indicated with the six-component vectors $\boldsymbol{\sigma}$ and $\boldsymbol{\varepsilon}$, respectively:

$$\boldsymbol{\sigma} = \left\{ \begin{array}{cccccc} \sigma_x & \sigma_y & \sigma_z & \tau_{xy} & \tau_{xz} & \tau_{yz} \end{array} \right\}^T \qquad \text{and} \qquad \boldsymbol{\varepsilon} = \left\{ \begin{array}{cccccc} \varepsilon_x & \varepsilon_y & \varepsilon_z & \gamma_{xy} & \gamma_{xz} & \gamma_{yz} \end{array} \right\}^T$$

2.2 J2 and Drucker-Prager plasticity

The J2 plasticity model [63] is a classical 3D stress-strain relation to describe the evolution of the plastic strains inside the materials. This is based on the decomposition

of the total strain $\boldsymbol{\varepsilon}$ into the elastic part $\boldsymbol{\varepsilon}^e$ and the plastic part $\boldsymbol{\varepsilon}^p$, leading to the definition of the following elastic constitutive law:

$$\boldsymbol{\sigma} = \mathbf{C}\,(\boldsymbol{\varepsilon} - \boldsymbol{\varepsilon}^p) = \mathbf{C}\,\boldsymbol{\varepsilon}^e \tag{2.1}$$

where $\mathbf{C}$ is the elastic isotropic stiffness matrix, depending on the Young's modulus E and on the Poisson ratio ν. During a general loading path, a Von Mises yield surface f governs the plastic growth, according to both an isotropic and kinematic hardening law. This yield surface can be expressed as:

$$f_{J2}(\boldsymbol{\sigma}, \boldsymbol{\zeta}, \alpha) = |\boldsymbol{\pi} - \boldsymbol{\zeta}| - \sqrt{\frac{2}{3}}(\sigma_y + H_i\alpha) \tag{2.2}$$

where $\boldsymbol{\pi}$ is the deviatoric part of the stress vector $\boldsymbol{\sigma}$ and is computable through the operator $\mathbf{P}$, i.e.:

$$\boldsymbol{\pi} = \mathbf{P}\,\boldsymbol{\sigma} \tag{2.3}$$

with:

$$\mathbf{P} = \frac{1}{3}\begin{bmatrix} 2 & -1 & -1 & 0 & 0 & 0 \\ -1 & 2 & -1 & 0 & 0 & 0 \\ -1 & -1 & 2 & 0 & 0 & 0 \\ 0 & 0 & 0 & 3 & 0 & 0 \\ 0 & 0 & 0 & 0 & 3 & 0 \\ 0 & 0 & 0 & 0 & 0 & 3 \end{bmatrix} \tag{2.4}$$

$\boldsymbol{\zeta}$ is the kinematic back stress and α the isotropic hardening variable. Their evolution laws are related to the rate of change of plastic deformations $\dot{\boldsymbol{\varepsilon}}^p$, following an associative flow rule and resulting as:

$$\dot{\boldsymbol{\varepsilon}}^p = \dot{\lambda}\frac{\partial f}{\partial \boldsymbol{\sigma}} = \dot{\lambda}\,\mathbf{n}, \qquad \dot{\alpha} = \sqrt{\frac{2}{3}}\,\dot{\lambda}, \qquad \dot{\boldsymbol{\zeta}} = \frac{2}{3}H_k\dot{\boldsymbol{\varepsilon}}^p \tag{2.5}$$

where the $\dot{\diamond} = \partial\diamond/\partial t$ indicates the derivative with respect to a pseudo-time variable t. In the Eqs. (2.5), $\mathbf{n} = \boldsymbol{\eta}/|\boldsymbol{\eta}|$ is the normal to the yield surface, with $\boldsymbol{\eta} = \boldsymbol{\pi} - \boldsymbol{\zeta}$, and $\dot{\lambda}$ is the plastic multiplier, which is assumed to obey the following Karush–Kuhn–Tucker complementary conditions:

$$\dot{\lambda} \geq 0, \qquad f_{J2}(\boldsymbol{\sigma}, \boldsymbol{\zeta}, \alpha) \leq 0, \qquad \dot{\lambda} f_{J2}(\boldsymbol{\sigma},\boldsymbol{\zeta},\alpha)=0 \tag{2.6}$$

and the consistency requirement:

$$\dot{\lambda}\dot{f_{J2}}(\boldsymbol{\sigma}, \boldsymbol{\zeta}, \alpha) = 0 \tag{2.7}$$

The incremental form of Eq. (2.1) is expressed as:

$$\dot{\boldsymbol{\sigma}} = \mathbf{C}^{ep}\,\dot{\boldsymbol{\varepsilon}} \tag{2.8}$$

where $\mathbf{C}^{ep}$ is the elasto-plastic tangent stiffness matrix. During an elastic loading or unloading state, this is equal to the elastic stiffness $\mathbf{C}$, whereas during a plastic loading state it is evaluated as:

$$\mathbf{C}^{ep} \equiv \mathbf{C}^{ep}_{J2} = \mathbf{C} - \frac{4G^2\,\dot{\lambda}}{|\boldsymbol{\eta}|}\left(\mathbf{I} - \frac{\mathbf{1}\,\mathbf{1}^T}{3} - \mathbf{n}\,\mathbf{n}^T\right) - \frac{4G^2\,\mathbf{n}\,\mathbf{n}^T}{2G + 2/3(H_i + H_k)} \tag{2.9}$$

where $\mathbf{I}$ is the 6×6 identity matrix and $\mathbf{1}$ is a vector that extracts the volumetric part of $\boldsymbol{\sigma}$, resulting as:

$$\mathbf{1} = [1 \quad 1 \quad 1 \quad 0 \quad 0 \quad 0]^T \tag{2.10}$$

G and K are the shear and bulk moduli, respectively, while σ_y, H_i and H_k are material parameters denoting the yield strength, the isotropic hardening modulus and the kinematic hardening modulus, respectively. In the general case, the isotropic and kinematic hardening modulus can be assumed as function of α to account for nonlinear hardening evolution [63], i.e. $H_i(\alpha)$ and $H_k(\alpha)$. However the present work considers only the case of linear hardening, that is constant H_i and H_k are assumed.

The plastic yield function at the first onset of the plastic process ($\boldsymbol{\varepsilon}^p = \mathbf{0}$, $\boldsymbol{\zeta} = \mathbf{0}$ and $\alpha = 0$) is plotted in Fig. 2.2 adopting the parameters in Table 2.1. Fig. 2.2*a*

Table 2.1: Mechanical parameters adopted for the J2 plasticity.

$E = 30\,000\,\text{MPa}$	$\nu = 0.2$	$\sigma_y = 30.0\,\text{MPa}$	$H_i = 0.005\,E$	$H_k = 0.020\,E$

shows the yield function in the principal stress space where f_{J2} (green surface) is a cylinder with the axis parallel to the octaedric axis. Its representation in the $\sigma_1 - \sigma_2$ stress plane is the ellipse in Fig. 2.2*b*, showing that the yield function intersects all the principal axis at the same value $\pm\sigma_y$, which is the yield strength of the material. This results in a symmetrical behavior of the model in the tensile and compressive stress state conditions, as observed in Fig. 2.4*a*, where an example of cyclic uni-axial response is given.

Because of this symmetry in the mechanical response, the J2 plasticity model is more suitable for the representation of metal material. On the contrary, to govern the evolution fo the plastic strains $\boldsymbol{\varepsilon}^p$ in brittle material, the Drucker-Prager plasticity model with linear isotropic and kinematic hardening [84, 88, 89] represents a better choice. This model can be seen as an extension of the J2 plasticity, where the yield function is assumed to be also dependent on the volumetric part of the stress tensor,

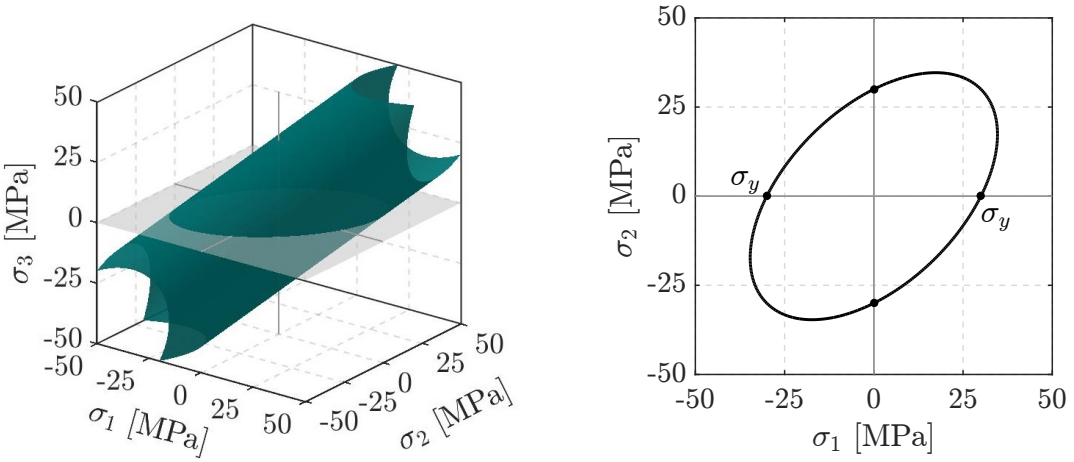

(*a*) In the principal stress space $\sigma_1 - \sigma_2 - \sigma_3$. **(*b*)** In the principal stress plane $\sigma_3 = 0$.

Figure 2.2: Plastic yield function f_{J2} at the first onset of the plastic process.

that is on the first invariant $I_1 = \mathbf{1}^T \bar{\boldsymbol{\sigma}}$:

$$f_{DP}(\boldsymbol{\sigma}, \boldsymbol{\zeta}, \alpha) = |\boldsymbol{\pi} - \boldsymbol{\zeta}| - \sqrt{\frac{2}{3}}(\sigma_y + H_i \alpha) + \mu\, I_1 = f_{J2} + \mu\, I_1 \tag{2.11}$$

with μ being an additional mechanical parameter governing the ratio between the yield strength in tension and compression. In fact, the term $\mu\, I_1$ in Eq. (2.11) transforms the cylindrical yield function of the J2 plasticity in a cone having the same axis and the tip in the tri-axial tensile domain. Following [90], the yield strength σ_y and the frictional coefficient μ can be evaluated on the basis of the uni-axial tensile and compressive strengths, σ_t and σ_c, as:

$$\sigma_y = \frac{2\,\sigma_c\,\sigma_t}{\sigma_c + \sigma_t}, \qquad \mu = \sqrt{\frac{2}{3}}\left(\frac{\sigma_c - \sigma_t}{\sigma_c + \sigma_t}\right) \tag{2.12}$$

The 3D and 2D representation of the Drucker-Prager yield function are given in Fig. 2.3 adopting the parameter in Table 2.2. In this case, the yield function intersects the

Table 2.2: Mechanical parameters adopted for the J2 plasticity.

$E = 30\,000$ MPa	$\nu = 0.2$	$\sigma_t = 3.3$ MPa $\sigma_c = 30.0$ MPa	$H_i = 0.005\,E$	$H_k = 0.020\,E$

negative axes at $-\sigma_c$ and the positive axis at $\sigma_t < |\sigma_c|$, allowing for a non-symmetric behavior in the tensile and compressive stress state conditions. Fig. 2.4*b* gives an example of cyclic uni-axial response for this model.

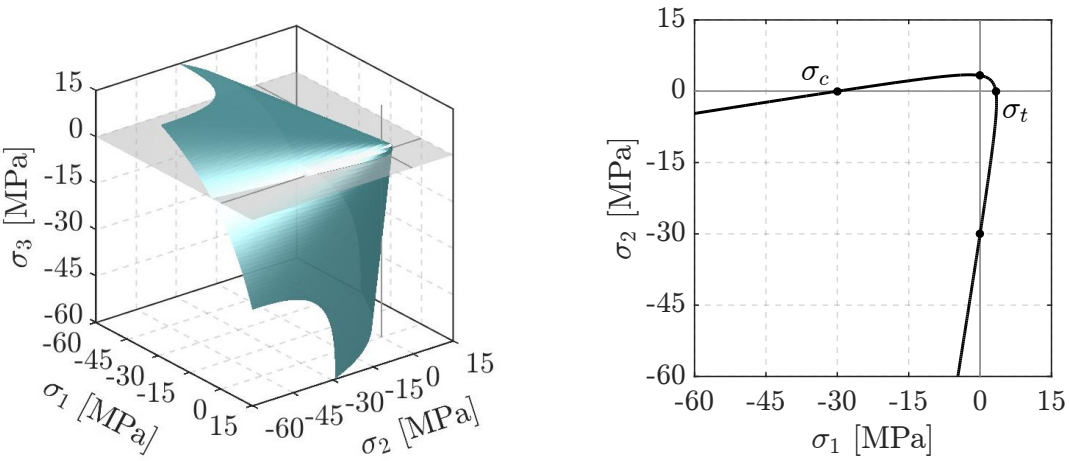

(*a*) In the principal stress space $\sigma_1 - \sigma_2 - \sigma_3$. **(*b*)** In the principal stress plane $\sigma_3 = 0$.

Figure 2.3: Plastic yield function f_{DP} at the first onset of the plastic process.

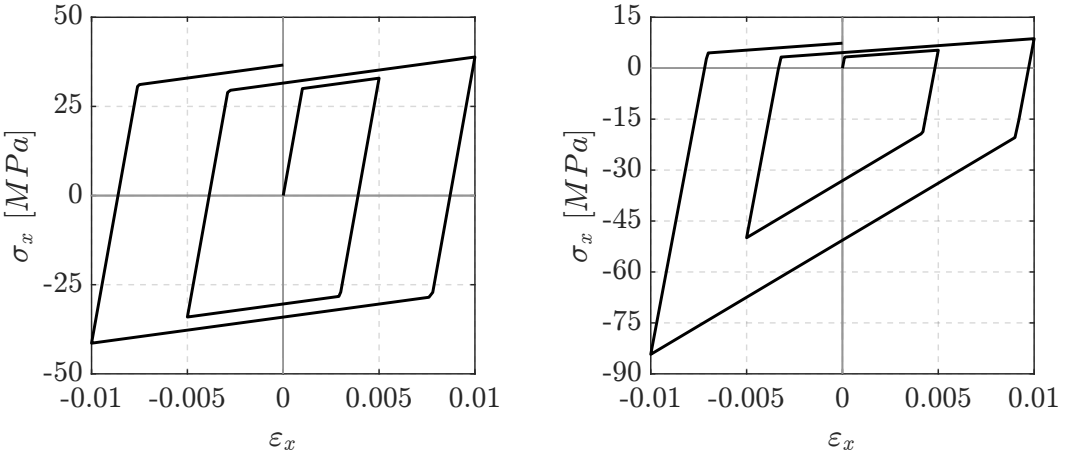

(*a*) J2 plasticity. **(*b*)** Drucker-Prager plasticity.

Figure 2.4: Cyclic uni-axial behavior under imposed strain history for the J2 and Drucker-Prager model (parameters in Table 2.1 for J2 and parameters in Table 2.2 for Drucker-Prager).

For the Drucker-Prager plasticity the elasto-plastic stiffness can be evaluated as:

$$\mathbf{C}^{ep} \equiv \mathbf{C}^{ep}_{DP} = \mathbf{C}^{ep}_{J2} - \frac{6GK\mu\, \mathbf{n}\, \mathbf{1}^T}{2G + 2/3(H_i + H_k)} \tag{2.13}$$

while all the other equations defined for the J2 plasticity remain the same. In fact, when $\sigma_t = \sigma_c$, the Drucker-Prager model degenerates in the J2 one, because $\sigma_y = \sigma_t = \sigma_c$ and $\mu = 0$.

2.3 Basic concepts for damage models

When a brittle material is subjected to high levels of stresses, micro-cracks, voids and dislocations can emerge. These produce a reduction in both the stiffness and strength, which need to be accounted for in a numerical model. To describe the behavior of brittle material, characterized by these degrading mechanisms, a common approach is the adoption of isotropic damage constitutive models. The basic idea of these models is to represent the macroscopic behavior of the general infinitesimal volume of the material with a classical isotropic stress–strain relation, introducing into the stress-strain relationship an internal scalar variable D, representing all the microscopic phenomena. In particular, the total stress–strain relation representing the material response is defined considering an effective stiffness matrix $\tilde{\mathbf{C}}$, exspressed as a function of the internal variable D that is used to modify the initial elastic stiffness matrix $\mathbf{C}$:

$$\boldsymbol{\sigma} = \tilde{\mathbf{C}}\left(\mathbf{C}, D\right)\, \boldsymbol{\varepsilon} \tag{2.14}$$

An easy way to define the evolution of $\tilde{\mathbf{C}}$ is to assume the strain equivalence principle, stating that the strain state of the real damaged material is the same state considered in the constitutive law and represented by the strain vector $\boldsymbol{\varepsilon}$. This principle leads to the following expression of Eq. (2.14):

$$\boldsymbol{\sigma} = (1 - D)\, \mathbf{C}\boldsymbol{\varepsilon} = (1 - D)\, \bar{\boldsymbol{\sigma}} \tag{2.15}$$

with $\tilde{\mathbf{C}}\left(\mathbf{C}, D\right) = (1 - D)\, \mathbf{C}$ and D ranging from 0 to 1, where $D = 0$ corresponds to the initial undamaged state of the material and $D = 1$ to the complete degraded state. The vector $\bar{\boldsymbol{\sigma}} = \mathbf{C}\,\boldsymbol{\varepsilon}$ is called effective stress vector and it represents the stress state in an equivalent fictitious material where no damage occurs. This is equal to:

$$\bar{\boldsymbol{\sigma}} = \mathbf{C}\,\boldsymbol{\varepsilon} = \frac{\boldsymbol{\sigma}}{(1 - D)} \tag{2.16}$$

An alternative way to define the evolution of $\tilde{\mathbf{C}}$ is to assume the complementary energy equivalence principle [91], stating that the complementary energy of an infinitesimal real damaged material volume is equivalent to that resulting from the constitutive law. In this case $\tilde{\mathbf{C}}\left(\mathbf{C}, D\right) = (1 - D)^2\, \mathbf{C}$, that is Eq. (2.14) become:

$$\boldsymbol{\sigma} = (1 - D)^2\, \mathbf{C}\,\boldsymbol{\varepsilon} = (1 - D)^2\, \bar{\boldsymbol{\sigma}} \qquad \text{with} \quad \bar{\boldsymbol{\sigma}} = \mathbf{C}\,\boldsymbol{\varepsilon} = \frac{\boldsymbol{\sigma}}{(1 - D)^2} \tag{2.17}$$

In both cases, the evolution of D depends on the mechanical state of the material and, in general, on some internal variables Y_i (with $i = 1, 2, \dots$), evolving on the basis

of a loading-unloading damage limit function $f_D(\boldsymbol{\sigma}, \boldsymbol{\varepsilon}, Y_i)$. According to the second law of the thermodynamics, the damage is an irreversible process satisying the Clausius-Duhem inequality. Its evolution is ruled by Karush-Kuhn-Tucker conditions and the consistency condition, resulting as:

$$\dot{D} \geq 0 \qquad f_D(\boldsymbol{\sigma}, \boldsymbol{\varepsilon}, Y_i) \leq 0 \qquad \dot{D}\, f_D(\boldsymbol{\sigma}, \boldsymbol{\varepsilon}, Y_i) = 0 \qquad \dot{D}\, \dot{f}_D(\boldsymbol{\sigma}, \boldsymbol{\varepsilon}, Y_i) = 0 \tag{2.18}$$

For instance, in the pioneering model proposed by Mazars in 1986 [78], based on the strain equivalence principle and on the assumption of zero plastic strains, the damage limit function depends on an equivalent strain measure ε_{eq} and on an internal variable Y, which is function of D, i.e.:

$$f_D(\varepsilon_{eq}, D) = \varepsilon_{eq} - Y(D) \tag{2.19}$$

The equivalent strain measure ε_{eq} is defined as function of the positive (tensile) principal strains ε_i, with $i = 1, \ldots, 3$:

$$\varepsilon_{eq} = \sqrt{\sum_{i=1}^{3} \langle \varepsilon_i \rangle_+^2} \tag{2.20}$$

where $\langle \diamond \rangle_+$ denotes the Mac'Auley brackets, selecting the positive part of the variable $\diamond$, and $Y(D)$ is the internal variable related to the damage growth, so that $Y(0) = \varepsilon_{0,t}$ is the initial damage threshold. D is obtained combining two different variables, D_t and D_c, for the tensile and the compressive behavior, respectively, introduced to represent the unilateral effects, typical of the concrete-like materials. The following evolution laws are stated for both:

$$D_h = 1 - \frac{\varepsilon_{0,t}(1 - A_h)}{\varepsilon_{eq}} - A_h\, e^{-B_h(\varepsilon_{eq} - \varepsilon_{0,t})} \qquad \text{with} \quad h = t, c \tag{2.21}$$

The latest version of the model, called μ model [81], considers two different equivalent strain measures, defined as:

$$\varepsilon_{eq,t} = \frac{I_{\varepsilon 1}}{2\,(1 - 2\,\nu)} + \frac{\sqrt{3 J_{\varepsilon 2}}}{2\,(1 + \nu)} \qquad \varepsilon_{eq,c} = \frac{I_{\varepsilon 1}}{5\,(1 - 2\,\nu)} + \frac{6\sqrt{3 J_{\varepsilon 2}}}{5\,(1 + \nu)} \tag{2.22}$$

where $\varepsilon_{eq,t}$ is related to the cracking phenomena in tension and is associated to the internal variable Y_t, whereas $\varepsilon_{eq,c}$ is related to the crushing phenomena in compression and is associated to the internal variable Y_c. Hence, two limit functions are considered, resulting as:

$$f_t(\varepsilon_{eq,t}, Y_t) = \varepsilon_{eq,t} - Y_t, \qquad f_c(\varepsilon_{eq,c}, Y_c) = \varepsilon_{eq,c} - Y_c \tag{2.23}$$

$I_{\varepsilon 1}$ and $J_{\varepsilon 2}$ are the first invariant of the strain tensor and the second invariant of the deviatoric strain tensor, respectively. The damage variable D is expressed as function of a single internal variable Y, following the same evolution laws (2.21):

$$D = 1 - \frac{Y_0(1-A)}{Y} - A\, e^{-B(Y-Y_0)} \tag{2.24}$$

where Y is a combination of Y_t and Y_c, with Y_0 its initial threshold (see [64, 80, 81] for the details of the two models). Fig. 2.5 shows an example of (a) cyclic uni-axial response for this model, (b**i**) the assigned strain history and (b**ii**) the related evolution of the damage variable. In the same figures, the main steps of the two cycles performed in the loading path are indicated with capital letters.

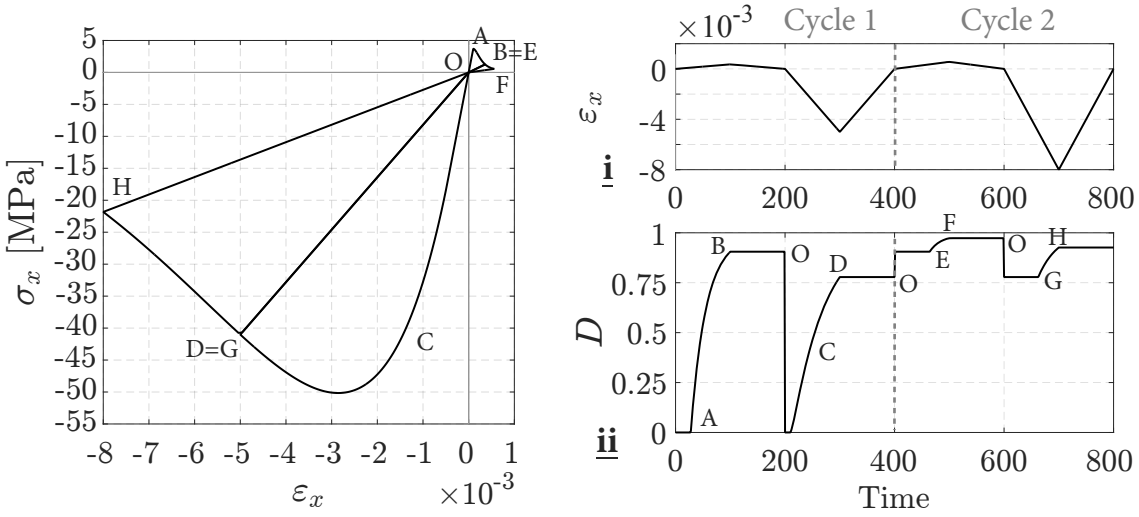

(***a***) Stress/strain relation. (***b***) **i**: Strain history - **ii**: Damage evolution.

Figure 2.5: Cyclic uni-axial behavior under imposed strain history for the μ model.

Many other formulations of damage models can be found in the literature, e.g. [82,86,87], proposing different definitions of the limit functions, of the equivalent strain measures and of the damage evolution laws. For instance, Simo and Ju [92] define the equivalent strain measure as equal to the material internal energy:

$$\varepsilon_{eq} = \frac{1}{2}\boldsymbol{\varepsilon}^T\, \mathbf{C}\, \boldsymbol{\varepsilon} = \frac{1}{2}\boldsymbol{\varepsilon}^T\, \boldsymbol{\sigma} \tag{2.25}$$

which is more suitable for metal materials, whereas de Vree et al. [93] assume:

$$\varepsilon_{eq} = \frac{\kappa-1}{2\kappa(1-2\nu)} I_{\varepsilon 1} + \frac{1}{2\kappa}\sqrt{\left(\frac{\kappa-1}{1-2\nu} I_{\varepsilon 1}\right)^2 + \frac{12\kappa}{(1+\nu)^2} J_{\varepsilon 2}} \tag{2.26}$$

with κ being the ratio between the tensile and compressive damage stress thresholds.

2.4 Proposed 3D plastic-damage material model

This section describes the 3D plastic-damage model proposed in this work, which is a modified and enriched version of that proposed in [2]. The first part of the section introduces the theoretical aspects of the model, whereas the second part describes the meaning of the model parameters and their calibration. The equation in Sec. 2.3, described for the elastic-damage models, are extended to account for the plastic strains $\boldsymbol{\varepsilon}^p$, i.e. to defined a plastic-damage model.

2.4.1 Model definition and fundamental equations

The stress-strain law is defined according to complementary equivalence principle, i.e.:

$$\boldsymbol{\sigma} = (1-D)^2\,\mathbf{C}\,(\boldsymbol{\varepsilon}-\boldsymbol{\varepsilon}^p) = (1-D)^2\,\bar{\boldsymbol{\sigma}} \tag{2.27}$$

The Drucker-Prager plasticity with linear kinematic and isotropic hardening, introduced in Sec. 2.2, is adopted to govern the evolution of the plastic strains $\boldsymbol{\varepsilon}^p$. The main equations of the Drucker-Prager model, i.e. Eqs. (2.11), (2.5) and (2.13), are expressed in terms of the effective stress vector $\bar{\boldsymbol{\sigma}}$ as follows:

$$f(\bar{\boldsymbol{\sigma}},\boldsymbol{\zeta},\alpha) = |\mathbf{P}\bar{\boldsymbol{\sigma}}-\boldsymbol{\zeta}| - \sqrt{\frac{2}{3}}(\sigma_y + H_i\alpha) + \mu\, I_1 = f_{J2} + \mu\, I_1 \tag{2.28}$$

$$\dot{\boldsymbol{\varepsilon}}^p = \dot{\lambda}\frac{\partial f}{\partial \bar{\boldsymbol{\sigma}}} = \dot{\lambda}\,\bar{\mathbf{n}}, \qquad \dot{\alpha} = \sqrt{\frac{2}{3}}\,\dot{\lambda}, \qquad \dot{\boldsymbol{\zeta}} = \frac{2}{3}H_k\dot{\boldsymbol{\varepsilon}}^p \tag{2.29}$$

$$\mathbf{C}^{ep} = \mathbf{C} - \frac{4G^2\,\dot{\lambda}}{|\bar{\boldsymbol{\eta}}|}\left(\mathbf{I} - \frac{\mathbf{1}\,\mathbf{1}^T}{3} - \bar{\mathbf{n}}\,\bar{\mathbf{n}}^T\right) - \frac{4G^2\;\bar{\mathbf{n}}\,\bar{\mathbf{n}}^T + 6GK\mu\;\bar{\mathbf{n}}\,\mathbf{1}^T}{2G + 2/3(H_i+H_k)} \tag{2.30}$$

with $\bar{\mathbf{n}} = \bar{\boldsymbol{\eta}}/|\bar{\boldsymbol{\eta}}|$ and $\bar{\boldsymbol{\eta}} = \mathbf{P}\,\bar{\boldsymbol{\sigma}} - \boldsymbol{\zeta}$. The independent material elasto-plastic parameters are the uni-axial tension and compression strengths, σ_t and σ_c, related to σ_y and μ through Eq. (2.12), and the hardening parameters H_k and H_i.

The rate constitutive relation is deduced by differentiating Eq. (2.27) with respect to the pseudo-time variable t:

$$\dot{\boldsymbol{\sigma}} = (1-D)^2\,\mathbf{C}\,(\dot{\boldsymbol{\varepsilon}}-\dot{\boldsymbol{\varepsilon}}^p) - 2(1-D)\,\mathbf{C}(\boldsymbol{\varepsilon}-\boldsymbol{\varepsilon}^p)\dot{D} = \mathbf{C}_t\,\dot{\boldsymbol{\varepsilon}} \tag{2.31}$$

where $\mathbf{C}_t$ is the material tangent stiffness matrix, resulting as:

$$\mathbf{C}_t = (1-D)^2\,\mathbf{C}^{ep} - 2(1-D)\,\mathbf{C}\,\boldsymbol{\varepsilon}^e\,\frac{\partial D}{\partial \boldsymbol{\varepsilon}} \tag{2.32}$$

To account for the unilateral effects typical of brittle-like materials, two different

variables are introduced for the damage due to prevailing tensile state, $D_t \in [0,1]$, and the damage due to prevailing compression state, $D_c \in [0,1]$. Their evolution processes are governed by the loading/unloading limit functions $f_t(Y_t, D_t)$ and $f_c(Y_c, D_c)$, defined as follows:

$$f_t(Y_t, D_t) = Y_t - Y_{0t} - (a_t Y_t + k_t) D_t \tag{2.33}$$

$$f_c(Y_c, D_c) = Y_c - Y_{0c} - (a_c Y_c + k_c) D_c \tag{2.34}$$

where Y_t and Y_c are two equivalent strain measures defined in the following, and Y_{0t}, Y_{0c}, a_t, a_c, k_t and k_c are material parameters governing the damage threshold (Y_{0t} and Y_{0c}) and the rate of the damage evolution (a_t, a_c, k_t and k_c). Fig. 2.6 plots $f_t(Y_t, D_t)$ and $f_c(Y_c, D_c)$ in both the principal strain plane $\varepsilon_1 - \varepsilon_2$ and stress plane $\sigma_1 - \sigma_2$ for a virgin material and adopting the parameters in Table 2.3.

Table 2.3: Mechanical parameters adopted for the proposed damage model.

$E = 30\,000\,\text{MPa}$	$\nu = 0.2$		
$\sigma_t = 3.3\,\text{MPa}$	$\sigma_c = 30.0\,\text{MPa}$	$H_i = 0.001\,E$	$H_k = 0.700\,E$
$Y_{0t} = 7.2 \cdot 10^{-5}$	$k_t = 2.0 \cdot 10^{-5}$	$a_t = 0.8$	
$Y_{0c} = 3.6 \cdot 10^{-4}$	$k_c = 5.0 \cdot 10^{-3}$	$a_c = 0.1$	$\beta = 0.0$

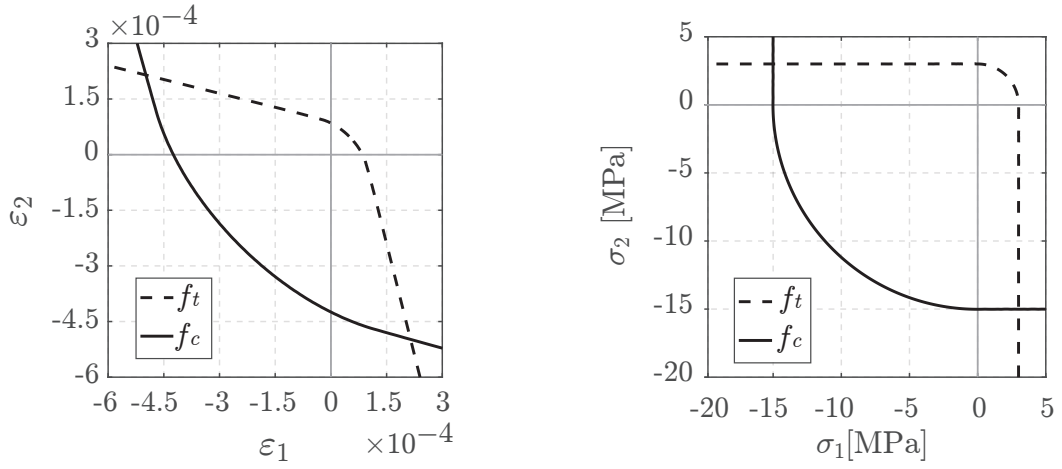

(*a*) Principal strain plane $\varepsilon_3 = 0$.

(*b*) Principal stress plane $\sigma_3 = 0$.

Figure 2.6: Damage limit functions f_t and f_c at the first onset of the damage processes.

The evolution of D_t and D_c follows the classical Karush-Kuhn-Tucker and consistency condition, resulting as:

$$\dot{D}_h \geq 0, \qquad f_h \leq 0, \qquad \dot{D}_h\, f_h = 0, \qquad \dot{D}_h\, \dot{f}_h = 0 \qquad \text{with} \quad h = t, c \tag{2.35}$$

together with the condition $D_t \geq D_c$, ensuring that the damage emerging during a compressive state is not recovered in a successive tensile state.

Once the evolution problems of the two damage variables D_t and D_c have been solved, the overall variable D is evaluated as the combination of them, in the form:

$$D = \alpha_t \, D_t + \alpha_c \, D_c \tag{2.36}$$

where α_t and α_c are weighting coefficients. Their expressions are defined as:

$$\alpha_t = \frac{\eta_t^2}{\eta_t^2 + \eta_c^2}, \qquad \alpha_c = \frac{\eta_c^2}{\eta_c^2 + \eta_t^2} = 1 - \alpha_t \tag{2.37}$$

with:

$$\eta_t = \frac{Y_t^e}{Y_{0t} + (a_t Y_t^e + k_t)D}, \qquad \eta_c = \frac{Y_c^e}{Y_{0c} + (a_t Y_c^e + k_c)D}$$

The introduced strain measures Y_t and Y_c are related to the total strain vector $\boldsymbol{\varepsilon}$, whereas Y_t^e and Y_c^e are related to its elastic part $\boldsymbol{\varepsilon}^e$. These are defined as:

$$Y_t = \sqrt{\sum_{i=1}^{3} \langle e_i \rangle_+^2}, \qquad Y_c = \sqrt{\sum_{i=1}^{3} \langle e_i \rangle_-^2 - \beta \sum_{j \neq k} \langle e_j \rangle_- \langle e_k \rangle_-} \tag{2.38}$$

$$Y_t^e = \sqrt{\sum_{i=1}^{3} \langle e_i^e \rangle_+^2}, \qquad Y_c^e = \sqrt{\sum_{i=1}^{3} \langle e_i^e \rangle_-^2 - \beta \sum_{j \neq k} \langle e_j^e \rangle_- \langle e_k^e \rangle_-} \tag{2.39}$$

where β is an additional material parameter governing the shape of the limit function in compression and e_i and e_i^e, for $i = 1, 2, 3$, are equivalent total and elastic strains respectively, defined as:

$$e_i = (1 - 2\nu)\hat{\varepsilon}_i + \nu \sum_{j=1}^{3} \hat{\varepsilon}_j, \qquad e_i^e = (1 - 2\nu)\hat{\varepsilon}_i^e + \nu \sum_{j=1}^{3} \hat{\varepsilon}_j^e \tag{2.40}$$

being ε_i and ε_i^e the principal total and elastic strains.

2.4.2 Meaning and calibration of the material parameters

The proposed plastic-damage model depends on two elastic parameter, the Young modulus E and the Poisson ratio ν, and on further eleven material parameters: four of them are the Drucker-Prager model's parameters, σ_t, σ_c, H_k and H_i; the other seven ones are the damage model's parameters, three related to the tensile behavior, Y_{0t}, a_t and k_t, and four related to the compressive behavior, Y_{0c}, a_c, k_c and β.

The parameter calibration starts from defining the stress damage thresholds σ_{0t} and

σ_{0c} for the tensile and the compressive responses. Considering an uni-axial stress state (Fig. 2.7*a*), a typical concrete-like material exhibits a maximum strength in tension $\sigma_{t,max}$, $10 \div 12$ times smaller than that in compression $\sigma_{c,max}$. Moreover, the tensile strength degrades quickly after the damage activation, so that σ_{0t} is generally equal to $\sigma_{t,max}$. On the contrary, σ_{0c} is generally smaller than $\sigma_{c,max}$. In this stress condition, if the damage is activated before the plastic yielding, the strain damage thresholds ε_{0t} and ε_{0c}, related to σ_{0t} and σ_{0c}, depend only on the parameters Y_{0t} and Y_{0c} respectively, because in tension $\alpha_t = 1$ and $\alpha_c = 0$; the opposite in compression. Hence:

$$Y_{0t} = \varepsilon_{0t}(1 - \nu - 2\nu^2), \qquad Y_{0c} = \varepsilon_{0c}(1 - \nu - 2\nu^2) \tag{2.41}$$

with Y_{0t} and Y_{0c} representing the equivalent strain measure thresholds. Although no

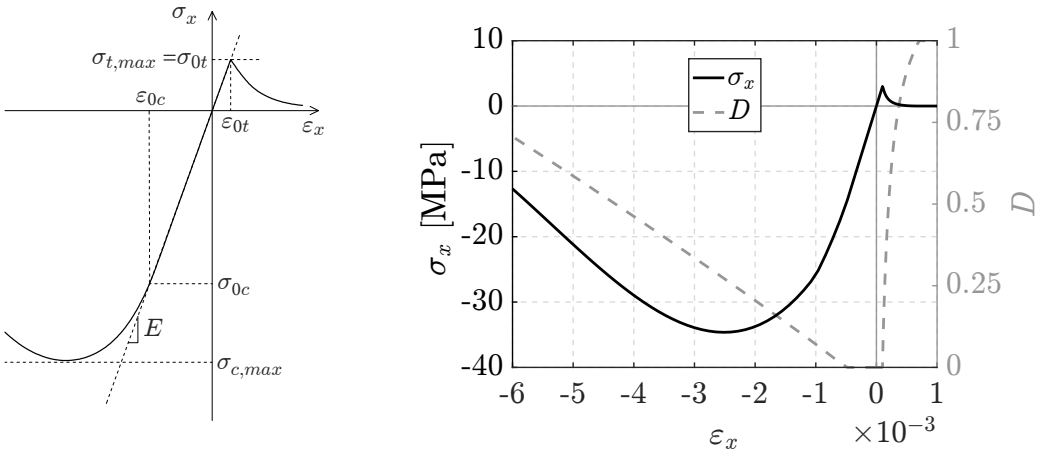

(***a***) Schematic representation. (***b***) Numerical response.

Figure 2.7: Monotonic uni-axial behavior in tension and compression for the proposed damage model with damage thresholds.

limitation exists for them, the following values are suggested for σ_t, σ_c, Y_{0t} and Y_{0c}:

$$\begin{aligned} \sigma_t &\geq \sigma_{t,max} \qquad \text{and} \qquad Y_{0t} = \sigma_{t,max}\,(1 - \nu - 2\nu^2)/E \\ \sigma_c &= \sigma_{c,max} \qquad \text{and} \qquad Y_{0c} < \sigma_{c,max}\,(1 - \nu - 2\nu^2)/E \end{aligned}$$

given the maximum strengths $\sigma_{t,max}$ and $\sigma_{c,max}$ of the real material (usually $Y_{0c} = 5 \div 10\, Y_{0t}$). Then, H_i, H_k, a_t, a_c, k_t and k_c can be set to reproduce the plastic strain growth and the damage evolution in both the monotonic and the cyclic cases. The monotonic responses obtained with the parameters in Table 2.3 is shown in Fig. 2.7*b* and an example of cyclic uni-axial behavior is shown in Fig. 2.8.

In particular, the isotropic hardening coefficient H_i influences the increment of strength that the material exhibits during subsequent loading cycles. For instance,

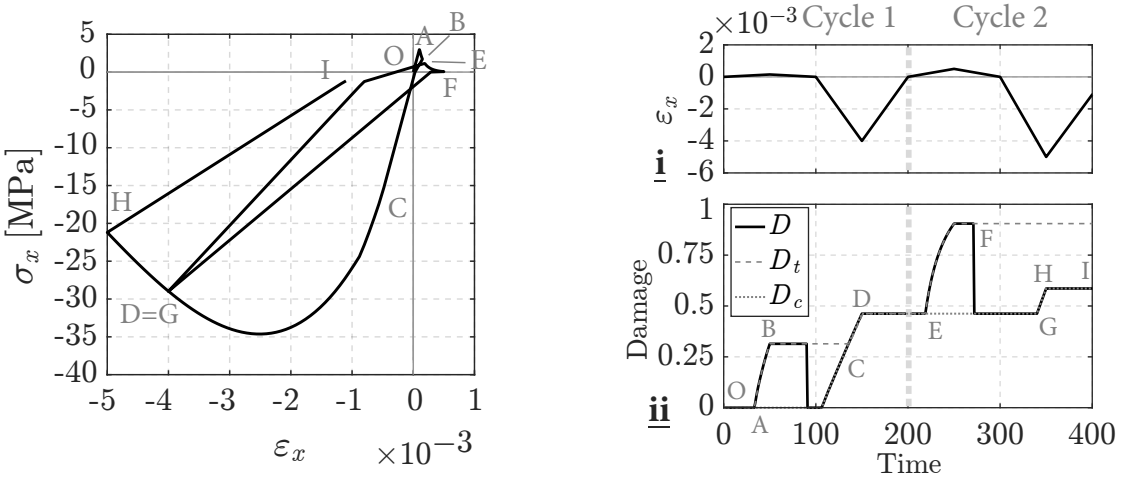

(***a***) Stress/strain relation.

(***b***) **i**: Strain history - **ii**: Damage evolution.

Figure 2.8: Cyclic uni-axial behavior under imposed strain history for the proposed damage model - $\varepsilon_x = (0.15, -4.0, 0.5, -5.0, -1.1) \cdot 10^{-3}$ (the gray capital letters indicate the main steps of the loading path).

Fig. 2.9*a* shows the cyclic response in Fig. 2.8*a* for two different values of H_i. For $H_i = 0.001\,E$ (dashed line), in the compressive part of the first cycle, the material reaches, before unloading, the stress related to the point D; at the second cycle, after switching from tension to compression, the same compressive stress value is obtained and then the material keeps degrading. By contrast, for $H_i = 0.020\,E$ (solid line) the stress obtained at the second cycle (point G) is higher than that obtained at the first one (point D').

The kinematic hardening parameter H_k, instead, governs the plastic strain growth, as shown in Fig. 2.9*b*. Here, the experimental test by Karsan et al. [67] (gray line) is reproduced adopting two sets of parameters (the other parameters are the ones in Table 2.3):

Numerical 1: $H_k = 0.15\,E$, $k_c = 4.5 \cdot 10^{-3}$ (solid black line);

Numerical 2: $H_k = 0.45\,E$, $k_c = 3.8 \cdot 10^{-3}$ (solid dashed line).

The set 1, with smaller value of H_k, leads to larger residual plastic strains after the unloading and (in this case) better represents the experimental behavior. On the contrary, the set 2, with a bigger value of H_k, leads to a smaller amount of residual plastic strains. However, because H_k also influences the increment of the effective stresses after the yielding, from Eq. (2.27) results that it also controls the level of stress reached in the post-elastic zone, that is it influences the post-elastic material strength, and its calibration is correlated to the calibration of the parameters a_t, a_c, k_t and k_c. In particular, k_t and k_c govern the damage rate growth in tension and

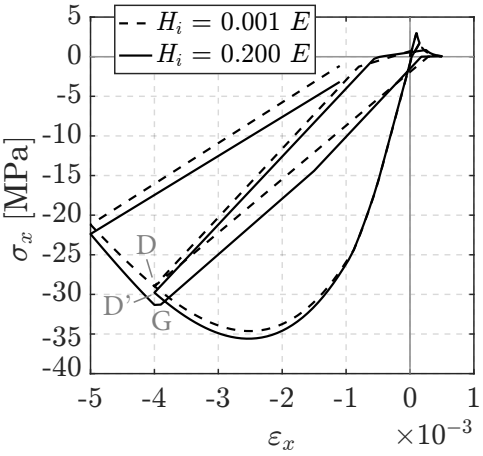

(*a*) Cyclic behavior for different values of the parameter H_i.

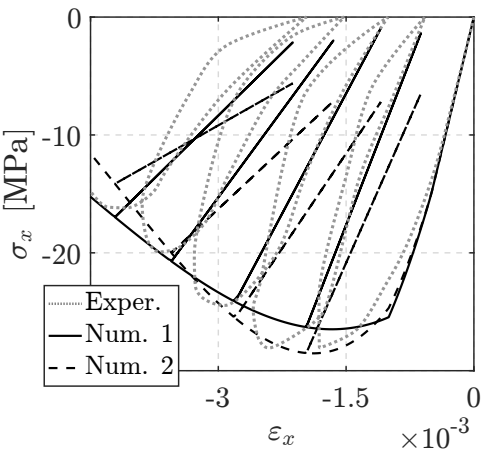

(*b*) Cyclic behavior in compression for different values of the parameter H_k.

Figure 2.9: Influence of H_i and H_k in the proposed damage model .

compression, respectively; whereas, a_t and a_c control the softening branch slope of the material response. These parameters are subjected to the following limitations:

$$k_{t/c} \geq 0, \qquad a_{t/c} \in [0, 1] \tag{2.42}$$

and are defined so that the higher are their values the more ductile is the material response. Fig. 2.10 shows some examples for the compressive case.

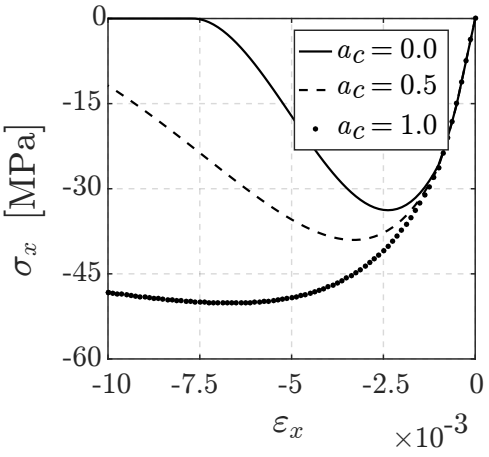

(*a*) Monotonic behavior in compression for different values of the parameter a_c.

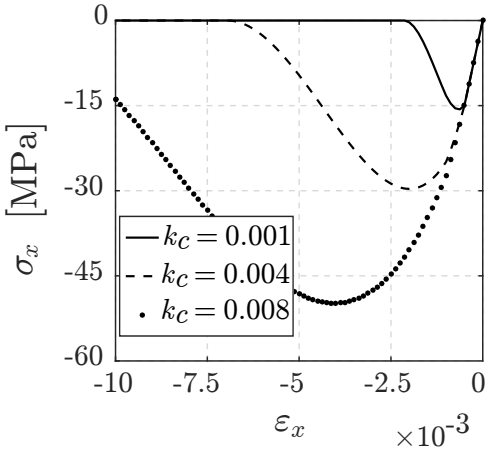

(*b*) Monotonic behavior in compression for different values of the parameter k_c.

Figure 2.10: Influence of a_c and k_c in the proposed damage model (the other parameters are the ones in Table 2.3).

Finally, the parameter $\beta \in [0, 1]$ governs the shape of the damage limit function f_c

in the compressive-compressive part of the domain, as shown in Fig. 2.11*a*. Hence, it can be set to correctly reproduce the material failure envelope. Fig. 2.11*b*, contains the material failure envelope in the principal stress plane (black lines), assuming $\sigma_3 = 0$ and normalizing σ_1 and σ_2 with respect to the uni-axial compressive strength $\sigma_{c,max} =$ 34.6 MPa. In the same figure, the experimental data 1 and 2 (gray lines) refer to the tests from Kupfer et al. [66] on concrete specimens with an unconfined uni-axial compressive strength of 35.1 MPa and 59.0 MPa, respectively.

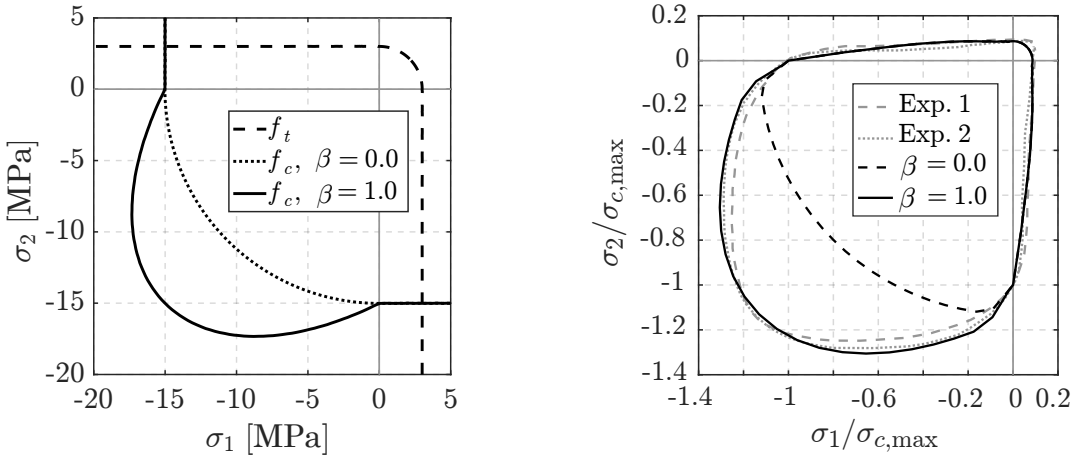

(*a*) Damage limit function f_c for different values of β.

(*b*) Material failure envelope in the principal stress plane $\sigma_3 = 0$.

Figure 2.11: Influence of β in the proposed damage model (the other parameters are those contained in Table 2.3).

Regarding the cyclic behavior, it is important to note the ability of the model in simulating the unilateral effects typical of the concrete, that is the crack closure/opening. In fact, as shown by the damage evolution paths in Fig. 2.8*b*.**ii**, when the stress state switches from tension to compression (from B to C and from F to G) the damage is recovered and it assumes the maximum value reached in the previous compressive phase (i.e. the virgin material state for the first cycle). By contrast, when the stress state switches from compression to tension (from D to E), the damage is not recovered, that is its value remains constant to the maximum value assumed in compression (or this becomes equal to the maximum value reached in the previous tensile path, if this is bigger); in fact the point B and E in the stress-strain graph do not coincide.

Finally, the response under pure shear loading is shown in Fig. 2.12 in terms of shear stress τ_{xy} vs shear strain γ_{xy}, for (*a*) the monotonic and (*b*) the cyclic case. Under this loading condition, the behavior is strongly characterized by the tensile damage growth and thus its evolution has basically the same path of that obtained under tensile uni-axial stress. The tensile damage occurs for both the positive and the negative shear

stress values, hence, as expected, no unilater effects and no damage recover appears in Fig. 2.12*b*.

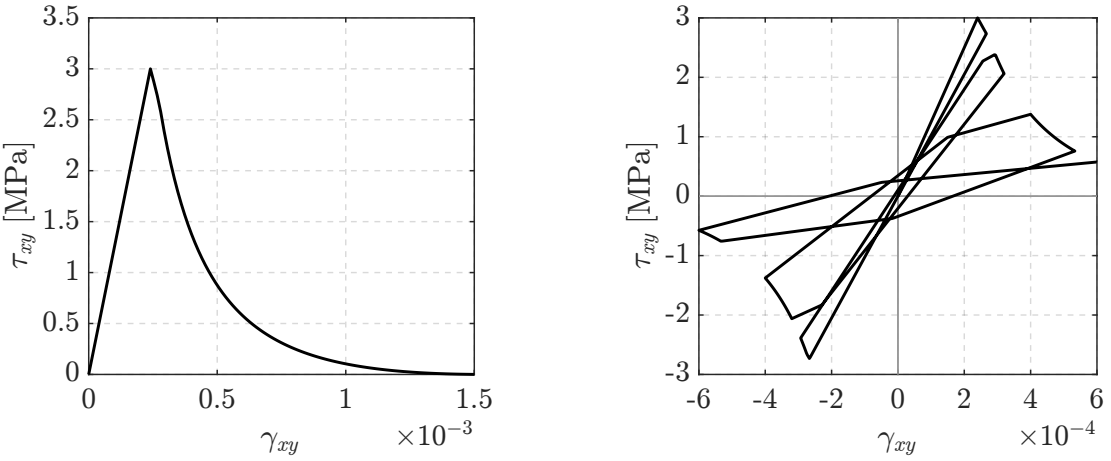

(***a***) Monotonic behavior.

(***b***) Cyclic behavior.

Figure 2.12: Monotonic and cyclic behavior under under pure shear stress state for the proposed damage model.

Chapter 3

Beam-column FE formulation

3.1 General

As widely shown in literature, force-based and mixed beam-column FEs are the most efficient formulations for the analysis of framed structures. However, only few models to date are formulated to satisfactorily represent the effects produced by shear and torsional loads. This chapter describes a 2-node, three-dimensional (3D) beam-column FE based on a modified Hu-Washizu variational potential, as proposed by Le Corvec in [1]. With respect to the standard Hu-Washizu mixed formulation, with only three independent fields, i.e. displacements, strains and stresses, Le Corvec's formulation introduces a fourth additional field, describing the out-of-plane displacements due to the warping of the element cross-section. This leads to the definition of a four-field mixed formulation, which is adopted in the present work to investigate on the effects of cross-section warping on the degrading behavior of RC frames. The cross-section warping displacements are included in the formulation through a classical interpolatory approach, that is they are interpolated in the element volume with the addition of a variable number of local degrees of freedom (DOF) to those commonly used for the beam FE and with the definition of specific shape functions. This is performed at two independent levels: along the axis and over the cross-section, selecting the shape functions within the class of the Lagrange polynomials. Hence, the evolution of the warping displacements during the loading process and the coupling between the shear and torsion with the normal stress components are taken into account.

Further important improvements are here proposed with respect to the model in [1]. Indeed, the introduction of the local DOFs associated to the warping field presents two drawbacks: (1) it increases the overall computational burden and (2) it reduces the numerical robustness; the latter issue results from the procedure proposed in [1] for eliminating the cross-section rigid body motions from the additional warping field.

Aiming to (1) reduce the number of additional DOFs, the present work extends the element formulation to the adoption of Hermite 2D polynomials for the interpolation of the warping displacements over the cross-section area, since with the same order of integration these polynomials require less parameters than the Lagrange one [94]. Moreover, aiming to (2) increase the element robustness, this work proposes a new way for eliminating the cross-section rigid body motions from the warping field.

The description of the adopted FE formulations starts with a preliminary overview of classical beam-column force-based formulations. In particular, Sec. 3.2 presents the classical Timoshenko model, giving the basic issues characterizing the equilibrated approaches [14, 25, 95, 96]; for sake of completeness, the Euler-Bernoulli model is also described. Sec. 3.3 presents a generalized 3D version of the enhanced model proposed in [51]. In this formulation, to (partially) remove the hypothesis of rigid body section and to account for the shear effects, particular assumptions are made for the shear strain distributions over the cross-section, basing on linear elastic analytical solutions. Finally, the adopted formulation including cross-section warping is described in Sec. 3.4. Small displacements and strains are assumed for all the models.

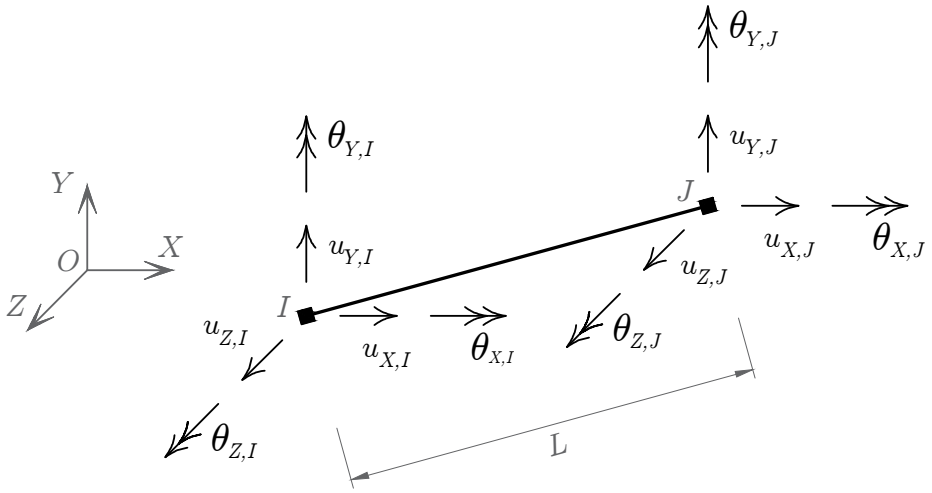

Figure 3.1: Finite element global reference system: nodal displacement vector components.

First, a global reference system (O, X, Y, Z) is defined, where the 2-node standard 3D element has twelve DOFs, corresponding to the nodal displacement components (Fig. 3.1), that is three translations and three rotations at each node, listed in the vectors $\mathbf{u}_I$, $\mathbf{u}_J$, $\boldsymbol{\theta}_I$ and $\boldsymbol{\theta}_J$. The undeformed element length is indicated with L, corresponding to the distance between the two end nodes I and J. The displacement components are collected in the vector $\mathbf{u}$, resulting as:

$$\mathbf{u} = \left\{ \mathbf{u}_I^T \quad \boldsymbol{\theta}_I^T \quad \mathbf{u}_J^T \quad \boldsymbol{\theta}_J^T \right\}^T \tag{3.1}$$

The corresponding nodal force components are collected in the vector $\mathbf{p}$, resulting as:

$$\mathbf{p} = \left\{ \mathbf{p}_I^T \quad \mathbf{m}_I^T \quad \mathbf{p}_J^T \quad \mathbf{m}_J^T \right\}^T \tag{3.2}$$

with $\mathbf{p}_I$, $\mathbf{p}_J$, $\mathbf{m}_I$ and $\mathbf{m}_J$ being the nodal force and moment vectors.

According to the equilibrated approach, the rigid body motions of the element are eliminated and the formulation is referred to the local basic reference system (I, x, y, z), shown in Fig. 3.2. The axis x is parallel to the direction going from node I to node J, while y and z are the cross-section principal axes. The deformation DOFs are collected in the basic displacement vector $\mathbf{v}$, defined as:

$$\mathbf{v} = \{ u_{x,J} \quad \theta_{z,I} \quad \theta_{z,J} \quad \theta_{x,J} \quad \theta_{y,I} \quad \theta_{y,J} \}^T \tag{3.3}$$

where $u_{x,J}$ is the translation of the node J parallel to x, $\theta_{z,I}$ and $\theta_{z,J}$ are the nodal rotations around z, $\theta_{y,I}$ and $\theta_{y,J}$ are the nodal rotations around y and $\theta_{x,J}$ is the rotation at node J around x. The vector $\mathbf{v}$ is related to the vector $\mathbf{u}$, by the following compatibility expression:

$$\mathbf{v} = \mathbf{a}_g \, \mathbf{u} \tag{3.4}$$

where $\mathbf{a}_g$ is the kinematic matrix, defined as:

$$\mathbf{a}_g = \begin{bmatrix} -1 & 0 & 0 & 0 & 0 & 0 & 1 & 0 & 0 & 0 & 0 & 0 \\ 0 & 1/L & 0 & 0 & 0 & 1 & 0 & -1/L & 0 & 0 & 0 & 0 \\ 0 & 1/L & 0 & 0 & 0 & 0 & 0 & -1/L & 0 & 0 & 0 & 1 \\ 0 & 0 & 0 & -1 & 0 & 0 & 0 & 0 & 0 & 1 & 0 & 0 \\ 0 & 0 & -1/L & 0 & 1 & 0 & 0 & 0 & 1/L & 0 & 0 & 0 \\ 0 & 0 & -1/L & 0 & 0 & 0 & 0 & 0 & 1/L & 0 & 1 & 0 \end{bmatrix} \tag{3.5}$$

The basic force vector $\mathbf{q}$, corresponding to the vector $\mathbf{v}$, results as:

$$\mathbf{q} = \{ p_{x,J} \quad m_{z,I} \quad m_{z,J} \quad m_{x,J} \quad m_{y,I} \quad m_{y,J} \}^T \tag{3.6}$$

where $p_{x,J}$ is the force parallel to x at node J, $m_{z,I}$ and $m_{z,J}$ are the nodal moments around z, $m_{y,I}$ and $m_{y,J}$ are the nodal moments around y and $m_{x,J}$ is the moment at node J around x.

By imposing the virtual work equivalence, the element global stiffness matrix $\hat{\mathbf{k}}$ and the element force vector $\mathbf{p}$ in the global system are related to the basic variables through the transpose of the matrix $\mathbf{a}_g$ [95]:

$$\hat{\mathbf{k}} = \mathbf{a}_g^T \, \mathbf{f}^{-1} \, \mathbf{a}_g, \qquad \mathbf{p} + \mathbf{p}_{rp} = \mathbf{a}_g^T \, \mathbf{q} \tag{3.7}$$

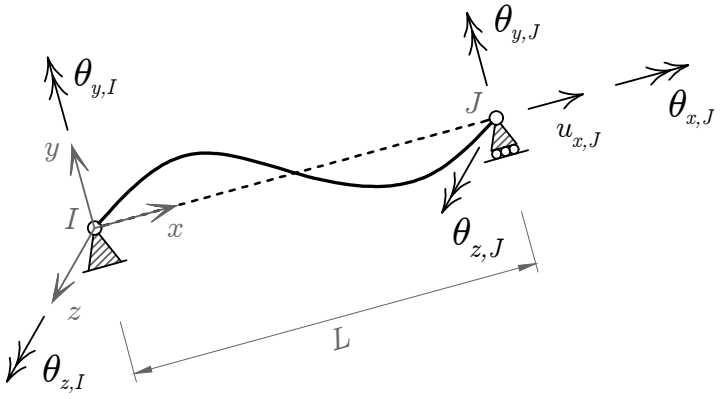

Figure 3.2: Finite element local reference system: basic displacement components.

where $\mathbf{f}$ is the element basic flexibility matrix and $\mathbf{p}_{rp}$ are the element nodal forces due the loads distributed along the element axis.

The following sections discuss the definition of $\mathbf{f}$ and the equations governing the element kinematic, static and constitutive laws for the different formulations. Only the case of prismatic beams with uniform cross-sections is considered.

3.2 The Timoshenko and Euler-Bernoulli force-based formulations

The Timoshenko beam theory is based on the rigid plane cross-section assumption. Hence, at each point of the local axis x, the generalized section displacement vector $\mathbf{u}_s(x)$ is defined as:

$$\mathbf{u}_s(x) = \{u(x) \quad \theta_z(x) \quad v(x) \quad \theta_x(x) \quad \theta_y(x) \quad w(x)\}^T \tag{3.8}$$

where $u(x)$, $v(x)$ and $w(x)$ are the translation components of the cross-section at x, and $\theta_x(x)$, $\theta_y(x)$ and $\theta_z(x)$ are its rotations (Fig. 3.3a). The displacements $\mathbf{u}_m(x,y,z)$ at the generic point M of the cross-section are, in general, described by the three fields $u_x(x,y,z)$, $u_y(x,y,z)$ and $u_z(x,y,z)$, representing the material displacements along x, y and z, respectively. Given the assumption of rigid plane cross-section, $\mathbf{u}_m(x,y,z)$ corresponds to the section rigid displacement $\mathbf{u}_r(x,y,z)$, resulting as:

$$\mathbf{u}_r(x,y,z) = \left\{ \begin{array}{c} u_{r,x}(x,y,z) \\ u_{r,y}(x,y,z) \\ u_{r,z}(x,y,z) \end{array} \right\} = \mathbf{a}_s(y,z)\,\mathbf{u}_s(x) \tag{3.9}$$

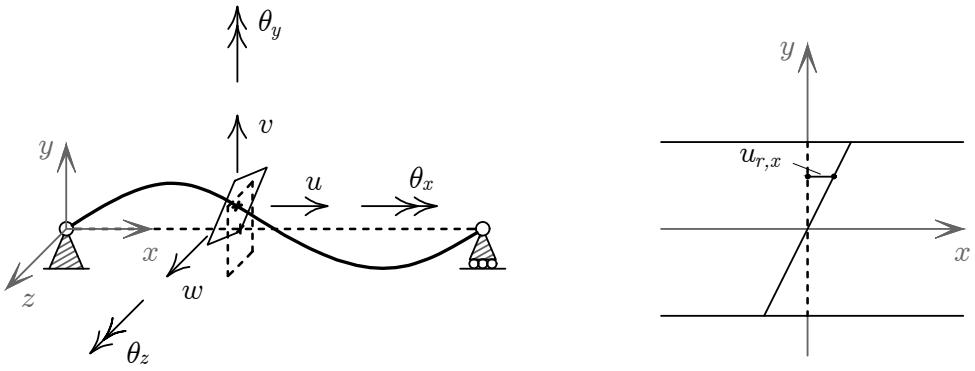

(*a*) Section displacement vector components. **(*b*)** Point axial displacement.

Figure 3.3: Cross-section rigid displacements.

where $u_{r,x}(x,y,z)$, $u_{r,y}(x,y,z)$ and $u_{r,z}(x,y,z)$ are the components of the material point displacements associated to the cross-sections rigid body motion and $\mathbf{a}_s(y,z)$ is the compatibility operator defined as:

$$\mathbf{a}_s(y,z) = \begin{bmatrix} 1 & -y & 0 & 0 & z & 0 \\ 0 & 0 & 1 & -z & 0 & 0 \\ 0 & 0 & 0 & y & 0 & 1 \end{bmatrix} \tag{3.10}$$

The compatible strain vector $\boldsymbol{\varepsilon}_m(x,y,z)$ at M is, in general, described by the three strain fields $\varepsilon_x(x,y,z)$, $\gamma_{xy}(x,y,z)$ and $\gamma_{xz}(x,y,z)$, corresponding to the material point axial strain along x and the shear strains in the planes $x-y$ and $x-z$, respectively. As for the displacements, in this case $\boldsymbol{\varepsilon}_m(x,y,z)$ is equivalent to the contributes $\boldsymbol{\varepsilon}_r(x,y,z)$ compatible with the section rigid displacements and resulting as:

$$\boldsymbol{\varepsilon}_r(x,y,z) = \left\{ \begin{array}{c} \varepsilon_{r,x}(x,y,z) \\ \gamma_{r,xy}(x,y,z) \\ \gamma_{r,xz}(x,y,z) \end{array} \right\} = \mathbf{a}_s(y,z)\,\mathbf{e}(x) \tag{3.11}$$

The generalized section deformation vector $\mathbf{e}(x)$ is introduced in Eq. (3.11), as:

$$\mathbf{e}(x) = \left\{ \begin{array}{c} \varepsilon_G(x) \\ \chi_z(x) \\ \gamma_y(x) \\ \chi_x(x) \\ \chi_y(x) \\ \gamma_z(x) \end{array} \right\} = \left\{ \begin{array}{c} u'(x) \\ \theta'_z(x) \\ v'(x) - \theta_z(x) \\ \theta'_x(x) \\ \theta'_y(x) \\ w'(x) + \theta_y(x) \end{array} \right\} \tag{3.12}$$

with $\varepsilon_G(x)$ being the axial deformation, $\chi_z(x)$ and $\chi_y(x)$ the flexural curvatures, $\chi_x(x)$ the torsional curvature and $\gamma_y(x)$ and $\gamma_z(x)$ the shear deformations; $\diamond' = \partial\diamond/\partial x$ denotes the derivative with respect to x of the variable $\diamond$.

The stress components work-conjugated with the strain quantities in $\boldsymbol{\varepsilon}_m(x,y,z)$ are collected in the stress vector $\boldsymbol{\sigma}_m(x,y,z)$, defined as:

$$\boldsymbol{\sigma}_m(x,y,z) = \left\{ \begin{array}{c} \sigma_x(x,y,z) \\ \tau_{xy}(x,y,z) \\ \tau_{xz}(x,y,z) \end{array} \right\} \tag{3.13}$$

where σ_x is the normal stress along the beam axis direction, and τ_{xy} and τ_{xz} are the shear stresses in the cross-section plane parallel to y and z, respectively. By enforcing the virtual work equivalence for the cross-section as:

$$\delta\mathbf{e}^T(x)\,\mathbf{s}(x) = \int_A \delta\boldsymbol{\varepsilon}_r^T(x,y,z)\,\boldsymbol{\sigma}_m(x,y,z)\,dA \tag{3.14}$$

the following definition of $\mathbf{s}(x)$ is deduced [97]:

$$\mathbf{s}(x) = \int_A \mathbf{a}_s^T(y,z)\,\boldsymbol{\sigma}_m(x,y,z)\,dA = \left\{ \begin{array}{c} N(x) \\ M_z(x) \\ T_y(x) \\ M_x(x) \\ M_y(x) \\ T_z(x) \end{array} \right\} \tag{3.15}$$

$N(x)$ being the axial stress, $M_z(x)$ and $M_y(x)$ the bending moments, $M_x(x)$ the torsional moment and $T_y(x)$ and $T_z(x)$ the shear forces. By differentiating Eq. (3.15) with respect to the $\mathbf{e}(x)$, the tangent section stiffness matrix $\mathbf{k}_s(x)$ is obtained:

$$\mathbf{k}_s(x) = \int_A \mathbf{a}_s^T(y,z)\,\mathbf{k}_m(x,y,z)\,\mathbf{a}_s(y,z)\,dA \tag{3.16}$$

governing the incremental generalized section constitutive relation:

$$\dot{\mathbf{s}}(x) = \mathbf{k}_s(x)\,\dot{\mathbf{e}}(x) \tag{3.17}$$

The tangent material stiffness matrix is defined as: $\mathbf{k}_m(x,y,z) = \partial\boldsymbol{\sigma}_m(x,y,z)/\partial\boldsymbol{\varepsilon}_m(x,y,z)$. This is involved in the material incremental stress-strain law as:

$$\dot{\boldsymbol{\sigma}}_m(x,y,z) = \mathbf{k}_m(x,y,z)\,\dot{\boldsymbol{\varepsilon}}_m(x,y,z) \tag{3.18}$$

As a consequence of the assumption of rigid plane sections, the material strains $\boldsymbol{\varepsilon}_m(x,y,z) \equiv \boldsymbol{\varepsilon}_r(x,y,z)$ in Eq. (3.11) assume linear distributions over the cross-section and, for linear elastic material, this implies linear distributions for the material stresses $\boldsymbol{\sigma}_m(x,y,z)$ as well. Such a result is not suitable for a real frame structures where the warping of cross-sections leads to higher order distributions of the stress/strain fields, even for linear elastic conditions. Hence, some specific corrections need to be introduced. In particular, the axial strain $\varepsilon_x(x,y,z)$ in a prismatic homogeneous beam assumes a non linear distribution only for particular warping deformations of the cross-sections and/or under specific warping constrain (shear-lag effect), with the warping of the cross-section becoming relevant for some applications. By contrast, the influence of the warping effect on the shear strains $\gamma_{xy}(x,y,z)$ and $\gamma_{xz}(x,y,z)$ is more often essential. In fact, only constant and linear strain distributions are considered in the Timoshenko beam theory and the equivalences $\gamma_{r,xy}(x,y,z) = \gamma_y(x) - z\,\chi_x(x)$ and $\gamma_{r,xz}(x,y,z) = \gamma_z(x) + y\,\chi_x(x)$ in Eq. (3.11) do not ensure the longitudinal equilibrium of the element [51, 98]. Hence, the classical shear correction factors ψ_y and ψ_z and the torsional correction factor ψ_x need to be introduced. Eq. (3.11) is thus rewritten introducing a modified matrix $\mathbf{a}_{s,T}(y,z)$:

$$\boldsymbol{\varepsilon}_r(x,y,z) = \mathbf{a}_{s,T}(y,z)\,\mathbf{e}(x) \tag{3.19}$$

with:

$$\mathbf{a}_{s,T}(y,z) = \begin{bmatrix} 1 & -y & 0 & 0 & z & 0 \\ 0 & 0 & \sqrt{\psi_y} & -z\sqrt{\psi_x} & 0 & 0 \\ 0 & 0 & 0 & y\sqrt{\psi_x} & 0 & \sqrt{\psi_z} \end{bmatrix}$$

and Eqs. (3.15) and (3.16) become:

$$\mathbf{s}(x) = \int_A \mathbf{a}_{s,T}^T(y,z)\,\boldsymbol{\sigma}_m(x,y,z)\,dA \tag{3.20}$$

$$\mathbf{k}_s(x) = \int_A \mathbf{a}_{s,T}^T(y,z)\,\mathbf{k}_m(x,y,z)\,\mathbf{a}_{s,T}(y,z)\,dA \tag{3.21}$$

For linear elastic material response, $\mathbf{k}_m(x,y,z)$ is a diagonal matrix depending on the Young's and shear moduli, E and G, i.e:

$$\mathbf{k}_m^{LE} = \begin{bmatrix} E & 0 & 0 \\ 0 & G & 0 \\ 0 & 0 & G \end{bmatrix} \tag{3.22}$$

Hence, for a homogeneous section, the tangent stiffness matrix $\mathbf{k}_{s,T}(x)$ result as:

$$\mathbf{k}_s^{LE} = \begin{bmatrix} EA & -ES_z & 0 & 0 & ES_y & 0 \\ -ES_z & EI_z & 0 & 0 & -ES_{yz} & 0 \\ 0 & 0 & G\psi_y A & -G\sqrt{\psi_y\psi_x}S_y & 0 & 0 \\ 0 & 0 & -G\sqrt{\psi_y\psi_x}S_y & G\psi_x I_\rho & 0 & G\sqrt{\psi_z\psi_x}S_z \\ ES_y & -ES_{yz} & 0 & 0 & EI_y & 0 \\ 0 & 0 & 0 & G\sqrt{\psi_z\psi_x}S_z & 0 & G\psi_z A \end{bmatrix} \tag{3.23}$$

where S_y, S_z and S_{yz} are the section first moments of area, I_z and I_y are the second moment of area with respect to the axes z and y respectively and I_ρ is the polar moment of area. If the local element axes y and z are chosen as the principal cross-section axes, the matrix $\mathbf{k}_s(x)$ assumes the following standard diagonal forms:

$$\mathbf{k}_s^{LE} = \begin{bmatrix} EA & 0 & 0 & 0 & 0 & 0 \\ 0 & EI_z & 0 & 0 & 0 & 0 \\ 0 & 0 & GA_y^* & 0 & 0 & 0 \\ 0 & 0 & 0 & GJ & 0 & 0 \\ 0 & 0 & 0 & 0 & EI_y & 0 \\ 0 & 0 & 0 & 0 & 0 & GA_z^* \end{bmatrix} \tag{3.24}$$

where EA is the section axial stiffness, EI_z and EI_y are the section bending stiffnesses with respect to y and z respectively, GJ is the section torsional stiffness, $J = \psi_x I_\rho$ being the torsional inertia, and GA_y^* and GA_z^* are the section shear stiffnesses with respect to y and z respectively, $A_y^* = \psi_y A$ and $A_z^* = \psi_z A$ being the shear areas. When Eq. (3.24) is considered, no coupling between the generalized section forces exists.

In any case, following the equilibrated formulation, the stress vector $\mathbf{s}(x)$ is expressed as a function of the basic element force vector $\mathbf{q}$ as:

$$\mathbf{s}(x) = \mathbf{b}(x)\,\mathbf{q} + \mathbf{s}_q(x) \qquad \text{with} \quad \mathbf{b}(x) = \begin{bmatrix} 1 & 0 & 0 & 0 & 0 & 0 \\ 0 & \frac{x}{L} - 1 & \frac{x}{L} & 0 & 0 & 0 \\ 0 & -\frac{1}{L} & -\frac{1}{L} & 0 & 0 & 0 \\ 0 & 0 & 0 & 1 & 0 & 0 \\ 0 & 0 & 0 & 0 & \frac{x}{L} - 1 & \frac{x}{L} \\ 0 & 0 & 0 & 0 & \frac{1}{L} & \frac{1}{L} \end{bmatrix} \tag{3.25}$$

where $\mathbf{b}(x)$ is the equilibrium matrix and $\mathbf{s}_q(x)$ is the generalized section stress vector due to the loads distributed along the element axis. Eq. (3.25) can be introduced in

the inverse form of Eq. (3.17), obtaining:

$$\dot{\mathbf{e}}(x) = \mathbf{f}_s(x)\,\dot{\mathbf{s}}(x) = \mathbf{f}_s(x)\,\mathbf{b}(x)\,\dot{\mathbf{q}} \tag{3.26}$$

where $\mathbf{f}_s(x) = \mathbf{k}_s^{-1}(x)$ is the tangent section flexibility matrix. The virtual work equivalence is enforce for the beam, stating that the work done by the virtual basic forces $\delta\mathbf{q}$ on the basic deformations $\mathbf{v}(x)$ is the same as the work done by the virtual generalized stress $\mathbf{s}(x)$ on the generalized deformations $\mathbf{e}(x)$ along L, i.e. [95]:

$$\delta\mathbf{q}^T\,\mathbf{v} = \int_0^L \delta\mathbf{s}^T(x)\,\mathbf{e}(x)\,dx \tag{3.27}$$

By introducing Eq. (3.25), the following compatibility condition results:

$$\mathbf{v} = \int_0^L \mathbf{b}^T(x)\,\mathbf{e}(x)\,dx \tag{3.28}$$

By differentiating Eq. (3.28) with respect to $\mathbf{q}$ and introducing Eq. (3.26), the tangent element flexibility matrix $\mathbf{f}$ is obtained:

$$\mathbf{f} = \frac{\partial\mathbf{v}}{\partial\mathbf{q}} = \int_0^L \mathbf{b}^T(x)\,\mathbf{f}_s(x)\,\mathbf{b}(x)\,dx \tag{3.29}$$

corresponding to the inverse of the element basic stiffness matrix $\mathbf{k}$ and governing the incremental element basic constitutive relation, i.e.:

$$\dot{\mathbf{q}} = \mathbf{k}\,\dot{\mathbf{v}} \qquad \text{with} \qquad \mathbf{k} = \mathbf{f}^{-1} \tag{3.30}$$

Starting from the Timoshenko beam formulation described above, the Euler-Bernoulli theory can be derived, imposing that the cross-sections remain plane and orthogonal to the beam axis after deformations. This assumption implies that the shear deformations $\gamma_y(x)$ and $\gamma_z(x)$ are zero along the entire beam, leading to the following relationship between the cross-section transversal displacements and rotations:

$$\gamma_y(x) = \frac{\partial v(x)}{\partial x} - \theta_z(x) = 0, \qquad \gamma_z(x) = \frac{\partial w(x)}{\partial x} + \theta_y(x) = 0 \tag{3.31}$$

In this case, the shear/torsional variables are neglected and only the axial/bending behavior of the beam is taken into account. In fact, the independent generalized section displacement components in the vector $\mathbf{u}_s(x)$ are:

$$\mathbf{u}_{s,EB}(x) = \{u(x) \quad v(x) \quad w(x)\}^T \tag{3.32}$$

and the generalized section deformations in the vector $\mathbf{e}(x)$ result as:

$$\mathbf{e}_{EB}(x) = \left\{ \begin{array}{c} \varepsilon_G(x) \\ \chi_z(x) \\ \chi_y(x) \end{array} \right\} = \left\{ \begin{array}{c} u'(x) \\ v''(x) \\ -w''(x) \end{array} \right\} \tag{3.33}$$

Hence, the only compatible material strain $\boldsymbol{\varepsilon}_r(x, y, z)$ due to the section rigid displacements is the axial one:

$$\boldsymbol{\varepsilon}_{r,EB}(x, y, z) = \varepsilon_{r,x}(x, y, z) = \varepsilon_G(x) - y\,\chi_z(x) + z\,\chi_y(x) = \mathbf{a}_{s,EB}(y, z)\,\mathbf{e}(x) \tag{3.34}$$

$\mathbf{a}_{s,EB}(y, z)$ being the compatibility matrix defined as:

$$\mathbf{a}_{s,EB}(y, z) = \left[\begin{array}{ccc} 1 & -y & z \end{array} \right] \tag{3.35}$$

and the axial stress $\sigma_x(x, y, z)$ is the only material stress component, $\boldsymbol{\sigma}_{m,EB}(x, y, z) = \sigma_x(x, y, z)$. The shear strains $\gamma_{xy}(x, y, z)$ and $\gamma_{xz}(x, y, z)$ and the shear stresses $\tau_{xy}(x, y, z)$ and $\tau_{xz}(x, y, z)$ are neglected.

Eqs. (3.15) - (3.17) are modified accordingly, giving the following definitions of the generalized section force vector and of the tangent section stiffness matrix:

$$\mathbf{s}_{EB}(x) = \int_A \mathbf{a}_{s,EB}^T(y, z)\,\sigma_x(x, y, z)\,dA = \left\{ \begin{array}{c} N_x(x) \\ M_z(x) \\ M_y(x) \end{array} \right\} \tag{3.36}$$

$$\mathbf{k}_{s,EB}(x) = \int_A \mathbf{a}_{s,EB}^T(y, z)\,k_{m,x}(x, y, z)\,\mathbf{a}_{s,EB}(y, z)\,dA \tag{3.37}$$

with Eq. (3.18) resulting as:

$$\dot{\sigma}_x(x, y, z) = k_{m,x}(x, y, z)\,\dot{\varepsilon}_{r,x}(x, y, z) \tag{3.38}$$

and $k_{m,x}(x, y, z) = \partial\sigma_x(x, y, z)/\partial\varepsilon_x(x, y, z)$ being the tangent material stiffness.

Under linear elastic material response, $k_{m,x}(x, y, z) = E$ and $\mathbf{k}_{s,EB}(x)$ result as:

$$\mathbf{k}_{s,EB}^{LE} = \left[\begin{array}{ccc} EA & -ES_z & ES_y \\ -ES_z & EI_z & -ES_{yz} \\ ES_y & -ES_{yz} & EI_y \end{array} \right] \tag{3.39}$$

reducing to the following standard diagonal form for y and z assumed as the principal

cross-section axes:

$$\mathbf{k}_{s,EB}^{LE} = \begin{bmatrix} EA & 0 & 0 \\ 0 & EI_z & 0 \\ 0 & 0 & EI_y \end{bmatrix} \tag{3.40}$$

The equilibrium Eq. (3.25) becomes:

$$\mathbf{s}_{EB}(x) = \mathbf{b}_{EB}(x)\,\mathbf{q} + \mathbf{s}_{q,EB}(x) \tag{3.41}$$

with $$\mathbf{b}_{EB}(x) = \begin{bmatrix} 1 & 0 & 0 & 0 & 0 & 0 \\ 0 & \frac{x}{L}-1 & \frac{x}{L} & 0 & 0 & 0 \\ 0 & 0 & 0 & 0 & \frac{x}{L}-1 & \frac{x}{L} \end{bmatrix}$$

$\mathbf{b}_{EB}(x)$ and $\mathbf{s}_{q,EB}(x)$ are the reduced versions of $\mathbf{b}(x)$ and $\mathbf{s}_{q,EB}$, respectively. Eqs. (3.28) and (3.29) are modified accordingly, giving the following definitions of the element compatibility equation and of the element basic flexibility matrix:

$$\mathbf{v} = \int_0^L \mathbf{b}_{EB}^T(x)\,\mathbf{e}_{EB}(x)\,dx \tag{3.42}$$

$$\mathbf{f} = \int_0^L \mathbf{b}_{EB}^T(x)\,\mathbf{f}_{s,EB}(x)\,\mathbf{b}_{EB}(x)\,dx \tag{3.43}$$

with $\mathbf{f}_{s,EB}(x) = \mathbf{k}_{s,EB}^{-1}(x)$ and $\mathbf{f} = \mathbf{k}^{-1}$. Note that Eqs. (3.42) and (3.43) do not account for the torsional behavior of the beam, since the fourth column of the matrix $\mathbf{b}_{EB}(x)$ is zero. This means that the torsional basic deformation $\theta_{x,J}$ coming from the integral in Eq. (3.42) is always zero and the flexibility matrix $\mathbf{f}$ result singular. For practical purposes, a correction of both these definitions is then necessary. Indeed, during the element state determination, described in Sec. 5.2.1, the value of $\theta_{x,J}$ can always be assumed equal to the compatible one given by Eq. (3.4) and the following incremental basic constitutive relation can be used for the torsional component:

$$\dot{m}_{x,J} = \frac{GJ}{L}\,\dot{\theta}_{x,J} \tag{3.44}$$

where GJ/L is the element tangent torsional stiffness (usually assumed constantly equal to its linear elastic value).

Henceforth, the standard Timoshenko and Euler-Bernoulli models are indicated as TFF (Timoshenko Force-Based Formulation) beam and EBFF (Euler-Bernoulli Force-Based Formulation) beam, respectively.

3.3 Enhanced formulation with non-uniform shear strain distribution

The generalized 3D version of the enhanced model proposed in [51] is described in the following. Adopting a simplified approach, it accounts for non-uniform shear strain distributions over the element cross-section due to the warping. In particular, referring to the Timoshenko beam theory, the hypothesis of rigid body section is maintained, assuming Eq. (3.8) for the definition of the generalized section displacement vector $\mathbf{u}_s(x)$ and Eq. (3.9) for the material point displacement vector $\mathbf{u}_m(x,y,z) \equiv \mathbf{u}_r(x,y,z)$. However, the modified following expression is assumed for the compatible material strain vector $\boldsymbol{\varepsilon}_m(x,y,z)$:

$$\boldsymbol{\varepsilon}_m(x,y,z) = \left\{ \begin{array}{c} \varepsilon_x(x,y,z) \\ \gamma_{xy}(x,y,z) \\ \gamma_{xz}(x,y,z) \end{array} \right\} = \bar{\mathbf{a}}_s(y,z)\,\mathbf{e}(x) \tag{3.45}$$

with
$$\bar{\mathbf{a}}_s(y,z) = \left[\begin{array}{cccccc} 1 & -y & 0 & 0 & z & 0 \\ 0 & 0 & \rho_{yy}(y,z) & -z\sqrt{\psi_x} & 0 & \rho_{yz}(y,z) \\ 0 & 0 & \rho_{zy}(y,z) & y\sqrt{\psi_x} & 0 & \rho_{zz}(y,z) \end{array} \right]$$

The generalized section deformation vector $\mathbf{e}(x)$ is the standard one, given in Eq. (3.12), whereas the compatible matrix $\bar{\mathbf{a}}_s(y,z)$ in this case depends on four functions defined over the cross-section area: $\rho_{yy}(y,z)$ and $\rho_{zy}(y,z)$ describe the shear strain distributions associated to the generalized deformation $\gamma_y(x)$; similarly, $\rho_{yz}(y,z)$ and $\rho_{zz}(y,z)$ describe the shear strain distributions associated to the generalized deformation $\gamma_z(x)$. These functions are evaluated under the assumption of linear elastic

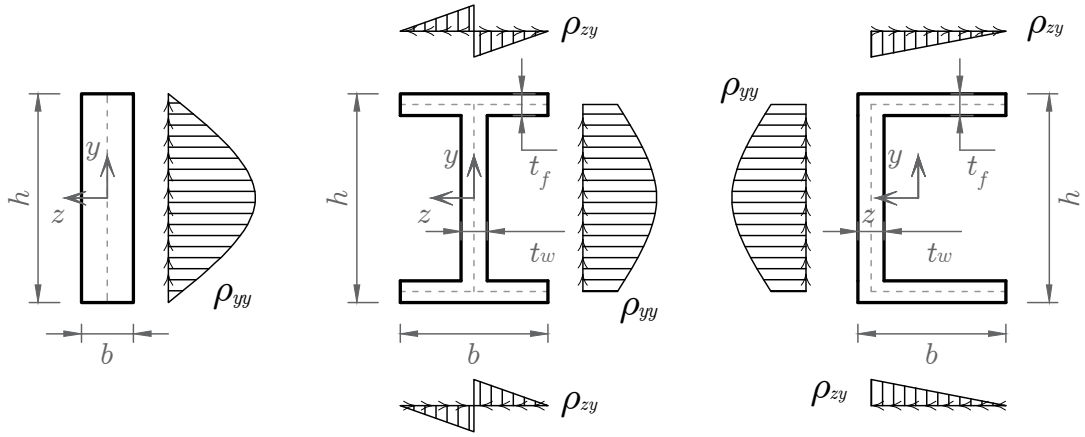

Figure 3.4: Linear elastic solutions for the shear strain distribution associated to the generalized deformation $\gamma_y(x)$, for rectangular, I-shaped and channel sections.

material response for a specific shape of the cross-section and are assumed to be valid for the nonlinear case as well. For instance, these can be evaluated for thin-walled beam referring to the classical Jourawsky theory, that is under the assumption of constant shear strain distribution across the thickness of the cross-section. In Fig. 3.4, a schematic representation of $\rho_{yy}(y,z)$ and $\rho_{zy}(y,z)$ is shown for a I-shaped and a channel section. For the rectangular sections, $\rho_{zy}(y,z) = \rho_{yz}(y,z) = 0$ and the other two functions result as:

$$\rho_{yy}(y,z) = \frac{5}{4}\left(1 - 4\frac{y^2}{h^2}\right), \qquad \rho_{zz}(y,z) = \frac{5}{4}\left(1 - 4\frac{z^2}{b^2}\right) \tag{3.46}$$

Once the compatible matrix $\bar{\mathbf{a}}_s(y,z)$ in Eq. (3.45) is defined, the element formulation can be derived following the same steps as for the TFF beam. In particular, the forces $\mathbf{s}(x)$ in Eqs. (3.15) and the matrix $\mathbf{k}_s(x)$ in Eq. (3.16) result as:

$$\mathbf{s}(x) = \int_A \bar{\mathbf{a}}_s^T(y,z)\,\boldsymbol{\sigma}_m(x,y,z)\,dA \tag{3.47}$$

$$\mathbf{k}_s(x) = \int_A \bar{\mathbf{a}}_s^T(y,z)\,\mathbf{k}_m(x,y,z)\,\bar{\mathbf{a}}_s(y,z)\,dA \tag{3.48}$$

with $\boldsymbol{\sigma}_m(x,y,z)$ and $\mathbf{k}_m(x,y,z)$ defined in Eqs. (3.13) and (3.18), respectively. The other Eqs. (3.25) - (3.30) are modified accordingly. Henceforth, this model is indicated as ETFF (Enhanced Timoshenko Force-Based Formulation) beam.

A similar model is proposed in [1], where an additional improvement is proposed to better represent the torsional behavior of the beam. In particular, referring to the formulation in [99], the generalized section deformation vector $\mathbf{e}(x)$ is extended as:

$$\hat{\mathbf{e}}(x) = \{\varepsilon_G(x) \quad \chi_z(x) \quad \gamma_y(x) \quad \chi_x(x) \quad \chi_y(x) \quad \gamma_z(x) \quad \zeta(x)\}^T \tag{3.49}$$

where $\zeta(x) = \theta_x''(x) = \chi_x'(x)$ governs the warping displacements of the cross-section, so that the material point displacements $\mathbf{u}_m(x,y,z)$ result as:

$$\mathbf{u}_m(x,y,z) = \begin{Bmatrix} u_x(x,y,z) \\ u_y(x,y,z) \\ u_z(x,y,z) \end{Bmatrix} = \mathbf{u}_r(x,y,z) + \begin{Bmatrix} \omega(y,z)\,\theta_x'(x) \\ 0 \\ 0 \end{Bmatrix} \tag{3.50}$$

and the material strains $\boldsymbol{\varepsilon}_m(x,y,z)$ result as:

$$\boldsymbol{\varepsilon}_m(x,y,z) = \begin{Bmatrix} \varepsilon_x(x,y,z) \\ \gamma_{xy}(x,y,z) \\ \gamma_{xz}(x,y,z) \end{Bmatrix} = \hat{\mathbf{a}}_s(y,z)\,\hat{\mathbf{e}}(x) \tag{3.51}$$

with:

$$\hat{\mathbf{a}}_s(y,z) = \begin{bmatrix} 1 & -y & 0 & 0 & z & 0 & \omega(y,z) \\ 0 & 0 & \rho_{yy}(y,z) & -z + \frac{\partial \omega(y,z)}{y} & 0 & \rho_{yz}(y,z) & 0 \\ 0 & 0 & \rho_{zy}(y,z) & y + \frac{\partial \omega(y,z)}{z} & 0 & \rho_{zz}(y,z) & 0 \end{bmatrix}$$

$\omega(y,z)$ is the warping function [100] and represents the deformed (warping) shape of the cross-section under torsional loads. This can be defined in closed form for linear elastic material and particular section geometries and then adopted in the nonlinear case.

With the previous definitions, the generalized section force vector $\mathbf{s}(x)$ becomes:

$$\hat{\mathbf{s}}(x) = \int_A \hat{\mathbf{a}}_s^T(y,z)\, \boldsymbol{\sigma}_m(x,y,z)\, dA = \begin{Bmatrix} N(x) \\ M_z(x) \\ T_y(x) \\ M_x(x) \\ M_y(x) \\ T_z(x) \\ B(x) \end{Bmatrix} \tag{3.52}$$

where the additional generalized variable $B(x)$ is the bi-moment:

$$B(x) = \int_A \omega(y,z)\, \sigma_x(x,y,z)\, dA \tag{3.53}$$

Similarly, the tangent section stiffness matrix $\mathbf{k}_s(x)$ becomes:

$$\hat{\mathbf{k}}_s(x) = \int_A \hat{\mathbf{a}}_s^T(y,z)\, \mathbf{k}_m(x,y,z)\, \hat{\mathbf{a}}_s(y,z)\, dA \tag{3.54}$$

Under linear elastic material response, for a homogeneous section with y and z chosen as the principal cross-section axes, the constitutive relationship for the bi-moment assumes the following expression:

$$B(x) = E \int_A \omega^2(y,z)\, dA\, \zeta(x) = E\Gamma\, \zeta(x) \tag{3.55}$$

where $\Gamma = \int_A \omega^2(y,z)\, dA$ is the warping inertia of the cross-section and $E\Gamma$ represents its warping rigidity.

Despite the improvement proposed in [1], the enhanced model described in this section presents some drawbacks. The main one is related to the assumption made for the compatibility matrix in Eq. (3.51). Indeed, as the functions $\rho_{yy}(y,z)$, $\rho_{zy}(y,z)$,

$\rho_{yz}(y,z)$, $\rho_{zz}(y,z)$ and $\omega(y,z)$ are defined with respect to a linear elastic material response, when nonlinear behaviors emerge, the resulting strain distributions in general do not satisfy the cross-section equilibrium. Once, $\rho_{yy}(y,z)$, $\rho_{zy}(y,z)$, $\rho_{yz}(y,z)$, $\rho_{zz}(y,z)$ and $\omega(y,z)$ are chosen, $\varepsilon_x(x,y,z)$, $\gamma_{xy}(x,y,z)$ and $\gamma_{xz}(x,y,z)$ result as linear combinations of the functions in $\hat{\mathbf{a}}_s(y,z)$, the generalized section deformations $\hat{\mathbf{e}}(x)$ being the combination coefficients (to be found during the element state determination); no additional condition is imposed to ensure that the resulting strain distributions correctly represent the nonlinear behavior of the cross-section and locally satisfy the equilibrium. An example of this problem is given in Sec. 6.4. Moreover, the model fails in providing a complete representation of the effects due to possible warping constraints applied at the element boundaries. With the assumption in Eq. (3.51) warping constraints can be taken into account imposing that $\theta_x'(x) = 0$ at the ends of the beam, but this only affects the torsional behavior of the element, while the shear one is unchanged.

3.4 A 3D mixed beam-column finite element with section warping

The 3D beam FE proposed in [1] is briefly described in the following, focusing the attention on the enhancements introduced in the present work. The adopted FE accounts for the section warping through a four-field mixed variational formulation. Henceforth, it is indicated as WMF (Warping Mixed Formulation) beam.

3.4.1 Element kinematics

At each point of the local axis x, the generalized section displacement vector $\mathbf{u}_s(x)$ is defined according to the classical assumption of rigid plane cross-sections, that is as in Eq. (3.8) which is rewritten in the following (Fig. 3.5*a*):

$$\mathbf{u}_s(x) = \{u(x) \quad \theta_z(x) \quad v(x) \quad \theta_x(x) \quad \theta_y(x) \quad w(x)\}^T$$

To describe the warping of the beam cross-sections, this hypothesis is partially removed, assuming that these can undergo out-of-plane deformations, although remaining rigid in their plane. Hence, the displacements $\mathbf{u}_m(x,y,z)$ at the generic point M of the cross-section is expressed as the additive composition of the rigid part $\mathbf{u}_r(x,y,z)$

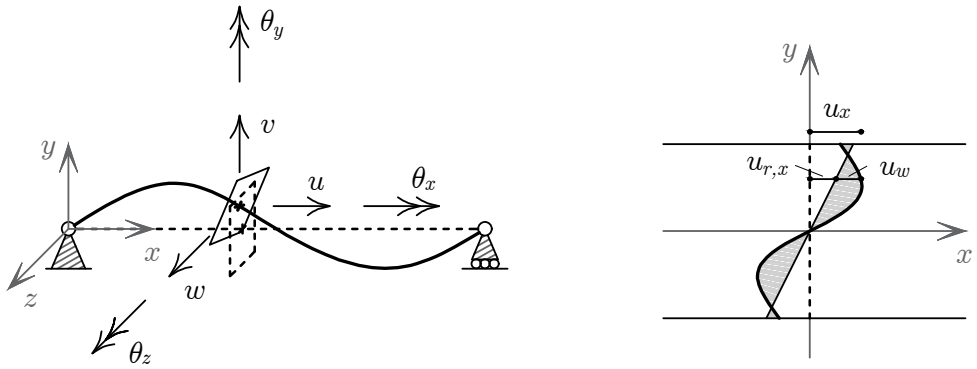

(*a*) Displacement vector components. **(*b*)** Material axial displacement.

Figure 3.5: Cross-section warping displacements.

and the displacements associated to the warping $\mathbf{u}_w(x, y, z)$ (Fig. 3.5*b*):

$$\mathbf{u}_m(x, y, z) = \left\{ \begin{array}{l} u_x(x, y, z) \\ u_y(x, y, z) \\ u_z(x, y, z) \end{array} \right\} = \mathbf{u}_r(x, y, z) + \mathbf{u}_w(x, y, z) \tag{3.56}$$

As a consequence of the in-plane section undeformability, i.e. $\varepsilon_y = \varepsilon_z = \gamma_{yz} = 0$, the warping displacement fields have non-zero values only in the x direction, that is:

$$\mathbf{u}_w(x, y, z) = \{u_w(x, y, z) \quad 0 \quad 0\}^T \tag{3.57}$$

Hence, the vector $\mathbf{u}_m(x, y, z)$ can be expressed as:

$$\mathbf{u}_m(x, y, z) = \mathbf{a}_s(y, z)\, \mathbf{u}_s(x) + \{u_w(x, y, z) \quad 0 \quad 0\}^T \tag{3.58}$$

with the matrix $\mathbf{a}_s(y, z)$ defined in Eq. (3.10).

By applying the compatibility operator, the material strains at M result as:

$$\varepsilon_x(x, y, z) = \frac{\partial u(x)}{\partial x} - y\frac{\partial \theta_z(x)}{\partial x} + z\frac{\partial \theta_y(x)}{\partial x} + \frac{\partial u_w(x, y, z)}{\partial x} \tag{3.59}$$

$$\gamma_{xy}(x, y, z) = -\theta_z(x) + \frac{\partial v(x)}{\partial x} - z\frac{\partial \theta_x(x)}{\partial x} + \frac{\partial u_w(x, y, z)}{\partial y} \tag{3.60}$$

$$\gamma_{xz}(x, y, z) = \theta_y(x) + \frac{\partial w(x)}{\partial x} + y\frac{\partial \theta_x(x)}{\partial x} + \frac{\partial u_w(x, y, z)}{\partial z} \tag{3.61}$$

leading to the following expression of the strain vector $\boldsymbol{\varepsilon}_m(x,y,z)$:

$$\boldsymbol{\varepsilon}_m(x,y,z) = \left\{ \begin{array}{c} \varepsilon_x(x,y,z) \\ \gamma_{xy}(x,y,z) \\ \gamma_{xz}(x,y,z) \end{array} \right\} = \mathbf{a}_s(y,z)\,\mathbf{e}(x) + \boldsymbol{\varepsilon}_w(x,y,z) \tag{3.62}$$

where $\mathbf{e}(x)$ is the standard generalized section deformation vector in Eq. (3.12) and $\boldsymbol{\varepsilon}_w(x,y,z)$ contains the vector collecting the strains due to the warping displacement $u_w(x,y,z)$. This is defined as:

$$\boldsymbol{\varepsilon}_w(x,y,z) = \left\{ \frac{\partial u_w(x,y,z)}{\partial x} \quad \frac{\partial u_w(x,y,z)}{\partial y} \quad \frac{\partial u_w(x,y,z)}{\partial z} \right\}^T \tag{3.63}$$

The virtual work equivalence (Eq. (3.14)) can be applied , considering the virtual rigid strains $\delta\boldsymbol{\varepsilon}_r(x,y,z) = \mathbf{a}_s(y,z)\,\delta\mathbf{e}(x)$. This leads to the definition of the standard generalized section forces $\mathbf{s}(x)$, as in Eq. (3.15) which is rewritten in the following:

$$\mathbf{s}(x) = \int_A \mathbf{a}_s^T(y,z)\,\boldsymbol{\sigma}_m(x,y,z)\,dA$$

The section forces $\mathbf{s}$ satisfy the equilibrium along the element axis (Eq. (3.25)), that is:

$$\mathbf{s}(x) = \mathbf{b}(x)\,\mathbf{q} + \mathbf{s}_q(x)$$

Finally, the force field $p_w(x,y,z)$ is introduced. It is work conjugated with the warping displacement $u_w(x,y,z)$ and arises when this is constrained in some sections.

3.4.2 Warping displacement interpolation

The warping displacement field $u_w(x,y,z)$ is interpolated according to the classical approach based on the use of shape functions. The study in [1] interpolates $u_w(x,y,z)$ along the element axis x independently from the interpolation over the cross-section. The Gauss-Lobatto integration rule is used to set along the element axis the location of n_w interpolation points, at x_1, ..., x_i, ..., x_{n_w}, and a set of 1D Lagrange polynomials $\mathrm{N}_i(x)$ is defined with respect to these points. An example is shown in Fig. 3.6. The warping displacement field, thus, results as:

$$u_w(x,y,z) = \sum_{i=1}^{n_w} N_i(x)\,u_{w,i}(x_i,y,z) \tag{3.64}$$

where $u_{w,i}(x_i,y,z)$ is the warping displacement field of the cross-section placed at x_i.

Then, $u_{w,i}(x_i,y,z)$ is interpolated over each of these n_w cross-sections by subdi-

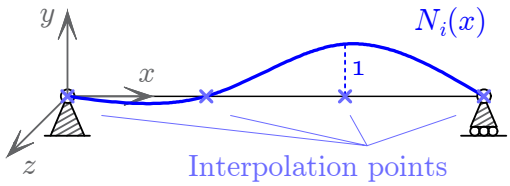

Figure 3.6: Lagrange polynomials for the warping interpolation along the element axis: cubic polynomial $N_3(x)$ related to the third of $n_w = 4$ interpolation points.

viding them into several rectangular patches: in every patch, a regular distribution of interpolation points is assumed, for a total of s_w points (Fig. 3.7). According to them,

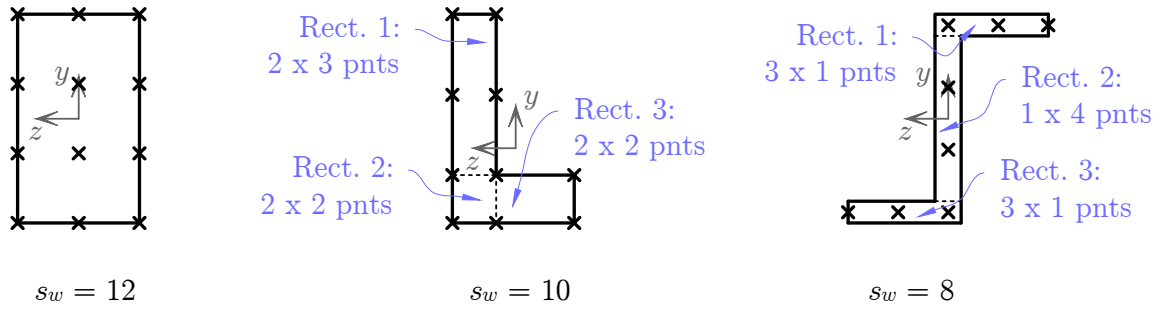

Figure 3.7: Warping interpolation points over the element cross-section.

a set of m_w 2D interpolation functions $\mathrm{M}_j(y, z)$ is defined. Each of them corresponds to an additional warping DOF for the element.

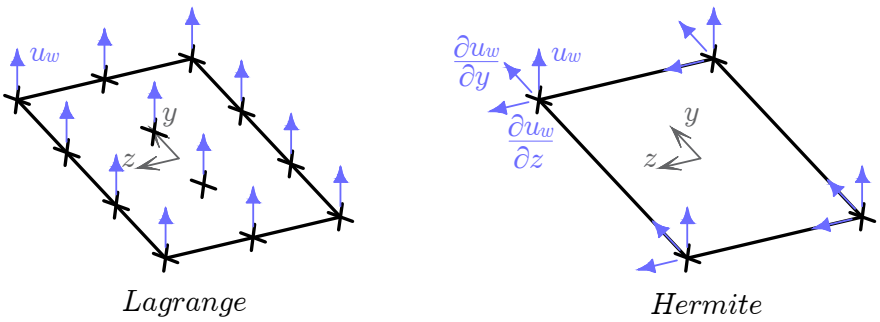

Figure 3.8: Warping DOFs at each point for the Lagrange and the Hermite polynomials.

Lagrange polynomials are used in [1] for the functions $\mathrm{M}_j(y, z)$. In this work, the element formulation is extended to the adoption of Hermite polynomials and pro and cons of the resulting interpolation are explored. For the Lagrange polynomials only one internal DOF is required at each of the s_w interpolation points, corresponding to its warping displacement u_w; the total number m_w of warping DOFs is thus equal to s_w. By contrast, Hermite polynomials require three internal DOFs at each point, one

corresponding to the warping displacement u_w and two corresponding to the derivatives $\partial u_w/\partial y$ and $\partial u_w/\partial z$. In this case the total number m_w of warping DOFs is equal to $3\,s_w$ (Fig. 3.8). Fig. 3.9 shows some examples of both kinds of interpolation functions.

Henceforth, $u_{w,ij}$ denotes the generic $j-$th warping DOF at the section x_i, coinciding with the displacements u_w for the Lagrange polynomials, and with the displacements u_w and their derivatives for the Hermite polynomials:

$$\{u_{w,1}, \quad u_{w,2}, \quad u_{w,3}, \ldots\} = \{u_w^{pnt\,1}, \quad u_w^{pnt\,2}, \quad u_w^{pnt\,3}, \ldots\} \quad \textit{Lagrange} \tag{3.65}$$

$$\{u_{w,1}, \quad u_{w,2}, \quad u_{w,3}, \ldots\} = \{u_w^{pnt\,1}, \quad \frac{\partial u_w^{pnt\,1}}{\partial y}, \quad \frac{\partial u_w^{pnt\,1}}{\partial z}, \ldots\} \quad \textit{Hermite} \tag{3.66}$$

Hence, the warping displacement field at the $i-$th cross-section can be written as:

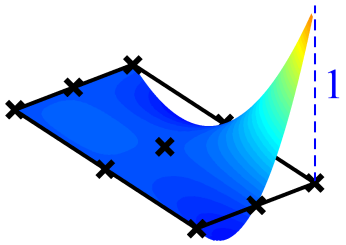

(*a*) Lagrange polynomial for u_w in a rectangular section - $m_w = 9$.

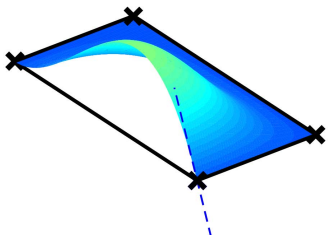

(*b*) Lagrange polynomial for $\partial u_w/\partial y$ in a rectangular section - $m_w = 12$.

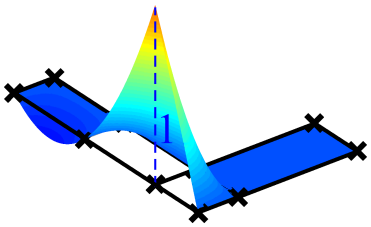

(*c*) Lagrange polynomial for u_w in an L-Shaped section - $m_w = 10$.

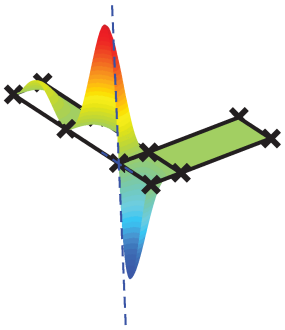

(*d*) Lagrange polynomial for $\partial u_w/\partial y$ in an L-Shaped section- $m_w = 30$.

Figure 3.9: Example of warping interpolation function in a rectangular cross-section and in a cross-section composed by a set of rectangular portions.

$$u_{w,i}(x_i, y, z) = \sum_{j=1}^{m_w} M_j(y, z)\, u_{w,ij} = \mathbf{M}(y, z)\, \mathbf{u}_{w,i} \tag{3.67}$$

where $\mathbf{u}_{w,i}$ is a column vector collecting all the m_w warping DOFs $u_{w,ij}$ of the $i-$th cross-section and $\mathbf{M}(y, z)$ is a row vector containing all the related m_w shape functions

$M_j(y,z)$. Finally, introducing Eq. (3.67) into Eq. (3.64), the total field $u_w(x,y,z)$ results as:

$$u_w(x,y,z) = \sum_{i=1}^{n_w} N_i(x)\,\mathbf{M}(y,z)\,\mathbf{u}_{w,i} = \bar{\mathbf{N}}(x)\bar{\mathbf{M}}(y,z)\,\mathbf{u}_w \tag{3.68}$$

where $\bar{\mathbf{N}}(x)$ is a row vector containing all the n_w shape functions $N_i(x)$ defined along the element axis, $\bar{\mathbf{M}}(y,z)$ is a $n_w \times (n_w\, m_w)$ block diagonal matrix defined as:

$$\bar{\mathbf{M}}(y,z) = \begin{bmatrix} \mathbf{M}(y,z) & \mathbf{0} & \dots & \mathbf{0} \\ \mathbf{0} & \mathbf{M}(y,z) & \dots & \mathbf{0} \\ \vdots & \vdots & \ddots & \vdots \\ \mathbf{0} & \mathbf{0} & \dots & \mathbf{M}(y,z) \end{bmatrix} \tag{3.69}$$

and the vector $\mathbf{u}_w$ collects all the warping DOFs of the beam FE as:

$$\mathbf{u}_w = \begin{Bmatrix} \mathbf{u}_{w,1}^T & \mathbf{u}_{w,2}^T & \dots & \mathbf{u}_{w,i}^T & \dots & \mathbf{u}_{w,n_w}^T \end{Bmatrix}^T \tag{3.70}$$

Accordingly, the vector $\mathbf{p}_w$ is defined containing the warping forces $p_{w,i}$ work-conjugated with the warping DOFs, as:

$$\mathbf{p}_w = \begin{Bmatrix} \mathbf{p}_{w,1}^T & \mathbf{p}_{w,2}^T & \dots & \mathbf{p}_{w,i}^T & \dots & \mathbf{p}_{w,n_w}^T \end{Bmatrix}^T \tag{3.71}$$

where $\mathbf{p}_{w,i}$ collects the warping forces of the $i-$th cross-section.

Basing on the boundary conditions imposed for the warping quantities, the additional warping DOFs in $\mathbf{u}_w$ and the work-conjugated forces in $\mathbf{p}_w$ are treated in different ways. The study in [1] distinguishes two cases:

1. The warping DOFs are treated as external variables and are added to the standard twelve ones;

2. The warping DOFs are treated as internal variables, i.e. they are condensed out with the evaluation of the element flexibility matrix, as detailed later; only the standard twelve DOFs in Eq. (3.1) result as actual independent element variables.

In both cases, warping displacement constraints can be applied. When the warping DOFs are treated as external variables, the warping displacement constraints are applied with the standard approach typical of the FE method; the corresponding forces $p_{w,ij}$ are non-zero and result as constraint reactions. Moreover, instead of applying the constraints, in this case it is also possible to apply external forces corresponding to the $p_{w,ij}$. When the warping DOFs are treated as internal variables, the warping displacement constraints are applied enforcing specific conditions on the $u_{w,ij}$ and modifying

the element flexibility matrix. No external load can be applied at these DOFs. Only the case of internal warping DOFs is considered in this work and no partial constraint is assumed in the correlation studies, that is at general $ij-$th warping point either the condition of fully restrained warping DOF $u_{w,ij} = 0$ ($p_{w,ij} \neq 0$) or the condition of totally free warping displacement $p_{w,ij} = 0$ ($u_{w,ij} \neq 0$) is enforced. Note that, in practical cases, the warping displacement is restrained for a whole cross-section of the element (or more of them), that is the displacement field $u_w(x, y, z)$ is zero over the entire section area. For both the Lagrange and the Hermite interpolation polynomials, this can be obtained ensuring that $u_{w,ij} = 0$ for all warping DOFs located at that cross-section, even though for the Hermite polynomials some of them represent the derivatives of the warping displacement field. In fact, if $u_w(x, y, z) = 0$ over the entire section area, then its derivatives are zero as well.

3.4.3 Variational formulation

The equations governing the element state determination, for evaluating the element flexibility matrix and the internal force vector, are derived on the basis of a modified Hu-Washizu variational principle, that is on the definition of an energy functional depending on four independent fields: the three standard ones [14] $\mathbf{u}_m(x, y, z)$, $\boldsymbol{\varepsilon}_m(x, y, z)$ and $\boldsymbol{\sigma}_m(x, y, z)$ and the additional warping displacement field $u_w(x, y, z)$. The functional is written as:

$$\Pi(\mathbf{u}_m, \boldsymbol{\varepsilon}_m, \boldsymbol{\sigma}_m, u_w) = \int_V \boldsymbol{\sigma}^T \left[\boldsymbol{\varepsilon}_m(\mathbf{u}_m) - \boldsymbol{\varepsilon}_m\right] dV + \int_V W(\boldsymbol{\varepsilon}_m)\, dV - \Pi_{ext} \tag{3.72}$$

where $W(\boldsymbol{\varepsilon}_m)$ is the internal potential energy and Π_{ext} is the external load potential.

Following the formulation in [1], Eq. (3.72) is modified introducing Eqs. (3.58) and (3.62) and the Hu-Washizu functional Π is expressed in terms of the generalized section displacement $\mathbf{u}_s(x)$ and deformations $\mathbf{e}(x)$, resulting as:

$$\Pi(\mathbf{u}_s, \mathbf{e}, \boldsymbol{\sigma}_m, u_w) = \int_V \boldsymbol{\sigma}^T \mathbf{a}_s^T \left[\mathbf{e}(\mathbf{u}_s) - \mathbf{e}\right] dV + \int_V W(\mathbf{e}, u_w)\, dV - \mathbf{u}^T \mathbf{p} - \int_0^L \mathbf{u}_s^T \mathbf{b}_s\, dx \tag{3.73}$$

Here, the external load potential is written in terms of the nodal quantities $\mathbf{u}$ and $\mathbf{p}$ and of the loads $\mathbf{b}_s$ distributed along the element axis. The stationarity of $\Pi(\mathbf{u}_s, \mathbf{e}, \boldsymbol{\sigma}_m, u_w)$ with respect to the four independent fields provides the following governing equations:

Stationarity w.r.t.:	Governing equation:	
$\mathbf{u}_s(x)$	$\mathbf{a}_g^T \mathbf{q} = \mathbf{p} + \mathbf{p}_{rp}$	(3.74)
$\mathbf{e}(x)$	$\boldsymbol{\sigma}_m(x, y, z) = \hat{\boldsymbol{\sigma}}[\boldsymbol{\varepsilon}_m(x, y, z)]$	(3.75)

$$\boldsymbol{\sigma}_m(x,y,z) \qquad \mathbf{v} = \int_0^L \mathbf{b}^T(x)\,\mathbf{e}(x)\,dx \tag{3.76}$$

$$u_w(x,y,z) \qquad \mathbf{p}_{w,i} = \int_0^L \frac{\partial \mathrm{N}_i(x)}{\partial x}\mathbf{s}_w^x(x)\,dx + \int_0^L \mathrm{N}_i(x)\,\mathbf{s}_w^{yz}(x)\,dx \tag{3.77}$$

The first three are the classical equations of a standard three-field mixed FE formulation. Equation (3.74) is obtained by enforcing the stationarity with respect to $\mathbf{u}_s(x)$ and introducing Eqs. (3.4), (3.15) and (3.25); this represents the element equilibrium. Eq. (3.75) is obtained by enforcing the stationarity with respect to $\mathbf{e}(x)$ and represents the general nonlinear constitutive law governing the response of the material. Eq. (3.76) is derived by enforcing the stationarity with respect to $\boldsymbol{\sigma}_m(x,y,z)$ and introducing Eqs. (3.4) and (3.15); this represents the weak form element compatibility.

The additional Eq. (3.77) represents the section equilibrium condition related to the warping effects. This requires the loads $\mathbf{p}_{w,i}$ at the cross-section x_i to be equal to the integral of the stresses $\mathbf{s}_w^x$ and $\mathbf{s}_w^{yz}$, due to the section warping and defined as:

$$\mathbf{s}_w(x) = \left\{ \begin{array}{c} \mathbf{s}_w^x(x) \\ \mathbf{s}_w^{yz}(x) \end{array} \right\} = \left\{ \begin{array}{c} \int_A \mathbf{a}_w^x(y,z)^T\,\boldsymbol{\sigma}_m(x,y,z)\,dA \\ \int_A \mathbf{a}_w^{yz}(y,z)^T\,\boldsymbol{\sigma}_m(x,y,z)\,dA \end{array} \right\} \tag{3.78}$$

where and $\mathbf{a}_w^{yz}(y,z)$ are two matrices with dimensions $3 \times m_w$, composed as follows:

$$\mathbf{a}_w^x(y,z) = \left[\begin{array}{c} \mathbf{M}(y,z) \\ \mathbf{0} \\ \mathbf{0} \end{array} \right], \qquad \mathbf{a}_w^{yz}(y,z) = \left[\begin{array}{c} \mathbf{0} \\ \frac{\partial \mathbf{M}(y,z)}{\partial y} \\ \frac{\partial \mathbf{M}(y,z)}{\partial z} \end{array} \right] \tag{3.79}$$

To implement the developed FE in a standard displacement-based numerical code, a specific solution algorithm need to be conceived, as described in Sec. 5.2.2. This requires the linearization of the governing equations and the definition the element flexibility matrix $\mathbf{f}$. The linearized form of Eqs. (3.74) - (3.77) result as:

$$\mathbf{a}_g^T\,\Delta\mathbf{q} = \Delta\mathbf{p} \tag{3.80}$$

$$\Delta\boldsymbol{\sigma}_m = \frac{\partial \hat{\boldsymbol{\sigma}}[\boldsymbol{\varepsilon}_m(x,y,z)]}{\partial \boldsymbol{\varepsilon}_m}\,\Delta\boldsymbol{\varepsilon}_m(x,y,z) = \mathbf{k}_m\,\Delta\boldsymbol{\varepsilon}_m(x,y,z) \tag{3.81}$$

$$\Delta\mathbf{v} = \int_0^L \mathbf{b}^T(x)\,\Delta\mathbf{e}(x)\,dx \tag{3.82}$$

$$\Delta\mathbf{p}_{w,i} = \int_0^L \frac{\partial \mathrm{N}_i(x)}{\partial x}\Delta\mathbf{s}_w^x(x)\,dx + \int_0^L \mathrm{N}_i(x)\,\Delta\mathbf{s}_w^{yz}(x)\,dx \tag{3.83}$$

After some manipulations (see [1]), the following set of equations is obtained:

$$\hat{\mathbf{k}}\,\Delta\mathbf{u} = \Delta\mathbf{p} \tag{3.84}$$

$$\Delta\mathbf{s}(x) = \mathbf{k}_s(x)\,\Delta\mathbf{e}(x) + \sum_{i=1}^{n_w}\left[\frac{\partial \mathrm{N}_i}{\partial x}(x)\tilde{\mathbf{k}}^x_{sw}(x) + \mathrm{N}_i(x)\,\tilde{\mathbf{k}}^{yz}_{sw}(x)\right]\Delta\mathbf{u}_{w,i} \tag{3.85}$$

$$\Delta\mathbf{v} = \int_0^L \mathbf{b}^T(x)\,\Delta\mathbf{e}(x)\,dx \tag{3.86}$$

$$\Delta\mathbf{p}_{w,i} = \int_0^L \frac{\partial \mathrm{N}_i(x)}{\partial x}\Delta\mathbf{s}^x_w(x)\,dx + \int_0^L \mathrm{N}_i(x)\,\Delta\mathbf{s}^{yz}_w(x)\,dx \tag{3.87}$$

together with the linearized form of the section equilibrium equation, resulting as:

$$\Delta\mathbf{s}(x) = \mathbf{b}(x)\,\Delta\mathbf{q} = \mathbf{b}(x)\,\mathbf{f}^{-1}\,\Delta\mathbf{v} \tag{3.88}$$

In particular, Eq. (3.85) represents the generalized section constitutive law and is obtained by linearizing Eq. (3.15) and introducing Eq. (3.81). Following the same procedure, the linearized forms of Eqs. (3.78) is derived, resulting as:

$$\Delta\mathbf{s}^x_w(x) = \tilde{\mathbf{k}}^x_{ws}(x)\,\Delta\mathbf{e}(x) + \sum_{i=1}^{n_w}\left[\frac{\partial \mathrm{N}_i(x)}{\partial x}\tilde{\mathbf{k}}^x_{ww}(x) + \mathrm{N}_i(x)\,\tilde{\mathbf{k}}^{xy}_{ww}(x)\right]\Delta\mathbf{u}_{w,i} \tag{3.89}$$

$$\Delta\mathbf{s}^{yz}_w(x) = \tilde{\mathbf{k}}^{yz}_{ws}(x)\,\Delta\mathbf{e}(x) + \sum_{i=1}^{n_w}\left[\frac{\partial \mathrm{N}_i(x)}{\partial x}\tilde{\mathbf{k}}^{yx}_{ww}(x) + \mathrm{N}_i(x)\,\tilde{\mathbf{k}}^{yz}_{ww}(x)\right]\Delta\mathbf{u}_{w,i} \tag{3.90}$$

Eqs (3.88), (3.89) and (3.90) contain two contributions, one depending on $\mathbf{e}(x)$, i.e. on the cross-section rigid motions, and one related to the section warping deformations.

The standard section stiffness matrix and the additional section warping stiffness matrices are defined as follows:

$$\mathbf{k}_s = \int_A \mathbf{a}_s^T\,\mathbf{k}_m\,\mathbf{a}_s\,dA \tag{3.91}$$

$$\tilde{\mathbf{k}}^x_{sw} = \left(\int_A \mathbf{a}_s^T\,\mathbf{k}_m\,\mathbf{a}^x_w\,dA\right)\boldsymbol{\Gamma} = \mathbf{k}^x_{sw}\,\boldsymbol{\Gamma} \tag{3.92}$$

$$\tilde{\mathbf{k}}^{yz}_{sw} = \left(\int_A \mathbf{a}_s^T\,\mathbf{k}_m\,\mathbf{a}^{yz}_w\,dA\right)\boldsymbol{\Gamma} = \mathbf{k}^{yz}_{sw}\,\boldsymbol{\Gamma} \tag{3.93}$$

$$\tilde{\mathbf{k}}^x_{ws} = \boldsymbol{\Gamma}^T\left(\int_A (\mathbf{a}^x_w)^T\,\mathbf{k}_m\,\mathbf{a}_s\,dA\right) = \boldsymbol{\Gamma}^T\,\mathbf{k}^x_{ws} \tag{3.94}$$

$$\tilde{\mathbf{k}}^{yz}_{ws} = \boldsymbol{\Gamma}^T\left(\int_A (\mathbf{a}^{yz}_w)^T\,\mathbf{k}_m\,\mathbf{a}_s\,dA\right) = \boldsymbol{\Gamma}^T\,\mathbf{k}^{yz}_{ws} \tag{3.95}$$

$$\tilde{\mathbf{k}}^x_{ww} = \boldsymbol{\Gamma}^T\left(\int_A (\mathbf{a}^x_w)^T\,\mathbf{k}_m\,\mathbf{a}^x_w\,dA\right)\boldsymbol{\Gamma} + \boldsymbol{\Psi} = \boldsymbol{\Gamma}^T\,\mathbf{k}^x_{ww}\,\boldsymbol{\Gamma} + \boldsymbol{\Psi} \tag{3.96}$$

$$\tilde{\mathbf{k}}^{yz}_{ww} = \boldsymbol{\Gamma}^T\left(\int_A (\mathbf{a}^{yz}_w)^T\,\mathbf{k}_m\,\mathbf{a}^{yz}_w\,dA\right)\boldsymbol{\Gamma} + \boldsymbol{\Psi} = \boldsymbol{\Gamma}^T\,\mathbf{k}^{yz}_{ww}\,\boldsymbol{\Gamma} + \boldsymbol{\Psi} \tag{3.97}$$

$$\tilde{\mathbf{k}}^{xy}_{ww} = \boldsymbol{\Gamma}^T\left(\int_A (\mathbf{a}^x_w)^T\,\mathbf{k}_m\,\mathbf{a}^{yz}_w\,dA\right)\boldsymbol{\Gamma} + \boldsymbol{\Psi} = \boldsymbol{\Gamma}^T\,\mathbf{k}^{xy}_{ww}\,\boldsymbol{\Gamma} + \boldsymbol{\Psi} \tag{3.98}$$

$$\tilde{\mathbf{k}}_{ww}^{yx} = \mathbf{\Gamma}^T \left(\int_A (\mathbf{a}_w^{yz})^T \, \mathbf{k}_m \, \mathbf{a}_w^x \, dA \right) \mathbf{\Gamma} + \mathbf{\Psi} = \mathbf{\Gamma}^T \, \mathbf{k}_{ww}^{yx} \, \mathbf{\Gamma} + \mathbf{\Psi} \tag{3.99}$$

where $\mathbf{\Gamma}$ and $\mathbf{\Psi}$ are a projection and a correction matrix, respectively, and defined later.

Substituting Eq. (3.88) into Eq. (3.85) the increment of the section strains $\Delta\mathbf{e}$ is computed, resulting as:

$$\Delta\mathbf{e}(x) = \mathbf{k}_s^{-1}(x) \left\{ \mathbf{b}(x) \, \Delta\mathbf{q} - \sum_{i=1}^{n_w} \left[\frac{\partial \mathrm{N}_i}{\partial x}(x) \tilde{\mathbf{k}}_{sw}^x(x) + \mathrm{N}_i(x) \, \tilde{\mathbf{k}}_{sw}^{yz}(x) \right] \Delta\mathbf{u}_{w,i} \right\} \tag{3.100}$$

Eq. (3.100) is introduced in Eqs. (3.89) and (3.90) and the resulting expressions of $\Delta\mathbf{s}_w^x(x)$ and $\Delta\mathbf{s}_w^{yz}(x)$ are used in the warping equilibrium Eq. (3.87), whose compact form, thus, results as:

$$\Delta\mathbf{p}_w = \mathbf{b}_{ws} \, \Delta\mathbf{q} + \mathbf{k}_{ww} \, \Delta\mathbf{u}_w \tag{3.101}$$

$\Delta\mathbf{u}_w$ and $\Delta\mathbf{p}_w$ being the increments of $\mathbf{u}_w$ and $\mathbf{p}_w$, respectively. After manipulating the governing equations, the element basic flexibility matrix $\mathbf{f}$ is derived, expressed as the sum of two terms, as:

$$\mathbf{f} = \mathbf{f}_s + \mathbf{f}_w = \int_0^L \mathbf{b}^T \, \mathbf{k}_s^{-1} \, \mathbf{b} \, dx + \mathbf{b}_{sw} \, \mathbf{k}_{ww}^{-1} \, \mathbf{b}_{ws} \tag{3.102}$$

where $\mathbf{f}_s$ is the classical flexibility matrix, according to the equilibrated beam formulation, and $\mathbf{f}_w$ represents the contribution due to the warping effects. The matrices $\mathbf{k}_{ww}$, $\mathbf{b}_{ws}$ and $\mathbf{b}_{sw}$ are defined as follows:

$$\begin{gathered} \mathbf{k}_{ww} = \begin{bmatrix} \mathbf{k}_{w,1,1} & \dots & \mathbf{k}_{w,1,n_w} \\ \vdots & \ddots & \vdots \\ \mathbf{k}_{w,n_w,1} & \dots & \mathbf{k}_{w,n_w,n_w} \end{bmatrix} \\ \mathbf{b}_{ws} = \begin{bmatrix} \mathbf{b}_{ws,1} \\ \vdots \\ \mathbf{b}_{ws,n_w} \end{bmatrix} \qquad \text{and} \qquad \mathbf{b}_{sw} = [\mathbf{b}_{sw,1} \quad \dots \quad \mathbf{b}_{sw,n_w}] \end{gathered} \tag{3.103}$$

where:

$$\begin{aligned} \mathbf{k}_{w,i,n} &= \int_0^L \tilde{\mathbf{k}}_{ww,i,n} - \tilde{\mathbf{k}}_{ws,i} \, \mathbf{k}_{ss}^{-1} \, \tilde{\mathbf{k}}_{sw,n} \, dx \\ \mathbf{b}_{ws,i} &= \int_0^L \tilde{\mathbf{k}}_{ws,i} \, \mathbf{k}_{ss}^{-1} \, \mathbf{b} \, dx \qquad \text{and} \qquad \mathbf{b}_{sw,i} = \int_0^L \mathbf{b}^T \, \mathbf{k}_{ss}^{-1} \, \tilde{\mathbf{k}}_{sw,i} \, dx \\ \tilde{\mathbf{k}}_{ww,i,n} &= \frac{\partial \mathrm{N}_i}{\partial x} \left[\frac{\partial \mathrm{N}_n}{\partial x} \tilde{\mathbf{k}}_{ww}^x + \mathrm{N}_n \tilde{\mathbf{k}}_{ww}^{xy} \right] + \mathrm{N}_i \left[\frac{\partial \mathrm{N}_n}{\partial x} \tilde{\mathbf{k}}_{ww}^{yx} + \mathrm{N}_n \tilde{\mathbf{k}}_{ww}^{yz} \right] \end{aligned}$$

$$\tilde{\mathbf{k}}_{ws,i} = \frac{\partial \mathrm{N}_i}{\partial x}\tilde{\mathbf{k}}^x_{ws} + \mathrm{N}_i\,\tilde{\mathbf{k}}^{yz}_{ws} \qquad \text{and} \qquad \tilde{\mathbf{k}}_{sw,i} = \frac{\partial \mathrm{N}_i}{\partial x}\tilde{\mathbf{k}}^x_{sw} + \mathrm{N}_i\,\tilde{\mathbf{k}}^{yz}_{sw}$$

When the matrix $\mathbf{k}_m$ is symmetric, both the $\mathbf{f}_s$ and $\mathbf{f}_w$ are symmetric too, since $\tilde{\mathbf{k}}^x_{sw} = \left(\tilde{\mathbf{k}}^x_{ws}\right)^T$, $\tilde{\mathbf{k}}^{yz}_{sw} = \left(\tilde{\mathbf{k}}^{yz}_{ws}\right)^T$ and $\tilde{\mathbf{k}}^{xy}_{ww} = \left(\tilde{\mathbf{k}}^{yx}_{ww}\right)^T$, so that $\mathbf{b}_{sw} = \mathbf{b}^T_{ws}$ and $\mathbf{k}_{ww}$ is symmetric as well. Conversely, if $\mathbf{k}_m$ is non symmetric, $\mathbf{b}_{sw} \neq \mathbf{b}^T_{ws}$ and $\mathbf{k}_{ww}$ is non symmetric.

Eq. (3.102) states that the warping of the cross-sections gives an additional contribution to the element stiffness, due to the matrix $\mathbf{k}_{ww}$, which depends only on the warping interpolation functions and on the material stiffness. To ensure the non-singularity of this matrix, the cross-section rigid body motions have to be eliminated from the displacement field $u_w(x, y, z)$, that is the following condition needs to be satisfied:

$$\int_A \begin{pmatrix} 1 \\ y \\ z \end{pmatrix} u_{w,i}(x_i, y, z)\, dA = \int_A \begin{pmatrix} 1 \\ y \\ z \end{pmatrix} \mathbf{M}(y, z)\, \mathbf{u}_{w,i}\, dA = \mathbf{0} \tag{3.104}$$

Therefore, the interpolation functions $\mathrm{M}_j(y, z)$, defined in Eq. (3.67), is conveniently modified. To this end, the procedure described in [1] could be followed, which is here generalized to the case of Hermite interpolation functions. This is based on the definition of the projection matrix $\mathbf{\Gamma}$ and the correction matrix $\mathbf{\Psi}$ in Eqs. (3.91) - (3.99), as:

$$\mathbf{\Gamma} = \mathbf{I}(m_w) - \mathbf{R}\,\mathbf{V} \qquad \text{and} \qquad \mathbf{\Psi} = \psi\,\mathbf{V}^T\,\mathbf{V} \tag{3.105}$$

$\mathbf{I}(m_w)$ being the $m_w \times m_w$ identity matrix and $\mathbf{R}$ the $m_w \times 3$ matrix, representing the rigid body motions of the element section. This contains the coordinates of the s_w warping points as follows:

$$\mathbf{R} = \begin{bmatrix} \alpha_1\,\mathbf{r}_1 & \alpha_2\,\mathbf{r}_2 & \alpha_3\,\mathbf{r}_3 \end{bmatrix} \tag{3.106}$$

Lagrange | *Hermite*

$$\underset{\mathbf{r}_1}{\begin{Bmatrix} 1 \\ 1 \\ 1 \\ \vdots \\ 1 \\ 1 \\ 1 \end{Bmatrix}} \quad \underset{\mathbf{r}_2}{\begin{Bmatrix} y_1 \\ y_2 \\ y_3 \\ \vdots \\ y_{s_w-2} \\ y_{s_w-1} \\ y_{s_w} \end{Bmatrix}} \quad \underset{\mathbf{r}_3}{\begin{Bmatrix} z_1 \\ z_2 \\ z_3 \\ \vdots \\ z_{s_w-2} \\ z_{s_w-1} \\ z_{s_w} \end{Bmatrix}} \qquad \underset{\mathbf{r}_1}{\begin{Bmatrix} 1 \\ 0 \\ 0 \\ \vdots \\ 1 \\ 0 \\ 0 \end{Bmatrix}} \quad \underset{\mathbf{r}_2}{\begin{Bmatrix} y_1 \\ 1 \\ 0 \\ \vdots \\ y_{s_w} \\ 1 \\ 0 \end{Bmatrix}} \quad \underset{\mathbf{r}_3}{\begin{Bmatrix} z_1 \\ 0 \\ 1 \\ \vdots \\ z_{s_w} \\ 0 \\ 1 \end{Bmatrix}}$$

Finally, $\mathbf{V}$ is a $3 \times m_w$ matrix containing the average values and the first moments of

the shape functions over the cross section:

$$\mathbf{V} = \int_A \begin{pmatrix} 1 \\ y \\ z \end{pmatrix} \mathbf{M}(y,z)\, dA \tag{3.107}$$

and α_1, α_2 and α_3 are constants determined imposing that the product $\mathbf{V}\,\mathbf{R}$ is equal to a 3×3 identity matrix.

In this work, taking advantage of the Gram-Schmidt orthonormalization [101], a new definition of $\mathbf{\Gamma}$ and $\mathbf{\Psi}$ is suggested, which does not depend on the matrix $\mathbf{R}$ and on the constant ψ. In particular, the rows of $\mathbf{V}$ are linear independent vectors and they form the basis of the subspace $\mathbb{S}$ representing the section rigid body motions for the $M_j(y,z)$. Hence, the matrix $\mathbf{\Lambda} = \mathbf{V}^T \left(\mathbf{V}\,\mathbf{V}^T\right)^{-1} \mathbf{V}$ is the matrix projecting the vector $\mathbf{M}(y,z)$ into $\mathbb{S}$. Applying the Gram-Schmidt orthonormalization on $\mathbf{V}$, the orthogonal matrix $\hat{\mathbf{V}}$ is computed and the matrix $\mathbf{\Lambda}$ simply becomes $\mathbf{\Lambda} = \hat{\mathbf{V}}^T\hat{\mathbf{V}}$. Therefore, the projection matrix $\mathbf{\Gamma}$, which is the matrix projecting $\mathbf{M}(y,z)$ in the orthogonal complement of $\mathbb{S}$, is evaluated as:

$$\mathbf{\Gamma} = \mathbf{I}(m_w) - \hat{\mathbf{V}}^{\mathbf{T}}\,\hat{\mathbf{V}} \tag{3.108}$$

and the correction matrix $\mathbf{\Psi}$ is evaluated as:

$$\mathbf{\Psi} = \hat{\mathbf{V}}^T\,\hat{\mathbf{V}} \tag{3.109}$$

Chapter 4

Regularization technique

4.1 General

FE models adopting strain-softening constitutive relations are likely to exhibit damage and strain localization effects. In fact, when the material reaches its maximum strength and experiences the post-peak branch of the constitutive response, the behavior becomes unstable, leading to the ill-posedness of the structure governing equations. From a computational point of view, the stability of the material depends on the satisfaction of the following inequality, imposing that the scalar product of the incremental stresses $\dot{\boldsymbol{\sigma}}$ and the incremental strains $\dot{\boldsymbol{\varepsilon}}$ must be strictly positive [72]:

$$\dot{\boldsymbol{\sigma}}^T \dot{\boldsymbol{\varepsilon}} = \dot{\boldsymbol{\varepsilon}}^T \mathbf{C}_t^T \dot{\boldsymbol{\varepsilon}} > 0 \tag{4.1}$$

In Eq. (4.1) the incremental form of a general constitutive law (e.g Eq. (2.31)) is introduced to express the material stresses in terms of material strains and the tangent stiffness matrix $\mathbf{C}_t$ is considered. In the post-peak part of the material response, the $\mathbf{C}_t$ is no longer positive definite and thus Eq. (4.1) is not satisfied, that is the material results unstable.

As known, this effect usually produces strain/damage localization and the related mesh-sensitivity problems and this makes difficult to identify the real softening response of the structure. For beam-column FEs, this issue affects the whole element length in displacement-based models and a single quadrature cross-section along the element axis in force-based models [96]. Indeed, displacement-based formulations evaluate the cross-section deformations, and thus the material strains and damage, from the cross-section displacements, which are interpolated over the element length considering the nodal DOFs and a fixed set of shape functions. Hence, during the softening part of the structural response, strains and damage localize in one element of the mesh (or a

group of them), while the rest of the structure unloads. This is also typical of both 2D and 3D FEs based on the interpolation of displacement fields over the element domain. By contrast, force-based formulations evaluate the material strains and damage at each quadrature cross-section independently, considering the generalized section forces equilibrated with the nodal forces and the constitutive relation. In fact, for practical purposes it is common to evaluate the integral over the element length, appearing in element governing equations, through a numerical integration rule. For instance, Eq. (3.29), defining the element flexibility matrix for the TFF beam, is used in the form:

$$\mathbf{f} = \int_L \mathbf{b}^T(x)\,\mathbf{f}_s(x)\,\mathbf{b}(x)\,dx \simeq \sum_{t=1}^{n_{qs}} \mathbf{b}^T(x_t)\,\mathbf{f}_s(x_t)\,\mathbf{b}(x_t)\,w_t$$

where the x_t, with $t = 1, \ldots, n_{qs}$, are the locations along the axis of the quadrature cross-sections and the w_t, with $t = 1, \ldots, n_{qs}$ are the associated quadrature weights. On these weights depends the localization zone length. Fig. 4.1 shows an example. A

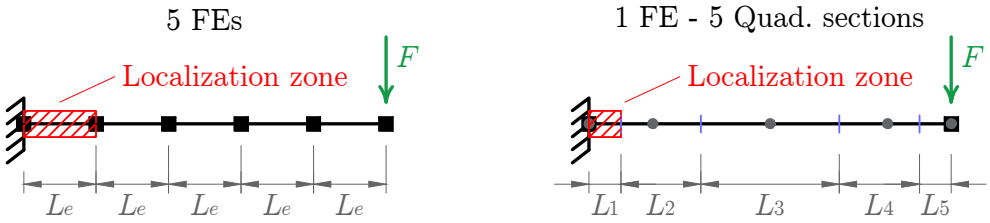

(*a*) Displacement-based FEs (*b*) Force-based FEs

Figure 4.1: Example of localization zone length for beam-column FEs.

cantilever beam is subjected to a transversal load at the free end, so that the maximum stress occurs at the fixed end. For displacement-based elements, the beam is discretized with 5 FEs (the black square dots represent the end nodes) and the localization zone is represented by the length L_e of the element that is closest to the fixed end; in the example, all the element have the same length, but it has no influence on the localization zone. For force-based elements, only one element can be used to discretize the beam and five quadrature points are adopted (gray dots). A weighting length equal to $w_t \frac{L}{2}$ is associated to each quadrature cross-section. In the figure these lengths are the distances L_1 to L_5 between the blue vertical bars. In this case, the localization zone is represented by the weighting length L_1 associated to the quadrature point closest to the fixed end. This means that for displacement-based models the localization zone depends on the FE size, whereas for force-based and mixed models this is related to the number of quadrature cross-sections adopted for the most stressed element changes. For both displacement- and force-based FEs, the adoption of a regularization technique

is mandatory to obtain an objective representation of the structural response.

The most common approaches for regularizing the softening response of FE models are the nonlocal integral procedures and the gradient methods [2,102], which are usually applied for displacement-based formulations. These are based on the idea that damage occurring in a certain point of the structure depends on the stress/strain state of a representative volume of material surrounding that point. Hence, during the evaluation of the structural response, each element has to take into account for the material response evolution occurring in the points lying in its neighborhood and this requires the adoption of some specific routines. For force-based beam-column FEs, a different approach is proposed in [96], where the element regularization is performed taking advantage on the 1D numerical integration rule adopted to evaluate the integral over the element length. This technique calibrates the weighting lengths associated to the end quadrature points (where the localization occurs) so that the resulting solution does not depend on the total number of the element quadrature points. Hence, this method does not require the nonlocal "interaction" between the elements of the mesh and results to be very efficient from a computational point of view. Basing on the same idea, a similar regularizing method is proposed in [23] and [103], aiming to generalize the original proposal in [96] and to solve the drawbacks of that approach. In all cases, the method only applies to force-based beam-column elements and thus its adoption makes it difficult to compare the responses obtained with 2D and 3D models.

After giving an overview on these techniques and on the standard nonlocal formulation in Sec. 4.2, Sec. 4.3 presents regularization approach adopted for the correlation studies of this work. Referring to the 3D material model in Sec. 2.4, this formulation consists of a nonlocal integral definition of the material strains, which are evaluated from nonlocal measures of the generalized deformations. To optimize the computational burden, the adopted formulation assumes a specific weighting function to perform the nonlocal integral evaluation in the element volume.

4.2 Overview on the standard methods

This section presents two standard techniques to regularize the softening behavior of damaging structures. The first one is the approach proposed in [96] and later on adopted and improved in [23] and [103]. This method, which is only applicable to force-based and mixed beam-column FEs, ensures the objectivity of the structural response by controlling the quadrature weights associated to the cross-sections of the element and results very efficient and cheap. The second technique is the classical nonlocal formulation approach applicable to any kind of FE.

4.2.1 1D integration rules for force-based and mixed beam elements

In force-based and mixed beam-column FEs, the definition of the element governing equations requires the integration over the element length L of specific fields. In the TFF and the ETFF models described in Secs. 3.2 and 3.3, these integrals are performed in Eqs. (3.28) and (3.29) to evaluate the compatible basic deformations $\mathbf{v}$ and the basic tangent flexibility matrix $\mathbf{f}$, i.e.:

$$\mathbf{v} = \int_L \mathbf{b}^T(x)\,\mathbf{e}(x)\,dx, \qquad \mathbf{f} = \int_L \mathbf{b}^T(x)\,\mathbf{f}_s(x)\,\mathbf{b}(x)\,dx$$

As described above, for the general case of nonlinear material responses, their solutions is usually obtained through a numerical integration method, as:

$$\mathbf{v} \simeq \sum_{t=1}^{n_{qs}} \mathbf{b}^T(x_t)\,\mathbf{e}(x_t)\,w_t, \qquad \mathbf{f} \simeq \sum_{t=1}^{n_{qs}} \mathbf{b}^T(x_t)\,\mathbf{f}_s(x_t)\,\mathbf{b}(x_t)\,w_t$$

Considering that for common framed structures where the lateral loads are predominant, the maximum stress usually arises at the end cross-sections (unless particular distributed load are applied), the Gauss-Lobatto (GL) scheme is the most suitable to perform the integration, because this includes the end points and allows to evaluate their response [96] (see for example Fig. 4.1*b*). With the definition of the equilibrium matrix $\mathbf{b}(x)$ in Eq. (3.25), for an homogeneous beam with uniform cross-section, the minimum number of GL points needed to correctly evaluate the initial elastic stiffness of the element is $n_{qs} = 3$. The same is true for the EBFF model in Sec. 3.2.

Similar considerations hold for the WMF models described in Sec. 3.4. In this case, the integration over the element length is also performed to evaluate the warping forces $\mathbf{p}_{w,i}$ in Eq. (3.77), i.e.:

$$\mathbf{p}_{w,i} = \int_0^L \frac{\partial \mathrm{N}_i(x)}{\partial x}\mathbf{s}_w^x(x)\,dx + \int_0^L \mathrm{N}_i(x)\,\mathbf{s}_w^{yz}(x)\,dx,$$

and the warping matrices $\mathbf{k}_{ww}$, $\mathbf{b}_{sw}$ and $\mathbf{b}_{ws}$ in Eq. (3.103). Hence, the accuracy of the numerical integration also depends on the polynomials chosen for the interpolation functions $N_i(x)$ in Eq. (3.64). If r_x is the maximum order of the functions $N_i(x)$, that is $n_w = r_x + 1$ warping sections are located along the element axis, for an homogeneous beam with uniform cross-sections (considering also Eq. (3.89), (3.90) and(3.100)) the minimum number of GL points needed to correctly evaluate the initial elastic stiffness of the element is $n_{qs} = r_x + 2 = n_w + 1$.

Taking advantage of stress concentration occurring at the end cross-sections, Ad-

dessi and Ciampi [96] proposed to perform the numerical integration subdividing the element into three parts: two end parts, where the damage localization is supposed to occur, and a middle one, which can either remain elastic or being damaged as well. Fig. 4.2 gives an example where the different parts are bounded by vertical blue bars and the quadrature cross-sections are indicated by the gray dots. The numerical integration is performed independently in each part: the GL scheme or the Gauss-Radau (GR) scheme [23] is always applied for the end ones, because it is necessary to have a quadrature cross-section placed at each element end, whereas the middle part can be discretized with any numerical scheme (in the figure, the GL scheme is adopted here as well). In particular, the lengths L_i, L_m and L_j of the three parts are set on the basis of the two characteristic lengths $L_{c,i}$ and $L_{c,j}$. Considering that the damage localization occur at the end cross-sections, $L_{c,i}$ and $L_{c,j}$ determine the width of the localization zones at the ends I and J, respectively.

Once the five parameters $L_{c,i}$, $L_{c,j}$, n_i, n_m and n_j are defined, the basic idea of the method consists in forcing the localization to occur in the two end zones $L_{c,i}$ and $L_{c,j}$. This is done choosing the length L_i and L_j so that the quadrature weights associated to the ends I and J are equal to $L_{c,i}$ and $L_{c,j}$, respectively. Indeed, if n_i is the number

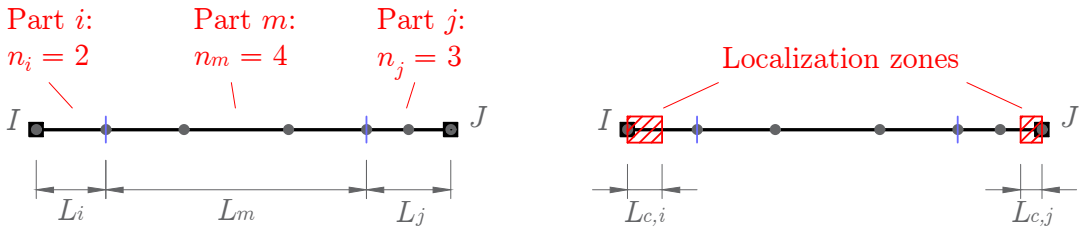

(a) Element subdivided in 3 parts

(b) Quadrature weights for the ends I and J

Figure 4.2: Example of Addessi-Ciampi regularization rule: (a) the element is divided in 3 parts i, m and j, with different lengths: (b) the quadrature weights for the first node of the part i and the last node of the part j are set equal to $L_{c,i}$ and $L_{c,j}$.

of quadrature cross-sections placed in the part i of the element, the length L_i need to chosen so that:

$$L_{c,i} = \frac{L_i}{2} w_i \qquad \rightarrow \qquad L_i = 2\, L_{c,i}\, w_i \tag{4.2}$$

where w_i is the quadrature weight associated to the first point in the adopted adimensional quadrature scheme with n_i points, i.e. $w_i = 2/n_i(n_i - 1)$ for the GL scheme and $w_i = 2/n_i^2$ for the GR scheme. Similarly:

$$L_{c,j} = \frac{L_j}{2} w_j \qquad \rightarrow \qquad L_j = 2\, L_{c,j}\, w_j \tag{4.3}$$

where w_j is the quadrature weight associated to the last point in the adopted adimen-

sional quadrature scheme with n_j points, i.e. $w_j = 2/n_j(n_j - 1)$ for the GL scheme and $w_j = 2/n_j^2$ for the GR scheme. Consequently:

$$L_m = L - L_i - L_j \tag{4.4}$$

where L is the total length of the element. The parameter $L_{c,i}$, $L_{c,j}$, n_i, n_m and n_j must always be selected so that from Eq. (4.4) results $L_m > 0$.

Note that, in practical situations, the damage localization usually occurs only in one of the two end zones of the beam, that is either in $L_{c,i}$ or in $L_{c,j}$. Yet, which of the zones is really involved is generally unknown before the analysis. Hence, both of them need to be considered during the structural model definition, adopting the approach now described. By contrast, if this information is known (as for the cantilever beam in Fig. 4.1, where the localization can only occur at the fixed end), a similar approach can be used. It consists in dividing the element in only two parts, considering only one of the two localization zones, either $L_{c,i}$ or $L_{c,j}$. Fig. 4.3 shows two examples.

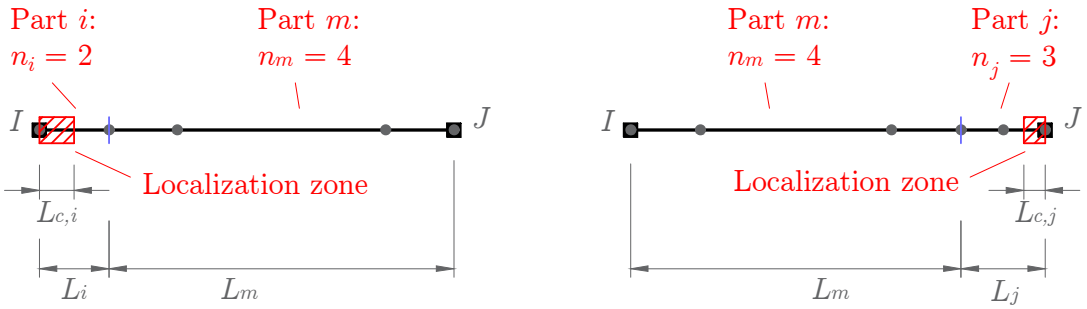

(a) Element subdivided in L_i and L_m

(b) Element subdivided in L_m and L_j

Figure 4.3: Examples of Addessi-Ciampi regularization rule where the element is subdivided in only 2 parts.

Regardless of which subdivision is adopted (in 3 parts or in 2 parts), another important observation concerns the number of quadrature cross-sections placed in each part of the element with respect to quadrature scheme adopted. Indeed, two cases can be considered:

1. The number of quadrature cross-sections n_i and n_j in the end parts is grater than 1. In this case, these cross-sections are placed accordingly to the GL or the GR scheme (Fig. 4.2). If the GR scheme is used, the Gauss-Legrende scheme should be used in the middle part of the element, to reduce the total number of quadrature cross-sections and thus the computational cost. By contrast, if the GL scheme is used, it is more convenient to use the GL scheme in the middle part of the element as well. In fact, each quadrature cross-section located at the

boundaries of the middle part of the element can be used for both the numerical integration of the middle part and the numerical integration in the adjacent end part. Hence, keeping the order of accuracy the same, the total number of quadrature cross-section results lower. For instance, the element in Fig. 4.2 considers a total number of 7 quadrature cross-sections, that is only 7 cross-sections are evaluated during the Element State Determination, even though it uses a 2-, 4- and 3-points scheme in each part, respectively.

2. The number of quadrature cross-sections n_i and n_j in the end parts is equal to 1. In this case, these cross-sections are usually placed at the element ends, endpoint scheme (Part i of the element in Fig. 4.4), but they can also be placed at the center of each part, midpoint scheme (Part j of the element in Fig. 4.4) even though their quadrature weights are always equal to $L_{c,i} = L_i$ and $L_{c,j} = L_j$, respectively [23]. This second choice, however, can lead to an overestimation of the element resistance (or of its yielding resisting forces), as shown in [23], because the quadrature cross-sections, where the stresses are monitored, do not coincide with element ends, where the maximum values arise. Hence, the endpoint scheme is usually preferred. In any case, to reduce the total number of quadrature cross-sections, the Gauss-Legrende scheme should be used in the middle part.

The case of $n_i = n_j = 1$ can be also used to reproduce the classical plastic hinges model. Indeed, if the material response of the central part of the element is assumed linear elastic, the final model results as a beam with material nonlinearities concentrated at the ends, where the lengths associated to the plastic hinges are $L_{c,i}$ and $L_{c,j}$. The study in [23] shows that, in this case, the contribute of the middle elastic part to the element flexibility matrix $\mathbf{f}$ and to the element basic deformation $\mathbf{v}$ can be easily evaluated considering only the element geometry, the material elastic properties and the element basic forces $\mathbf{q}$, that is by-passing the actual evaluation of the quadrature cross-sections states, which is required only at the end quadrature points.

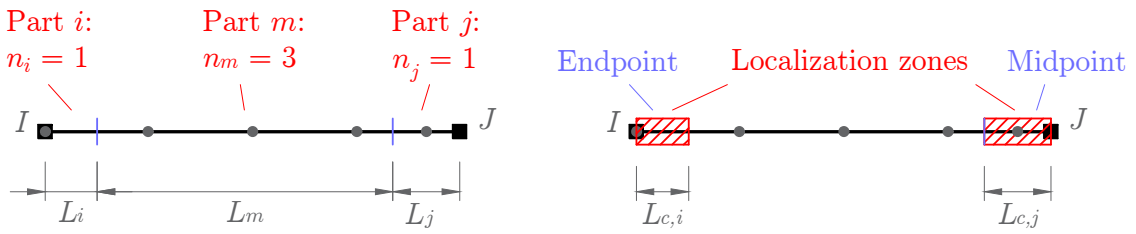

(a) Element subdivided in 3 parts

(b) Quadrature weights for the ends I and J

Figure 4.4: Examples of Addessi-Ciampi regularization rule with one quadrature cross-section in the end parts.

In all cases, the regularization approach here described presents three drawbacks. Firstly, the method does not ensure the correct evaluation of the initial elastic stiffness of the beam. In fact, only if each part of the element is discretized with enough quadrature cross-sections the element stiffness matrix is correctly integrated, but this may result in very onerous model. For instance, for the TFF model it is necessary to place 3 GL points in each part, resulting in a total of 7 quadrature cross-sections, or 2 GR points in the ends part and 2 Gauss-Legendre points in the middle part, resulting in a total of 6 quadrature cross-sections. However, the error provided by adopting less quadrature points is usually negligible (except in special cases) compared with order of magnitude of the element stiffness. Hence, a computationally inexpensive model can be always adopted without significant loss of accuracy.

Secondly, even though the method efficiently regularizes strain-softening response, it can fail in representing correctly a strain-hardening and thus it can only be used when it is known a-priori that a specific element is going to show a pure elasto-softening behavior, without any hardening. This is proved in the study by Scott and Hamutcuoglu [103], where an alternative approach is also proposed to solve this issue. In particular, the purpose of the study is to define a general regularization approach that can be applied for elements showing both hardening and softening behavior. Hence, they formulate a method based on the interpolatory quadrature scheme and on the introduction of two additional quadrature cross-sections, properly located along the beam axis. Unfortunately, the location of these additional cross-sections still depends on the nature of the element behavior, that is they need to be close to the element ends for hardening behaviors and far from them for softening behaviors. Hence, considering also that the interpolatory scheme increases the computational cost of the model, it is not clear what advantage this model offer over the standard one described above and thus it is not considered for the correlation studies of this work.

The last important drawback is that the regularization approach proposed by Addessi and Ciampi does not really avoid the damage localization. As described, it allows to set the width of the localization zone, but the localization still occurs and, if not well controlled, it can lead to unexpected results. For this reason, the present work uses a regularization approach which is based on the nonlocal integral formulation, as described in the following sections.

4.2.2 Standard nonlocal formulation for FEs

The standard nonlocal approach for FEs was introduced by Pijaudier-Cabot and Bazant in [104], basing on the formulations proposed by Kroner [105], Kunin [106] and others. These original proposals state that the stresses of a material point needs to be eval-

uated considering the response of a whole neighborhood of that point and evaluating the mean values of the strains occurring in it. In other words, they assume the local response in terms of stresses to be dependent not only on the (local) strains of the considered point, but also on those occurring around it. Adopting a similar hypotesis, Pijaudier-Cabot and Bazant introduced an important enhancement to the formulation, that is they distinguish between the influence that the nonlocal variables have on the material stresses and that they have on the damage variables. Indeed, they consider that the elastic and the elasto-plastic (hardening) response of the material should not be modified by the nonlocal formulation, as opposed to the softening one. Hence, they assumes that the nonlocal strains do not act directly on the material stresses, but they are used to modified only the damage variables.

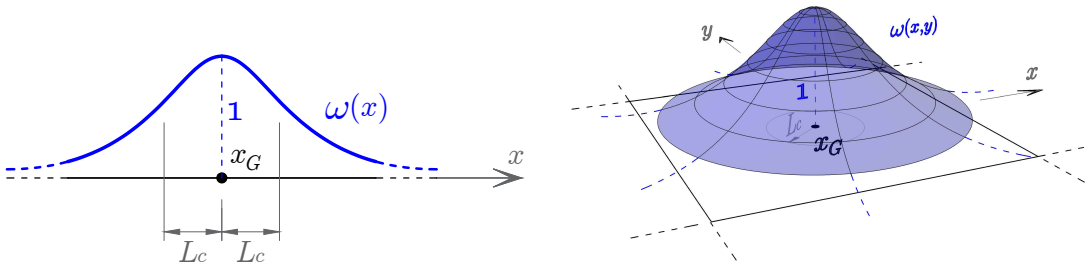

(*a*) 1D formulation (*b*) 2D formulation

Figure 4.5: Schematic representation of the Gaussian function ω adopted as weighting function for the standard nonlocal integration.

In a general 3D local damage model, as in Sec. 2.3 where the nonlinear constitutive law is given by Eq. (2.15), the damage variable D is only function of the local strains (generally represented by one or more equivalent measures ε_{eq}), $D(\boldsymbol{\varepsilon})$. In this case, the standard nonlocal formulation can be defined assuming D as function of nonlocal strains $\tilde{\boldsymbol{\varepsilon}}$, i.e. $D(\tilde{\boldsymbol{\varepsilon}})$. These are derived by averaging the local strains in a specific reference material volume V_r. Indeed, the formulation evaluates $\tilde{\boldsymbol{\varepsilon}}$ as:

$$\tilde{\boldsymbol{\varepsilon}} = \frac{\int_{V_r} \boldsymbol{\varepsilon}(x,y,z)\,\omega(x,y,z)\,dV}{\int_{V_r} \omega(x,y,z)\,dV} \tag{4.5}$$

$\omega(x,y,z)$ being a weighting function introduced in the averaging process. Usually, $\omega(x,y,z)$ is associated to a given characteristic length L_c, related to the radius of the reference volume and assumed as a material property. Many different expressions can be adopted for $\omega(x,y,z)$; a common one is the following:

$$\omega(x,y,z) = \exp\left(-\frac{\Delta d^2}{2L_c^2}\right) \tag{4.6}$$

In Eq. (4.6), the averaging process is extended to the whole material volume V and the function $\omega(x, y, z)$ is used to define the reference volume. Here, $\Delta d = |\mathbf{x} - \mathbf{x}_G|$ is the distance between the point G located at $\mathbf{x}_G = \{x_G,\ y_G,\ z_G\}^T$, where the non-local strains $\tilde{\boldsymbol{\varepsilon}}$ has to be evaluated and the point located at $\mathbf{x} = \{x,\ y,\ z\}^T$. The corresponding 1D and 2D expressions result as:

$$\tilde{\boldsymbol{\varepsilon}} = \frac{\int_L \boldsymbol{\varepsilon}(x)\,\omega(x)\,dx}{\int_L \omega(x)\,dx} \qquad \text{with} \qquad \omega(x) = \exp\left(-\frac{\Delta x^2}{2L_c^2}\right) \tag{4.7}$$

and

$$\tilde{\boldsymbol{\varepsilon}} = \frac{\int_A \boldsymbol{\varepsilon}(x,y)\,\omega(x,y)\,dA}{\int_A \omega(x,y)\,dA} \qquad \text{with} \qquad \omega(x,y) = \exp\left(-\frac{\Delta x^2 + \Delta y^2}{2L_c^2}\right) \tag{4.8}$$

respectively, where $\Delta x = x - x_G$ and $\Delta y = y - y_G$. In Eq. (4.7) the weighting function $\omega(x)$ is a one-dimensional Gaussian function centered in x_G and having the inflection points at $x = x_G \pm L_c$ (Fig. 4.5*a*). The function is equal to 1 in x_G and tends to zero moving away from this point. Eq. (4.8) is the two-dimensional version, whose representation is given in Fig. 4.5*b*.

As shown, for all the three Eqs. (4.6), (4.7) and (4.8), the representative volume V_r, being a segment in the 1D case and a circle in the 2D case, is defined through the weighting function ω. Indeed, one can consider that for all the material points farther than $4L_c$ from $\mathbf{x}_G$ the function ω is so small that the contribute of the strains is negligible at those points.

The main drawback of the nonlocal approaches is the increase of computational cost they imply. In fact, the nonlocal variables are in general evaluated for each quadrature point of each element and this means that every time the Element State Determination is performed (e.g. Sec. 5.2 for beam-column FEs) the local variables of the entire structure need to be pre-emptively computed and stored. The general expressions defined in Eq. (4.5) refer to the definition of the nonlocal formulation in terms of nonlocal strains. In this case, the local strains of all the quadrature points of all the FEs need to be computed and stored before each Element State Determination and, then, they are used to compute the nonlocal strains. However, many different approaches can be considered, that is other variables can be assumed for the nonlocal averaging process. For instance, one can directly evaluate the nonlocal values of the equivalent strain measure ε_{eq} and/or of the damage internal variables, when this allows to simplify the calculation. Obviously, it depends on the specific FE formulations adopted to model the structure and this need to be chosen very carefully. Moreover, as suggested in [104], even though the structure is 3D (or 2D) the averaging process

can be performed considering only one principal direction, if specific constraint allows to neglect the effects produced in the others. For instance, in a standard Timoshenko or Euler-Bernoulli beam-column FE (as the ones described in Sec. 3.2) the hypothesis of rigid plane section prevents the localization in the cross-section plane and allows to evaluate the nonlocal variables considering only the direction parallel to the element axis. The nonlocal formulation adopted in this work considers all these concepts and, to reduce the increase of computational cost due to the averaging process, it defines an optimized procedure to evaluate the nonlocal variables for the different FE types.

4.3 Adopted nonlocal damage formulation

The adopted regularization technique is based on the nonlocal integral formulation. Although the approach can be easily applied to any damage model, in the following it is defined referring to the proposed 3D material model in Sec. 2.4. In this material model, the damage variable D is obtained from the combination of two variables D_t and D_c, through two weighting coefficients α_t and α_c (Eq. (2.36)). D_t and D_c are evaluated on the basis of the total material strains $\boldsymbol{\varepsilon}(x,y,z)$, whereas α_t and α_c are evaluated on the basis of the elastic part $\boldsymbol{\varepsilon}^e(x,y,z)$. The main criteria of the proposed nonlocal formulation consists in computing the nonlocal variables $\tilde{\boldsymbol{\varepsilon}}(x,y,z)$ corresponding to the total strains and to use them for the definition of D_t and D_c. By contrast, the elastic strains $\boldsymbol{\varepsilon}^e(x,y,z)$ used to define α_t and α_c remain local, as these coefficients simply measure the tensile and the compressive state of the considered material point.

The definition of the nonlocal variables $\tilde{\boldsymbol{\varepsilon}}(x,y,z)$ depends on the FE type adopted to model the structure. The two following parts of the section describe the new criteria for defining these variables, referring to a beam-column (1D), a 2D and a 3D FE model. These criteria are, however, based on the same approach and, thus, they allow to easily correlate the different techniques.

4.3.1 Nonlocal model for beam-column FEs

In beam-column FEs, the nonlocal strains $\tilde{\boldsymbol{\varepsilon}}$ derive from the nonlocal definition of the generalized section deformations $\mathbf{e}(x)$, computed at each quadrature cross-section as:

$$\tilde{\mathbf{e}}(x) = \frac{\int_S \mathbf{e}(x)\,\omega(x)\,dx}{\int_S \omega(x)\,dx} \qquad \text{with} \qquad \omega(x) = \begin{cases} \exp\left(-\frac{\Delta x^2}{2L_c^2}\right) & \text{if} \quad \Delta x \leq 2L_c \\ 0 & \text{if} \quad \Delta x > 2L_c \end{cases} \tag{4.9}$$

$\Delta x = x - x_G$ measuring the distance between the cross-section located at x_G, where $\tilde{\mathbf{e}}$ is evaluated, and that located at x (in any other element of the structure domain

S), contributing with its deformation $\mathbf{e}(x)$ to the averaged deformation measure in x_G. The parameter L_c influences the extension of the averaging process. In fact, the weighting coefficient $\omega(x)$ is a Gaussian function having the same shape of that in Eq. (4.7) but it is truncated at $\Delta x = \pm 2\, L_c$. This function is schematically represented in Fig. 4.6. As described in Sec. 4.2, the contribute of the cross-section farther than $4L_c$ from x_G is negligible and thus, to reduce the computational cost, the averaging process can be restricted to the relevant neighborhood of the considered point by truncating the weighting function $\omega(x)$.

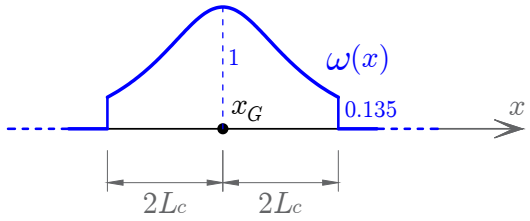

Figure 4.6: Schematic representation of the function $\omega_x(x, y)$ adopted as weighting function for the adopted 1D nonlocal integration.

Eq. (4.9) is used in the WMF model described in Sec. 3.4, considering that the material strains here consist of two parts (Eq. (3.62)): one part $\mathbf{a}_s(y, z)\, \mathbf{e}(x)$ depending on the generalized section deformations and the other part $\boldsymbol{\varepsilon}_w(x, y, z)$ depending on the warping displacements $u_w(x, y, z)$; the latter are interpolated in the entire element volume and the definition of $\mathbf{a}_s(y, z)\, \mathbf{e}(x)$ ensure that the localization in the plane of the section is not possible. Hence, the strain-damage can localize only at the quadrature cross-section along the beam axis. The nonlocal total strains in each fiber of the cross-section can thus be evaluated as:

$$\tilde{\boldsymbol{\varepsilon}}(x, y, z) = \mathbf{a}_s(y, z)\, \tilde{\mathbf{e}}(x) + \boldsymbol{\varepsilon}_w(x, y, z) \tag{4.10}$$

The same observation can be done for the TFF and the ETFF models in Secs. 3.2 and 3.3. In the cases, the nonlocal variables can be computed with the same Eq. (4.10), but neglecting the contribution of $\boldsymbol{\varepsilon}_w(x, y, z)$ and adopting the appropriate compatibility matrix $\mathbf{a}_s$.

4.3.2 Nonlocal model for 2D and 3D FEs

In standard 2D and 3D FEs the nonlocal strains $\tilde{\boldsymbol{\varepsilon}}(x, y, z)$ can be derived from the extension of Eq. (4.9) to two and three dimensions, respectively. For instance, for 2D membrane FEs, if $x-y$ is the plane of the element, at every quadrature point G the local

deformation measures consist in the three in-plane strains $\mathbf{e}(x,y) = \{\varepsilon_x,\ \varepsilon_y,\ \gamma_{xy}\}^T$; for 2D plate FEs, if $x-y$ is the plane of the element, at every quadrature point G the local deformation measures consist in the three plate curvatures and the two plate shear deformations $\mathbf{e}(x,y) = \{\chi_x,\ \chi_y,\ \chi_{xy},\ \gamma_{xz},\ \gamma_{yz}\}^T$. For these FEs, Eq. (4.9) becomes:

$$\tilde{\mathbf{e}}(x,y) = \frac{\int_S \mathbf{e}(x,y)\,\omega(x,y)\,dxdy}{\int_S \omega(x,y)\,dxdy} \tag{4.11}$$

with:

$$\omega(x,y) = \exp\left(-\frac{\Delta x^2 + \Delta y^2}{2L_c^2}\right)$$

$\Delta x = x - x_G$ and $\Delta y = y - y_G$ measuring the axis projections of the distance between the quadrature point located at $\mathbf{x}_G = \{x_G,\ y_G\}^T$, where $\tilde{\mathbf{e}}$ is evaluated, and that located at $\mathbf{x} = \{x,\ y\}^T$.

For 3D FEs, if $x-y-z$ is the space of the element and the deformation measures at every quadrature point G are the strains $\mathbf{e}(x,y,z) = \{\varepsilon_x,\ \varepsilon_y,\ \varepsilon_z,\ \gamma_{xy},\ \gamma_{xz},\ \gamma_{yz}\}^T$, Eq. (4.11) becomes:

$$\tilde{\mathbf{e}}(x,y,z) = \frac{\int_V \mathbf{e}(x,y,z)\,\omega(x,y,z)\,dxdydz}{\int_V \omega(x,y,z)\,dxdydz} \tag{4.12}$$

with:

$$\omega(x,y,z) = \exp\left(-\frac{\Delta x^2 + \Delta y^2 + \Delta z^2}{2L_c^2}\right)$$

4.3.3 Nonlocal model validation

To validate the proposed regularization technique, two series of numerical test are performed on two simplified structural model. The first model refers to a rectangular RC wall subjected to in-plane cyclic horizontal loads [107] (WSH6) and the second model refers to a U-shaped RC wall subjected to bi-axial cyclic horizontal loads [108, 109]. Both structures show relevant shear stress/strain effects and their cyclic and monotonic numerical response is analyzed in Sec. 6.4. The two validating models of this section represent these shear walls, with the same geometries but considered as plain concrete structures.

For the rectangular wall (Fig. 4.7), the proposed plastic-damage model in Sec. 2.4 is used, adopting the material parameters in Table 4.1. Because the goal is to analyze the transition from the hardening branch of the response (pre-peak) to the softening one (post-peak), the material parameters are conveniently chosen to emphasize this transition and they differ from those adopted in Sec. 6.4.

Two different kinds of FEs are used to model the wall. The first one is the WMF

Table 4.1: Mechanical parameters adopted for the plain concrete rectangular shear wall.

$E = 37\,000\,\text{MPa}$	$\nu = 0.2$		
$\sigma_t = 50.0\,\text{MPa}$	$\sigma_c = 60.0\,\text{MPa}$	$H_i = 0.001\,E$	$H_k = 0.850\,E$
$Y_{0t} = 1.95 \cdot 10^{-5}$	$k_t = 1.0 \cdot 10^{-3}$	$a_t = 0.95$	
$Y_{0c} = 4.67 \cdot 10^{-4}$	$k_c = 7.0 \cdot 10^{-3}$	$a_c = 0.2$	$\beta = 1.0$

beam-column FE described in Sec. 3.4 and the second one is the standard 2D 9-nodes quadrilateral FE (from the FEDEASLab library). For the beam-column model a fiber discretization of the cross-section is adopted, as described in Sec. 5.3.2, considering fifteen fibers uniformly distributed along the width of the wall (Fig. 4.7*b*), according to the midpoint rule [29]. Moreover, the warping displacement field is assumed constant across the thickness of the wall and fifth order Lagrange polynomials are defined to interpolate its variation along the width, according to Eq. (3.62) and to the distribution of $m_w = 6$ warping DOFs in Fig. 4.7*c*. The warping displacements are assumed as restrained at the bottom of the wall and free at the top [110]. Hence, one element with six warping interpolation sections, $n_w = 6$, is used over the height to capture non uniform warping distributions and thirteen Gauss-Lobatto quadrature cross-sections are adopted. For the 2D model, six quadrilateral FEs are uniformly distributed along the width of the wall and twelve are uniformly distributed along the height. In both models, the top and the bottom slabs are assumed as rigid elements.

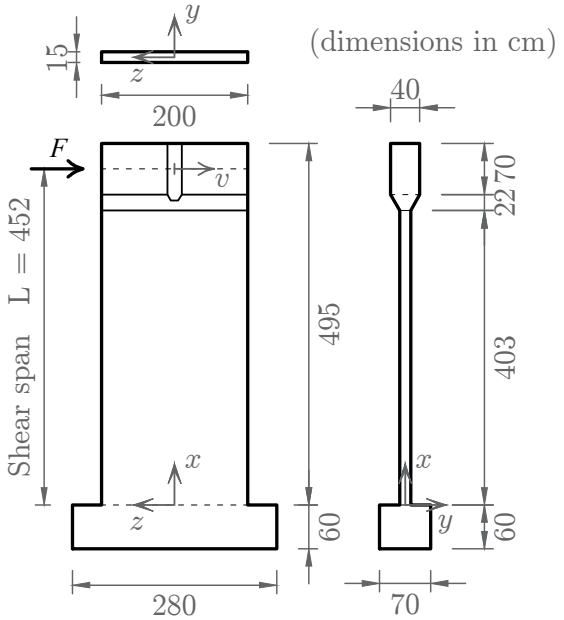

(*a*) Specimen geometry

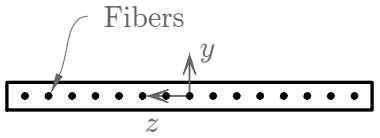

(*b*) Fiber discretization

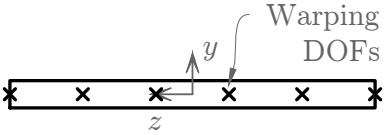

(*c*) Warping DOFs distribution

Figure 4.7: Plain rectangular shear wall: geometry and model discretization.

Fig. 4.8 compares the global responses, in terms of applied load F vs top displacement v, obtained with the two kind of FEs. In particular, for the beam-column FE and the 2D model the proposed nonlocal formulation is applied adopting the approach in Eq. (4.9) and Eq. (4.11), respectively, with $L_c = 15$ or 30 cm, and considering that the reference plane for the 2D model is the $x - z$ plane. Fig. 4.8 plots the compari-

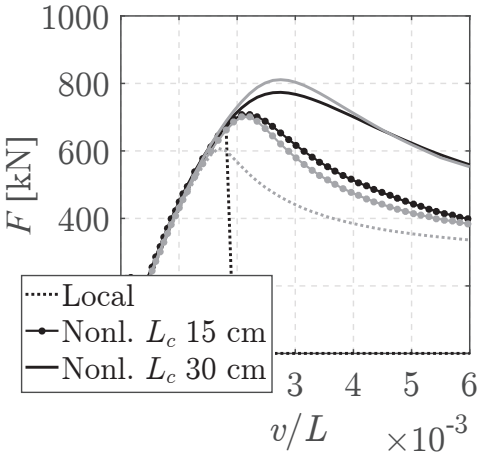

Figure 4.8: Applied horizontal load vs horizontal drift for the plain rectangular wall under monotonic loads - The black and the gray lines lines represent the solutions obtained with the beam-column FE and the 2D FEs, respectively.

son between the models in terms of applied load F vs top displacement v and shows that both the models localize, if no regularization is provide, whereas their responses perfectly matches when the same value of L_c is chosen for them.

Similar comparisons are conducted for the U-shaped wall (Fig. 4.9). The proposed plastic-damage model in Sec. 2.4 is used as well, adopting the material parameters in Table 4.2, which are conveniently chosen to emphasize this transition from the hardening branch of the response (pre-peak) to the softening one (post-peak) (they differ from the ones adopted in Sec. 6.4). Two different kinds of FEs are used to model

Table 4.2: Mechanical parameters adopted for the plain concrete rectangular shear wall.

$E = 28\,000$ MPa	$\nu = 0.25$		
$\sigma_t = 12.0$ MPa	$\sigma_c = 15.0$ MPa	$H_i = 0.001\,E$	$H_k = 0.800\,E$
$Y_{0t} = 3.35 \cdot 10^{-6}$	$k_t = 1.5 \cdot 10^{-3}$	$a_t = 0.80$	
$Y_{0c} = 2.00 \cdot 10^{-5}$	$k_c = 3.0 \cdot 10^{-3}$	$a_c = 0.8$	$\beta = 0.5$

the wall. The first one is the WMF beam-column FE described in Sec. 3.4 and the second one is a 4-nodes shell FE with Mixed Interpolation of Tensorial Component (MITC) [111] (from the FEDEASLab library). For the beam-column model the fiber discretization of the cross-section in Fig. 4.9*b* is adopted, as described in Sec. 5.3.2; in

each rectangular patch of the cross-section the fibers follow the midpoint integration rule [29]. Moreover, the warping displacement field is interpolated, according to Eq. (3.62) and to the distribution of $m_w = 12$ warping DOFs in Fig. 6.45*c*, which considers linear Hermite polynomials across the thickness and cubic Hermite polynomials along the web and the flanges. The warping displacements are assumed as restrained at the top and at the bottom of the wall [110]. Hence, one element with five warping interpolation sections, $n_w = 5$, is used over the height to capture non uniform warping distributions and thirteen Gauss-Lobatto quadrature cross-sections are adopted. For the shell model, seven quadrilateral FEs are uniformly distributed along the web of the wall, five along each flange and eighteen along the height. In both models, the top and the bottom slabs are assumed as rigid elements.

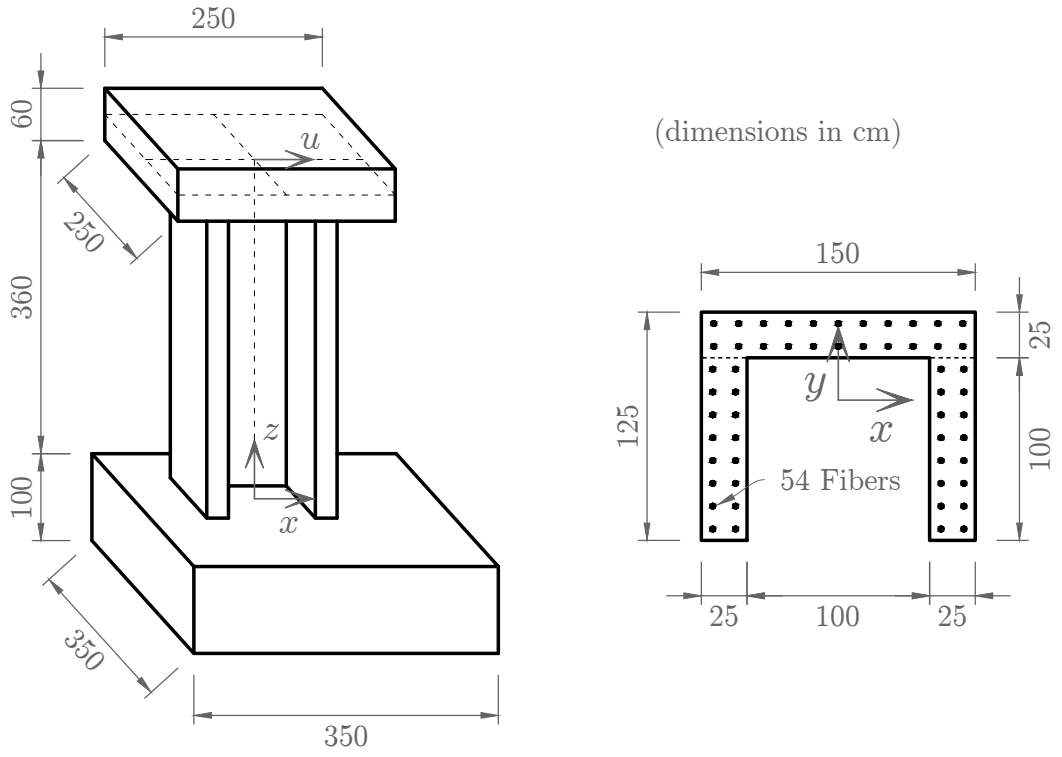

(*a*) Specimen geometry (*b*) Section geometry and fiber model

Figure 4.9: Plain U-shaped shear wall: geometry and model discretization.

Fig. 4.10 compares the global responses, in terms of applied load F_x vs top displacement u, obtained with the two kind of FEs. Eq. (4.9) and Eq. (4.11) are considered for the beam-column FE and the shell model, respectively, with $L_c = 10 \text{ or } 30$ cm. For the shell model, the FE reference plane is the $x - z$ plane for the web of the wall and the $y - z$ plane for the flanges.

As for the rectangular wall, the adopted regularization gives a good match between

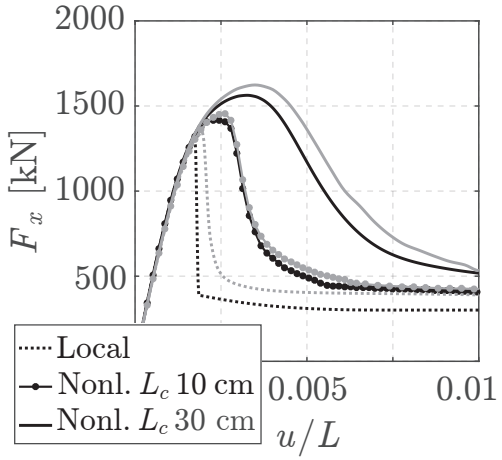

Figure 4.10: Applied horizontal load F_x vs horizontal drift u/L for the plain U-shaped shear wall under monotonic loads - The black and the gray lines lines represent the solutions obtained with the beam-column FE and the shell FEs, respectively.

the shell and beam-column model, although in this case large values of the characteristic length produce slightly higher responses for the shell model with respect to the beam-column one.

Chapter 5

Computational aspects and solution algorithm

5.1 General

The mixed beam-column FE with section warping described in Sec. 3.4 is implemented in the Matlab toolbox FEDEASLab [112], together with the standard and the enhanced Timoshenko models in Sec. 3.2 and Sec. 3.3. To determine the solution of nonlinear structural problems, FEDEASLab adopts a classical step-by-step time discretization, as usual for FE codes. At each time step, it applies a load increment to the structure and iteratively evaluates the nodal displacements and the element deformations through a Newton-Raphson (N-R) algorithm. In particular, during the general N-R iteration, the algorithm considers a set of trial values for the nodal displacements of each element and it evaluates and assembles the corresponding nodal forces and stiffness matrices. Referring to the variables in Sec. 3.1, this means that the vector $\mathbf{u}$ is given for each element at each iteration and the corresponding force vector $\mathbf{p}$ and stiffness matrix $\hat{\mathbf{k}}$ are evaluated. This process is called Element State Determination. Considering Eqs. (3.4) and (3.7), for mixed and force-based FEs it translates to evaluating the resisting basic forces $\mathbf{q}$ and the tangent flexibility matrix $\mathbf{f}$ under given basic deformations $\mathbf{v}$.

This chapter describes the most efficient procedures required for the Element State Determination of the implemented FEs. In particular, Sec. 5.2 explains the linearized solution procedure for the TFF, the ETFF and the WMF element. Sec. 5.3 describes the Section State Determination, that is the evaluation of the cross-section response, which can be seen as a nested process required during the determination of the element state. A fiber model discretization is adopted to evaluate the integrals over the cross-section area, allowing for the multi-axial coupling of the stress components. Finally, Sec. 5.4 describes the Material State Determination, i.e. the evaluation of the material

response needed at each fiber during the determination of the cross-section state. An optimized condensation procedure is proposed to compute the relevant stress components from the six ones involved in a 3D material model and the linearized solution procedure for the plastic-damage model in Sec. 2.4.

5.2 Element State Determination

The first part of this section discusses the solution algorithm adopted for the Element State Determination of the TFF beam described in Sec. 3.2. The original version of this algorithm was proposed in [10] for the EBFF beam and then adopted by many authors for its efficiency and its low computational cost. It is based on a nested iterative procedure used to enforce simultaneously the element equilibrium and the compatibility conditions at every N-R iteration. Later, Neuenhofer and Filippou [95] proposed an enhanced version where the nested iterations are by-passed, determining and storing the element residual deformations in the current N-R iteration and using them in the following one. In this non-iterative scheme the element equilibrium and the compatibility conditions are satisfied only when the N-R procedure is concluded and only a linear approximation of the element response is evaluated at each iteration, globally reducing the computational cost. Saritas and Soydas [12] presented a unified description of both versions, showing how the latter can regarded a special case of the former. This unified scheme, which is here re-described, is also applicable to standard TFF and the ETFF model, simply considering the appropriate governing equations.

The second part of the section presents the solution algorithm for the WMF beam described in Sec. 3.4. A solution algorithm for this FE is also described in [1], but a new more general and more efficient one is proposed in this work, following the idea of non-iterative scheme in [95]. Indeed, it can be seen as an extended version of the algorithm for the standard beam accounting for the contribute of the warping displacement field $u_w(x, y, z)$.

In both part of the section, the solution algorithm refers to the evaluation of a single FE response during one of the N-R iterations performed in a general loading step. The superscripts 'k' and '$k+1$' denote the previous and current N-R iteration, respectively.

5.2.1 Linearized solution procedure for the standard force-based elements

The solution procedure for the standard force-based Timoshenko beam is defined considering the element equilibrium Eq. (3.25), the element compatibility Eq. (3.28) and

the incremental section constitutive Eq. (3.26), together with the incremental form of the element basic constitutive relation, governed by the element flexibility matrix $\mathbf{f}$ in Eq. (3.29) and resulting as:

$$\dot{\mathbf{q}} = \mathbf{f}^{-1}\,\dot{\mathbf{v}} \tag{5.1}$$

$\mathbf{v}$ and $\mathbf{q}$ are the element basic deformation and force vectors in Eq. (3.3) and (3.6), respectively. In the following, the main steps of the algorithm are summarized and they are recapped in Table 5.1:

1) At the global N-R current iteration $k+1$ the nodal displacement vector $\mathbf{u}^{k+1}$ and its increment $\Delta\mathbf{u}^{k+1}$ are given;

2) The basic deformation increment $\Delta\mathbf{v}^{k+1} = \mathbf{a}_g\,\Delta\mathbf{u}^{k+1}$ is computed, by means of Eq. (3.4) and the element basic forces are updated, using the element basic flexibility matrix at the previous iteration:

$$\Delta\mathbf{q}^{k+1} = \left(\mathbf{f}^{\,k}\right)^{-1}\,\mathbf{a}_g\,\Delta\mathbf{u}^{k+1} \qquad \rightarrow \qquad \mathbf{q}^{k+1} = \mathbf{q}^{k} + \Delta\mathbf{q}^{k+1}$$

3) To enforce both the element equilibrium and compatibility conditions, a nested iterative procedure is performed; the superscript 'l' and '$l+1$' denote the previous and current internal iteration, respectively; at the beginning of this nested procedure $l = 0$, the initialized state is set equal to the state at k and $q^1 = q^{k+1}$:

   a) At each cross-section, the increment of the generalized deformations is evaluated, inverting the linearized form of Eq. (3.26) and using the section stiffness matrix at the previous iteration:

$$\Delta\mathbf{e}^{l+1} = \left(\mathbf{k}_s^{l}\right)^{-1}\,\mathbf{b}\,\Delta\mathbf{q}^{l+1}$$

   b) The total deformation values are computed and the Section State Determination is performed, as described in Sec. 5.3 to obtain the generalized section forces and the section stiffness matrix:

$$\mathbf{e}^{l+1} = \mathbf{e}^{l} + \Delta\mathbf{e}^{l+1} \qquad \rightarrow \qquad \mathbf{s}^{l+1} \quad \text{and} \quad \mathbf{k}_s^{l+1}$$

   c) The residual section forces, i.e. the difference between the balanced ones (Eq. (3.25)) and the constitutive ones are computed and they are used to evaluate of the residual section deformations:

$$\bar{\mathbf{s}}^{l+1} = \mathbf{b}\,\mathbf{q}^{l+1} + \mathbf{s}_p^{l+1} - \mathbf{s}^{l+1} \qquad \rightarrow \qquad \bar{\mathbf{e}}^{l+1} = \left[\mathbf{k}_s^{l+1}\right]^{-1}\,\bar{\mathbf{s}}^{l+1}$$

d) By means of Eqs. (3.28) and (3.29), the residual of the compatible basic deformations and the basic element flexibility matrix are computed:

$$\bar{\mathbf{v}}^{l+1} = \mathbf{a}_g\,\mathbf{u}^{k+1} - \int_0^L \mathbf{b}^T \left(\mathbf{e}^{l+1} + \bar{\mathbf{e}}^{l+1}\right) dx$$
$$\mathbf{f}^{l+1} = \int_0^L \mathbf{b}^T \left(\mathbf{k}_s^{l+1}\right)^{-1} \mathbf{b}\, dx$$

e) The basic element forces are updated:

$$\Delta\mathbf{q}^{l+1} = \left(\mathbf{f}^{l+1}\right)^{-1} \bar{\mathbf{v}}^{l+1} \qquad \rightarrow \qquad \mathbf{q}^{l+1} = \mathbf{q}^{l+1} + \Delta\mathbf{q}^{l+1}$$

f) The following residual internal energy is evaluated:

$$\bar{W}^{l+1} = \int_0^L \left(\bar{\mathbf{s}}^{l+1}\right)^T \bar{\mathbf{e}}^{l+1}\, dx$$

If this results less then a specified tolerance or $l \geq I_{max}$, (I_{max} being the maximum number of internal iterations), the nested iterative procedure is stopped, otherwise the procedure returns to the step 3*a*;

4) The current state at $k+1$ is set equal to the converged state at $l+1$, with $\tilde{\mathbf{e}}^{k+1} = \mathbf{e}^{l+1}$ and $\tilde{\mathbf{s}}^{k+1} = \mathbf{s}^{l+1}$; then, the generalized section deformations and the generalized section forces are updated, the latter ones according to the equilibrium:

$$\mathbf{e}^{k+1} = \tilde{\mathbf{e}}^{k+1} + \left(\mathbf{k}_s^{k+1}\right)^{-1} \left[\underbrace{\mathbf{b}\,\mathbf{q}^{k+1} + \mathbf{s}_p^{k+1}}_{\mathbf{s}^{k+1}} - \tilde{\mathbf{s}}^{k+1}\right]$$

5) Finally, the element stiffness matrix and force vector are evaluated, by means of Eqs. (3.7):

$$\hat{\mathbf{k}}^{k+1} = \mathbf{a}_g^T \left(\mathbf{f}^{k+1}\right)^{-1} \mathbf{a}_g \qquad \text{and} \qquad \mathbf{p}^{k+1} = \mathbf{a}_g^T\,\mathbf{q}^{k+1} - \mathbf{p}_{rq}^{k+1}$$

As shown, at each N-R iteration, the element basic deformation $\mathbf{v}^{k+1} = \mathbf{a}_g\,\mathbf{u}^{k+1}$ are given and the algorithm aims to determine $\mathbf{f}^{k+1}$ and $\mathbf{q}^{k+1}$. To do so, first a linearized approximation of the $\mathbf{q}$ is evaluated at the step 2 and then the nested process at step 3 is applied. This process operates separately on each element cross-section to find the generalized deformations $\mathbf{e}$ corresponding to the equilibrated forces $\mathbf{s}$. Hence, the section constitutive law is linearized and an approximation of the section constitutive response is evaluated at the step 3*a* and 3*b*. At the step 3*c*, the section forces derived

Table 5.1: Element State Determination for the standard Timoshenko beam.

1)	$\mathbf{u}^{k+1}$ and $\Delta\mathbf{u}^{k+1}$ are given		
2)	$\Delta\mathbf{q}^{k+1} = \left(\mathbf{f}^{k}\right)^{-1} \mathbf{a}_g \, \Delta\mathbf{u}^{k+1}$	$\rightarrow$	$\mathbf{q}^{k+1} = \mathbf{q}^{k} + \Delta\mathbf{q}^{k+1}$
	Initialization: State at $l = 0$ set equal to state at k; $q^1 = q^{k+1}$		
3a)	$\Delta\mathbf{e}^{l+1} = \left(\mathbf{k}_s^{l}\right)^{-1} \mathbf{b} \, \Delta\mathbf{q}^{l+1}$		
3b)	Section State Determination (Table 5.3)		
	$\mathbf{e}^{l+1} = \mathbf{e}^{l} + \Delta\mathbf{e}^{l+1}$	$\rightarrow$	$\mathbf{s}^{l+1}$ and $\mathbf{k}_s^{l+1}$
3c)	$\bar{\mathbf{s}}^{l+1} = \mathbf{b}\,\mathbf{q}^{l+1} + \mathbf{s}_p^{l+1} - \mathbf{s}^{l+1}$	$\rightarrow$	$\bar{\mathbf{e}}^{l+1} = \left[\mathbf{k}_s^{l+1}\right]^{-1} \bar{\mathbf{s}}^{l+1}$
3d)	$\bar{\mathbf{v}}^{l+1} = \mathbf{a}_g \, \mathbf{u}^{k+1} - \int_0^L \mathbf{b}^T \left(\mathbf{e}^{l+1} + \bar{\mathbf{e}}^{l+1}\right) dx$		
	$\mathbf{f}^{l+1} = \int_0^L \mathbf{b}^T \left(\mathbf{k}_s^{l+1}\right)^{-1} \mathbf{b} \, dx$		
3e)	$\Delta\mathbf{q}^{l+1} = \left(\mathbf{f}^{l+1}\right)^{-1} \bar{\mathbf{v}}^{l+1}$	$\rightarrow$	$\mathbf{q}^{l+1} = \mathbf{q}^{l+1} + \Delta\mathbf{q}^{l+1}$
3f)	If $\bar{W}^{l+1} = \int_0^L \left(\bar{\mathbf{s}}^{l+1}\right)^T \bar{\mathbf{e}}^{l+1} \, dx < tol.$ or $l \geq I_{max}$	$\rightarrow$	Exit
	otherwise	$\rightarrow$	Go to step 3a
	State at $k+1$ set equal to state at $l+1$; $\tilde{\mathbf{e}}^{k+1} = \mathbf{e}^{l+1}$ and $\tilde{\mathbf{s}}^{k+1} = \mathbf{s}^{l+1}$		
4)	$\mathbf{e}^{k+1} = \tilde{\mathbf{e}}^{k+1} + \left(\mathbf{k}_s^{k+1}\right)^{-1} \left[\underbrace{\mathbf{b}\,\mathbf{q}^{k+1} + \mathbf{s}_p^{k+1}}_{\mathbf{s}^{k+1}} - \tilde{\mathbf{s}}^{k+1} \right]$		
5)	$\hat{\mathbf{k}}^{k+1} = \mathbf{a}_g^T \left(\mathbf{f}^{k+1}\right)^{-1} \mathbf{a}_g$ and		$\mathbf{p}^{k+1} = \mathbf{a}_g^T \, \mathbf{q}^{k+1} - \mathbf{p}_{rq}^{k+1}$

from the constitutive relationship are compared with the equilibrated ones and the residuals $\bar{\mathbf{s}}$ is used to compute the related residual deformations. If the integral along the element axis of the section deformations $\mathbf{e}$ plus their residual $\bar{\mathbf{e}}$ doesn't match the given basic deformations $\mathbf{v}$ (step 3d), the residual difference is used to correct the estimated $\mathbf{q}$ (step 3e) and another iteration is performed, otherwise the nested process ends. The convergence condition at the step 3f is an alternative way of imposing the element compatibility condition $\bar{\mathbf{v}} = \mathbf{0}$ (to within a specified tolerance).

The non-iterative version of the presented algorithm is obtained simply setting $I_{max} = 1$. In this way, the residual basic deformations $\bar{\mathbf{v}}$ are included in the basic forces $\mathbf{q}$, which are used to evaluate the global nodal forces $\mathbf{p}$ (step 5) for the global iterative process. When the global N-R process ends, that is the global equilibrium is

satisfied, the element compatibility condition $\bar{\mathbf{v}} = \mathbf{0}$ is satisfied as well.

Note that the algorithm also applies to the EBFF and the ETFF model described in Secs. 3.2 and 3.3, respectively. However, in these cases the generalized section deformations $\mathbf{e}$, the generalized section forces $\mathbf{s}$, the section stiffness matrix $\mathbf{k}_s$, the equilibrium matrix $\mathbf{b}$ and the Section State Determination process need to be evaluated with the specific expression indicate in the same sections.

5.2.2 Linearized solution procedure for the element with section warping

The original element state determination algorithm for the mixed element with section warping is proposed in [1], where a nested iterative process is used to enforce the element equilibrium, the element compatibility condition and the warping equilibrium. It is based on the linearized form of the governing equations described in Sec. 3.4, which properly account for the warping displacement field $u_w(x, y, z)$.

Basing on this algorithm, a new one is proposed in the following. It allows to choose between the iterative or the non-iterative form, resulting as an extended version of the scheme presented in [12] for the standard elements. In particular, with respect to the standard FE case, which is described before, the additional linearized governing Eq. (3.101) need to be taken into account. As mentioned in Sec. 3.4, for the general case considered in this work, the additional warping DOFs are fully restrained $u_{w,ij} = 0$ ($p_{w,ij} \neq 0$) at some element cross-sections and they are totally free $p_{w,ij} = 0$ ($u_{w,ij} \neq 0$) at the remaining ones. Hence, Eq. (3.101) can be split in the part associated to the free (subscript 'f') and the restrained DOFs (subscript 'r'):

$$\left\{ \begin{array}{c} \Delta\mathbf{p}_{w,f} \\ \Delta\mathbf{p}_{w,r} \end{array} \right\} = \left[\begin{array}{c} \mathbf{b}_{ws,f} \\ \mathbf{b}_{ws,r} \end{array} \right] \Delta\mathbf{q} + \left[\begin{array}{cc} \mathbf{k}_{ww,ff} & \mathbf{k}_{ww,fr} \\ \mathbf{k}_{ww,rf} & \mathbf{k}_{ww,rr} \end{array} \right] \left\{ \begin{array}{c} \Delta\mathbf{u}_{w,f} \\ \mathbf{0} \end{array} \right\} \tag{5.2}$$

The first part gives the increment of the free warping DOFs:

$$\Delta\mathbf{u}_{w,f} = \mathbf{k}_{ww,ff}^{-1} \left(\Delta\mathbf{p}_{w,f} - \mathbf{b}_{ws,f}\, \Delta\mathbf{q}\right) \tag{5.3}$$

which can be used in the second part to compute the increment of the warping forces associated to the restrained DOFs (see step 4):

$$\Delta\mathbf{p}_{w,r} = \mathbf{b}_{ws,r}\, \Delta\mathbf{q} + \mathbf{k}_{ww,rf} \underbrace{\mathbf{k}_{ww,ff}^{-1} \left(\Delta\mathbf{p}_{w,f} - \mathbf{b}_{ws,f}\, \Delta\mathbf{q}\right)}_{\Delta\mathbf{u}_{w,f}} \tag{5.4}$$

Note that in the linearized form of Eq. (5.2) the increment of the restrained warping

DOFs $\Delta\mathbf{u}_{w,r}$ is always assumed to be zero, whereas the forces $\Delta\mathbf{p}_{w,f}$ work-conjugate with the free DOFs are in general non zero. Their total values $\mathbf{p}_{w,f}$ are zero, because of the warping equilibrium Eq. (3.77). However, this condition is achieved only at the end of the algorithm, when the convergence conditions are satisfied. Taking advantage of these definitions, the algorithm is defined as follows:

1) At the global N-R current iteration $k+1$ the nodal displacement vector $\mathbf{u}^{k+1}$ and its increment $\Delta\mathbf{u}^{k+1}$ are given;

2) The basic deformation increment $\Delta\mathbf{v}^{k+1} = \mathbf{a}_g\,\Delta\mathbf{u}^{k+1}$ is computed, by means of Eq. (3.4) and the element basic forces are updated, using the element basic flexibility matrix at the previous iteration:

$$\Delta\mathbf{q}^{k+1} = \left(\mathbf{f}^{\,k}\right)^{-1}\,\mathbf{a}_g\,\Delta\mathbf{u}^{k+1} \qquad \rightarrow \qquad \mathbf{q}^{k+1} = \mathbf{q}^{k} + \Delta\mathbf{q}^{k+1}$$

3) To enforce the element equilibrium, the compatibility condition and the warping equilibrium, a nested iterative procedure is performed; the superscript 'l' and '$l+1$' denote the previous and current internal iteration, respectively; at the beginning of this nested procedure $l = 0$, the initialized state is set equal to the state at k and $q^1 = q^{k+1}$:

   a) The free warping DOFs $\mathbf{u}_{w,f}$ are updated computing their increments by means of Eq. (5.3):

$$\Delta\mathbf{u}^{l+1}_{w,f} = \left(\mathbf{k}^{l}_{ww,ff}\right)^{-1}\left[\bar{\mathbf{p}}^{l}_{w,f} - \mathbf{b}^{l}_{ws,f}\,\Delta\mathbf{q}^{l+1}\right] \qquad \rightarrow \qquad \mathbf{u}^{l+1}_{w,f} = \mathbf{u}^{l}_{w,f} + \Delta\mathbf{u}^{l+1}_{w,f}$$

   where $\bar{\mathbf{p}}^{l}_{w,f}$ are the residual values of the warping forces associated to the free DOFs from the previous internal iteration (step $3h$); they are initialized as zero at the beginning of the nested procedure;

   b) At each cross-section, the increment of the generalized deformations is evaluated, by means of Eq. (3.100) and using the section stiffness matrices at the previous iteration:

$$\Delta\mathbf{e}^{l+1} = \left(\mathbf{k}^{l}_{s}\right)^{-1}\left[\mathbf{b}\,\Delta\mathbf{q}^{l+1} - \sum_{i=1}^{n_w}\tilde{\mathbf{k}}^{l}_{sw,i}\,\Delta\mathbf{u}^{l}_{w,i}\right]$$

   c) The deformation total values are computed and the Section State Determination is performed, as described in Sec. 5.3 to obtain the standard and the

warping generalized section forces and section stiffness matrices:

$$\begin{matrix}\mathbf{e}^{l+1} = \mathbf{e}^{l} + \Delta\mathbf{e}^{l+1} \\ \mathbf{u}_{w}^{l+1}\end{matrix} \quad \rightarrow \quad \begin{matrix}\mathbf{s}^{l+1},\ \mathbf{s}_{w}^{x,l+1} \text{ and } \mathbf{s}_{w}^{yz,l+1} \\ \mathbf{k}_{s}^{l+1},\ \mathbf{k}_{sw}^{x,l+1},\ \mathbf{k}_{sw}^{yz,l+1},\ \text{etc.}\end{matrix}$$

d) The warping stiffness matrices $\mathbf{b}_{sw}^{l+1}$, $\mathbf{b}_{ws}^{l+1}$ and $\mathbf{k}_{ww}^{l+1}$ are computed as well, using Eqs. (3.103);

e) The warping forces $\mathbf{p}_{w}^{l+1}$ for the current internal iteration are obtained integrating the warping forces over the element length (Eq. (3.77)):

$$\mathbf{p}_{w,i}^{l+1} = \int_{0}^{L} \left[\frac{\partial \mathrm{N}_i}{\partial x} \mathbf{s}_{w}^{x,l+1} + \mathrm{N}_i\, \mathbf{s}_{w}^{yz,l+1} \right] dx \quad \rightarrow \quad \mathbf{p}_{w}^{l+1} = \left\{ \mathbf{p}_{w,1}^{l+1^T},\ \ldots,\ \mathbf{p}_{w,n_w}^{l+1^T} \right\}^T$$

f) The residual section forces, i.e. the difference between the balanced ones (Eq. (3.25)) and the constitutive ones are computed:

$$\bar{\mathbf{s}}^{l+1} = \mathbf{b}\, \mathbf{q}^{l+1} + \mathbf{s}_{p}^{l+1} - \mathbf{s}^{l+1}$$

g) The $\bar{\mathbf{s}}^{l+1}$ are used to evaluate the corresponding warping forces:

$$\bar{\mathbf{p}}_{ws,i}^{l+1} = \int_{0}^{L} \tilde{\mathbf{k}}_{ws,i}^{l+1} \left(\mathbf{k}_{s}^{l+1} \right)^{-1} \bar{\mathbf{s}}^{l+1}\, dx \quad \rightarrow \quad \bar{\mathbf{p}}_{ws}^{l+1} = \left\{ \bar{\mathbf{p}}_{ws,1}^{l+1^T},\ \ldots,\ \bar{\mathbf{p}}_{ws,n_w}^{l+1^T} \right\}^T$$

h) The vector $\bar{\mathbf{p}}_{ws}^{l+1}$ is decomposed into the part associated to the free DOFs and the part associated to the restrained ones, as done in Eq. (5.2):

$$\bar{\mathbf{p}}_{ws}^{l+1} = \left\{ \bar{\mathbf{p}}_{ws,f}^{l+1^T},\quad \bar{\mathbf{p}}_{ws,r}^{l+1^T} \right\}^T$$

The former is used to compute the residual of the warping forces associated to the free DOFs, that is the difference between the target values $\mathbf{p}_{w,f} = \mathbf{0}$ and the current ones:

$$\bar{\mathbf{p}}_{w,f}^{l+1} = \mathbf{0} - \mathbf{p}_{w,f}^{l+1} - \bar{\mathbf{p}}_{ws,f}^{l+1} = -\left(\mathbf{p}_{w,f}^{l+1} + \bar{\mathbf{p}}_{ws,f}^{l+1} \right)$$

i) The residual warping displacements are computed and they are used to evaluate the residual section deformations:

$$\bar{\mathbf{u}}_{w,f}^{l+1} = \left(\mathbf{k}_{ww,ff}^{l+1} \right)^{-1} \bar{\mathbf{p}}_{w,f}^{l+1} \qquad \rightarrow \qquad \bar{\mathbf{e}}^{l+1} = \left(\mathbf{k}_{s}^{l+1} \right)^{-1} \left[\bar{\mathbf{s}}^{l+1} - \sum_{i=1}^{n_w} \tilde{\mathbf{k}}_{sw,i}^{l+1}\, \bar{\mathbf{u}}_{w}^{l+1} \right]$$

j) By means of Eqs. (3.76) and (3.102), the residual of the compatible basic

deformations and the basic element flexibility matrix are computed:

$$\bar{\mathbf{v}}^{l+1} = \mathbf{a}_g\,\mathbf{u}^{k+1} - \int_0^L \mathbf{b}^T\,\left(\mathbf{e}^{l+1} + \bar{\mathbf{e}}^{l+1}\right)\,dx$$
$$\mathbf{f}^{l+1} = \int_0^L \mathbf{b}^T\,\left(\mathbf{k}_s^{l+1}\right)^{-1}\,\mathbf{b}\,dx \;+\; \mathbf{b}_{sw,f}\,\mathbf{k}_{ww,ff}^{-1}\,\mathbf{b}_{ws,f}$$

k) The basic forces are updated:

$$\Delta\mathbf{q}^{l+1} = \left(\mathbf{f}^{l+1}\right)^{-1}\,\bar{\mathbf{v}}^{l+1} \qquad \rightarrow \qquad \mathbf{q}^{l+1} = \mathbf{q}^{l+1} + \Delta\mathbf{q}^{l+1}$$

l) The following residual internal energy is evaluated:

$$\bar{W}^{l+1} = \int_0^L \left(\bar{\mathbf{s}}^{l+1}\right)^T\,\bar{\mathbf{e}}^{l+1}\,dx \;+\; \bar{\mathbf{p}}_{w,f}^{l+1^T}\,\bar{\mathbf{u}}_{w,f}^{l+1}$$

If this results less then a specified tolerance or $l \geq I_{max}$, (I_{max} being the maximum number of internal iterations), the nested iterative procedure is stopped, otherwise the procedure returns to the step 3*a*;

4) The current state at $k+1$ is set equal to the converged state at $l+1$, with $\tilde{\mathbf{e}}^{k+1} = \mathbf{e}^{l+1}$, $\tilde{\mathbf{s}}^{k+1} = \mathbf{s}^{l+1}$, $\tilde{\mathbf{u}}_{w,f}^{k+1} = \mathbf{u}_{w,f}^{l+1}$ and $\tilde{\mathbf{p}}_{w,r}^{k+1} = \mathbf{p}_{w,r}^{l+1}$; then, the warping displacements are updated again, as well as the warping forces associated to the restrained DOFs (and evaluated at the step 3*e*):

$$\Delta\mathbf{u}_{w,f}^{k+1} = \left(\mathbf{k}_{ww,ff}^{k+1}\right)^{-1}\left[\bar{\mathbf{p}}_{w,f}^{k+1} - \mathbf{b}_{ws,f}^{k+1}\,\Delta\mathbf{q}^{k+1+1}\right] \qquad \rightarrow \qquad \mathbf{u}_{w,f}^{l+1} = \tilde{\mathbf{u}}_{w,f}^{k+1} + \Delta\mathbf{u}_{w,f}^{k+1}$$
$$\Delta\mathbf{p}_{w,r}^{k+1} = \mathbf{b}_{ws,r}^{k+1}\,\Delta\mathbf{q}^{k+1} + \mathbf{k}_{ww,rf}^{k+1}\,\Delta\mathbf{u}_{w,f}^{k+1} \qquad \rightarrow \qquad \mathbf{p}_{w,r}^{k+1} = \tilde{\mathbf{p}}_{w,r}^{k+1} + \Delta\mathbf{p}_{w,r}^{k+1}$$

5) The generalized section deformations and the generalized section stresses are updated, the latter ones according to the equilibrium:

$$\mathbf{e}^{k+1} = \tilde{\mathbf{e}}^{k+1} + \left(\mathbf{k}_s^{k+1}\right)^{-1}\left[\underbrace{\mathbf{b}\,\mathbf{q}^{k+1} + \mathbf{s}_p^{k+1}}_{\mathbf{s}^{k+1}} - \tilde{\mathbf{s}}^{k+1} - \sum_{i=1}^{n_w}\tilde{\mathbf{k}}_{sw,i}^{k+1}\,\Delta\mathbf{u}_{w,i}^{k+1}\right]$$

6) Finally, the matrix $\hat{\mathbf{k}}$ and vector $\mathbf{p}$ are evaluated, by means of Eqs. (3.7):

$$\hat{\mathbf{k}}^{k+1} = \mathbf{a}_g^T\,\left(\mathbf{f}^{k+1}\right)^{-1}\,\mathbf{a}_g \qquad \text{and} \qquad \mathbf{p}^{k+1} = \mathbf{a}_g^T\,\mathbf{q}^{k+1} - \mathbf{p}_{rq}^{k+1}$$

The non-iterative version is obtained simply setting $I_{max} = 1$. The main steps of the algorithm are summarized in Table 5.2, where the blue parts represent the additional

contributes, with respect to the standard element case, due to the warping variables. As shown, since the state determination is also governed by the warping Eq. (5.2), every time the element response is linearized the warping variables need to be considered and updated.

In particular, when the basic forces $\mathbf{q}$ are updated at the step 2, first the linearized approximation of the free warping displacements $\mathbf{u}_{w,f}$ needs to be computed (steps $3a$) and then it can be used to evaluate the linearized approximation of the section deformations $\mathbf{e}$ (step $3b$). Similarly, at the steps 4 and 5. For the same reason, the residual section deformations $\bar{\mathbf{e}}$ at the step $3i$ also depend on the residuals in terms of warping displacements, which needs to be evaluated from the residual forces $\bar{\mathbf{p}}_{w,f}$.

Table 5.2: Element State Determination for the mixed element with section warping.

1)	$\mathbf{u}^{k+1}$ and $\Delta\mathbf{u}^{k+1}$ are given
2)	$\Delta\mathbf{q}^{k+1} = \left(\mathbf{f}^{k}\right)^{-1} \mathbf{a}_g\, \Delta\mathbf{u}^{k+1} \quad \rightarrow \quad \mathbf{q}^{k+1} = \mathbf{q}^{k} + \Delta\mathbf{q}^{k+1}$
	Initialization: State at $l = 0$ set equal to state at k; $\quad q^1 = q^{k+1},\ \bar{\mathbf{p}}^0_{w,f} = \mathbf{0}$
3a)	$\Delta\mathbf{u}^{l+1}_{w,f} = \left(\mathbf{k}^{l}_{ww,ff}\right)^{-1} \left[\bar{\mathbf{p}}^{l}_{w,f} - \mathbf{b}^{l}_{ws,f}\, \Delta\mathbf{q}^{l+1}\right] \quad \rightarrow \quad \mathbf{u}^{l+1}_{w,f} = \mathbf{u}^{l}_{w,f} + \Delta\mathbf{u}^{l+1}_{w,f}$
3b)	$\Delta\mathbf{e}^{l+1} = \left(\mathbf{k}^{l}_{s}\right)^{-1} \left[\mathbf{b}\,\Delta\mathbf{q}^{l+1} - \sum_{i=1}^{n_w} \tilde{\mathbf{k}}^{l}_{sw,i}\, \Delta\mathbf{u}^{l}_{w,i}\right]$
3c)	Section State Determination (Table 5.4)
	$\mathbf{e}^{l+1} = \mathbf{e}^{l} + \Delta\mathbf{e}^{l+1},\ \mathbf{u}^{l+1}_{w} \quad \rightarrow \quad \mathbf{s}^{l+1},\ \mathbf{k}^{l+1}_{s},\ \mathbf{s}^{x,l+1}_{w},\ \mathbf{s}^{yz,l+1}_{w},\ \mathbf{k}^{x,l+1}_{sw},$ etc.
3d)	Evaluate $\mathbf{b}^{l+1}_{sw}$, $\mathbf{b}^{l+1}_{ws}$ and $\mathbf{k}^{l+1}_{ww}$
3e)	$\mathbf{p}^{l+1}_{w,i} = \int_0^L \left[\frac{\partial \mathrm{N}_i}{\partial x}\mathbf{s}^{x,l+1}_{w} + \mathrm{N}_i\, \mathbf{s}^{yz,l+1}_{w}\right] dx \quad \rightarrow \quad \mathbf{p}^{l+1}_{w} = \left\{\mathbf{p}^{l+1^T}_{w,1},\ \ldots,\ \mathbf{p}^{l+1^T}_{w,n_w}\right\}^T$
3f)	$\bar{\mathbf{s}}^{l+1} = \mathbf{b}\,\mathbf{q}^{l+1} + \mathbf{s}^{l+1}_{p} - \mathbf{s}^{l+1}$
3g)	$\bar{\mathbf{p}}^{l+1}_{ws,i} = \int_0^L \tilde{\mathbf{k}}^{l+1}_{ws,i} \left(\mathbf{k}^{l+1}_{s}\right)^{-1} \bar{\mathbf{s}}^{l+1}\, dx \quad \rightarrow \quad \bar{\mathbf{p}}^{l+1}_{ws} = \left\{\bar{\mathbf{p}}^{l+1^T}_{ws,1},\ \ldots,\ \bar{\mathbf{p}}^{l+1^T}_{ws,n_w}\right\}^T$
3h)	$\bar{\mathbf{p}}^{l+1}_{w,f} = -\left(\mathbf{p}^{l+1}_{w,f} + \bar{\mathbf{p}}^{l+1}_{ws,f}\right)$
3i)	$\bar{\mathbf{u}}^{l+1}_{w,f} = \left(\mathbf{k}^{l+1}_{ww,ff}\right)^{-1} \bar{\mathbf{p}}^{l+1}_{w,f} \quad \rightarrow \quad \bar{\mathbf{e}}^{l+1} = \left(\mathbf{k}^{l+1}_{s}\right)^{-1} \left[\bar{\mathbf{s}}^{l+1} - \sum_{i=1}^{n_w} \tilde{\mathbf{k}}^{l+1}_{sw,i}\, \bar{\mathbf{u}}^{l+1}_{w}\right]$
3j)	$\bar{\mathbf{v}}^{l+1} = \mathbf{a}_g\, \mathbf{u}^{k+1} - \int_0^L \mathbf{b}^T \left(\mathbf{e}^{l+1} + \bar{\mathbf{e}}^{l+1}\right) dx$
	$\mathbf{f}^{l+1} = \int_0^L \mathbf{b}^T \left(\mathbf{k}^{l+1}_{s}\right)^{-1} \mathbf{b}\, dx + \mathbf{b}_{sw,f}\, \mathbf{k}^{-1}_{ww,ff}\, \mathbf{b}_{ws,f}$
3k)	$\Delta\mathbf{q}^{l+1} = \left(\mathbf{f}^{l+1}\right)^{-1} \bar{\mathbf{v}}^{l+1} \quad \rightarrow \quad \mathbf{q}^{l+1} = \mathbf{q}^{l+1} + \Delta\mathbf{q}^{l+1}$
3f)	If $\bar{W}^{l+1} = \int_0^L \left(\bar{\mathbf{s}}^{l+1}\right)^T \bar{\mathbf{e}}^{l+1}\, dx + \bar{\mathbf{p}}^{l+1^T}_{w,f}\, \bar{\mathbf{u}}^{l+1}_{w,f} < tol.$ or $l \geq I_{max} \quad \rightarrow$ Exit
	otherwise $\quad \rightarrow$ Go to step 3a
	State at $k+1$ set equal to state at $l+1$; $\quad \tilde{\mathbf{e}}^{k+1} = \mathbf{e}^{l+1}, \tilde{\mathbf{s}}^{k+1} = \mathbf{s}^{l+1}, \tilde{\mathbf{u}}^{k+1}_{w,f} = \mathbf{u}^{l+1}_{w,f}$ and $\tilde{\mathbf{p}}^{k+1}_{w,r} = \mathbf{p}^{l+1}_{w,r}$
4)	$\Delta\mathbf{u}^{k+1}_{w,f} = \left(\mathbf{k}^{k+1}_{ww,ff}\right)^{-1} \left[\bar{\mathbf{p}}^{k+1}_{w,f} - \mathbf{b}^{k+1}_{ws,f}\, \Delta\mathbf{q}^{k+1}\right]$ $\Delta\mathbf{p}^{k+1}_{w,r} = \mathbf{b}^{k+1}_{ws,r}\, \Delta\mathbf{q}^{k+1} + \mathbf{k}^{k+1}_{ww,rf}\, \Delta\mathbf{u}^{k+1}_{w,f}$ $\quad \rightarrow \quad$ $\mathbf{u}^{k+1}_{w,f} = \tilde{\mathbf{u}}^{k+1}_{w,f} + \Delta\mathbf{u}^{k+1}_{w,f}$ $\mathbf{p}^{k+1}_{w,r} = \tilde{\mathbf{p}}^{k+1}_{w,r} + \Delta\mathbf{p}^{k+1}_{w,r}$
5)	$\mathbf{e}^{k+1} = \tilde{\mathbf{e}}^{k+1} + \left(\mathbf{k}^{k+1}_{s}\right)^{-1} \left[\underbrace{\mathbf{b}\,\mathbf{q}^{k+1} + \mathbf{s}^{k+1}_{p}}_{\mathbf{s}^{k+1}} - \tilde{\mathbf{s}}^{k+1} - \sum_{i=1}^{n_w} \tilde{\mathbf{k}}^{k+1}_{sw,i}\, \Delta\mathbf{u}^{k+1}_{w,i}\right]$
6)	$\hat{\mathbf{k}}^{k+1} = \mathbf{a}^T_g \left(\mathbf{f}^{k+1}\right)^{-1} \mathbf{a}_g \quad$ and $\quad \mathbf{p}^{k+1} = \mathbf{a}^T_g\, \mathbf{q}^{k+1} - \mathbf{p}^{k+1}_{rq}$

5.3 Section State Determination

The Section State Determination is the evaluation of the cross-section response in terms of section forces and stiffness matrices. It is used during the Element State Determination to obtained the generalized variables that are then integrated over the element length. In the first part of this section, the main aspects of this process are discussed distinguishing the case of the standard force-based beam/column element and the case of the WMF beam. Since the generalized section variables are obtained by integrating the material variables over the cross-section area, as detailed later, the fiber model discretizing approach is presented in the second part of the section and some comments on the possible 2D integration rule are given.

5.3.1 Evaluation of the section state for the standard and mixed elements

For a standard force-based element the Section State Determination consists in computing the resisting generalized section forces $\mathbf{s}(x)$ and the tangent section stiffness matrix $\mathbf{k}_s(x)$ under the given generalized section deformations $\mathbf{e}(x)$. One approach is to a-priori define the section response in terms of the generalized variables, that is to assume specific evolution laws for the $\mathbf{s}(x)$ and the $\mathbf{k}_s(x)$ as functions of $\mathbf{e}(x)$:

$$\mathbf{s}(x) = \hat{\mathbf{s}}\left[\mathbf{e}(x)\right] \qquad \text{and} \qquad \mathbf{k}_s(x) = \hat{\mathbf{k}}_s\left[\mathbf{e}(x)\right]$$

This allows to skip the evaluation of the material response and is common for linear elastic and elasto-plastic material responses, since in these cases the definition of the above functions is relatively easy. For other materials, such as degrading materials, this approach may result complex and not accurate and the representation of the coupling between the different stress components may results very hard.

Hence, a better solution consists in evaluating the generalized variables by integrating the material response over the cross-section area. Referring to the Timoshenko beam in Sec. 3.2 and to the step 3*b* of the algorithm described in Sec. 5.2.1, this is accomplished through Eqs. (3.19), (3.20) and (3.21). Indeed, the process is defined as follow:

1) The generalized section deformation $\mathbf{e}^{l+1}$ are given for the general current nested iteration $l+1$ performed during the Element State Determination;

2) The material strains over the cross-section area can be evaluated from the compatibility Eq. (3.19):

$$\boldsymbol{\varepsilon}_r^{l+1} = \mathbf{a}_{s,T}\,\mathbf{e}^{l+1}$$

3) The Material State Determination is performed, as described in Sec. 5.4 to obtain the material stresses and the material stiffness matrix:

$$\boldsymbol{\varepsilon}_r^{l+1} \qquad \rightarrow \qquad \boldsymbol{\sigma}_m^{l+1} \quad \text{and} \quad \mathbf{k}_m^{l+1}$$

4) Finally, the section generalized forces and stiffness matrix are evaluated integrating $\boldsymbol{\sigma}_m^{l+1}$ and $\mathbf{k}_m^{l+1}$ over the cross-section:

$$\mathbf{s}^{l+1} = \int_A \mathbf{a}_{s,T}^T \, \boldsymbol{\sigma}_m^{l+1} \, dA \qquad \text{and} \qquad \mathbf{k}_s^{l+1} = \int_A \mathbf{a}_{s,T}^T \, \mathbf{k}_m^{l+1} \, \mathbf{a}_{s,T} \, dA$$

Table 5.3: Section State Determination for the standard Timoshenko beam.

1)	$\mathbf{e}^{l+1}$ are given
2)	$\boldsymbol{\varepsilon}_r^{l+1} = \mathbf{a}_{s,T} \, \mathbf{e}^{l+1}$
3)	Material State Determination (Table 5.5) $\boldsymbol{\varepsilon}_r^{l+1} \rightarrow \boldsymbol{\sigma}_m^{l+1}$ and $\mathbf{k}_m^{l+1}$
4)	$\mathbf{s}^{l+1} = \int_A \mathbf{a}_{s,T}^T \, \boldsymbol{\sigma}_m^{l+1} \, dA$ and $\mathbf{k}_s^{l+1} = \int_A \mathbf{a}_{s,T}^T \, \mathbf{k}_m^{l+1} \, \mathbf{a}_{s,T} \, dA$

This procedure, summarized in Table 5.3, also applies to the ETFF model in Sec. 3.3 and to the EBFF beam. In the first case, Eqs. (3.45), (3.47) and (3.48) need to be used instead of Eqs. (3.19), (3.20) and (3.21), or equivalently Eqs. (3.51), (3.52) and (3.54) if the improved model proposed in [1] is considered; in the second case, the equations are defined according to Eqs. (3.34), (3.36) and (3.37).

For the mixed element with section warping, the Section State Determination (used at the step 3*c* of the algorithm in Sec. 5.2.2) also depends on the warping displacement field $u_w(x, y, z)$ and provides for the evaluation of the generalized forces $\mathbf{s}_w^x$ and $\mathbf{s}_w^{yz}$ and the warping stiffness matrices $\tilde{\mathbf{k}}_{sw}^x$, $\tilde{\mathbf{k}}_{sw}^{yz}$, $\tilde{\mathbf{k}}_{ws}^x$, $\tilde{\mathbf{k}}_{ws}^{yz}$, $\tilde{\mathbf{k}}_{ww}^x$, $\tilde{\mathbf{k}}_{ww}^{yz}$, $\tilde{\mathbf{k}}_{ww}^{xy}$ and $\tilde{\mathbf{k}}_{ww}^{yx}$. In particular, the compatibility condition, providing for the material strains, is represented by Eq. (3.62), which is expressed by the discretized form of the warping strains $\boldsymbol{\varepsilon}_w$ as follows:

$$\boldsymbol{\varepsilon}_m(x, y, z) = \mathbf{a}_s(y, z) \, \mathbf{e}(x) + \sum_{i=1}^{n_w} \left[\frac{\partial \mathrm{N}_i}{\partial x}(x) \, \mathbf{a}_w^x(y, z) + \mathrm{N}_i(x) \, \mathbf{a}_w^{yz}(y, z) \right] \mathbf{u}_{w,i} \tag{5.5}$$

Once the material strains are known, the Material State Determination is performed, as described in Sec. 5.4, and the generalized section variables are evaluated. The steps of the procedure are summarized in Table 5.4.

Table 5.4: Section State Determination for the mixed element with section warping.

1)	$\mathbf{e}^{l+1}$ are given
2)	$\boldsymbol{\varepsilon}_m^{l+1} = \mathbf{a}_s\,\mathbf{e}^{l+1} + \sum_{i=1}^{n_w}\left[\frac{\partial \mathrm{N}_i}{\partial x}\,\mathbf{a}_w^x + \mathrm{N}_i\,\mathbf{a}_w^{yz}\right]\,\mathbf{u}_{w,i}^{l+1}$
3)	Material State Determination (Table 5.5)
	$\boldsymbol{\varepsilon}_m^{l+1} \quad \rightarrow \quad \boldsymbol{\sigma}_m^{l+1}$ and $\mathbf{k}_m^{l+1}$
4)	$\mathbf{s}^{l+1} = \int_A \mathbf{a}_s^T\,\boldsymbol{\sigma}_m^{l+1}\,dA$ and $\mathbf{k}_s^{l+1} = \int_A \mathbf{a}_s^T\,\mathbf{k}_m^{l+1}\,\mathbf{a}_s\,dA$
	$\mathbf{s}_w^{x,l+1} = \int_A (\mathbf{a}_w^x)^T\,\boldsymbol{\sigma}_m^{l+1}\,dA$ and $\mathbf{s}_w^{yz,l+1} = \int_A (\mathbf{a}_w^{yz})^T\,\boldsymbol{\sigma}_m^{l+1}\,dA$
	$\tilde{\mathbf{k}}_{sw}^{x,l+1} = \left(\int_A \mathbf{a}_s^T\,\mathbf{k}_m^{l+1}\,\mathbf{a}_w^x\,dA\right)\,\boldsymbol{\Gamma}, \qquad \tilde{\mathbf{k}}_{sw}^{yz,l+1} = \left(\int_A \mathbf{a}_s^T\,\mathbf{k}_m^{l+1}\,\mathbf{a}_w^{yz}\,dA\right)\,\boldsymbol{\Gamma}, \quad$ etc.
	Eqs. (3.92) - (3.99)

5.3.2 Fiber section models and 2D integration rules

The step 4 of the Section State Determination procedures in Tables 5.3 and 5.4 requires the integration of the material stresses $\boldsymbol{\sigma}_m(x,y,z)$ and the material stiffness matrix $\mathbf{k}_m(x,y,z)$ over the cross-section area. For nonlinear material responses, the closed form solution of these integrals is not easy to find in a general case. Hence, to implement the described FEs in a standard numerical code, an approximate method is usually preferred. A common approach is the adoption of a fiber model [25,113] that basically consists in evaluating the integrals through a numerical integration rule. In other words, the element cross-section is discretized, selecting over it a finite number of points, to each of which a specific portion of the total area is associated. The portions of area correspond to the numerical integration weights w_p and each point P, together with its weight w_p, is called fiber (Fig. 5.1). If n_{ip} points are selected, located at (y_p, z_p) with $p = 1, \ldots, n_{ip}$, the material strains $\boldsymbol{\varepsilon}_m$ and related stresses $\boldsymbol{\sigma}_m$ and stiffness matrix $\mathbf{k}_m$ are only computed at these points. For instance, referring to Table 5.4, the steps 2 and 3 result as:

$$\boldsymbol{\varepsilon}_{m,p}^{l+1} = \mathbf{a}_s(y_p,z_p)\,\mathbf{e}^{l+1} + \sum_{i=1}^{n_w}\left[\frac{\partial \mathrm{N}_i(x)}{\partial x}\,\mathbf{a}_w^x(y_p,z_p) + \mathrm{N}_i(x)\,\mathbf{a}_w^{yz}(y_p,z_p)\right]\,\mathbf{u}_{w,i}^{l+1}$$

$$\downarrow$$

$$\boldsymbol{\sigma}_{m,p}^{l+1}\left(\boldsymbol{\varepsilon}_{m,p}^{l+1}\right) \quad \text{and} \quad \mathbf{k}_{m,p}^{l+1}\left(\boldsymbol{\varepsilon}_{m,p}^{l+1}\right)$$

with $p = 1, \ldots, n_{ip}$. Once the $\boldsymbol{\sigma}_m$ and $\mathbf{k}_m$ are known at all points, the 2D numerical integration is performed at the step 4, assuming that the material variables are constant

over the weighting area associated to the corresponding point, e.g.:

$$\mathbf{s}^{l+1} = \int_A \mathbf{a}_s^T \, \boldsymbol{\sigma}_m^{l+1} \, dA \simeq \sum_{p=1}^{n_{ip}} \mathbf{a}_s^T(y_p, z_p) \, \boldsymbol{\sigma}_{m,p}^{l+1} \, w_p$$

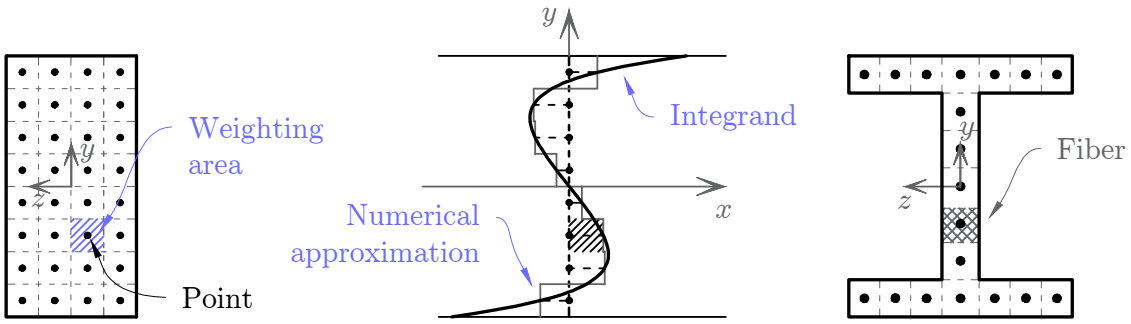

Figure 5.1: Examples of a fiber cross-section discretization (midpoint rule).

This approach is very useful and it can be applied for any material constitutive laws. However, some important considerations need to made. Assuming that the cross-section is subdivided into rectangular patches, the numerical integration can be performed independently in each patch and the individual contributions can then be added together. This can be also done to distinguish two parts of the cross-section made of different materials, e.g. in a composed steel-concrete beam, or to distinguish the confined from the unconfined part of reinforced concrete beam sections. In this case, the reinforcing bars can be considered as additional fibers, whose weighting areas correspond exactly to areas of the bars.

For a linear elastic and isotropic material response, if the TFF beam is adopted, the functions to be integrated during the Section State Determination are at most parabolic in both the y and z directions, as it results from Eqs. (3.19) - (3.23); the same happens for the EBFF beam (Eqs. (3.34) - (3.39)). Hence, to obtain the exact values of the generalized stresses $\mathbf{s}$ and of the section stiffness matrix $\mathbf{k}_s$, the best choice is to define the fiber locations and weights according to the 2D Gauss-Legendre integration rule. Indeed, this requires only a 2×2 grid of points for each rectangular patch of the cross-section. For the ETFF beam, the number of points depend on the order of the functions $\rho_{yy}(y,z)$, $\rho_{zy}(y,z)$, $\rho_{yz}(y,z)$, $\rho_{zz}(y,z)$ introduced in Eq. (3.45). Even so, the Gauss-Legendre integration rule is still the best scheme, since these functions are usually defined on a polynomial basis. The same occurs for the WMF beam. In this case, according to Eqs. (3.15), (3.62), (3.89) and (3.90), the integrand order also depends on the interpolation polynomial order chosen for the $M_j(y,z)$ in Eq. (3.67).

Hence, the exact integration is obtained adopting a grid of $n_y \times n_z$ for each rectangular patch, where:

$$n_y = r_y + 1 \geq 2 \qquad \text{and} \qquad n_z = r_z + 1 \geq 2$$

r_y and r_z being the polynomial order in the in the y and the z direction respectively for the interpolation polynomials defined in the considered patch.

On the contrary, for a nonlinear material response, no general assumption can be made on the integrand order, hence the previous observations are no longer valid. However, Kostic and Filippou [29] demonstrated that the best approach for this case is to define the fibers according to midpoint integration rule. This means that each rectangular patch is discretized with a uniform (equally spaced) grid of points. Each point is located at the midpoint of the associated weighting area, which has the same dimension for all the points (Fig. 5.1). Although, this does not provide an exact estimation of the initial elastic stiffness of the element, Kostic and Filippou showed that the error is negligible for practical purposes. Hence, this solution is adopted for the correlation studies of this work.

5.4 Material State Determination

The goal of the Material State Determination is to compute the stresses $\boldsymbol{\sigma}_m(x, y, z)$ and the tangent stiffness matrix $\mathbf{k}_m(x, y, z)$ for the given strains $\boldsymbol{\varepsilon}_m(x, y, z)$ at a specific material point M and in particular at each point used to perform the numerical integration previously described:

$$\boldsymbol{\varepsilon}_{m,p}^{l+1} \qquad \rightarrow \qquad \boldsymbol{\sigma}_{m,p}^{l+1}\left(\boldsymbol{\varepsilon}_{m,p}^{l+1}\right) \quad \text{and} \quad \mathbf{k}_{m,p}^{l+1}\left(\boldsymbol{\varepsilon}_{m,p}^{l+1}\right)$$

To do so, two tasks need to be addressed. Referring to a general 3D model, first the general solution procedure need to be applied, that is the algorithm to evaluate the six-component stress vector $\boldsymbol{\sigma}(x, y, z)$ and the full tangent stiffness matrix $\mathbf{C}_t$, for a given six-component strain vector $\boldsymbol{\varepsilon}(x, y, z)$. This, of course, depends the specific model adopted to describe the behavior of that material point and henceforth, it is referred to as 3D Material State Determination (to emphasize that it considers all the six material strains and stresses). Then, it is necessary to *extract* the relevant stress components in $\boldsymbol{\sigma}_m(x, y, z)$ from the six ones involved in the 3D model. As described in Chap. 3, the TFF, the ETFF and the WMF elements consider only the three strain independent variables $\boldsymbol{\varepsilon}_m = \{\varepsilon_x,\ \gamma_{xy},\ \gamma_{xz}\}^T$ and the three work conjugate stress components $\boldsymbol{\sigma}_m = \{\sigma_x,\ \tau_{xy},\ \tau_{xz}\}^T$. Hence, to incorporate a 3d material model in the FE one it is necessary to conveniently treat the remaining components of the 3D

stress and strain vectors, $\boldsymbol{\varepsilon}_c = \{\varepsilon_y,\ \varepsilon_z,\ \gamma_{yz}\}^T$ and $\boldsymbol{\sigma}_c = \{\sigma_y,\ \sigma_z,\ \tau_{yz}\}^T$, with a static condensation procedure.

The first part of this section explains the technique proposed to perform this condensing operation, presenting a new efficient algorithm, which is based on the classical iterative approach [51]. It allows to by-pass the iterative form, evaluating the required variables with a non-iterative scheme. The second part of the section presents the standard return mapping algorithms for the J2 and the DP plasticity described in Sec. 2.2, referring to the general case of six component stress/strain tensors, and the linearized solution procedure for the plastic-damage model in Sec. 2.4, based on a specific elasto-plastic-predictor/damage-corrector scheme.

5.4.1 Inclusion of the 3D material model in the fiber discretization: the nonlinear static condesation

To include a general 3D material model into a FE formulation that considers only some of the six stress components, a classical approach [45] consists in condensing out the stress components $\boldsymbol{\sigma}_c$ that are zero by finding the appropriate values of the strains $\boldsymbol{\varepsilon}_c$, i.e. the ones that satisfy the condition $\boldsymbol{\sigma}_c = \mathbf{0}$. For the TFF, the ETFF and the WMF beams, they are the three components lying in the section plane $\boldsymbol{\sigma}_c = \{\sigma_y,\ \sigma_z,\ \tau_{yz}\}^T$. Because of the nonlinear behavior of the material, this requires a nonlinear static condensation, which usually follows an iterative procedure. It is based on the partition of the six-component stress and strain vectors into the restrained (subscript 'm') and the condensed part (subscript 'c'), with the incremental stress-strain relation (e.g. Eq. (2.31)) thus resulting as:

$$\dot{\boldsymbol{\sigma}} = \mathbf{C}_t \dot{\boldsymbol{\varepsilon}} \qquad \rightarrow \qquad \left\{ \begin{array}{c} \dot{\boldsymbol{\sigma}}_m \\ \dot{\boldsymbol{\sigma}}_c \end{array} \right\} = \left[\begin{array}{cc} \mathbf{C}_{t,mm} & \mathbf{C}_{t,mc} \\ \mathbf{C}_{t,cm} & \mathbf{C}_{t,cc} \end{array} \right] \left\{ \begin{array}{c} \dot{\boldsymbol{\varepsilon}}_m \\ \dot{\boldsymbol{\varepsilon}}_c \end{array} \right\} \tag{5.6}$$

Referring to Tables 5.3 and 5.4, at the step 3, the condensation procedure starts considering the values of $\boldsymbol{\varepsilon}_m = \boldsymbol{\varepsilon}_m^{l+1}$ that are given from the step 2 and that remain fixed during the iterations, whereas the values of $\boldsymbol{\varepsilon}_c$ are initialized recalling them from the previous loading time step, $\boldsymbol{\varepsilon}_c = \boldsymbol{\varepsilon}_c^0$ (i.e. the values obtained and stored at the converged state of the global N-R algorithm performed for the loading step preceding the current one). Hence, a first 3D Material State Determination is performed, providing the initial estimation of the material response:

$$\boldsymbol{\varepsilon}^0 = \left\{ \begin{array}{c} \boldsymbol{\varepsilon}_m^{l+1} \\ \boldsymbol{\varepsilon}_c^0 \end{array} \right\} \qquad \rightarrow \qquad \boldsymbol{\sigma}^0 = \left\{ \begin{array}{c} \boldsymbol{\sigma}_m^0 \\ \boldsymbol{\sigma}_c^0 \end{array} \right\}, \quad \text{and} \quad \mathbf{C}_t^0 \left[\begin{array}{cc} \mathbf{C}_{t,mm}^0 & \mathbf{C}_{t,mc}^0 \\ \mathbf{C}_{t,cm}^0 & \mathbf{C}_{t,cc}^0 \end{array} \right]$$

For the material models adopted in this work the 3D Material State Determination follows the solution procedures described in the next sections. Then, the following iterative steps are performed, with the superscripts 'i' and '$i+1$' denoting the previous and current iterations, respectively:

1) The condensed strains $\boldsymbol{\varepsilon}_c$ are updated computing a corrective increment, aiming to obtain $\boldsymbol{\sigma}_c^{i+1} = \mathbf{0}$, i.e.:

$$\Delta\boldsymbol{\varepsilon}_c^{i+1} = -\left(\mathbf{C}_{t,cc}^{i}\right)^{-1} \boldsymbol{\sigma}_c^{i+1} \qquad \rightarrow \qquad \boldsymbol{\varepsilon}_c^{i+1} = \boldsymbol{\varepsilon}_c^{i+1} + \Delta\boldsymbol{\varepsilon}_c^{i+1}$$

2) The 3D Material State Determination is performed:

$$\boldsymbol{\varepsilon}^{i+1} = \left\{ \begin{array}{c} \boldsymbol{\varepsilon}_m^{l+1} \\ \boldsymbol{\varepsilon}_c^{i+1} \end{array} \right\} \qquad \rightarrow \qquad \boldsymbol{\sigma}^{i+1} = \left\{ \begin{array}{c} \boldsymbol{\sigma}_m^{i+1} \\ \boldsymbol{\sigma}_c^{i+1} \end{array} \right\} \quad \text{and} \quad \mathbf{C}_t^{i+1} = \left[\begin{array}{cc} \mathbf{C}_{t,mm}^{i+1} & \mathbf{C}_{t,mc}^{i+1} \\ \mathbf{C}_{t,cm}^{i+1} & \mathbf{C}_{t,cc}^{i+1} \end{array} \right]$$

3) If the convergence test $|\boldsymbol{\sigma}_c^{i+1}| < tollerance$ is satisfied, the condensation procedure ends, otherwise it restarts from the step 1.

The condensed material stiffness matrix is then given by:

$$\mathbf{k}_m = \mathbf{C}_{t,mm} - \mathbf{C}_{t,mc} \left(\mathbf{C}_{t,cc}\right)^{-1} \mathbf{C}_{t,cm} \tag{5.7}$$

Note that the same scheme can be used for an Euler-Bernoulli beam, simply considering that in this case the only independent strain is the axial one, $\boldsymbol{\varepsilon}_m = \varepsilon_x$ (with its work conjugate axial stress $\boldsymbol{\sigma}_m = \sigma_x$) and the remaining components to condense are $\boldsymbol{\varepsilon}_c = \{\varepsilon_y,\ \varepsilon_z, \gamma_{xy},\ \gamma_{xz},\ \gamma_{yz}\}^T$ (with $\boldsymbol{\sigma}_c = \{\sigma_y,\ \sigma_z,\ \tau_{xy},\ \tau_{xz}\ \tau_{yz}\}^T$).

However, to provide a less onerous solution, an alternative non-iterative consistent approach is here presented. The purpose is to bypass the iterations necessary to perform the material condensation, taking advantage of the element iterative process at the upper level. In particular, it follows these steps:

1) At the current element nested iteration $l+1$, the values of $\boldsymbol{\varepsilon}_m = \boldsymbol{\varepsilon}_m^{l+1}$ and its increment with respect to the previous element iteration $\Delta\boldsymbol{\varepsilon}_m = \boldsymbol{\varepsilon}_m^{l+1} - \boldsymbol{\varepsilon}_m^{l}$ are given and the condensed strains $\boldsymbol{\varepsilon}_c$ and the material stiffness matrix are recalled from the previous element nested iteration, $\boldsymbol{\varepsilon}_c = \boldsymbol{\varepsilon}_c^{l}$ and $\mathbf{C}_t = \mathbf{C}_t^{l}$;

2) The condensed strains $\boldsymbol{\varepsilon}_c$ are updated adding the linearized increment with respect to the previous element nested iteration:

$$\Delta\boldsymbol{\varepsilon}_c^{l+1} = -\left(\mathbf{C}_{t,cc}^{l}\right)^{-1} \mathbf{C}_{t,cc}^{l}\, \Delta\boldsymbol{\varepsilon}_m^{l+1} \qquad \rightarrow \qquad \boldsymbol{\varepsilon}_c^{l+1} = \boldsymbol{\varepsilon}_c^{l} + \Delta\boldsymbol{\varepsilon}_c^{l+1}$$

3) The 3D Material State Determination is performed:

$$\boldsymbol{\varepsilon}^{l+1} = \left\{ \begin{array}{c} \boldsymbol{\varepsilon}_m^{l+1} \\ \boldsymbol{\varepsilon}_c^{l+1} \end{array} \right\} \qquad \rightarrow \qquad \boldsymbol{\sigma}^{l+1} = \left\{ \begin{array}{c} \boldsymbol{\sigma}_m^{l+1} \\ \boldsymbol{\sigma}_c^{l+1} \end{array} \right\} \quad \text{and} \quad \mathbf{C}_t^{l+1} = \left[\begin{array}{cc} \mathbf{C}_{t,mm}^{l+1} & \mathbf{C}_{t,mc}^{l+1} \\ \mathbf{C}_{t,cm}^{l+1} & \mathbf{C}_{t,cc}^{l+1} \end{array} \right]$$

4) $\boldsymbol{\varepsilon}_c$ is updated again computing a corrective increment, aiming to obtain $\boldsymbol{\sigma}_c^{l+1} = \mathbf{0}$:

$$\Delta\boldsymbol{\varepsilon}_c^{l+1} = -\left(\mathbf{C}_{t,cc}^{l+1}\right)^{-1} \boldsymbol{\sigma}_c^{l+1} \qquad \rightarrow \qquad \boldsymbol{\varepsilon}_c^{l+1} = \boldsymbol{\varepsilon}_c^{l+1} + \Delta\boldsymbol{\varepsilon}_c^{l+1}$$

and it is stored for the next element iteration;

5) The condensed material stresses and stiffness matrix are computed as:

$$\boldsymbol{\sigma}_m^{l+1} = \boldsymbol{\sigma}_m^{l+1} + \mathbf{C}_{t,mc}^{l+1} \left(\mathbf{C}_{t,cc}^{l+1}\right)^{-1} \boldsymbol{\sigma}_c^{l+1} \quad \text{and} \quad \mathbf{k}_m^{l+1} = \mathbf{C}_{t,mm}^{l+1} - \mathbf{C}_{t,mc}^{l+1} \left(\mathbf{C}_{t,cc}^{l+1}\right)^{-1} \mathbf{C}_{t,cm}^{l+1}$$

Table 5.5: Non-iterative nonlinear static condensation.

1)	$\Delta\boldsymbol{\varepsilon}_c^{l+1} = -\left(\mathbf{C}_{t,cc}^{l}\right)^{-1} \mathbf{C}_{t,cc}^{l} \Delta\boldsymbol{\varepsilon}_m^{l+1} \qquad \rightarrow \qquad \boldsymbol{\varepsilon}_c^{l+1} = \boldsymbol{\varepsilon}_c^{l} + \Delta\boldsymbol{\varepsilon}_c^{l+1}$
2)	3D Material State Determination (Table 5.6)
	$\boldsymbol{\varepsilon}^{l+1} \qquad \rightarrow \qquad \boldsymbol{\sigma}^{l+1}$ and $\mathbf{C}_t^{l+1}$
3)	$\Delta\boldsymbol{\varepsilon}_c^{l+1} = -\left(\mathbf{C}_{t,cc}^{l+1}\right)^{-1} \boldsymbol{\sigma}_c^{l+1} \qquad \rightarrow \qquad \boldsymbol{\varepsilon}_c^{l+1} = \boldsymbol{\varepsilon}_c^{l+1} + \Delta\boldsymbol{\varepsilon}_c^{l+1}$
4)	$\boldsymbol{\sigma}_m^{l+1} = \boldsymbol{\sigma}_m^{l+1} + \mathbf{C}_{t,mc}^{l+1} \left(\mathbf{C}_{t,cc}^{l+1}\right)^{-1} \boldsymbol{\sigma}_c^{l+1}$
	$\mathbf{k}_m^{l+1} = \mathbf{C}_{t,mm}^{l+1} - \mathbf{C}_{t,mc}^{l+1} \left(\mathbf{C}_{t,cc}^{l+1}\right)^{-1} \mathbf{C}_{t,cm}^{l+1}$

With this technique, summarized in Table 5.5, only an approximation of the condensed strains $\boldsymbol{\varepsilon}_c$ is computed (step 2), linearizing the material behavior from the element iteration l to the $l+1$ and then (step 4) the residual values $\Delta\boldsymbol{\varepsilon}_c^{l+1}$ are added for the next step. Hence, in this case the nested element iterative process governs not only the Element State Determination, but also the material condensation, providing a simpler implementation of the 3D material model in the FE formulation. However, it is important to highlight that, as discussed in Sec. 5.2, the Element State Determination can be also performed with a non-iterative procedure: in this case the N-R algorithm represents the main iterative process governing the time-step integration, the element state determination and the material condensation as well.

Each of the condensation procedures described above represents a general approach

to perform the static condensation of a system of nonlinear equations, expressible as:

$$\mathbf{A}\,\mathbf{x} = \mathbf{y} \qquad \rightarrow \qquad \begin{bmatrix} \mathbf{A}_{mm} & \mathbf{A}_{mc} \\ \mathbf{A}_{cm} & \mathbf{A}_{cc} \end{bmatrix} \begin{Bmatrix} \mathbf{x}_m \\ \mathbf{x}_c \end{Bmatrix} = \begin{Bmatrix} \mathbf{y}_m \\ \mathbf{0} \end{Bmatrix}$$

$\mathbf{A} = \hat{\mathbf{A}}[\mathbf{x}]$ is the coefficient matrix, which is function of $\mathbf{x}$, $\mathbf{x}_m$ and $\mathbf{y}_c = \mathbf{0}$ are the given data and $\mathbf{x}_c$ and $\mathbf{x}_p$ are the unknowns. For the material condensation, the system of equations is represented by the constitutive stress-strain relation, which is linearized in the incremental form of Eq. (5.6). However the two procedures are generally valid. For instance, in the numerical examples of this paper, they are also used to enforce the plane stress conditions in 2D FEs, where the out-of-plane material stresses components are zero (i.e. if $x - y$ is the plane of the element, $\boldsymbol{\sigma}_c = \{\sigma_z,\ \tau_{xz},\ \tau_{yz}\}^T = \mathbf{0}$). In any case, the iterative approach fixes the given strains $\boldsymbol{\varepsilon}_m^{l+1}$ (i.e. the given unknowns $\mathbf{x}_m$) at the current element iteration and applies a standard iterative N-R algorithm to the condensed part of the constitutive relation (i.e. to $\mathbf{A}_{cm}\,\mathbf{x}_m + \mathbf{A}_{cc}\,\mathbf{x}_c = \mathbf{0}$). In fact, at every iteration, the condensed variables $\boldsymbol{\varepsilon}_m$ are updated using the residual condensed stresses $\mathbf{r}^{i+1} = \mathbf{0} - \boldsymbol{\sigma}_c^{i+1}$ and the consistent stiffness matrix $\mathbf{C}_{t,cc}^{i}$ (step 1). By contrast, the non-iterative approach starts from the material state at the previous element iteration l, linearizes the material response for that state and performs only one linear corrective step, significantly reducing the global computational cost.

5.4.2 Linearized solution procedure for the J2, the Drucker-Prager and the proposed 3D plastic-damage model

The 3D Material State Determination performed during the nonlinear static condensation in Table 5.5 is the general procedure to evaluate the six-component stress vector $\boldsymbol{\sigma}$ and tangent stiffness matrix $\mathbf{C}_t$ for a given six-component strain vector $\boldsymbol{\varepsilon}$. In the following, the classical procedure for the Drucker-Prager plasticity with linear hardening in Sec. 2.2 is first presented [61]. Then, it is used to define the linearized solution procedure proposed for the plastic-damage model described in Sec. 2.4. In both cases, the starting point is represented by the given total strains $\boldsymbol{\varepsilon}^{l+1}$ at the general current iteration $l+1$ and (step 3) and by recalling the material state at the previous iteration l (i.e. $\boldsymbol{\varepsilon}^l$, $\boldsymbol{\sigma}^l$, $\mathbf{C}_t^l$ and the history variables). The subscript '$n+1$' indicates the variables for the current state that need to be determined and the subscript 'n' indicates the variables at the previous evaluated state.

The Drucker-Prager solution algorithm can be summarized as follows:

1) For the current state the strain vector $\boldsymbol{\varepsilon}_{n+1}$ is set equal to the given total strains $\boldsymbol{\varepsilon}^{l+1}$ at the current element iteration $l+1$ and the previous material state is set

equal to the state at the element iteration l:

$$\boldsymbol{\varepsilon}_{n+1} = \boldsymbol{\varepsilon}^{l+1} \qquad \text{and} \qquad \Delta\boldsymbol{\varepsilon}_{n+1} = \boldsymbol{\varepsilon}^{l+1} - \boldsymbol{\varepsilon}^{l}$$

2) Considering the internal variables of the previous state, the increment of the strains is assumed to be elastic, that is an Elastic Prediction is preformed by means of Eq. (2.1):

$$\begin{aligned} &\boldsymbol{\varepsilon}^p_{n+1} = \boldsymbol{\varepsilon}^p_n, \qquad \boldsymbol{\zeta}_{n+1} = \boldsymbol{\zeta}_n, \qquad \alpha_{n+1} = \alpha_n \\ &\Delta\boldsymbol{\varepsilon}^p_{n+1} = \mathbf{0}, \qquad \Delta\boldsymbol{\varepsilon}^e_{n+1} = \Delta\boldsymbol{\varepsilon}_{n+1} \qquad \rightarrow \qquad \boldsymbol{\sigma}_{n+1} = \mathbf{C}\,(\boldsymbol{\varepsilon}_{n+1} - \boldsymbol{\varepsilon}^p_n) \end{aligned}$$

3) The yielding condition $f_{DP,n+1} = f_{DP}(\boldsymbol{\sigma}_{n+1}, \boldsymbol{\zeta}_n, \alpha_n) < 0$ (Eq. (2.11)) is checked: if $f_{DP,n+1} < 0$, the internal variables are stored with the tangent stiffness matrix assumed equal to the elastic one, $\mathbf{C}^{ep}_{n+1} = \mathbf{C}$, and the algorithm ends; otherwise the return mapping algorithm is performed:

   a) Considering that the adopted hardening model is linear [63], the plastic consistency parameter $\dot{\lambda}$ can be evaluated as:

$$\dot{\lambda}_{n+1} = \frac{f_{DP,n+1}}{2\,G + 2/3\,(H_k + H_i)}$$

   b) By means of Eqs. (2.5), first the plastic strains are updated:

$$\mathbf{n}_{n+1} = \frac{\boldsymbol{\pi}_{n+1} - \boldsymbol{\zeta}_n}{|\boldsymbol{\pi}_{n+1} - \boldsymbol{\zeta}_n|} \qquad \rightarrow \qquad \boldsymbol{\varepsilon}^p_{n+1} = \boldsymbol{\varepsilon}^p_n + \dot{\lambda}_{n+1}\,\mathbf{n}_{n+1}$$

   and then the internal variables are updated as well:

$$\alpha_{n+1} = \alpha_n + \sqrt{\frac{2}{3}}\dot{\lambda}_{n+1} \qquad \text{and} \qquad \boldsymbol{\zeta}_{n+1} = \frac{2}{3} H_k \boldsymbol{\varepsilon}^p_{n+1}$$

   c) Finally, the material stresses are evaluated:

$$\boldsymbol{\sigma}_{n+1} = \mathbf{C}\,(\boldsymbol{\varepsilon}_{n+1} - \boldsymbol{\varepsilon}^p_{n+1}) = \mathbf{C}\,\boldsymbol{\varepsilon}^e_{n+1}$$

   and the elasto-plastic tangent stiffness $\mathbf{C}^{ep}_{n+1}$ is obtained from Eq. (2.13).

Note that the algorithm also applies to the J2 plasticity in Sec. 2.2, simply assuming $\sigma_t = \sigma_c$, which leads to $\sigma_y = \sigma_t = \sigma_c$ and $\mu = 0$.

Including the described Drucker-Prager return mapping algorithm, the solution procedure for the proposed plastic-damage model is defined as a two-phases discretized

procedure. The first phase, called Elasto-Plastic Predictor Phase, involves the evaluation of the effective stresses $\bar{\boldsymbol{\sigma}}$ and of the elasto-plastic tangent stiffness $\mathbf{C}^{ep}$; the second phase, called Damage Corrector Phase, involves the evaluation of the damage variables and of the total quantities $\boldsymbol{\sigma}$ and $\mathbf{C}_t$. The procedure is summarized as follows:

1) For the current state the strain vector $\boldsymbol{\varepsilon}_{n+1}$ is set equal to the given total strains $\boldsymbol{\varepsilon}^{l+1}$ at the current element iteration $l+1$ and the previous material state is set equal to the state at the element iteration l:

$$\boldsymbol{\varepsilon}_{n+1} = \boldsymbol{\varepsilon}^{l+1} \qquad \text{and} \qquad \Delta\boldsymbol{\varepsilon}_{n+1} = \boldsymbol{\varepsilon}^{l+1} - \boldsymbol{\varepsilon}^{l}$$

2) Elasto-Plastic Predictor Phase - The damage evolution is *frozen*, with the related variables calculated for the previous state and the elasto-plastic problem is solved:

   a) Considering the internal variables of the previous state, the increment of the strains is assumed to be elastic, that is an Elastic Prediction is preformed by means of Eq. (2.1):

$$\begin{aligned} &\boldsymbol{\varepsilon}^{p}_{n+1} = \boldsymbol{\varepsilon}^{p}_{n}, \qquad \boldsymbol{\zeta}_{n+1} = \boldsymbol{\zeta}_{n}, \qquad \alpha_{n+1} = \alpha_{n} \\ &\Delta\boldsymbol{\varepsilon}^{p}_{n+1} = \mathbf{0}, \qquad \Delta\boldsymbol{\varepsilon}^{e}_{n+1} = \Delta\boldsymbol{\varepsilon}_{n+1} \qquad \rightarrow \qquad \bar{\boldsymbol{\sigma}}_{n+1} = \mathbf{C}\,(\boldsymbol{\varepsilon}_{n+1} - \boldsymbol{\varepsilon}^{p}_{n}) \end{aligned}$$

   b) The yielding condition $f_{n+1} = f(\bar{\boldsymbol{\sigma}}_{n+1}, \boldsymbol{\zeta}_n, \alpha_n) < 0$ (Eq. (2.28)) is checked: if $f_{n+1} < 0$, the internal variables are stored with the elasto-plastic stiffness matrix assumed equal to the elastic one, $\mathbf{C}^{ep}_{n+1} = \mathbf{C}$, and the algorithm continues from the step 3; otherwise a Plastic Correction is performed through the return mapping algorithm previously described and referring to the effective stresses (Eq. (2.28) and (2.29)):

$$\dot{\lambda}_{n+1} = \frac{f_{n+1}}{2\,G + 2/3\,(H_k + H_i)} \qquad \rightarrow \qquad \bar{\mathbf{n}}_{n+1} = \frac{\mathbf{P}\bar{\boldsymbol{\sigma}}_{n+1} - \boldsymbol{\zeta}_n}{|\mathbf{P}\bar{\boldsymbol{\sigma}}_{n+1} - \boldsymbol{\zeta}_n|}$$

$$\boldsymbol{\varepsilon}^{p}_{n+1} = \boldsymbol{\varepsilon}^{p}_{n} + \dot{\lambda}_{n+1}\,\bar{\mathbf{n}}_{n+1}$$

$$\alpha_{n+1} = \alpha_n + \sqrt{\frac{2}{3}}\dot{\lambda}_{n+1} \qquad \text{and} \qquad \boldsymbol{\zeta}_{n+1} = \frac{2}{3}H_k\boldsymbol{\varepsilon}^{p}_{n+1}$$

$$\bar{\boldsymbol{\sigma}}_{n+1} = \mathbf{C}\,(\boldsymbol{\varepsilon}_{n+1} - \boldsymbol{\varepsilon}^{p}_{n+1}) = \mathbf{C}\,\boldsymbol{\varepsilon}^{e}_{n+1} \qquad \text{and} \qquad \mathbf{C}^{ep} \text{ from Eq. (2.29)}$$

3) Damage Corrector Phase - The total and plastic strains are *frozen*, with the related variables calculated in the previous phase (step 2), and the damage evolution problem is solved:

a) The current principal total and elastic strains, $\boldsymbol{\varepsilon}_{i,n+1}$ and $\boldsymbol{\varepsilon}^e_{i,n+1}$ with $i = 1, \ldots, 3$, are computed;

b) Eqs. (2.40) are used to evaluate the equivalent strains, $\mathbf{e}_{i,n+1}$ and $\mathbf{e}^e_{i,n+1}$ with $i = 1, \ldots, 3$;

c) Eqs. (2.38) and (2.39) are used to evaluate the equivalent strain measures, $Y_{t,n+1}$, $Y_{c,n+1}$, $Y^e_{t,n+1}$ and $Y^e_{c,n+1}$;

d) The damage limit conditions (Eqs. (2.33) and (2.34)) are checked:

$$f_{t,n+1} = Y_{t,n+1} - Y_{0t} - (a_t\, Y_{t,n+1} + k_t) D_{t,n} < 0$$
$$f_{c,n+1} = Y_{c,n+1} - Y_{0c} - (a_c\, Y_{c,n+1} + k_c) D_{c,n} < 0$$

If $f_{t,n+1} < 0$ and $f_{c,n+1} < 0$, the previous values of the damage variables are assumed for the current steps, i.e. $D_{t,n+1} = D_{t,n}$ and $D_{c,n+1} = D_{c,n}$; otherwise ($f_{t,n+1} < 0$ or $f_{c,n+1} < 0$) the updated values that satisfy the Kuhn-Tacker and the consistency conditions are evaluated, that is:

$$D_{t,n+1} = \frac{Y_{c,n+1} - Y_{0c}}{a_c Y_{c,n+1} + k_c} \in [D_{t,n},\ 1] \quad \text{and} \quad D_{c,n+1} = \frac{Y_{c,n+1} - Y_{0c}}{a_c Y_{c,n+1} + k_c} \in [D_{c,n},\ 1]$$

e) The damage combination coefficients $\alpha_{t,n+1}$ and $\alpha_{c,n+1}$ are evaluated by means of Eq. (2.37), that is computing:

$$\eta_{t,n+1} = \frac{Y^e_{t,n+1}}{Y_{0t,n+1} + (a_{t,n+1} Y^e_{t,n+1} + k_{t,n+1}) D_n}$$
$$\eta_{c,n+1} = \frac{Y^e_{c,n+1}}{Y_{0c,n+1} + (a_{c,n+1} Y^e_{c,n+1} + k_{c,n+1}) D_n}$$

f) The total damage variable is updated by means of Eq. (2.36):

$$D_{n+1} = \alpha_{t,n+1}\, D_{t,n+1} + \alpha_{c,n+1}\, D_{c,n+1}$$

g) The updated value of D is used to compute the total stresses and the material stiffness matrix:

$$\boldsymbol{\sigma}_{n+1} = (1 - D_{n+1})^2 \mathbf{C}\, (\boldsymbol{\varepsilon}_{n+1} - \boldsymbol{\varepsilon}^p_{n+1})$$
$$\mathbf{C}_{t,n+1} = (1 - D_{n+1})^2\, \mathbf{C}^{ep}_{n+1}$$

In the last step of the Damage Corrector Phase, the material tangent stiffness matrix $\mathbf{C}_t$ is evaluated neglecting the contribute due to $\partial D / \partial \boldsymbol{\varepsilon}$ that appears in Eq. (2.32).

This results in considering the material secant stiffness, as it is usual for classical damage mechanics constitutive laws [80], which implies that the convergence of the iterative procedure does not follow a quadratic rate, as expected for the standard N-R procedure. The entire procedure is recapped in Table 5.6.

As mentioned, the 3D Material State Determination algorithms here described can be used during the static condensation procedure, for both the iterative and the non-iterative version (e.g. step 3 in Table 5.5 for the non iterative version). However, when a degrading material is considered, as for the proposed plastic-damage, the well-known numerical problems related to the ill-condition of the stiffness matrix [101] can occur. In fact, considering that in both cases the condensed strains are updated by inverting the matrix $\mathbf{C}_{t,cc}$, i.e.:

$$\Delta\boldsymbol{\varepsilon}_c = -\left(\mathbf{C}_{t,cc}\right)^{-1} \boldsymbol{\sigma}_c$$

if this matrix is singular or close-to-singular, the algorithms fail to converge and this is likely to happen in the softening part of the material response. As previously discussed, during each iteration, the proposed material model adopts the secant stiffness matrix instead of the tangent one. From the point of view of the invertibility of the stiffness matrix, this results in a more stable condition. However, when the damage variable D assumes high values, the secant matrix $\mathbf{C}_{t,cc}$ can results singular or close-to-singular as well and the convergence problems can still occur.

A straightforward solution to this problem consists in applying the nonlinear static condensation to the elasto-plastic material model (the Drucker-Prager plasticity), instead of applying it to the total plastic-damage one, that is to enforce the condition $\bar{\boldsymbol{\sigma}}_c = \mathbf{0}$, instead of $\boldsymbol{\sigma}_c = \mathbf{0}$. Indeed, because of Eq. (2.27), ensuring that the condensed components of the effective stresses $\bar{\boldsymbol{\sigma}}_c$ are zero is exactly equivalent to impose $\boldsymbol{\sigma}_c = \mathbf{0}$. In this way, the condensed stains $\boldsymbol{\varepsilon}_c$ are updated through the elasto-platic tangent stiffness and the ill-conditioning problems are avoided. In other words, the following approach can be used, as it is done in this present work:

1. Given the total strain vector $\boldsymbol{\varepsilon}_m = \boldsymbol{\varepsilon}_m^{l+1}$, the nonlinear static condensation is performed to evaluate $\boldsymbol{\varepsilon}_c$, with the procedure described in Table 5.5 (or alternatively with the classical iterative approach) and considering only the elasto-plastic material model, that is involving only the Elasto-Plastic Predictor Phase of the 3D Material State Determination (steps 1 and 2 in Table 5.6);

2. Once the static condensation process is over, the Damage Corrector Phase is performed (step 3 in Table 5.6), considering the given strains $\boldsymbol{\varepsilon}_m$ and the condensed ones $\boldsymbol{\varepsilon}_c$ just evaluated.

Table 5.6: Linearized solution algorithm for the proposed plastic-damage model.

1)	Previous state set equal to the state at the element iteration l
	$\boldsymbol{\varepsilon}_{n+1} = \boldsymbol{\varepsilon}^{l+1}$ and $\Delta\boldsymbol{\varepsilon}_{n+1} = \boldsymbol{\varepsilon}^{l+1} - \boldsymbol{\varepsilon}^{l}$
2)	Elasto-Plastic Predictor Phase (damage evolution frozen at n)
2a)	Elastic Prediction
	$\boldsymbol{\varepsilon}^{p}_{n+1} = \boldsymbol{\varepsilon}^{p}_{n}$, $\boldsymbol{\zeta}_{n+1} = \boldsymbol{\zeta}_{n}$, $\alpha_{n+1} = \alpha_n$
	$\Delta\boldsymbol{\varepsilon}^{p}_{n+1} = \mathbf{0}$, $\Delta\boldsymbol{\varepsilon}^{e}_{n+1} = \Delta\boldsymbol{\varepsilon}_{n+1}$ $\rightarrow$ $\bar{\boldsymbol{\sigma}}_{n+1} = \mathbf{C}\,(\boldsymbol{\varepsilon}_{n+1} - \boldsymbol{\varepsilon}^{p}_{n})$
2b)	If $f_{n+1} = f(\bar{\boldsymbol{\sigma}}_{n+1}, \boldsymbol{\zeta}_n, \alpha_n) < 0$ $\rightarrow$ Exit
	otherwise $\rightarrow$ Go to step 3
2c)	Plastic Correction
	$\dot{\lambda}_{n+1} = \frac{f_{n+1}}{2\,G + 2/3\,(H_k + H_i)}$ $\rightarrow$ $\bar{\mathbf{n}}_{n+1} = \frac{\mathbf{P}\bar{\boldsymbol{\sigma}}_{n+1} - \boldsymbol{\zeta}_n}{\lvert\mathbf{P}\bar{\boldsymbol{\sigma}}_{n+1} - \boldsymbol{\zeta}_n\rvert}$
	$\boldsymbol{\varepsilon}^{p}_{n+1} = \boldsymbol{\varepsilon}^{p}_{n} + \dot{\lambda}_{n+1}\,\bar{\mathbf{n}}_{n+1}$
	$\alpha_{n+1} = \alpha_n + \sqrt{\frac{2}{3}}\dot{\lambda}_{n+1}$ and $\boldsymbol{\zeta}_{n+1} = \frac{2}{3} H_k \boldsymbol{\varepsilon}^{p}_{n+1}$
3d)	$\bar{\boldsymbol{\sigma}}_{n+1} = \mathbf{C}\,(\boldsymbol{\varepsilon}_{n+1} - \boldsymbol{\varepsilon}^{p}_{n+1}) = \mathbf{C}\,\boldsymbol{\varepsilon}^{e}_{n+1}$ and $\mathbf{C}^{ep}$ from Eq. (2.29)
3)	Damage Corrector Phase (plastic strains frozen at $n+1$)
3a)	Evaluate $\boldsymbol{\varepsilon}_{i,n+1}$ and $\boldsymbol{\varepsilon}^{e}_{i,n+1}$, with $i = 1, \ldots, 3$
3b)	Evaluate $\mathbf{e}_{i,n+1}$ and $\mathbf{e}^{e}_{i,n+1}$, with $i = 1, \ldots, 3$
3c)	Evaluate $Y_{t,n+1}$, $Y_{c,n+1}$, $Y^{e}_{t,n+1}$ and $Y^{e}_{c,n+1}$
3d)	If $f_{t,n+1} < 0$ and $f_{c,n+1} < 0$ $\rightarrow$ $D_{t,n+1} = D_{t,n}$ and $D_{c,n+1} = D_{c,n}$
	otherwise $\rightarrow$ $D_{h,n+1} = \frac{Y_{h,n+1} - Y_{0h}}{a_h Y_{h,n+1} + k_h} \in [D_{t,h},\ 1]$ with $h = t, c$
3e)	$\eta_{t,n+1} = \frac{Y^{e}_{t,n+1}}{Y_{0t,n+1} + (a_{t,n+1} Y^{e}_{t,n+1} + k_{t,n+1}) D_n}$
	$\eta_{c,n+1} = \frac{Y^{e}_{c,n+1}}{Y_{0c,n+1} + (a_{c,n+1} Y^{e}_{c,n+1} + k_{c,n+1}) D_n}$
	$\alpha_{t,n+1} = \frac{\eta^2_{t,n+1}}{\eta^2_{t,n+1} + \eta^2_{c,n+1}}$ and $\alpha_{c,n+1} = 1 - \alpha_{t,n+1}$
3f)	$D_{n+1} = \alpha_{t,n+1}\,D_{t,n+1} + \alpha_{c,n+1}\,D_{c,n+1}$
3g)	$\boldsymbol{\sigma}_{n+1} = (1 - D_{n+1})^2 \mathbf{C}\,(\boldsymbol{\varepsilon}_{n+1} - \boldsymbol{\varepsilon}^{p}_{n+1})$
	$\mathbf{C}_{t,n+1} = (1 - D_{n+1})^2\,\mathbf{C}^{ep}_{n+1}$

Chapter 6

Correlation studies

6.1 General

This chapter presents a series of numerical applications investigating the performance of the numerical models previously described. The studies here conducted focus on two aspects, which represent the principal contributions of this work:

1. The performance of the WMF beam-column FE in Sec. 3.4, with specific attention to the advantages and disadvantages offered by the Hermite polynomials for the warping interpolation over the element cross-section. This FE is used to study the mechanical response of reinforced concrete (RC) frame structures under monotonic and cyclic loading conditions. The analyzed specimens highlight the effects of nonlinear mechanisms in presence of relevant warping deformations, comparing both the global and local responses with measured data from experimental tests and with standard beam and 2D FE formulations.

2. The performance of the proposed plastic-damage model described in Sec. 2.4 in reproducing the behavior of damaging material. All the RC specimens adopt this material model to represent the concrete response and the J2 plasticity model (Sec. 2.2) to represent the steel response.

The studies are divided in three groups. The first one (Sec. 6.2) refers to two different beams, subjected to a monotonic torsional load and to a cyclic transversal load, respectively. These are used as preliminary applications to test the ability of the WMF model in representing the warping of the beam cross-sections, regardless of the damaging constitutive law. The second group (Sec. 6.3) refers to a series of plain concrete (PC) and RC prismatic beams, subjected to monotonic torsional loads, and exhibiting relevant warping and damaging effects. Finally, the third group (Sec. 6.4) refers to two different RC shear walls, cyclically loaded by horizontals forces.

Hereafter, the warping point distribution over the element cross-section is indicated as follows (see, for example, Fig. 6.2): 'L' or 'H' specifies the class of interpolation functions, where 'L' refers to the Lagrange polynomials and 'H' the Hermite polynomials; then, a number in parentheses specifies the total number, m_w, of warping DOFs.

6.2 Preliminary analyses of steel beams

This section presents the analyses of two thin-walled beams exhibiting relevant cross-section warping phenomena. They focus on the warping displacement interpolation over the element cross-section and describe pros and cons of the Hermite polynomials over the Lagrange ones. Moreover, the analyses show the influence of the warping constraints eventually applied at the beam boundaries, for both linear elastic and elasto-plastic material responses.

6.2.1 Channel cantilever subjected to a torsional load

The first correlation study investigates the response of a thin-walled channel shaped cantilever subjected to a torsional couple at the free end. The specimen, having length $L = 18.0, \mathrm{m}$, has been studied for linear elastic conditions by several authors, Capurso [114], Tralli [115] and Back and Will [116], considering a Young's modulus and a shear modulus equal to $E = 30\,000\,\mathrm{MPa}$ and $G = 13\,000\,\mathrm{MPa}$, respectively. Fig. 6.1

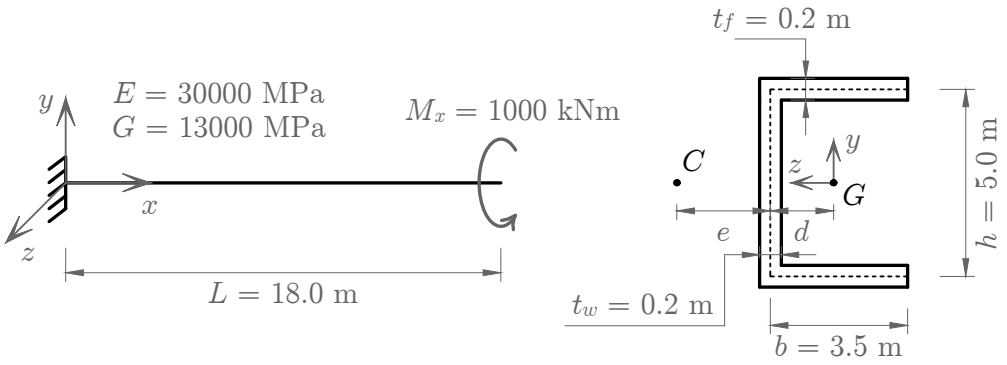

Figure 6.1: Channel cantilever subjected to a torsional load: specimen geometry.

shows the cantilever geometry and the cross-section dimensions. The points G and C correspond to the center of area and the shear center, respectively, being $d = 1.021\,m$ and $e = 1.414\,m$.

The numerical model consists in one WMF beam-column FE, with five Gauss-Lobatto quadrature cross-sections placed along the axis and a specific fiber discretiza-

tion defined for each of them. Moreover, Fig. 6.2 shows four different distributions of warping points located over the element cross-section and used to interpolate the warping displacement field u_w. The first two distributions adopt Lagrange polynomials, L1(8) and L2(20), and the other two use Hermite polynomials, H1(12) and H2(36). Both the distributions L1(8) and L2(20) adopt cubic and parabolic interpolation func-

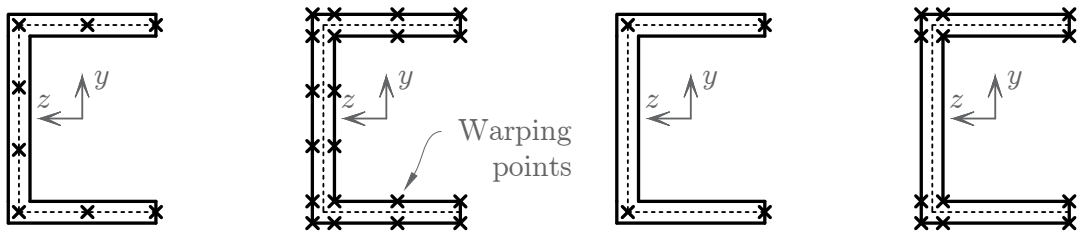

(*a*) Lagrange L1(8) (*b*) Lagrange L2(20) (*c*) Hermite H1(12) (*d*) Hermite H2(36)

Figure 6.2: Warping points distribution over the cross-section of the channel cantilever.

tions along the web and the flanges, respectively. However, L1(8) provides constant interpolation, whereas L2(20) provides linear interpolation across the thickness. The distribution H1(12) adopts cubic interpolation functions along both the web and the flanges and provides a linear interpolation over the thickness, yet involving a reduced number of DOFs. Finally, the distribution H2(36) adopts cubic interpolation functions in all the directions. Three different studies are conducted:

1. *Linear elastic - Warping free*
   Assuming a linear elastic material response, a torsional couple $M_x = 1000\,\text{kNm}$ is applied at the free end and the warping displacements at the fixed end are assumed to be free;

2. *Linear elastic - Warping restrained*
   Assuming a linear elastic material response, a torsional couple $M_x = 1000\,\text{kNm}$ is applied at the free end and the warping displacements at the fixed end are restrained;

3. *Elasto-plastic - Warping* restrained
   Assuming an elasto-plastic material response, a monotonically increasing torsional couple M_x is applied at the free end and the warping displacements at the fixed end are restrained.

Regarding the fiber cross-section discretization, the two linear elastic studies consider the Gauss-Legrende scheme to define the locations and weights of the fibers over the cross-section. To exactly integrate the element stiffness, they define a 4×4 grid of

fibers in each rectangular patch. By contrast, the elasto-plastic study considers the midpoint rule [29] and uses a fiber discretization with 8 fibers along each flange, 14 fibers along the web and 4 fibers across the thickness of the section (at the web/flanges intersections, a 4×4 grid of fibers is located), for a total of 152 fibers.

Linear elastic - Warping free

For the linear elastic case with warping free at the fixed end, the warping point distributions in Fig. 6.2 are compared. Only one warping section is located along the axis, $n_w = 1$, as constant torsion and uniform warping distribution is expected in this direction. The rotation $\Theta_x = \theta_x(x = L)$ of the free end is computed.

Table 6.1 compares the results for the WMF model with the numerical outcomes from Back and Will [116] and the analytical solution of the De Saint Venant's theory (DSV). For the latter, the torsional inertia of the cross-section is assumed according to the theory of the thin-walled beams [100], i.e $J = 0.032\,\mathrm{m}^4$.

Table 6.1: Free end rotation $\Theta_x = \theta_x(x = L)$ of the linear elastic channel cantilever with warping free at the fixed end.

	L1(8)	L2(20)	H1(12)	H2(36)	DSV	Back/Will
Θ_x $[10^{-2}\,\mathrm{rad}]$	17.308	4.234	1.286	2.246	4.327	4.304

Only the distribution L2(20) gives a solution agreeable to the reference ones (DSV and Back/Will), whereas the distribution L1(8) overestimates the free end rotation and the two distributions based on Hermite polynomials underestimate it. In fact, as Fig. 6.3 shows, the distribution L2(20) is able to represent the variation of the warping displacement across the thickness of the web and the flanges (Fig. 6.3*a*). As the section is very thin, this variation is practically linear, as the distribution L2(20) assumes. By contrast, the distribution L1(8) considers constant warping displacements across the thickness (Fig. 6.3*b*) and it, thus, underestimates the section rigidity. Indeed, the warping deformation of the section results almost five times larger.

A different problem occurs for the distributions H1(12) and H2(36). In fact, even though they account for higher order variations of the warping displacements across the thickness (Figs. 6.3*c* and 6.3*d*, e.g. H2(36) accounts for cubic variations), these lack in correctly representing the interaction between the web and the flanges, as it can be observed from the distribution of the material shear strains and stresses (Fig. 6.4). Indeed, the main contribution to the shear strains and stresses is represented by the derivatives along y and z of the warping displacements (Eq. (3.62)). When the section is very thin, shear strains and stresses change very fastly going from the web

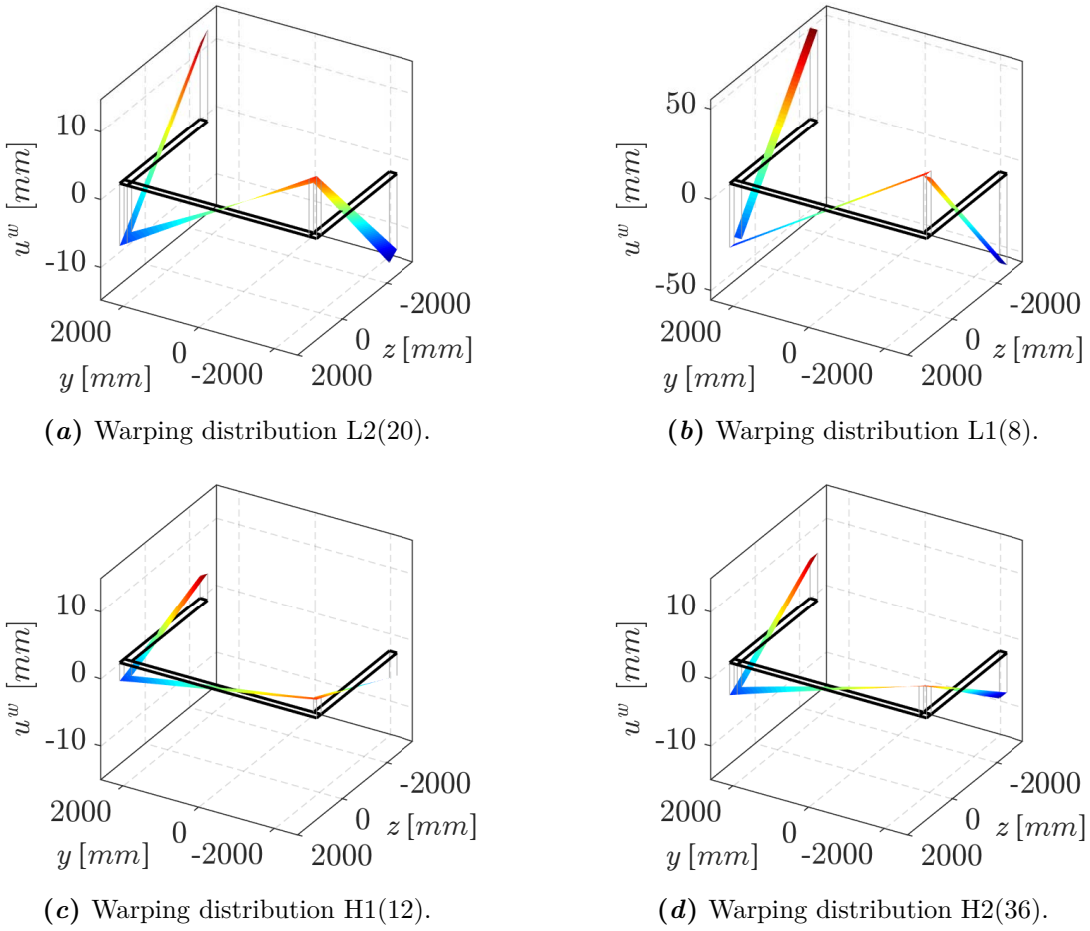

(*a*) Warping distribution L2(20).

(*b*) Warping distribution L1(8).

(*c*) Warping distribution H1(12).

(*d*) Warping distribution H2(36).

Figure 6.3: Linear elastic channel cantilever with warping free at the fixed end: warping displacement u_w of the free end cross-section.

to the flanges, or vice versa. Hence, the interpolation functions adopted to represent u_w should be able to follow these changes. Fig. 6.4 compares the shear stresses τ_{xy} and τ_{xz} for the distributions L2(20) and H1(12). L2(20) gives a solution that basically follows the shear flow due to the circulatory torsion (Figs. 6.4*a* and 6.4*b*), in perfect agreement with the classical thin-walled beam theory. Since the Lagrange interpolation (Eq. (3.65)) does not consider the warping derivatives $\partial u_w/\partial y$ and $\partial u_w/\partial z$ as DOFs, it captures the sharp variations of the shear stresses at web/flanges intersections very well, in truth providing a jump in the strain/stress distributions. On the contrary, the Hermite polynomials ensure the continuity of the warping derivatives $\partial u_w/\partial y$ and $\partial u_w/\partial z$, and, thus, they represent the shear strains (and the stresses for linear elastic materials) as continuous. In this way, when the section is very thin, the Hermite polynomials are not able to represent correctly the variation of these variables at the web/flanges intersection (Figs. 6.4*c* and 6.4*d*), influencing the response of the entire section and in general overestimating its rigidity.

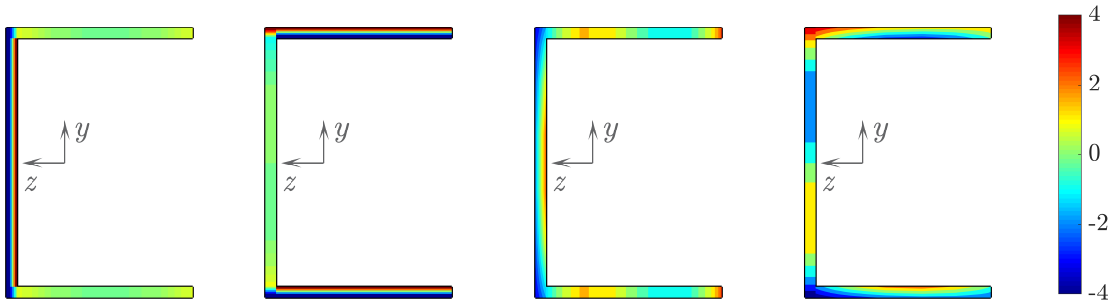

(*a*) L2(20) - τ_{xy} **(*b*)** L2(20) - τ_{xz} **(*c*)** H1(12) - τ_{xy} **(*d*)** H1(12) - τ_{xz}

Figure 6.4: Linear elastic channel cantilever with warping free at the fixed end: shear stresses τ_{xy} and τ_{xz} of the free end cross-section.

However, when the section is thicker, the Hermite interpolation results as the best balance between accuracy of the solution and computational effort. In fact, in this case, the effect described above is significantly reduced and the results provided are as accurate as those obtained with the Lagrange interpolation, but involving a lower number of warping DOFs. As an example, Fig. 6.5 illustrates the same results in Tab. 6.1 for different values of the cross-section thickness t and shows that, as the thickness increases, the difference in the solution between H1(12) and H2(36) with respect to L2(20) and DSV is significantly reduced.

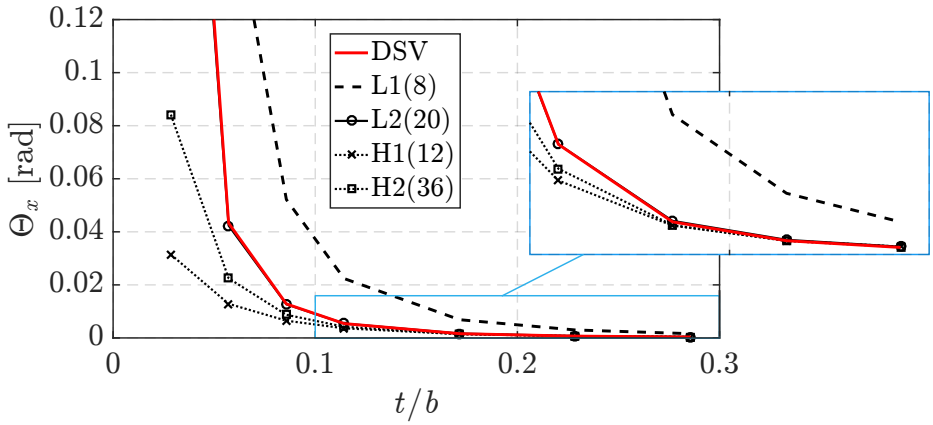

Figure 6.5: Free end rotation $\Theta_x = \theta_x(x = L)$ of the linear elastic channel cantilever with warping free at the fixed end, for variable cross-section thickness - $t = [0.1, 0.2, 0.3, 0.4, 0.6, 0.8, 1.0]$ m (b is the section width).

Linear elastic - Warping restrained

Basing on the outcomes of the warping free case, the linear elastic case with warping restrained at the fixed end considers only the distribution L2(20). However, four warping interpolation points are located along the axis, $n_w = 4$, that is cubic Lagrange poly-

nomials are defined to interpolate the warping displacement in this direction. Indeed, non uniform torsion is expected in this case and, thus, the variation of the cross-section rotation θ_x along the beam is monitored.

Table 6.2 compares the results of the WMF model with the numerical outcomes from Capurso [114], Tralli [115] and Back and Will [116] and with the analytical solution of the Vlasov's beam theory [100]. For the latter, the warping rigidity of the cross-section (Eq. (3.55)) is assumed equal to $\Gamma = 14.086\,\mathrm{m}^6$. The same results are summarized

Table 6.2: Torsional rotations $\theta_x(x)$ of the linear elastic channel cantilever with warping restrained at the fixed end.

	$\theta_x(x)$ $[10^{-3}\,\mathrm{rad}]$					
x [m]	L2(20)	Vlasov	Capurso	Tralli	Back/Will	Shell
3.0	0.187	0.163	0.193	0.193	0.188	0.241
6.0	0.658	0.611	0.669	0.667	0.660	0.741
9.0	1.348	1.284	1.368	1.369	1.354	1.423
12.0	2.204	2.124	2.233	2.234	2.215	2.280
15.0	3.170	3.075	3.207	3.209	3.185	3.310
18.0	4.188	4.081	4.236	4.239	4.210	4.343

in Fig. 6.6 (only the solution by Back and Will is plotted as reference), which also plots the analytical solution of the DSV theory. The solution of the WMF model, considering the warping constraints, perfectly matches with the reference ones, except for the DSV's, which obviously gives a significant stiffer response due to the absence of warping constraints. Table 6.2 and Fig. 6.6 also contain the numerical results

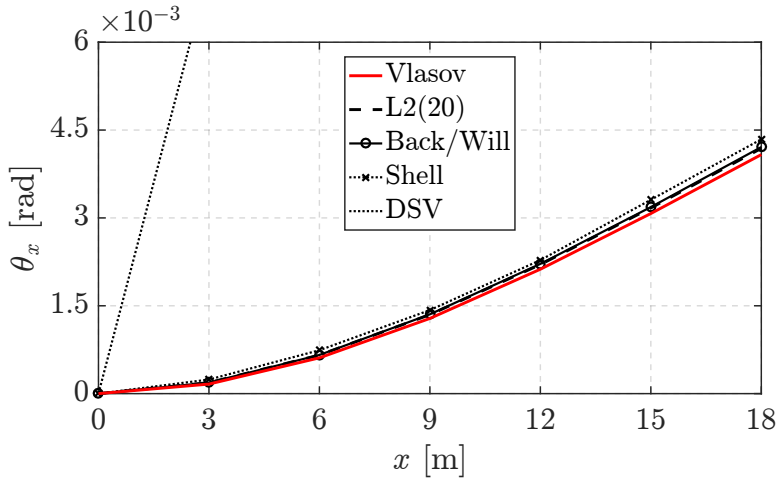

Figure 6.6: Torsional rotations $\theta_x(x)$ of the linear elastic channel cantilever with warping restrained at the fixed end.

obtained by modeling the cantilever with 2D 4-nodes shell FEs. The numerical model

is implemented in FEAP [117], and considers a total number of 5761 FEs and 37038 DOFs. Fig. 6.7 shows (a) the undeformed mesh and (b) the contour plot of the axial displacements $u(x, y, z)$ in the deformed shape of the cantilever.

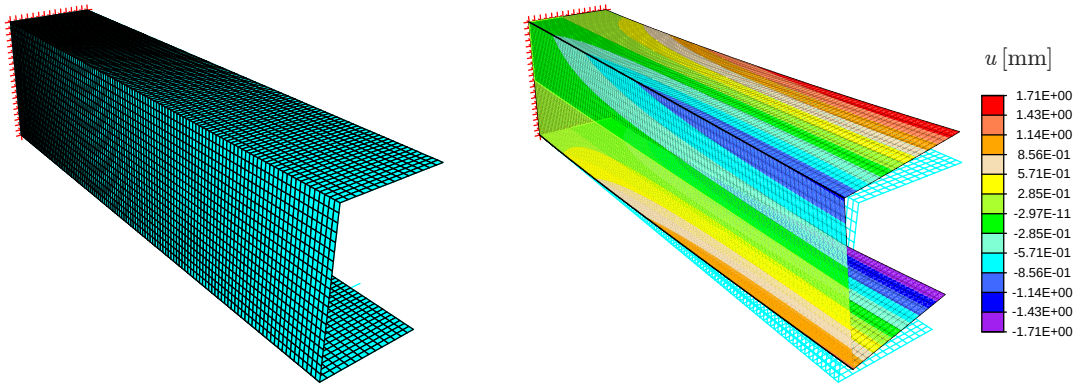

(*a*) Numerical model mesh: Web 120 × 20 FEs, Flanges 120 × 14 FEs.

(*b*) Deformed shape (displacements scaled by 40) and axial displacements $u(x, y, z)$.

Figure 6.7: Linear elastic channel cantilever with warping restrained at the fixed end: shell model.

Finally, Fig. 6.8 compares the warping displacements for the WMF beam, adopting the distribution L2(20), and those for the shell FEs, illustrating that the two numerical models perfectly agree. In particular, Fig. 6.8a shows the displacement $u(x, y, z)$ at the tip of the upper flange, at the mid-line, and Fig. 6.8b shows the deformed shape of the free end cross-section.

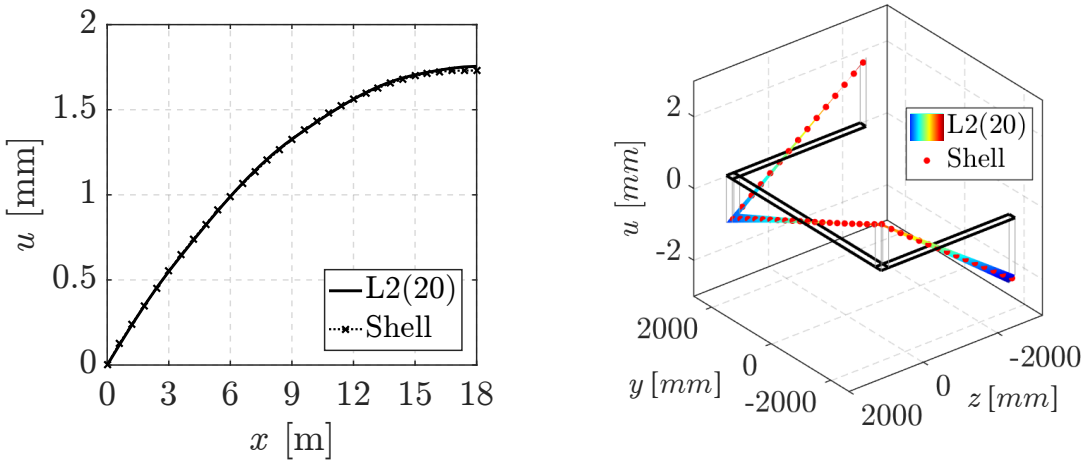

(*a*) Axial displacements of the tip of the upper flange, $u(x, 2.5\,\text{m}, -2.48\,\text{m})$.

(*b*) Axial displacements of the free end cross-section, $u(18\,\text{m}, y, z)$.

Figure 6.8: Linear elastic channel cantilever with warping restrained at the fixed end: axial displacements u obtained with the WMF and the shell model.

Elasto-plastic - Warping restrained

The elasto-plastic case with warping restrained at the free end considers the WMF model with the distribution L2(20) and four warping interpolation points along the axis, as for the corresponding elastic case. The J2 plasticity in Sec. 2.2 is adopted to model the constitutive response of the cantilever, adopting the yielding stress equal to $\sigma_y = 10\,\text{MPa}$ and the kinematic and isotropic hardening modulus equal to $H_k = 0.01\,E$ and $H_i = 0.001\,E$, respectively.

The applied torsional couple M_x is increased up to a value of 4000 kNm and the free end rotation is evaluated, comparing the results with those obtained with a shell model having the same mesh of that used for the elastic study. Fig. 6.9 plots the two global response curves (M_x vs Θ_x) and shows how the WMF beam-column FE correctly represents both the initial elastic branch and the subsequent plastic response. The solution obtained with the distribution H2(36) is also plotted, to emphasize that the issues observed for the linear elastic case with warping free also affects the case of warping restrained, for both the elastic and the plastic responses.

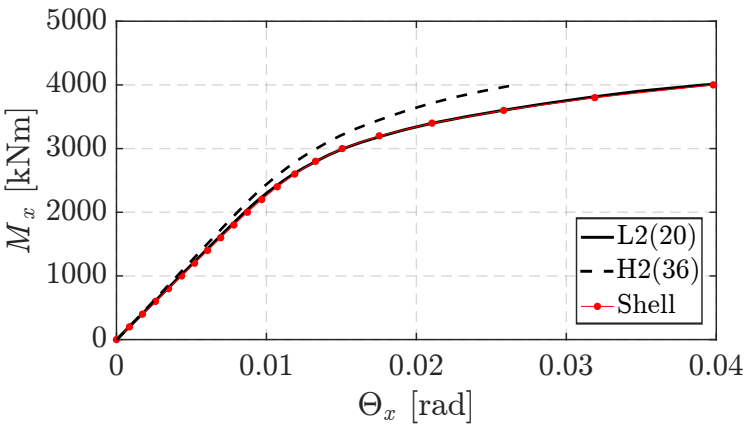

Figure 6.9: Elasto-plastic channel cantilever with warping restrained at the fixed end: applied couple M_x versus free end rotation $\Theta_x = \theta_x(x = L)$.

Finally, the local responses obtained with the WMF model, adopting the distribution L2(20), and with the shell model are compared. In particular, because of the equilibrium, during the entire loading path the cantilever is subjected to a uniform torsional moment equal to M_x. However, due to the warping constraints, the fixed end section exhibits higher levels of stresses with respect to the other beam cross-sections. Indeed, as the warping displacements $u_w(x, y, z)$ are restrained at the fixed end (Fig. 6.8*a*), the shear-lag effect occurs, influencing the axial stresses $\sigma_x(x, y, z)$ along the entire beam. These stresses assume the highest values at $x = 0$, where the plastic strains take place by first. Fig. 6.10 compares the axial stresses $\sigma_x(x, y, z)$ for the WMF and the shell models at this cross-section, for two different values of the applied

torsional couple: (*a*) $M_x = 1000\,\text{kNm}$, for which the cantilever still results elastic (it is the same load applied in the linear elastic study), and (*b*) $M_x = 4000\,\text{kNm}$, for which the cantilever presents plastic deformations. Very good agreement between the two models is shown in both conditions.

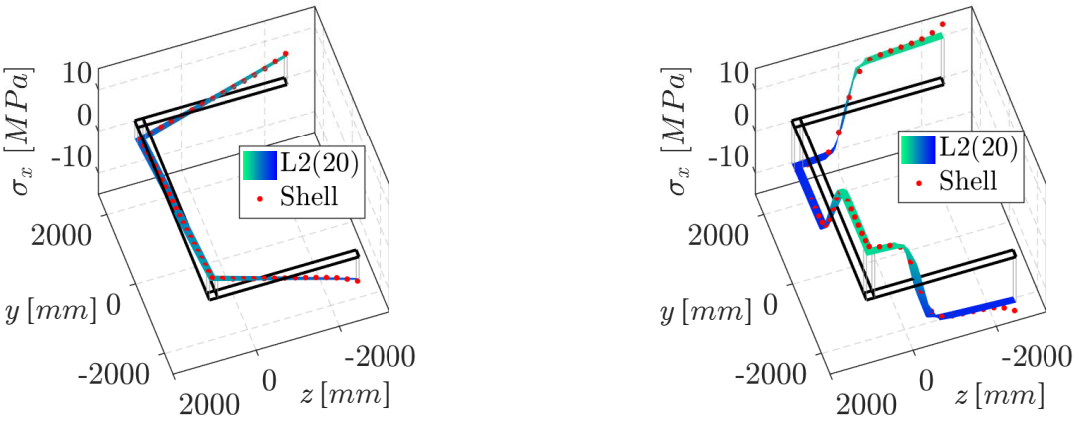

(***a***) Elastic - $M_x = 1000\,\text{kNm}$.

(***b***) Plastic - $M_x = 4000\,\text{kNm}$.

Figure 6.10: Elasto-plastic channel cantilever with warping restrained at the fixed end: axial stresses σ_x due to the shear-lag at the free end cross-section.

6.2.2 Steel shear link subjected to a transversal cyclic load

The second correlation study investigates the response of a steel shear link with I cross-section and subjected to transversal cyclic deformations. Le Corvec [1] has also analyzed this specimen to investigate the performance of the WMF beam-column FE, originally proposed in her work. Le Corvec interpolates the warping displacements with Lagrange polynomials both along the element axis and over the element cross-sections. Comparing the results with the experimental studies by Hjelmstad and Popov [118], she demonstrates the good capability of the model in representing both the global and the local responses of the link. The following study, instead, adopts Hermite polynomials for the warping interpolation over the element cross-section. The goal is to understand whether, in the case of shear forces, the Hermite interpolation leads to the same issues observed during the analysis of the channel cantilever in Sec. 6.2.1, in the case of torsion.

Fig. 6.11 shows the specimen geometry. The link is considered as fixed at one end and subjected to a cyclic transversal displacement v at the other. Following the study in [1], the material behavior is described through a generalized J2 plasticity model [119], adopting the parameters in Table 6.3. For both the web and the flanges the Poisson ratio is equal to $\nu = 0.3$ and the isotropic and the kinematic hardening are

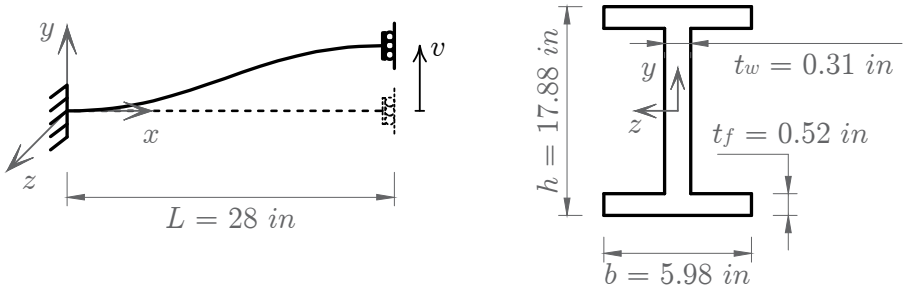

Figure 6.11: Shear link subjected to a transversal cyclic load: specimen geometry.

equal to $H_i = 0.0002\,E$ and $H_k = 0.0040\,E$, respectively. Moreover, the distance from the asymptotic yield surface to the yield function is equal to $\phi = f_u - f_y$, whereas the speed of the model in approaching the asymptotic behavior is equal to $\delta = 0.01\frac{f_y}{\phi}E$ [51].

Table 6.3: Mechanical parameters adopted for the steel shear link with I cross-section.

	Young modulus E	Yield strength f_y	Ultimate strength f_u
Web	28 300 ksi	39.5 ksi	60.1 ksi
Flanges	28 000 ksi	35.0 ksi	58.5 ksi

The numerical model consists of one WMF beam-column FE, with six Gauss-Lobatto quadrature cross-sections placed along the axis and a midpoint fiber discretization with a total of 34 fibers, that is 10 fibers along the web and a grid of 3×4 fibers in each flange (Fig. 6.12*a*). To interpolate the warping displacement field u_w over the cross-section, the model uses two distributions of warping points as in Figs. 6.12*b* and 6.12*c*. L(12) adopts Lagrange polynomials, with constant interpolation across the section thickness, parabolic interpolation along the flanges and cubic along the web; H(18) adopts Hermite polynomials, with linear interpolation across the section thickness and cubic interpolation along both the flanges and the web. The warping displacements

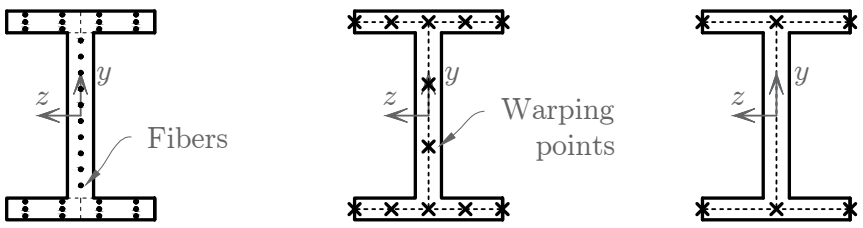

(*a*) Fiber model (*b*) Warping distr. L(12) (*c*) Warping distr. H(18)

Figure 6.12: Fiber model discretization and warping points distribution over the cross-section of the shear link.

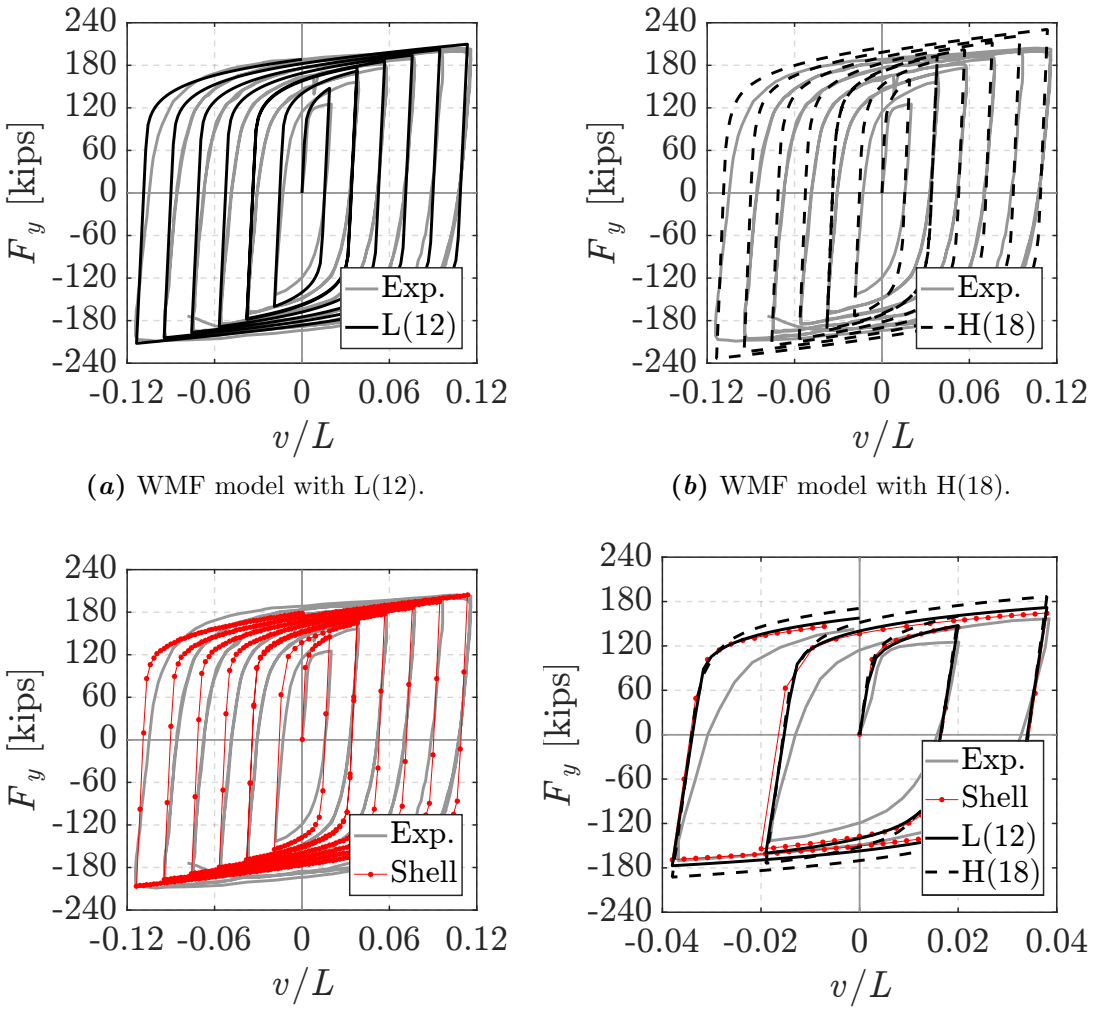

(***a***) WMF model with L(12).

(***b***) WMF model with H(18).

(***c***) Shell model.

(***d***) Comparison for the first cycles.

Figure 6.13: Shear link subjected to a transversal cyclic load: transversal force F_y versus shear drift v/L

are assumed as restrained at both the beam ends. Hence, four warping interpolation points are located along the axis, $n_w = 4$, that is cubic Lagrange polynomials are defined for the interpolation in this direction.

Fig. 6.13 shows the global responses obtained with the WMF model (black lines) and compares them with the experimental results (gray lines) in terms of transversal force F_y vs the shear drift v/L. In addition, a model implemented in FEAP [117] with 2D 4-nodes shell FEs is considered. This uses a total number of 480 FEs and 3402 DOFs, defining the mesh in Fig. 6.14. This figure also shows the contour plot of the axial displacements $u(x, y, z)$ at the end of the first loading ramp (before the first loading reversal), that is at $v/L = 0.02$. These displacements are zero at the element ends and assume the maximum values at the mid-span.

As Fig. 6.13 shows, the results for the WMF model with L(12), i.e. adopting

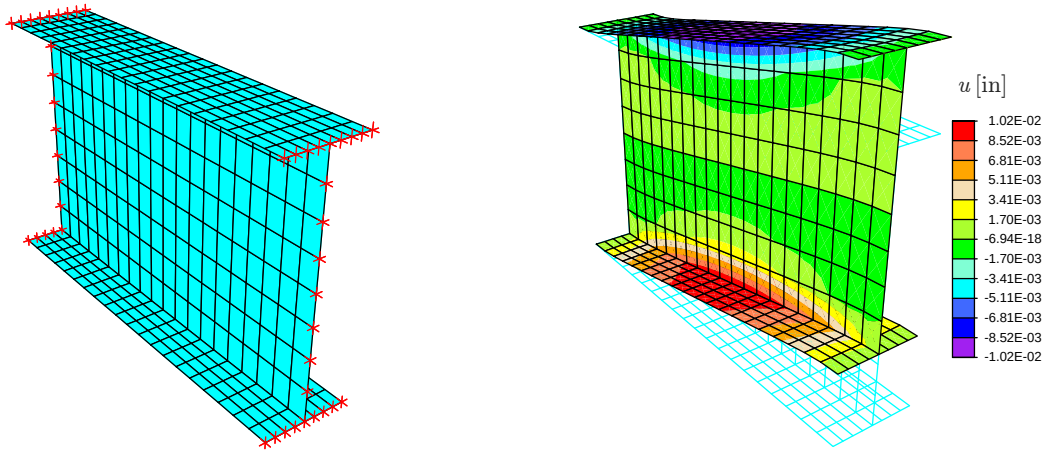

(*a*) Numerical model mesh: Web 20×8 FEs, Flanges 20 × 8 FEs.

(*b*) Deformed shape (displacements scaled by 10) and axial displacements $u(x, y, z)$.

Figure 6.14: Shear link subjected to a transversal cyclic load: shell model.

Lagrange polynomials, perfectly agree with the experimental data and the results of the shell model. By contrast, the WMF with the distribution H(18) slightly overestimates the beam strength. As observed in the study of the channel cantilever in Sec. 6.2.1, the Hermite interpolation gives a poor representation of the warping at the web/flanges intersections. Fig. 6.15 shows the distribution of the shear stresses τ_{xy} and τ_{xz} for the mid-span cross-section at the first loading step, when the link still behaves as elastic. Accordingly to the Jourawsky's theory for elastic thin-walled beams [120], the solution for the distribution L(12) considers τ_{xz} as linear in the flanges, where τ_{xy} is zero, and τ_{xy} as parabolic in the web, where τ_{xz} is zero. This solution perfectly matches the results obtained with the shell model. On the contrary, the solution for the distribution H(18) does not represent correctly the transition of the shear stress flux from the flanges to the web, although it captures the shear stresses across the thickness.

As discussed in Sec. 6.2.1, this issue with the Hermite interpolation only occurs for very thin sections. As use the goal of this work is the analysis of RC structures, where the thickness of the element cross-sections is usually high, the following studies still consider the Hermite polynomials for the warping interpolation and investigate the advantage they offer in the case of thicker cross-section beams.

6.3 RC beams under to monotonic torsional loads

This section presents the analyses of a series of prismatic beams under torsional loads. In particular, two different studies are performed. The first one analyzes three PC and three RC beams with either rectangular or T-shaped cross-section. The beams are

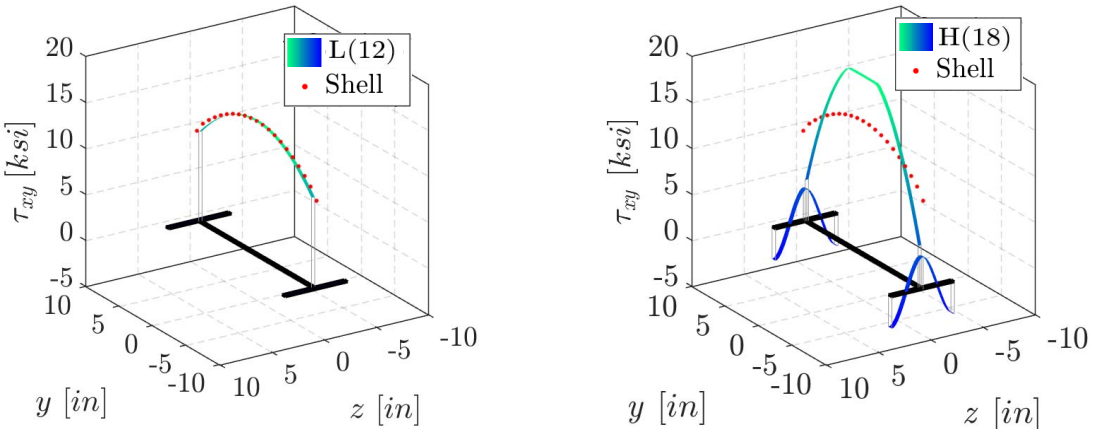

(a) Lagrange L(12): $\tau_{xy}(14\,\text{in}, y, z)$.

(b) Hermite H(18): $\tau_{xy}(14\,\text{in}, y, z)$.

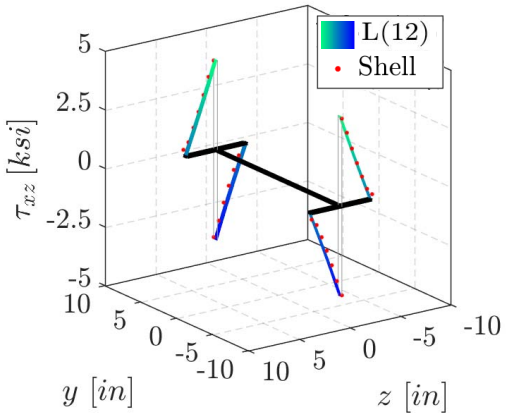

(c) Lagrange L(12): $\tau_{xz}(14\,\text{in}, y, z)$.

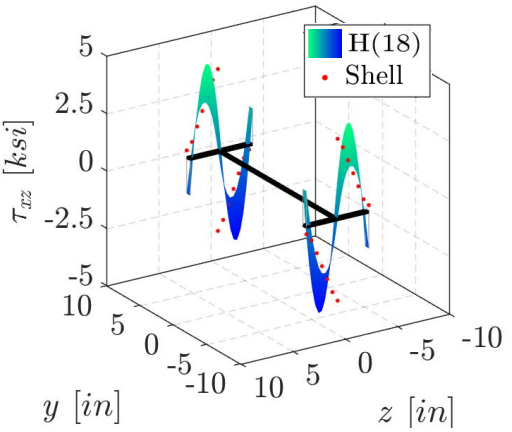

(d) Hermite H(18): $\tau_{xz}(14\,\text{in}, y, z)$.

Figure 6.15: Shear link subjected to a transversal cyclic load: shear stresses of the mid-span cross-section at the first elastic loading step $v/L = 0.0015$.

subjected to a monotonically increasing torsional couple applied at both the ends. The cross-section warping displacements are assumed to be free, producing uniform warping along the entire element length. Hence, the study investigates the performance of the WMF in representing the effects of the warping and its coupling with the damaging phenomena occurring in the specimens.

The second study analyzes a U-shaped RC beam. The specimen is fixed at both the ends, where the warping displacements are prevent, and a torsional couple acts at the mid-span. The influence of the warping constraints is, thus, discussed, focusing the attention on the shear-lag effect.

The 3D plastic-damage material model proposed in Sec. 2.4 describes the concrete constitutive behavior. Hence, the studies also aim to investigate the performances of this model in representing the concrete response under relevant shear stresses. The classical J2 plasticity in Sec. 2.2 describes the behavior of the steel bars.

6.3.1 Prismatic beams under uniform warping

The following correlation studies analyze six prismatic beams under pure torsion. All the specimens have a total length of 160 cm and are divided into three parts: two end parts of length L_e, reinforced so as to remain elastic, and a middle part of length L undergoing cracking and damage (Fig. 6.16). A torsional couple M_x is applied

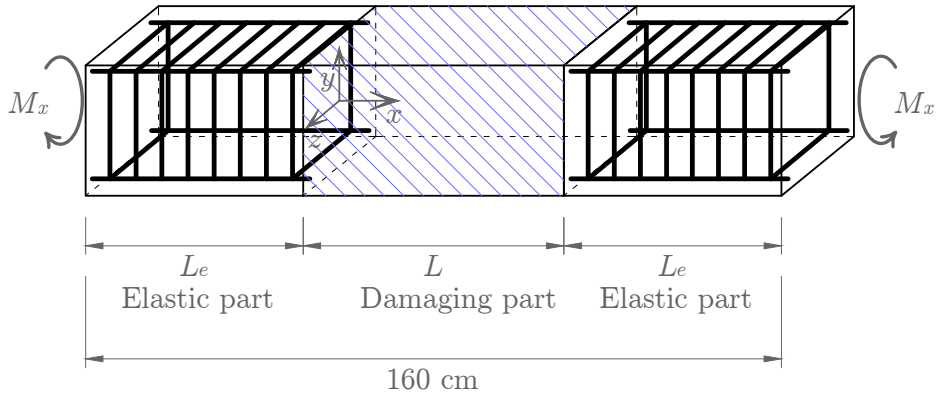

Figure 6.16: Beams subjected to end torsional loads: specimens geometry.

at both ends with a particular arrangement that allows the beam cross-sections to undergo warping. The PC and the RC cross-sections in Fig. 6.17 are considered for the central damaging part of the beam, following the experimental tests performed in [121] and [122]. The geometrical parameters are: $L = 60$ cm for the R(a), Rh(a) and Ts ($L_e = 50$ cm) and $L = 100$ cm for the Ra-c, Rb-c and T-c ($L_e = 30$ cm). Only the middle part is modeled in the numerical analysis, using one FE with one warping interpolation point located along the axis, $n_w = 1$, as a uniform warping distribution is expected in this direction. Three Gauss-Lobatto quadrature points are used for the integration along the FE with a midpoint fiber discretization made of 72 fibers for the rectangular cross-sections and 85 fibers for the T-shaped ones (Fig. 6.18). The reinforcing bars are treated as additional steel fibers.

Table 6.4: Mechanical parameters adopted for the beams subjected to end torsional loads.

	E [MPa]	σ_t [MPa]	Y_{0t} [10^{-5}]	k_t [10^{-4}]	a_t
R(a)	20 000	12.0	6.48	3.0	0.50
Rh(a)	20 000	12.0	1.19	2.0	0.50
Ts	25 000	18.0	5.18	2.6	0.55
Ra-c	20 000	12.0	9.72	2.4	0.80
Rb-c	20 000	12.0	5.40	2.5	1.00
T-c	30 000	21.0	7.20	1.0	1.00

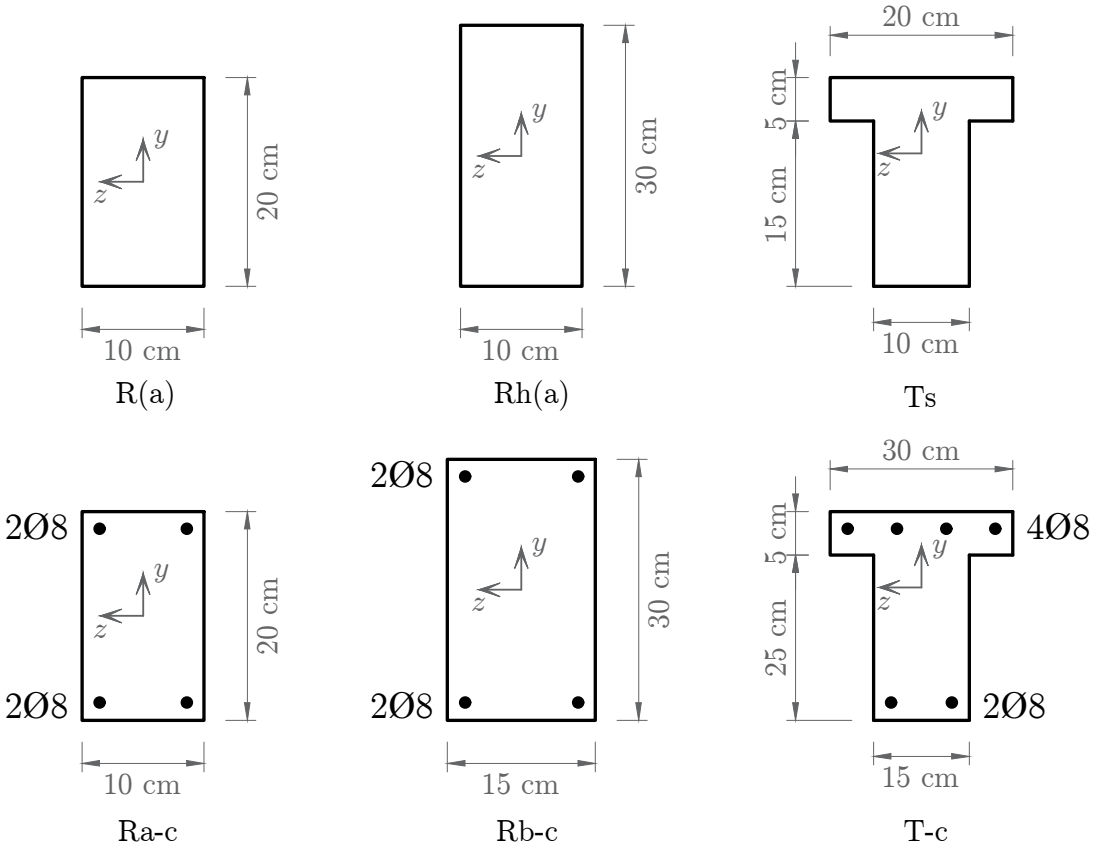

Figure 6.17: Beams subjected to end torsional loads: cross-sections dimensions.

(*a*) Rectangular. **(*b*)** T-shaped.

Figure 6.18: Beams subjected to end torsional loads: fiber model discretization.

Each specimens consider a different concrete mixture. Hence, a specific set of material parameters is defined for each numerical model, as given in Table 6.4, with $\nu = 0.2$, $\sigma_c = 30.0\,\text{MPa}$, $H_i = 0.001\,E$, $H_k = 0.7\,E$, $Y_{0c} = 5\,Y_{0t}$, $k_c = 5.0 \cdot 10^{-3}$, $a_c = 0.2$ and $\beta = 1.0$ for all of them. Modulus E is not specified in the two reference papers, thus, it is adjusted to reproduce the measured initial stiffness. As an example, Fig. 6.19 represents the concrete stress-strain relation for the Ra-c beam and the relative damage evolution law, in the case of uni-axial tension and compression. For the steel bars, the following material parameters are used: $E = 210\,000\,\text{MPa}$, $\nu = 0.3$, $\sigma_y = 560.0\,\text{MPa}$,

$H_i = 0.001\,E$ and $H_k = 0.01\,E$.

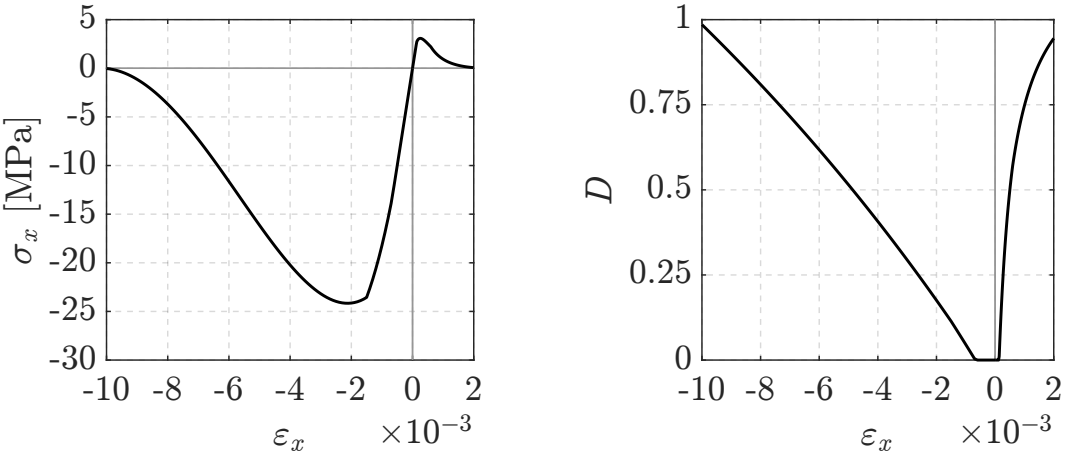

(*a*) Uni-axial stress-strain relation. **(*b*)** Damage evolution.

Figure 6.19: Monotonic uni-axial ($\sigma_x - \varepsilon_x$) behavior in tension and compression for the proposed damage model adopted for the Ra-c beam.

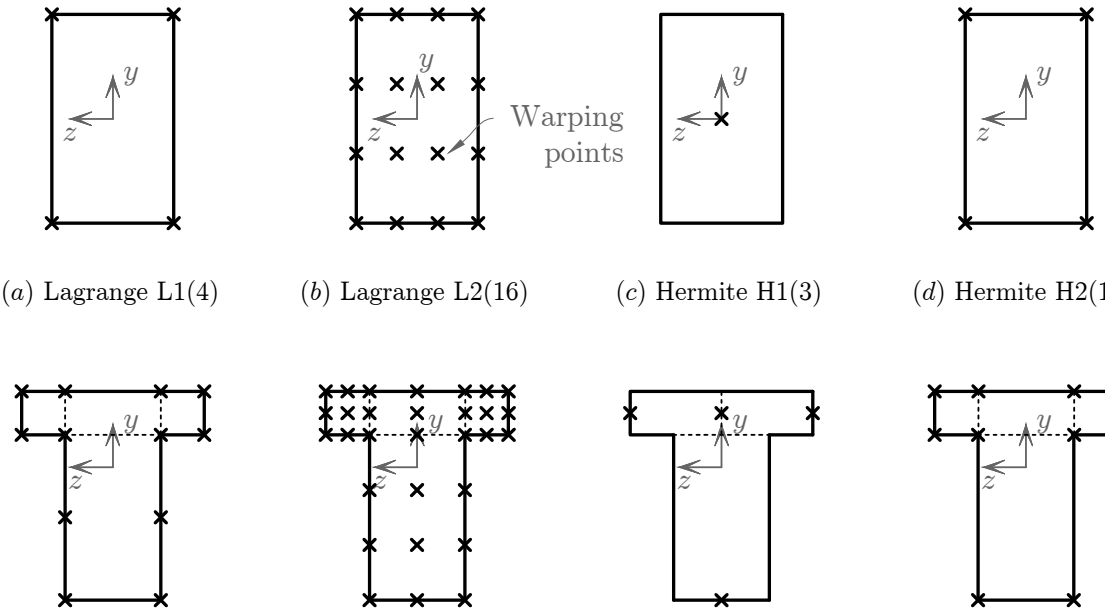

(*a*) Lagrange L1(4) (*b*) Lagrange L2(16) (*c*) Hermite H1(3) (*d*) Hermite H2(12)

(*e*) Lagrange L1(12) (*f*) Lagrange L2(30) (*g*) Hermite H1(12) (*h*) Hermite H2(30)

Figure 6.20: Warping points distribution over the cross-section of the beams subjected to end torsional loads.

The rectangular cross-sections consider the four different warping DOFs distributions in Figs. 6.20*a* - 6.20*d*. L1(4) and L2(16) adopt Lagrange polynomials and H1(3)

and H2(12) adopt Hermite polynomials. L1(4) and H1(3) provide a linear interpolation of u_w in both the y and z directions, whereas L2(16) and H2(12) provide a cubic interpolation. Similarly, the T-Shaped cross-sections consider the four warping DOFs

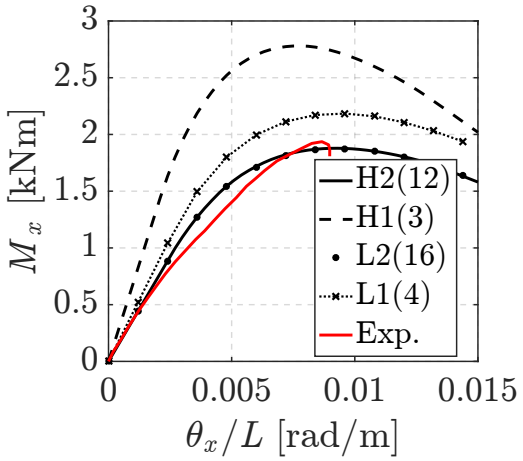

(*a*) R(a) - Different warping distributions.

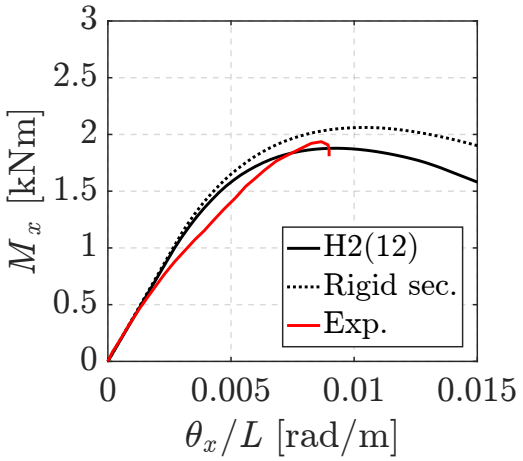

(*b*) R(a) - Numerical vs experimental.

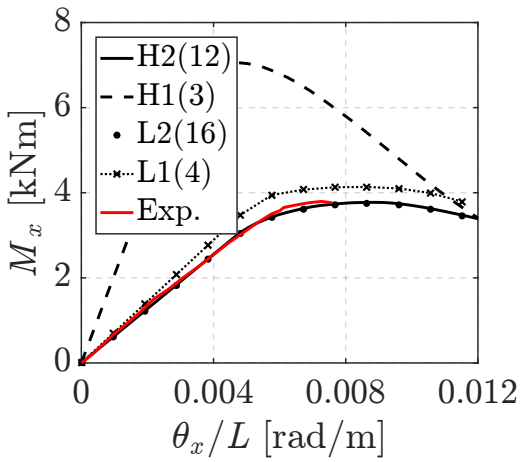

(*c*) Rh(a) - Different warping distributions.

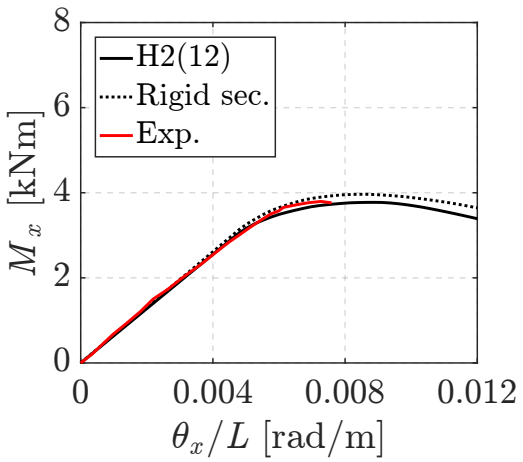

(*d*) Rh(a) - Numerical vs experimental.

Figure 6.21: Response of the rectangular PC beams, R(a) and Rh(a): moment vs rotation per unit length.

distributions in Figs. 6.20*e* - 6.20*h*, L1(12) and L2(30) adopting Lagrange polynomials and H1(12) and H2(30) adopting Hermite polynomials. L1(12) and H1(12) provide a linear interpolation of u_w in both the y and z directions, except for y direction in the cross-section web, where they provide a parabolic and a cubic interpolation, respectively. Finally, L2(30) and H2(30) provide a parabolic and a cubic interpolation, respectively, in both the y and z direction (for L2(30) this is cubic only for the y direction in the web).

Figs. 6.21*a* and 6.21*c* compare the global response of the two PC rectangular beams, R(a) and Rh(a), for the four warping distributions; the experimental results are de-

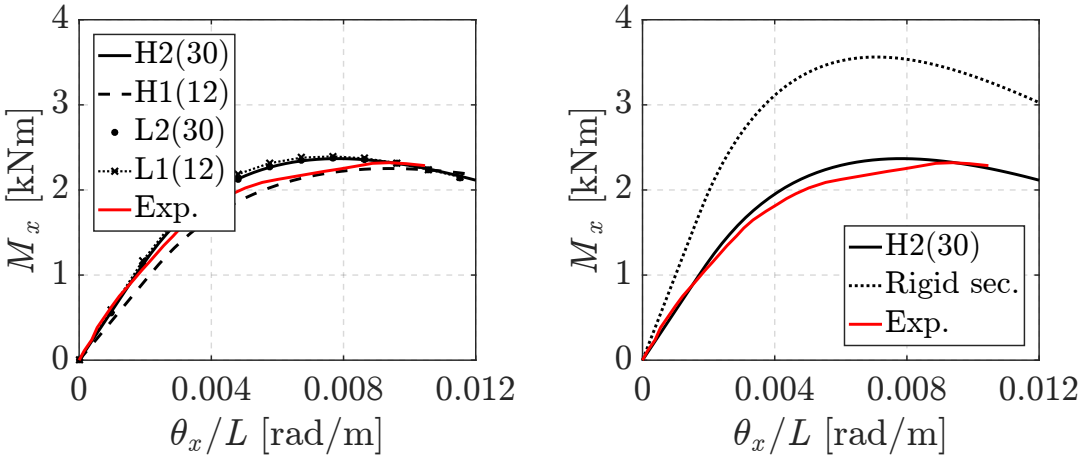

(*a*) Different warping distributions. **(*b*)** Numerical vs experimental.

Figure 6.22: Response of the T-shaped PC beam, Ts: moment vs rotation per unit length.

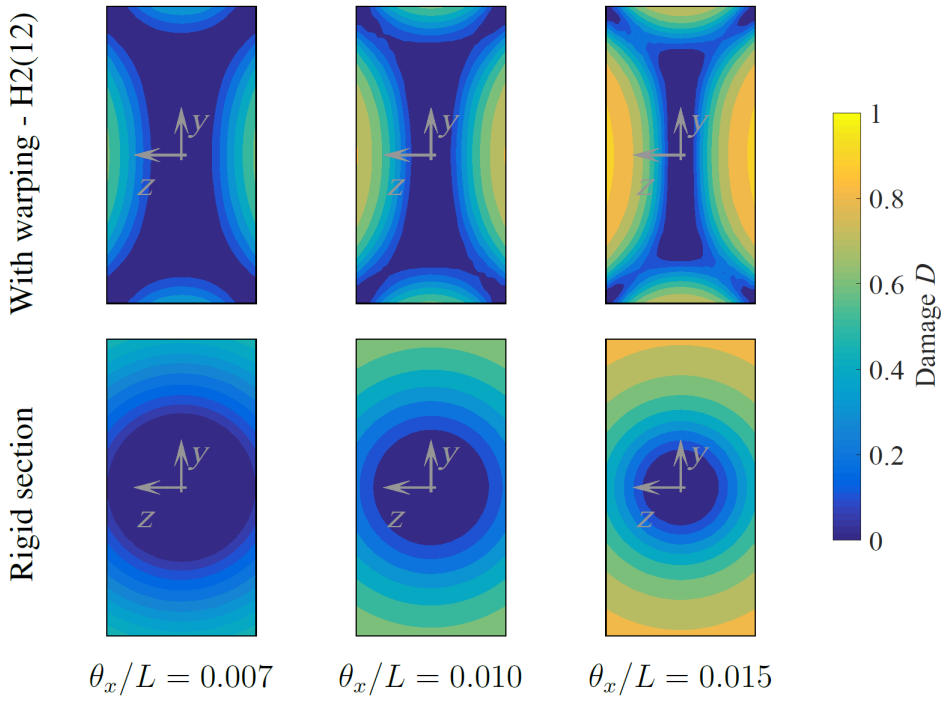

Figure 6.23: Evolution of the damage over the PC rectangular cross-section R(a) with and without warping.

noted in red. As shown, the distributions L2(16) and H2(12) give the same solution, which perfectly matches the experimental curves. Indeed, these both consider cubic order for the interpolation functions, which suffice in representing the warping of the beam cross-sections. However, the Hermite interpolation requires less warping DOFs than the Lagrange one. By contrast, the distributions L1(4) and H1(3), considering linear interpolation functions, overestimate the beams strength, because they fail in

representing the interaction between the warping deformations and the damaging effects taking place during the loading process. The same occurs for the PC T-shaped beam Ts, whose results are plotted in Fig. 6.22*a*. In this case, the distribution H2(30) gives the best solution of the set, since it adopts cubic interpolation functions in the y and z directions. The distribution L2(30) uses the same number of warping DOFs and, although it provides parabolic interpolation functions, it gives a solution that agrees very well with H2(30). The distribution L1(12), with linear interpolation functions, slightly overestimates the element strength, yet requiring a significantly smaller number of warping DOFs. Finally, the distribution H1(12), which uses the same number of warping DOFs of L1(12) with linear interpolation functions, slightly underestimates both the stiffness and the strength of the element. These results lead to the conclusion that Hermite polynomials are a better choice than Lagrange ones to interpolate the warping displacements of these cross-sections. In fact, they give satisfactory solutions, providing higher order interpolations with a smaller number of warping DOFs.

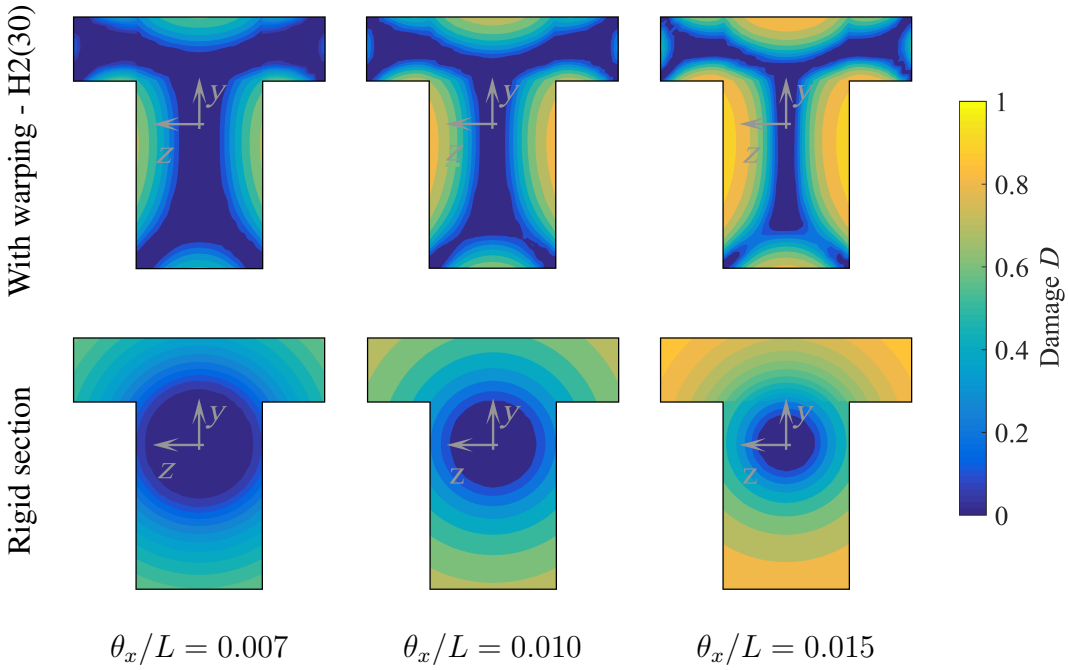

Figure 6.24: Evolution of the damage over the PC T-shaped cross-section Ts with and without warping.

Figs. 6.21*b*, 6.21*d* and 6.22*b* compare the results for the distribution H2(12) (rectangular beams) and H2(30) (T-shaped beam) with the experimental outcomes in [121] and with the analytical results reported in the same paper under the assumption of rigid cross-section. This last adopts a value of the polar moment of area based on the semi-analytical solution with Fourier series, that is $J = \alpha h b^3$ for the rectangular beams and $J = 6774\,\mathrm{cm}^4$ for the T-shaped beam. For the rectangular beams, b and h are the

cross-section width and depth, respectively, and $\alpha = 0.2291$ for the R(a) section and $\alpha = 0.2635$ for the Rh(a) sections. The figures show that the rigid section assumption

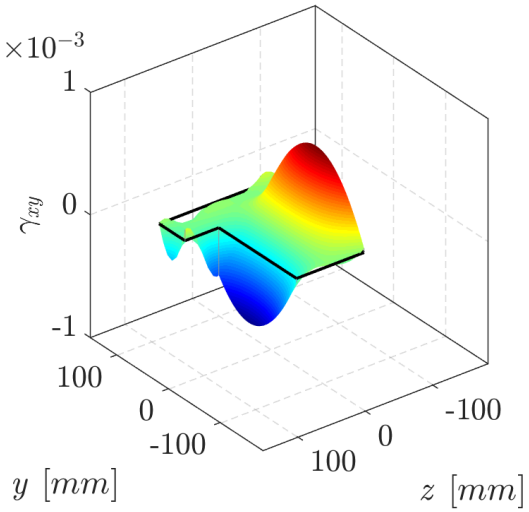

(*a*) WMF model with H2(30): $\gamma_{xy}(x, y, z)$.

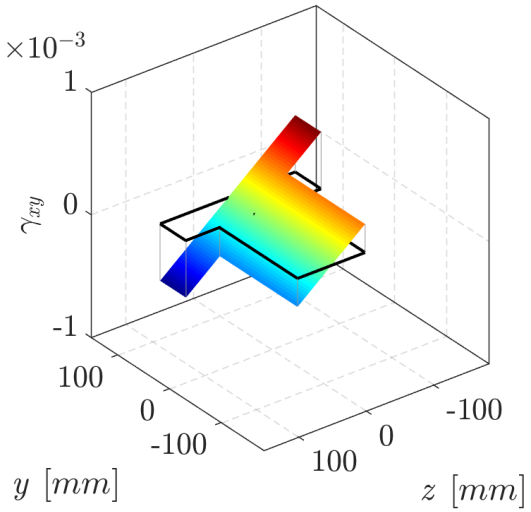

(*b*) Rigid section model: $\gamma_{xy}(x, y, z)$.

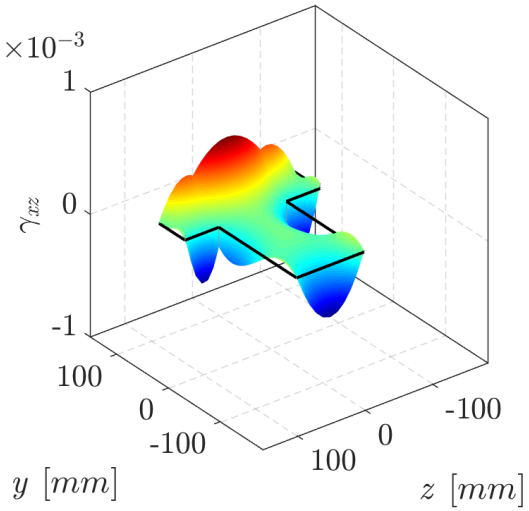

(*c*) WMF model with H2(30): $\gamma_{xz}(x, y, z)$.

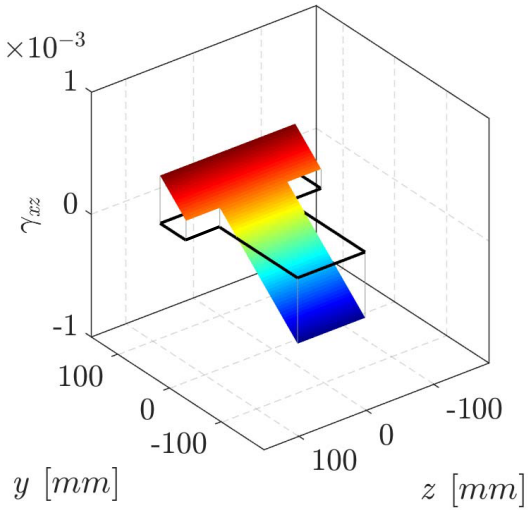

(*d*) Rigid section model: $\gamma_{xz}(x, y, z)$.

Figure 6.25: Shear strains in the plain concrete T-shaped beam (Ts) at $\theta_x/L = 0.007$.

overestimates the peak load, since the damage distribution over the cross-section is not captured correctly. This assumption has small influence on the global response of the rectangular beams, whereas it significantly affects that of the T-shaped one. However, in all cases it produces completely wrong results in terms of local responses, that is it does not correctly represent the material state evolution during the loading path. For instance, Figs. 6.23 and 6.24 show the distribution of damage variable D for the R(a) and the Ts beam, respectively, at three different values of the normalized torsional rotation. As shown, for the rigid section assumption, the damage distribution is similar to that of a circular section, where warping is not possible. Instead, in the presence of

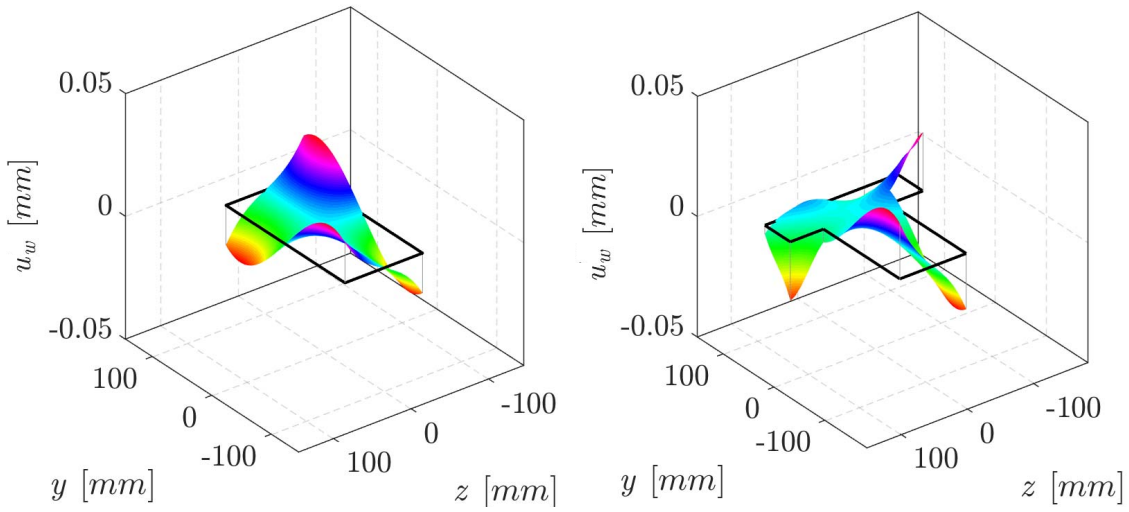

(*a*) Section R(a) with H2(12) at $\theta_x/L = 0.010$. **(*b*)** Section Ts with H2(30) at $\theta_x/L = 0.007$.

Figure 6.26: Warping displacement in the PC beam subjected to end torsional loads.

warping, the damage distribution is much more diffused over the whole cross-section. Indeed, in a prismatic beam under pure uniform torsion, the damage distribution over the element cross-sections follows the distribution of the shear strains. Fig. 6.25 shows γ_{xy} and γ_{xz} distributions for the T-shaped beam. Note that the section warping with H2(30) gives rise to parabolic shear strains γ_{xy} and γ_{xz} over the section. In contrast, the rigid section assumption is associated with a linear variation of these strains in the y and z directions (Eq. (3.11)). The same occurs for the rectangular beams [80, 123]. Fig. 6.26 shows the deformed shapes of the element cross-sections due to the warping for both R(a) and Ts beams.

Similar observations hold for the RC beams, whose global responses are shown in Fig. 6.27. The responses under the assumption of rigid cross-section are computed adopting a value of the polar moment of area based on the semi-analytical solution with Fourier series, that is $J = \alpha h b^3$ with $\alpha = 0.2291$ for the rectangular beams and $J = 32642\,\mathrm{cm}^4$ for the T-shaped beam. The responses of the plain concrete beam is superimposed on the same figures for comparison. These are obtained by the WMF beam model, adopting H2(12) for the rectangular beams and H2(30) for the T-shaped beam. The comparisons show that the reinforcing bars slightly increase the member strength under high values of torsional deformation, when the concrete is completely damaged. The experimental responses show greater strength under intermediate deformations, as the beam transitions from the uncracked to the fully cracked state, but this transitory behavior due to rough cracks and dowel action is not accounted for in the present numerical model.

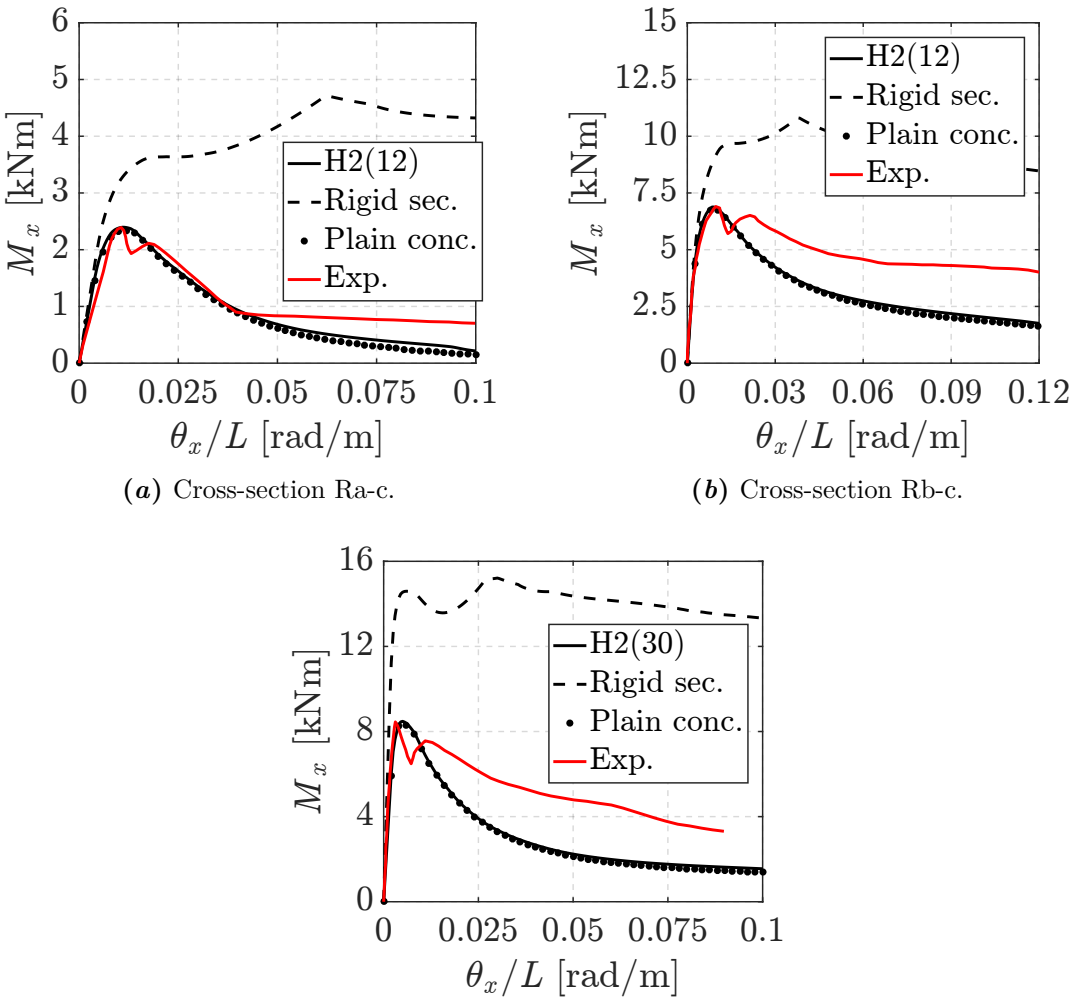

(*a*) Cross-section Ra-c.

(*b*) Cross-section Rb-c.

(*c*) Cross-section T-c.

Figure 6.27: Response of the RC beams subjected to end torsional loads: moment vs rotation per unit length.

6.3.2 U-shaped beam with warping constraints

The following correlation study analyzes the RC U-shaped beam in Fig. 6.28, experimentally tested by Chen et al. [124]. The specimen is subjected to a monotonically increasing torsional couple applied at the mid-span section, where a strengthened diaphragm plate is located. Both the ends are extended by two rectangular slabs to ensure the fully restrained boundary conditions at the supports. Because of the symmetry, the numerical model considers only one half of the beam, adopting one WMF beam-column FE. The diaphragm plate is considered as rigid and able to totally prevent the warping displacements at the beam mid-span. The warping displacements are fully restrained at the support sections, as well. Eleven quadrature points and four warping interpolation points, $n_w = 4$, are located along the FE axis, that is

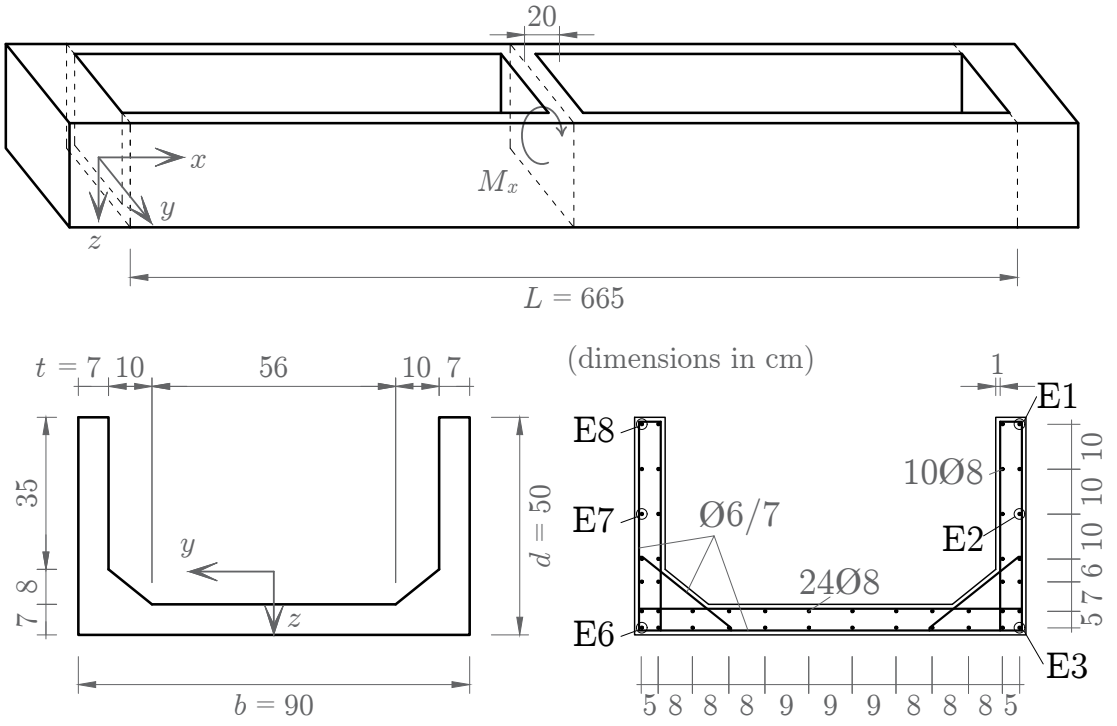

Figure 6.28: RC U-shaped beam under torsional loads: specimen geometry.

cubic interpolation functions, since the warping restraints give non-uniform warping in this direction; the locations of both the quadrature and warping points follow the Gauss-Lobatto integration rule scheme.

Unlike the beams analyzed in Sec. 6.3.1, this is subjected to non-uniform torsion, because of the warping variability along the x direction, which leads to non-uniform degrading phenomena along the element axis. Hence, the nonlocal regularization technique in Sec. 4.3 is adopted to prevent the damage localization and a characteristic length $L_c = 150\,\text{cm}$ is considered to evaluate the nonlocal variables as in Eqs. (4.9) and (4.10).

Fig. 6.29 shows (a) the fiber discretization of the cross-section, where the midpoint rule is used, and (b, c, d) three distributions of warping DOFs. All of them consider a cubic interpolation of the warping displacements along the web, whereas the interpolation along the flanges is parabolic in (b, c) L1(8) and L2(20) and is cubic in (d) H1(12); (b) L1(8) considers the warping displacements as constant across the thickness, whereas both (c, d) L2(20) and H1(12) provide a linear interpolation. The chamfer added at the connection between the flanges and the web is not considered in the model.

The material parameters in Table 6.5 govern the behavior of each concrete fiber, with Fig. 6.30 representing the corresponding uni-axial stress-strain relation and the damage evolution law. While, $E = 210\,000\,\text{MPa}$, $\nu = 0.3$ and $\sigma_y = 380\,\text{MPa}$ is assumed

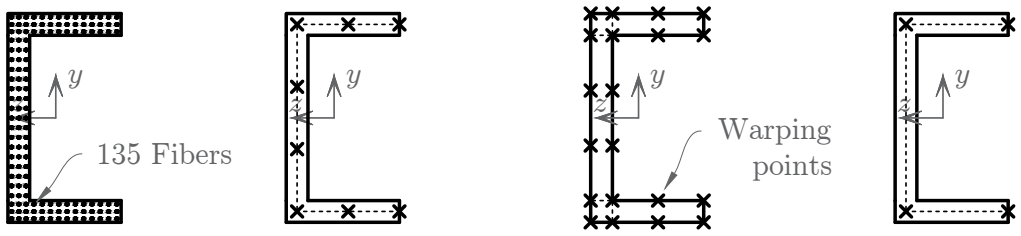

(*a*) Fiber model (*b*) Warp. distr. L1(8) (*c*) Warp. distr. L2(20) (*d*) Warp. distr. H1(12)

Figure 6.29: Fiber model discretization and warping points distribution over the cross-section of the U-shaped beam under torsion.

for the steel bars, with $H_i = 0.01\,E_s$ for the isotropic hardening and $H_k = 0.05\,E_s$ for the kinematic one.

Table 6.5: Mechanical parameters adopted for the U-shaped beam under torsional loads.

$E = 35\,000\,\text{MPa}$	$\nu = 0.2$		
$\sigma_t = 6.3\,\text{MPa}$	$\sigma_c = 40.0\,\text{MPa}$	$H_i = 0.001\,E$	$H_k = 0.700\,E$
$Y_{0t} = 7.64 \cdot 10^{-5}$	$k_t = 8.0 \cdot 10^{-5}$	$a_t = 0.95$	
$Y_{0c} = 3.53 \cdot 10^{-4}$	$k_c = 6.0 \cdot 10^{-3}$	$a_c = 0.77$	$\beta = 1.0$

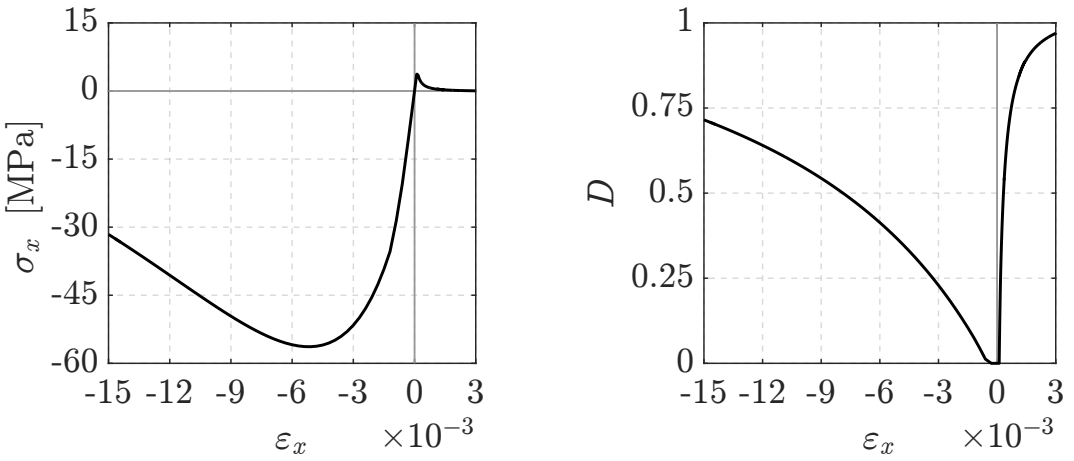

(***a***) Uni-axial stress-strain relation. (***b***) Damage evolution.

Figure 6.30: Monotonic uni-axial ($\sigma_x - \varepsilon_x$) behavior in tension and compression for the proposed damage model adopted for the U-shaped beam under torsion.

Fig. 6.31 shows the global response in terms of the section rotation θ_x vs the applied torsional couple M_x, obtained with different models and compared with the experimental outcomes (gray line with dots): the WMF model adopting the warping distributions L1(8) (dashed line), L2(20) (solid line) and H1(12) (solid line with dots)

and considering the warping constraints; the WMF model adopting the warping distribution H1(12), but assuming all the cross-sections free to warp (dotted line); standard TFF beam-column FE (Sec. 3.2), assuming a rigid section model (line with crosses). In the standard FE model, to simulate the warping constraints, the torsional inertia J at the supports and at the mid-span section is assumed equal to the polar moment of inertia, whereas in the other quadrature sections it is corrected accordingly to the classical thin-walled beam theory, i.e. $J = 1/3 \sum a\, b^3 \cong 20\,122\,\mathrm{cm}^4$.

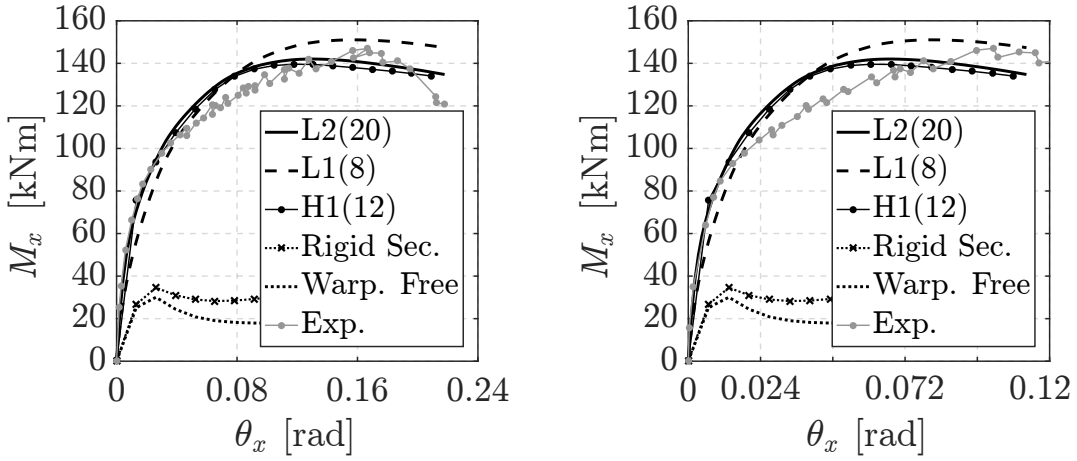

(***a***) Mid-span section.

(***b***) Quarter-span section.

Figure 6.31: RC U-shaped beam under torsional loads: applied torsional couple M_x vs section torsional rotation θ_x.

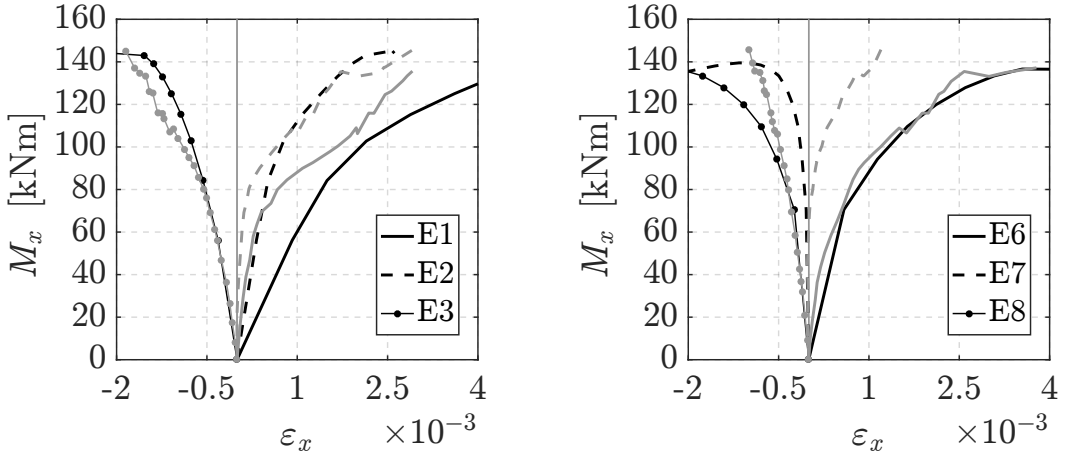

(***a***) Mid-span section - Right flange.

(***b***) Mid-span section - Left flange.

Figure 6.32: RC U-shaped beam under torsional loads: axial strains ε_x in the bars vs applied torsional couple M_x. - The black lines represent the numerical solutions obtained with the proposed FE with the L2(20) distribution and the gray lines represent the experimental data.

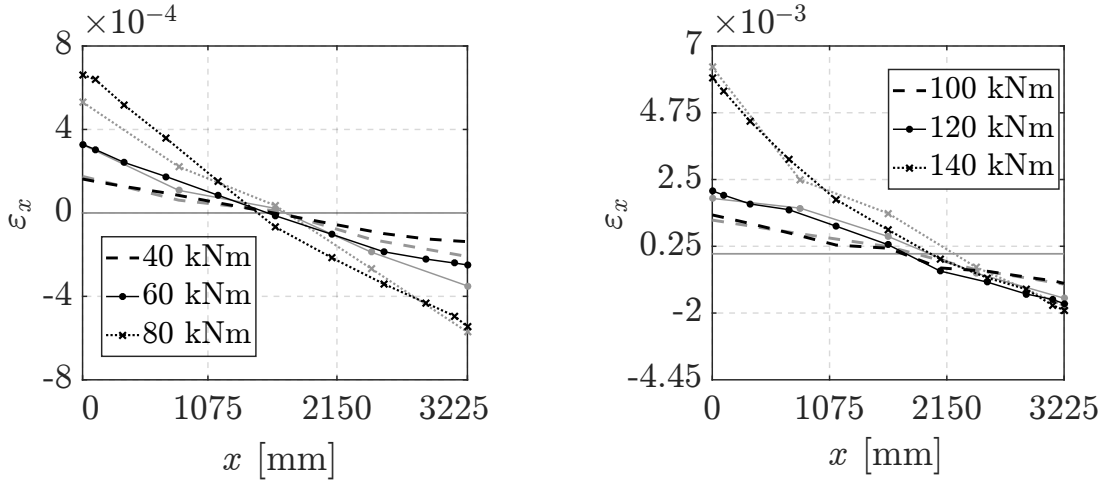

Figure 6.33: RC U-shaped beam under torsional loads: axial strains ε_x in the bar E3 for different values of the applied torsional couple M_x. - The black lines represent the numerical solutions obtained with the proposed FE with the L2(20) distribution and the gray lines represent the experimental data.

The WMF model with both the distributions L2(20) and H1(12) is able to predict accurately the entire behavior of the beam and in particular the initial stiffness and the maximum strength. L2(20), however, requires almost twice the warping DOFs required by H1(12). The same FE not including the warping constraints gives a completely underestimated solution. In particular, not only the obtained initial stiffness is lower, as obviously expected [100], but the beam strength is significantly reduced, as well. These results clearly point out the relevance of correctly modeling the warping constraints. In fact, the model including them is able to reproduce the actual axial strain and stress distributions along the beam, resulting by preventing the warping at the end and at the mid-span, i.e. the shear-lag effect. This effect is particularly relevant in this specimen, because it engages the contribution of the reinforcing bars. Figs. 6.32 and 6.33 show the axial strains obtained for the bars E1, E2, E3, E6, E7 and E8 (indicated as in Fig. 6.28). The model without warping constraints provides zero strains and zero stresses for all the bars. Moreover, as shown in Fig. 6.34, this gives a damage distribution over the cross-section that basically follows the shear flow due to the circulatory torsion (Fig. 6.35), in perfect agreement with the classical thin-walled beam theory, without accounting for the warping torsion [124]. Hence, it fails in correctly computing the element strength.

Similar considerations hold for the standard beam model solution, assuming rigid sections. In fact, as the model considering free warping along the element, this does not capture the shear-lag effect and underestimates the element strength.

Finally, the model adopting L1(8) distribution slightly underestimates the initial

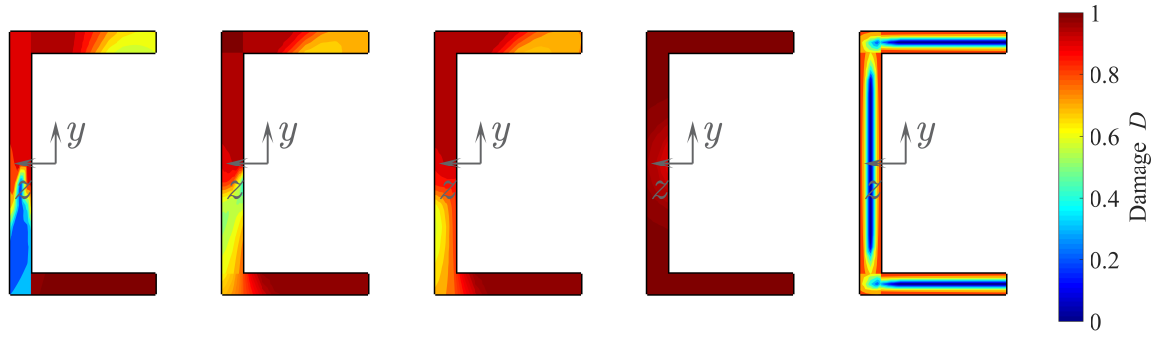

(*a*) L1(8) (*b*) L2(20) (*c*) H1(12) (*d*) Rigid sec. (*e*) Warp. free

Figure 6.34: Damage distribution at the mid-span section of the U-shaped beam under torsional loads. - $\theta_x = 0.12\,\text{rad}$.

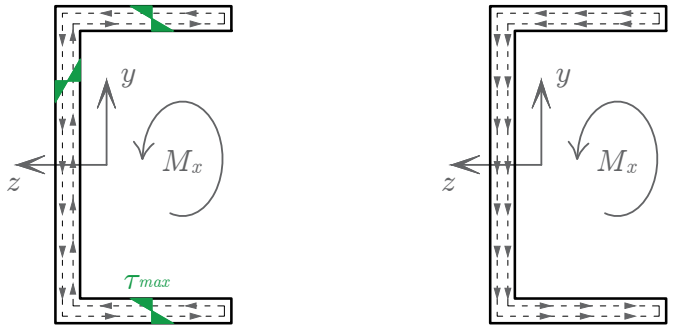

(*a*) Shear flow due to the circulatory torsion

(*b*) Shear flow due to the warping torsion

Figure 6.35: Torsional shear flow in a U-shaped member.

stiffness of the beam and overestimates its strength. This difference with respect to the other warping distributions is related to the less accurate warping interpolation provided over the cross-section. In fact, this model does not account for the rotations of the flanges and of the web around their mid-lines, but it assumes constant warping displacements across the thickness. Because of this approximation, the level of axial strains due to the shear-lag and the amount of damage result different, as shown in Figs. 6.34 and 6.36.

6.4 RC shear walls under cyclic horizontal loads

This section presents the analyses of two different RC specimens subjected to significant shear deformations. The first one is a rectangular wall under in-plane cyclic loads and the second one is a U-shaped wall under bi-axial cyclic horizontal loads. The studies focus on the performance of the WMF in representing the effects of the warping and

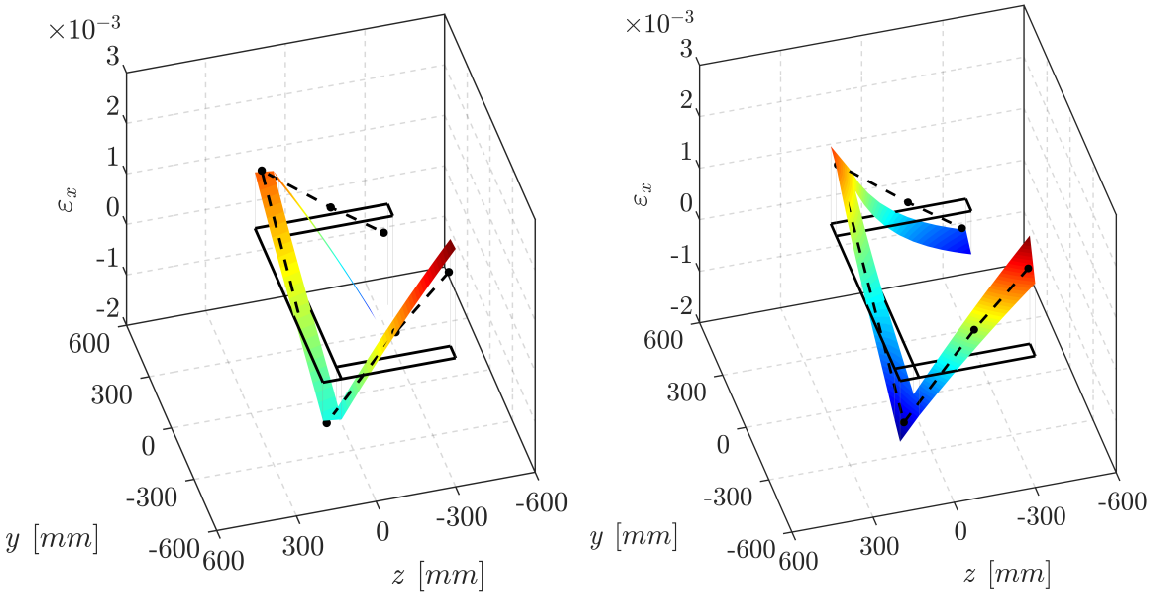

(*a*) Warping distr. L1(8). **(*b*)** Warping distr. H1(12).

Figure 6.36: Axial strains ε_x distribution at the mid-span section, due to the warping constraints in the U-shaped beam under torsion. - $M_x = 100\,\text{kNm}$ - The 3D surface represents the numerical solution and the dashed line represents the experimental data, with the markers corresponding to the external bars E1, E2, E3, E6, E7 and E8, as indicated in Fig. 6.28.

its coupling with the damaging phenomena, when cyclic transversal loads are applied to the beam elements. It also investigates on the advantages this FE model provides in describing the resulting stress/strain variable distributions over the beam cross-sections and their evolution for nonlinear material states. Two companion walls, yet assumed as plain concrete specimens, are used in Sec. 4.3 to validate the adopted nonlocal regularization formulation.

The 3D plastic-damage material model proposed in Sec. 2.4 describes the concrete constitutive behavior. Hence, the studies also investigate the performances of this model in representing the concrete response under relevant shear shear forces. The classical J2 plasticity in Sec. 2.2 describes the behavior of the steel bars.

6.4.1 Rectangular wall

This numerical test simulates the experimental study by Dazio et al. [107] on a rectangular shear wall, with geometry in Fig. 6.37. A cyclic horizontal force, acting in the plane of the wall, is applied at the top of the wall, so that the shear span is constantly equal to $L = 4.52\,\text{m}$, together with a constant vertical compressive load of 1480 N.

One WMF beam-column FE is adopted to represent the deformable part of the wall,

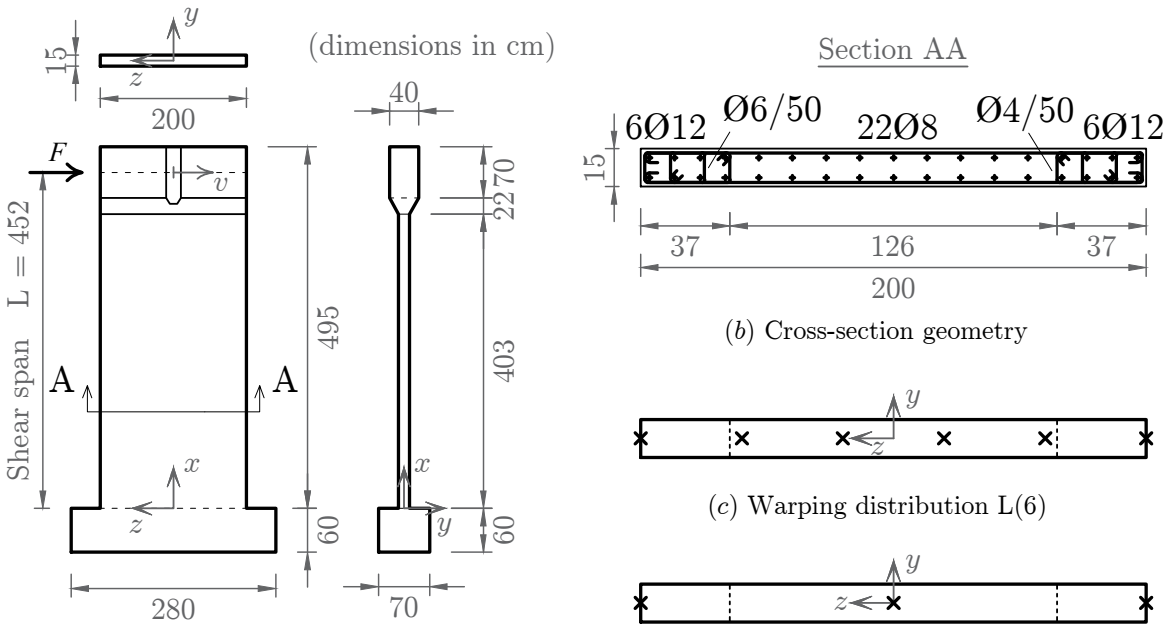

(*a*) Specimen geometry

(*b*) Cross-section geometry

(*c*) Warping distribution L(6)

(*d*) Warping distribution H(6)

Figure 6.37: RC rectangular shear wall: specimen geometry and model discretization.

modeling the top and the bottom slabs as rigid elements. The warping displacements are restrained at the bottom of the wall and assumed to be free at the top [110]. Hence, six warping interpolation points $n_w = 6$ are used over the height to describe non-uniform warping distributions. Thirteen Gauss-Lobatto quadrature cross-sections are adopted and a characteristic length $L_c = 30\,\text{cm}$ is set for the nonlocal model formulation in Eqs. (4.9) and (4.10). The fiber model considers one fiber across the thickness of wall and assumes a midpoint rule scheme along the width. The confined parts of the section are discretized independently from the inner part, placing four fibers in each of them and seven in the remaining part of the section, for a total of 15 fibers. Fig. 6.37 also shows (*c*, *d*) two distributions of warping DOFs: in both L(6) and H(6) the warping interpolation across the thickness of the wall is assumed constant and fifth order polynomials are defined for the interpolation along the width.

The material parameters in Table 6.6 are assumed for the concrete, with Fig. 6.38 representing the corresponding uni-axial stress-strain relation and the damage evolution law. In the confined parts, the increase of strength is simulated by $a_c = 0.8$. Finally, $E = 210\,000\,\text{MPa}$, $\nu = 0.3$ and $\sigma_y = 650\,\text{MPa}$ are the Young's modulus, the Poisson ratio and the plastic yield strength of the steel bars, with $H_i = 0.01\,E$ and $H_k = 0.05\,E$ the isotropic and kinematic hardening parameters.

Fig. 6.39 shows the global responses obtained with L(6) and H(6), in terms of applied load F vs top displacement v/L. The numerical results (black line) are com-

Table 6.6: Mechanical parameters for the reinforced concrete rectangular shear wall.

$E = 37\,000\,\text{MPa}$	$\nu = 0.2$		
$\sigma_t = 6.6\,\text{MPa}$	$\sigma_c = 60.0\,\text{MPa}$	$H_i = 0.001\,E$	$H_k = 0.700\,E$
$Y_{0t} = 9.72 \cdot 10^{-5}$	$k_t = 3.0 \cdot 10^{-4}$	$a_t = 0.8$	
$Y_{0c} = 5.84 \cdot 10^{-4}$	$k_c = 5.0 \cdot 10^{-3}$	$a_c = 0.1$	$\beta = 1.0$

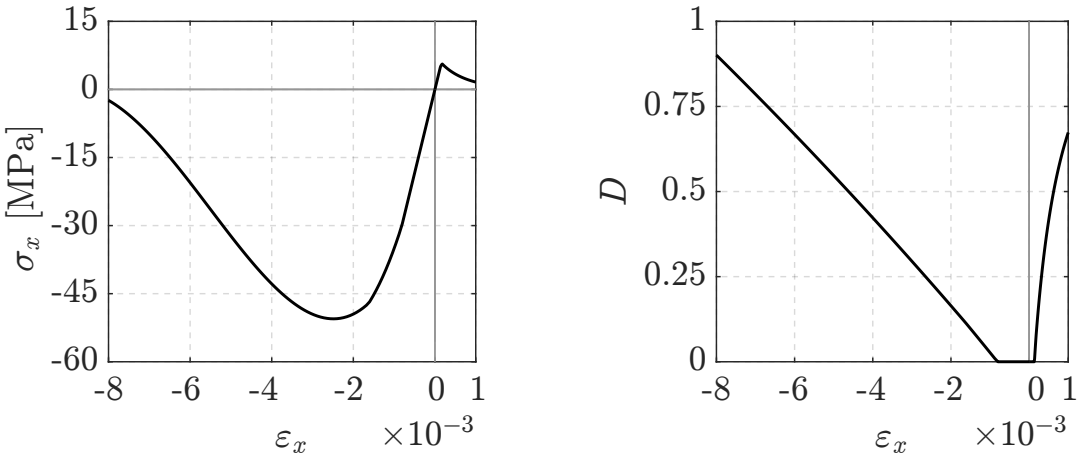

(***a***) Uni-axial stress-strain relation. (***b***) Damage evolution.

Figure 6.38: Monotonic uni-axial ($\sigma_x - \varepsilon_x$) behavior in tension and compression for the proposed damage model adopted for the rectangular shear wall.

pared with the experimental outcomes (gray line). The solution for the two warping interpolations are practically coincident, as the order of the warping interpolation over the cross-section is the same. Moreover, these perfectly agree with the experimental results, satisfactorily reproducing the evolution of the degrading process and predicting the maximum strength of the wall.

Before analyzing the cyclic behavior of the wall, a preliminary numerical study is conducted, applying the horizontal load monotonically. Fig. 6.40 compares the results of the WMF beam, adopting the distribution H(6), and that of a 2D 9-nodes quadrilateral FEs model implemented in FEDEASLab. For this model, in the z direction, two FEs are located in each confined part of the wall and four in the unconfined part; in the x direction, six FEs model the bottom part of the wall (having height equal to $L/4$) and eight FEs model the remaining part. A nonlocal formulation is applied adopting the definition in Eq. (4.11), with $L_c = 30\,\text{cm}$ and considering that the $x - z$ plane is the FE reference plane.

Fig. 6.40*a* compares the responses of the local models, that is those obtained without any regularization technique. Of course, these exhibit localization problems that occur differently for the two models [96]: in the beam-column model the damage

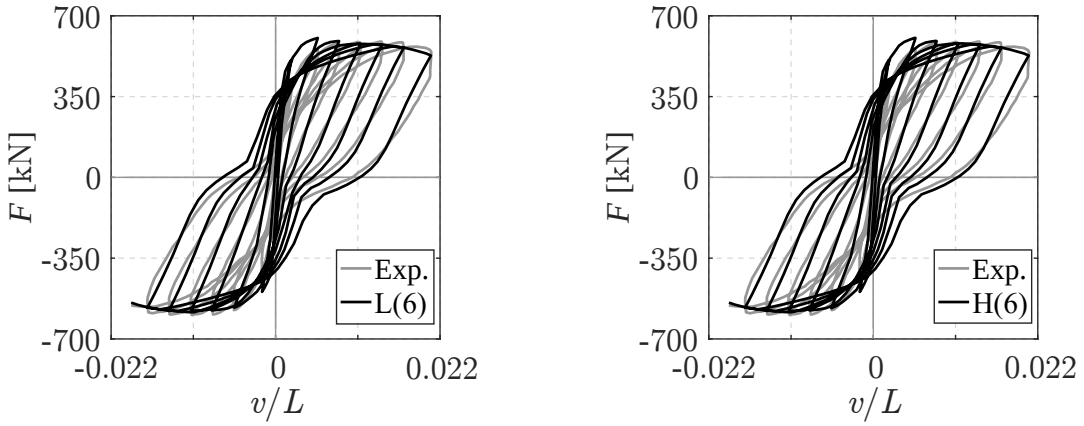

(***a***) Lagrange polynomials L(6).

(***b***) Hermite polynomials H(6).

Figure 6.39: RC rectangular shear wall under cyclic loads: applied horizontal load F vs horizontal drift v/L.

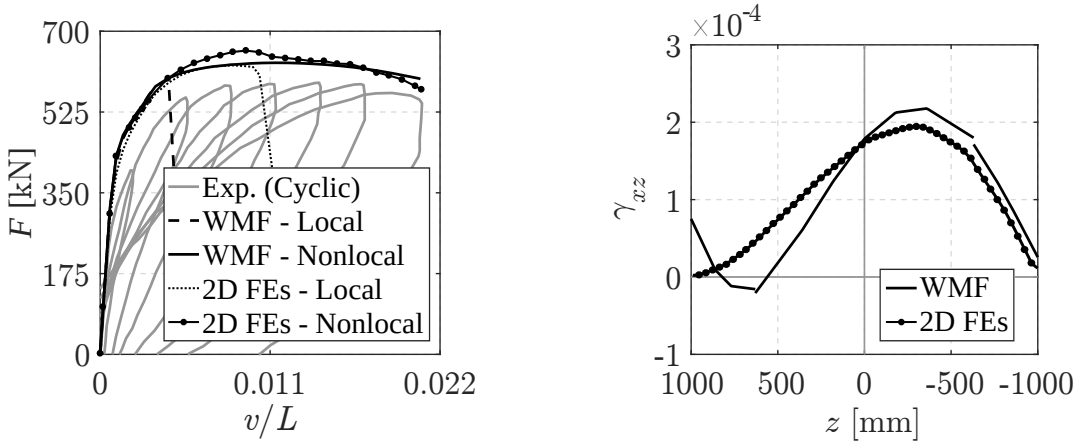

(***a***) Applied horizontal load F vs horizontal drift v/L.

(***b***) Shear strain $\gamma_{xz}(201.5\,\text{cm}, 0\,\text{cm}, z)$ at $v/L = 0.0023$ for the nonlocal models.

Figure 6.40: RC rectangular shear wall under monotonic loads.

localizes at the quadrature cross-section level, at the bottom of the wall, while in the 2D model it localizes at the element level (always at bottom).

By contrast, the nonlocal responses show a good match between the two models, as results also from the shear strain distributions in Fig. 6.40*b* for the half-height cross-section ($x = 2.015\,\text{m}$). Fig. 6.40*b* refers to a value of the horizontal drift equal to $v/L = 0.0023$.

Fig. 6.41 shows an additional comparison. Indeed, the monotonic response of the wall is also evaluated adopting the ETFF beam-column FE in Sec. 3.3, which always assumes a parabolic distribution of the shear strains γ_{xz} along the width of the cross-section. All the adopted model parameters are the same used for the WMF beam.

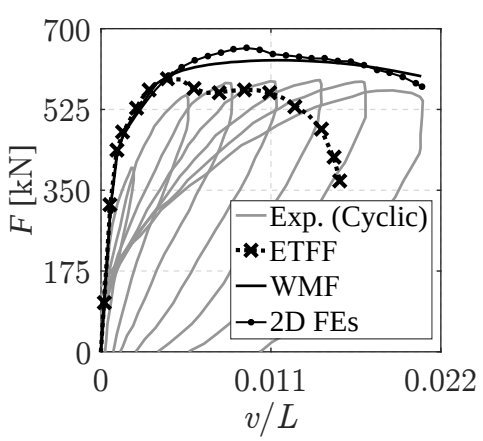

(***a***) Applied horizontal load F vs horizontal drift v/L.

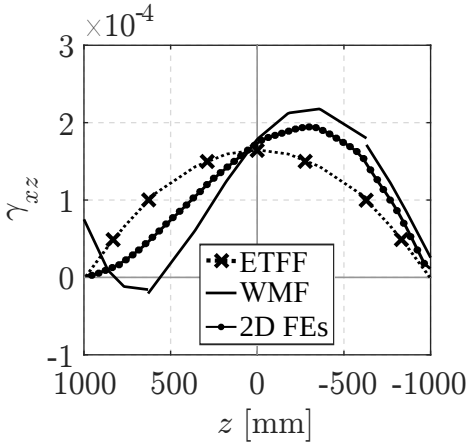

(***b***) Shear strain $\gamma_{xz}(201.5\,\text{cm}, 0\,\text{cm}, z)$ at $v/L = 0.0023$ for the nonlocal models.

Figure 6.41: Response of the RC rectangular shear wall under monotonic loads obtained with the ETFF beam-column FE.

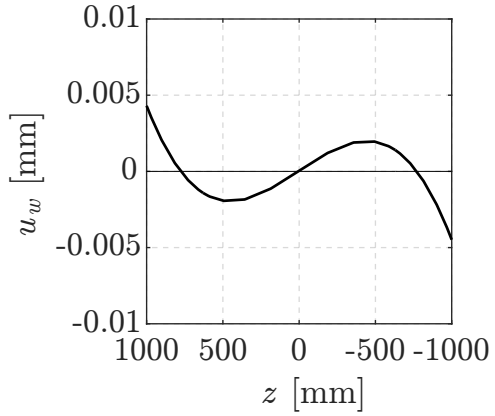

(***a***) Linear stage - $v/L = 0.0002$

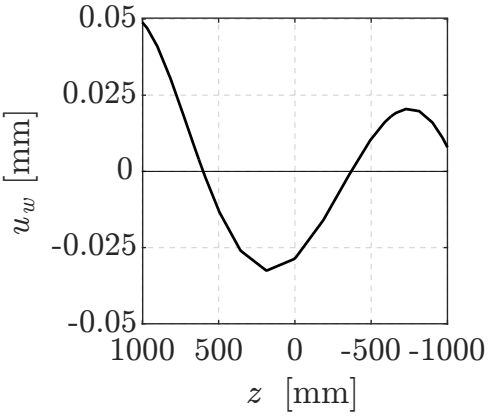

(***b***) Nonlinear stage - $v/L = 0.0023$

Figure 6.42: RC rectangular shear wall under monotonic loads: warping displacements of the half-heigth cross-section ($x = 2.015\,\text{m}$).

Fig. 6.41*a* shows the global response in terms of F vs v/L and clearly points out that this FE model fails in representing the nonlinear behavior of the wall, anticipating the structure failure. This is due to the assumption of parabolic shear strains made for this model, Eqs. (3.45) and (3.46), which does not allow to correctly describe the material state evolution during nonlinear stages. In fact, if one considers the first loading step, when the wall still exhibits a linear elastic response, the variation of the warping displacements is cubic along the width and that of the shear strains is parabolic; both are symmetric with respect to the vertical $x-$axis. Fig. 6.42*a* shows the warping displacements of the half-height cross-section for this stage. By contrast, when the material starts to degrade, because of the damaging progression due to the

increasing load, the left part of the wall (positive z values) undergoing tensile strains results more damaged then the right part (negative z values) under compression. As a consequence, the left part exhibits higher warping displacements and the distribution is no longer symmetric, as shown in Fig. 6.42b. Similarly, the distribution of the shear strains is a pseudo-parabola shifted in the compressed zone, representing the reacting part of the section and carrying the horizontal load. This effect is not captured by the ETFF model, as Fig. 6.41b shows. This plots the shear strain distributions as in Fig. 6.40b.

6.4.2 U-shaped wall

The last study investigates the experimental test by Pegon et al. [108, 109] on the RC U-Shaped shear wall in Fig. 6.43. The wall is horizontally loaded at the top in both

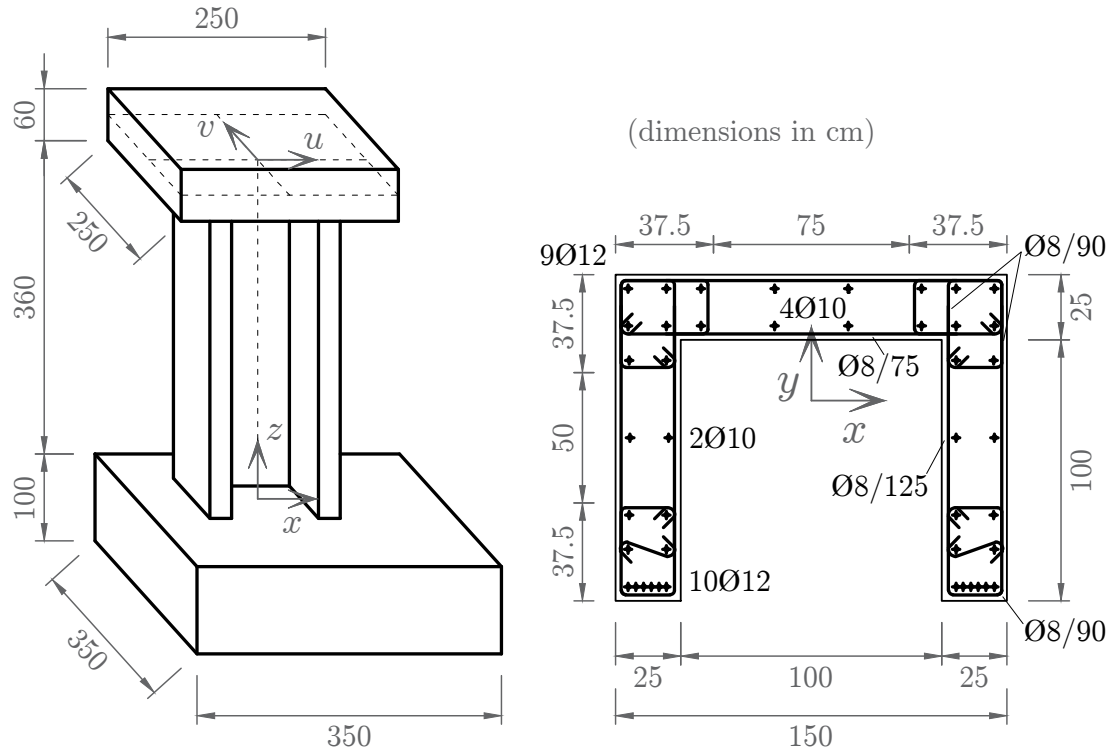

(a) Specimen geometry (b) Cross-section geometry

Figure 6.43: RC U-shaped shear wall: specimen geometry.

the directions x and y, controlling the displacements u and v according to the butterfly path in Fig. 6.44. The loading path is characterized by four butterfly cycles with two different amplitudes. The gray arrows in Figs. 6.44a and 6.44b indicate the shape of the first and the second cycles, respectively, where the maximum displacement in both the directions is 40 mm; the third and fourth cycles have the same shape of the first

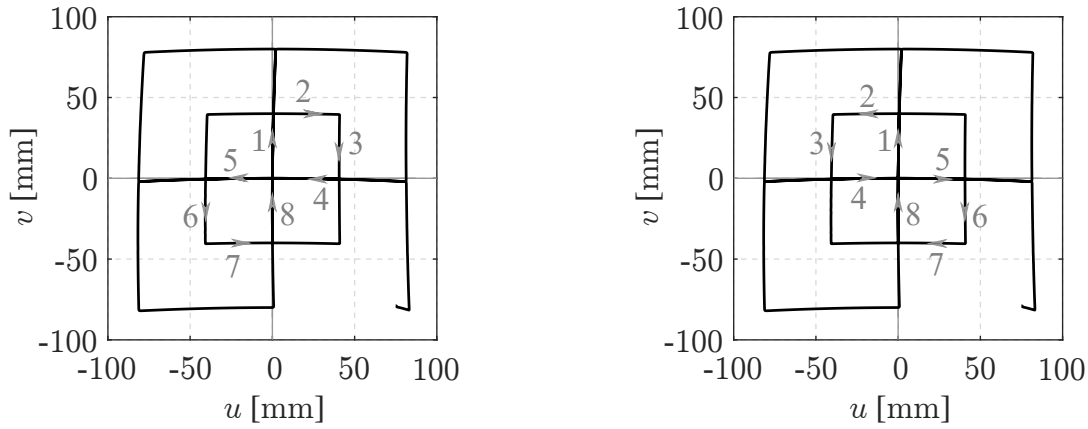

(***a***) First cycle. (***b***) Second cycle.

Figure 6.44: RC U-shaped shear wall: top displacements path.

two, but they are characterized by a maximum displacement of 80 mm. The forces are applied in the mid-plane of the top slab, where the torsional rotation is prevented. The shear span ratio is constantly equal to $L = 3.90$ m and the constant axial compression is equal to 2000 kN.

One WMF beam-column FE is adopted to model the deformable part of the wall, assuming the top and the bottom slabs as rigid. The warping displacements are restrained at both the end cross-sections [110]. The model uses five warping interpolation points, $n_w = 5$, are used over the height, that is fourth order Lagrange polynomials for the warping interpolation along the element axis, and thirteen Gauss-Lobatto quadrature cross-sections. Moreover, it considers a characteristic length $L_c = 30$ cm for the nonlocal model formulation represented by Eqs. (4.9) and (4.10).

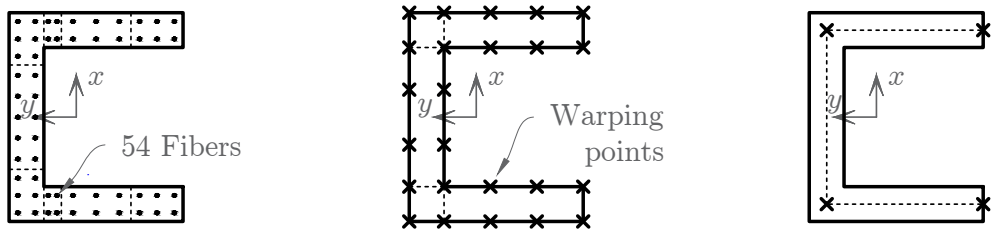

(*a*) Fiber model (*b*) Warp. distr. L(24) (*c*) Warp. distr. H(12)

Figure 6.45: Fiber model discretization (midpoint rule) and warping points distribution over the cross-section of the RC U-shaped shear wall.

Fig. 6.45 shows (*a*) the fiber discretization of the cross-section and (*b*, *c*) two distributions of warping DOFs. Both consider a cubic variation of the warping displacements along the web and the flanges and a linear variation across the thickness. However, L(24), adopting Lagrange polynomials, uses twice the number of warping DOFs used

by H(12), adopting Hermite polynomials.

Table 6.7 lists the parameters for the concrete, with Fig. 6.46 containing the corresponding uni-axial stress-strain relation and the damage evolution law. In the confined parts, that is at the tips of the flanges and at the intersections between these and the web, the increase of strength is simulated by $k_c = 2.8 \cdot 10^{-3}$ and $a_c = 0.8$. The general Menegotto-Pinto model modified by Filippou et al. [125] describes the behavior of the steel bars. $E = 200\,000\,\text{MPa}$, and $\sigma_y = 540\,\text{MPa}$ are the Young's modulus and the plastic yield strength and $b = 1.0\%$ the ratio between the hardening and the elastic stiffness. Moreover, the transition parameter R from the elastic to the plastic state is based on the following parameters: $R_0 = 20$, $a_1 = 18.5$ and $a_2 = 0.15$. No isotropic hardening is assumed.

Table 6.7: Mechanical parameters for the reinforced concrete U-shaped shear wall.

$E = 28\,000\,\text{MPa}$	$\nu = 0.25$		
$\sigma_t = 3.3\,\text{MPa}$	$\sigma_c = 30.0\,\text{MPa}$	$H_i = 0.001\,E$	$H_k = 0.800\,E$
$Y_{0t} = 6.70 \cdot 10^{-5}$	$k_t = 2.0 \cdot 10^{-4}$	$a_t = 0.8$	
$Y_{0c} = 4.02 \cdot 10^{-4}$	$k_c = 2.0 \cdot 10^{-3}$	$a_c = 0.4$	$\beta = 0.5$

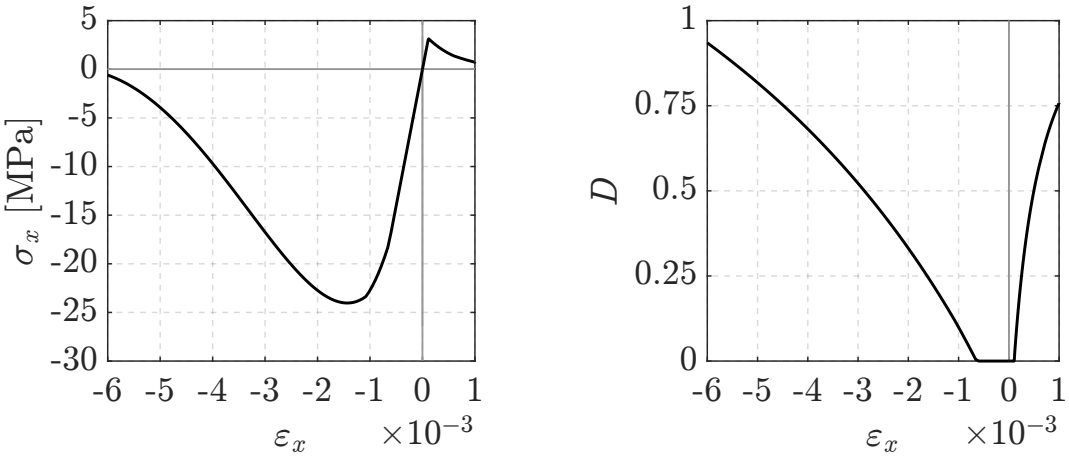

(*a*) Uni-axial stress-strain relation. **(*b*)** Damage evolution.

Figure 6.46: Monotonic uni-axial ($\sigma_x - \varepsilon_x$) behavior in tension and compression for the proposed damage model adopted for the U-shaped shear wall.

As in the rectangular wall test, the solutions for the two warping distributions H(24) and H(12) in terms of global variables are very close to each other, since the order of the warping interpolation over the cross-section is the same. Fig. 6.47 plots them for H(12). The figure shows (a, b) the evolution of the applied horizontal loads F_x and F_y in the two directions vs the normalized top displacements u/L and v/L, respectively,

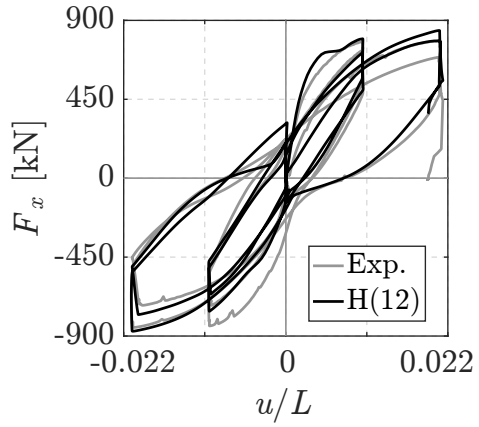

(*a*) Applied force F_x vs drift u/L.

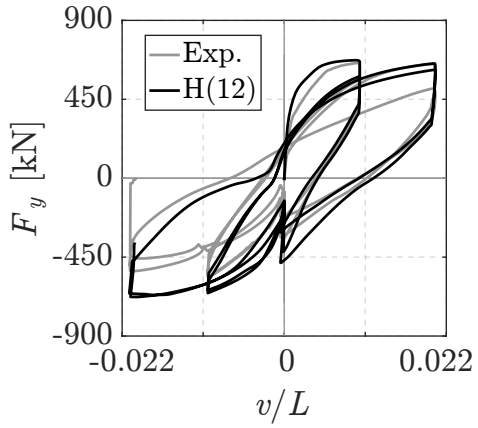

(*b*) Applied force F_y vs drift v/L.

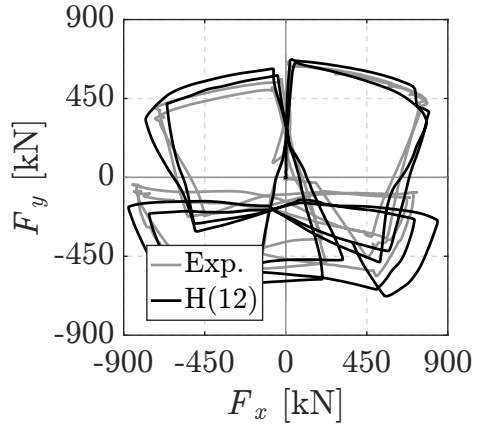

(*c*) Butterfly path of F_x and F_y.

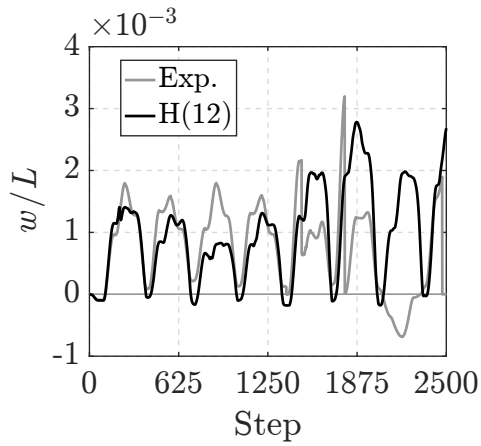

(*d*) Axial displacement w/L.

Figure 6.47: RC U-shaped shear wall under cyclic loads: global response.

(c) the relation between these forces and (d) the evolution of the normalized top vertical displacement w/L during the loading steps. The numerical results (black solid line) confirm the trend observed in the previous test, that is the good ability of the model in describing the reduction of strength occurring at every cycle. A certain gap between numerical and experimental results occurs only in the last cycles. Here, the FE model gives a solution that is higher in terms of strength with respect to the real specimen, in particular for the y direction force and the vertical displacement. This is due to the assumptions made in the numerical test. In fact, in the experimental test, part of the loss of strength is caused by the failure of the reinforcing bar, that in the last cycle leads to the collapse of the specimen. In the numerical analysis, the model adopted for the steel does not include the material degradation. Hence, this mechanisms is not captured.

As done for the rectangular shear wall, a preliminary numerical study is conducted,

considering only the first part of the first loading cycle, that is only the two branches indicated with the gray arrows 1 and 2 in Fig. 6.44*a*.

Fig. 6.48 compares the global results for the WMF beam, adopting H(12), and those obtained modeling (in FEDEASLab) the wall with 4-nodes shell Mixed Interpolation of Tensorial Component (MITC) FEs [111]. For this model, in the x direction, two FEs discretize each confined part of the wall and four the unconfined part; in the z direction, six FEs discretize the bottom part of the wall (having height equal to $L/4$) and eight FEs the remaining part. Moreover, a nonlocal formulation is applied adopting the

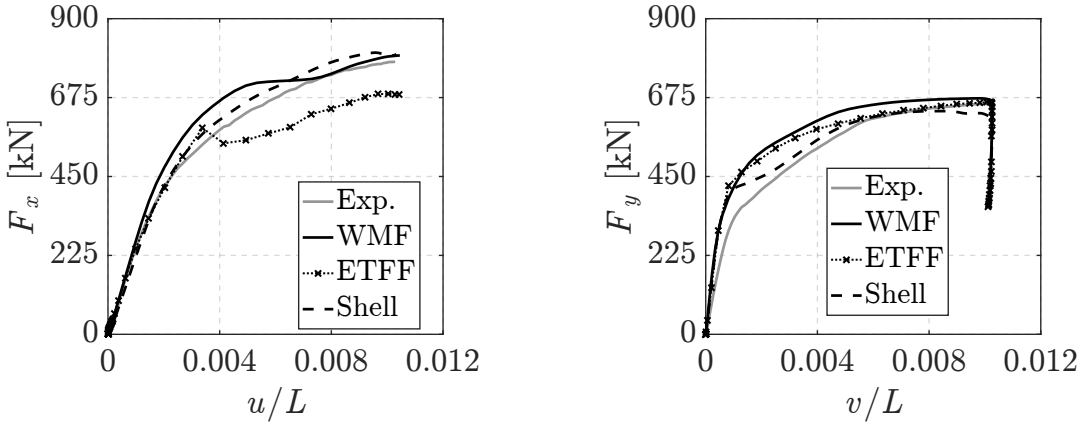

(*a*) Applied horizontal load F_x vs horizontal drift u/L.

(*b*) Applied horizontal load F_y vs horizontal drift v/L.

Figure 6.48: RC U-shaped shear wall under monotonic loads: global response.

definition in Eq. (4.11), with $L_c = 30\,\text{cm}$ and considering that the FE reference plane is the $x - z$ plane in the web of the wall and the $y - z$ plane in the flanges.

Fig. 6.48 also compares the results with the solution obtained adopting the ETFF beam-column FE in Sec. 3.3, which always assumes a fixed shape (but variable amplitudes) of the shear strains γ_{zx} and γ_{zy} over the cross-section, during the whole loading path. All the model parameters adopted for the ETFF beam are the same used for the WMF beam. As it happens for the rectangular shear wall, in contrast to the good match between the WMF beam, shell FEs and experimental outcomes, the ETFF beam fails in representing the nonlinear behavior of the wall, anticipating the structure failure. Indeed, because of the assumption on the shear strains distribution, the ETFF model is not able to correctly reproduce the material state evolution and the coupling between the shear stresses and the other stress components.

Finally, Fig. 6.49 compares the total vertical displacements $u(x, y, z)$ in (a) the half-height cross-section ($z = 1.8\,\text{m}$) and (b) the top cross-section ($z = 3.6\,\text{m}$) at the end of the loading path. For the half-height cross-section, the comparison involves the solution of the WMF model, adopting the distribution H(12), and that of the

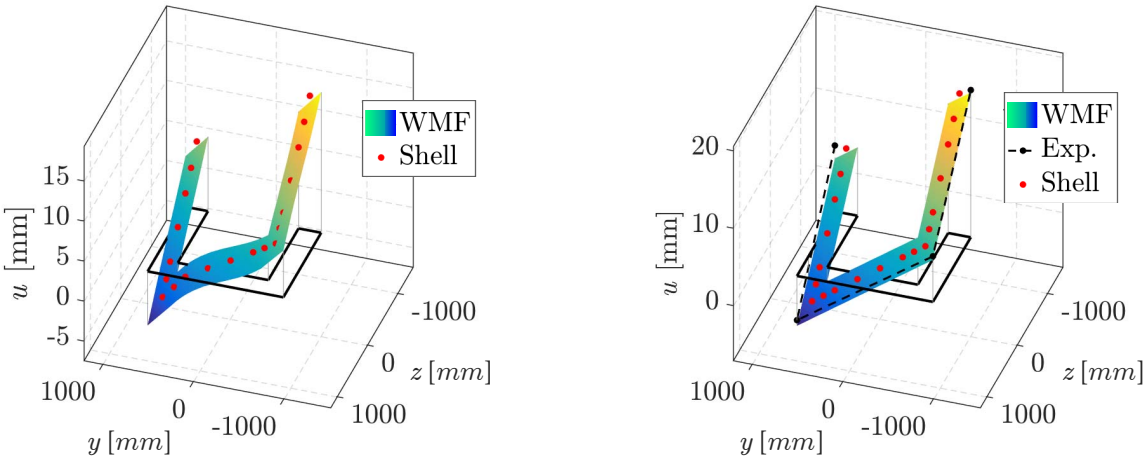

(*a*) Half-height section ($z = 1.8\,\mathrm{m}$). **(*b*)** Top section ($z = 3.6\,\mathrm{m}$).

Figure 6.49: Total vertical displacements u at the half-height and at the top sections in the RC U-shaped shear wall.

shell model. The results clearly show that the WMF beam is able to reproduce the cross-section warping deformation, here representing an important contribution of the total vertical displacement u. For the top cross-section, instead, the comparison also involves the experimental outcomes from [109] and the results show that the WMF beam easily accounts for the warping constraints and correctly reproduces the rigid body displacement of the element cross-section.

Chapter 7

Summary and conclusions

7.1 Summary

The objective of this work was the development of an efficient and accurate computational tool for the analysis of reinforced concrete (RC) structural beams subjected to relevant shear and torsional loads. The influence of non-uniform shear stress/strain distributions, due to out-of-plane deformations of the cross-section, and their interaction with the damaging behavior of RC frames, was the main focus, studying the relevance of correctly accounting for these effects in the numerical analyses and providing fundamental numerical models useful in today's practice.

Starting from the enhanced beam-column finite element model recently proposed in [1] and developed for linear and elasto-plastic material responses, the main goal was to extend its formulation to the analysis of RC structures and to investigate the element capability in reproducing the response of damaging frames. This has been accomplished by operating at different levels:

1. A new 3D plastic-damage material model has been developed to reproduce the behavior of brittle-like materials. This has been used to describe the constitutive response of the concrete in the framework of the fiber discretization procedure to derive the response of beam cross-sections. The proposed constitutive model adopts a Drucker-Prager plasticity formulation to describe the evolution of the plastic strains and to account for non-symmetric behavior in tension and compression. The damaging effects are modeled through the definition of two internal variables, conveniently combined to represent the unilateral effects. A specific predictor-corrector procedure is formulated and implemented to solve the non-linear material evolution problems. Some basic studies have been conducted to investigate the influence of the parameters defined for the material model and its ability in reproducing basic phenomena and experimental outcomes.

2. The beam-column FE model proposed in [1] is based on a four-field Hu-Washizu variational approach, where an additional independent displacement field is introduced, representing the warping deformation of the cross-sections. The warping displacement field is interpolated along the beam axis and over the cross-section, adopting Lagrange polynomials as interpolation functions. The current work has extended the model to allow the adoption of Hermite polynomials for the cross-section warping interpolation, in order to reduce the total number of element DOFs. Moreover, it has proposed a new more efficient procedure to remove the cross-section rigid body motions from the interpolatory definition of the warping displacement field, increasing the robustness of the element state computation.

3. A specific regularization technique is adopted to overcome the localization and mesh sensitivity problems typically occurring with softening materials. This is based on a nonlocal formulation, which is applied to the generalized element deformation quantities and which assumes a truncated Gaussian weighting function to limit the computational cost. The nonlocal formulation has been validated through two numerical tests on two plain concrete shear walls, comparing the solutions for the beam-column FEs and 2D plane or shell FEs.

4. An enhanced solution algorithm, with respect to that presented in [1], has been formulated and implemented for the beam-column FE with section warping. This allows to by-pass the iterative procedure used to enforce simultaneously the element equilibrium and the compatibility conditions, as it is usual for force-based and mixed FEs.

5. An efficient technique has been proposed to condense out the stress components derived by the 3D constitutive response and not directly included in the fiber section formulation. Basing on a standard iterative nonlinear static condensation, the proposed procedure considers a non-iterative scheme taking advantage of the global iterative solution scheme and avoiding the inner loop. Although this work applies it to the material stresses condensation of beam-column FEs, this condensation procedure is generally valid for any static condensation problems.

Three groups of correlation studies have been conducted: the first preliminary one on elastic and elasto-plastic thin-walled beams under shear and torsional loads; the second one on a series of plain concrete reinforced concrete prismatic beams subjected to monotonic torsion; the third one on two different reinforced concrete shear walls, cyclically loaded by horizontals forces.

7.2 Conclusions

The following conclusions can be drawn from the studies performed in this work:

1. The proposed plastic-damage model is able to satisfactorily describe the constitutive response of the brittle-materials under any kind of stress/strain state, uni-axial, bi-axial and tri-axial. All the phenomena, typical of brittle materials like concrete, can be accurately simulated, such as the non-symmetric behavior in tension and compression, the plastic strain growth, the unilateral effects under cyclic loads and the bi-axial confinement. The model formulation is accurate and computationally robust and the parameters definitions is very flexible and easy to calibrate.

2. The studies on the prismatic beams under torsional loads have shown that the introduction of the warping effects is essential, when relevant torsion is present. The classical beam models, based on the rigid cross-section assumption, give incorrect results, definitely underestimating the beam strength. Moreover, the correct introduction of the warping constraints is also fundamental to reproduce the real structural behavior.

3. The adoption of Hermite polynomials to interpolate the warping displacement field over the element cross-section has revealed as a better solution with respect to the original proposal based on the Lagrange polynomials. Indeed, the Hermite interpolation provides higher order interpolations function with a smaller number of warping DOFs. This is true for thicker cross-section frames, as usual for reinforced concrete specimens, eve though it is not a suitable solution for very thin-walled beams. The preliminary studies on elastic and elasto-plastic structures have shown that the adoption of Hermite polynomials, in this case, lead to a poor representation of the shear stress/strain distribution at web/flanges intersections, which usually leads to an overestimation of the section rigidity.

4. The studies on the shear wall specimens have highlighted the relevance of correctly representing the shear stress/strain variation over the element cross-section and its evolution during the nonlinear stages of the structural response.

5. The studies have also shown the benefits of the adopted regularization technique, as it is essential to obtain an objective mesh-independent response.

6. All the solution algorithms adopted for the FE models have been proved to be computationally efficient and accurate, even under complex loading configurations.

7.3 Recommendations for future developments

Several additional developments can be made to extend the study presented in this dissertation. Starting with the material model, it could be useful to enhanced the damage formulation to better reproduce tri-axial compressive stress states and to simulate the confinement effects, common in concrete structures [65, 81]. With this improvement, it could be possible to include in the WMF beam-column FE a better representation of the transverse reinforcements [51], which now are accounted for simply increasing the strength and the ductility of the concrete in the confined parts of the specimens.

Regardless of the adopted constitutive model, the description of the warping displacement in the WMF model could be further improved as well. Indeed, other kinds of functions could explored for the interpolation over the cross-section and along the beam axis, trying to identify an interpolation scheme that is suitable for both thin-walled (elasto-plastic) frames and thicker (reinforced concrete) frames, in order to better represent the stress/strain distribution inside the elements.

For thin-walled frames, it would be also beneficial to extend the formulation by including the cross-section in-plane deformations and the geometric nonlinearities, to describe buckling phenomena and perform stability analyses of steel structures.

Moreover, the FE formulation could be extended to the case of curved and/or tapered beams, which usually exhibit relevant issues related to the cross-section warping and to the effect of shear and torsion [126, 127].

Another interesting development is the extension of the FE formulation on the basis of a geometrically nonlinear approach, such as a corotational approach. This would allow the analyses of structures subjected to severe torsional/shear deformations and the description of buckling and post-buckling behavior of thin-walled frames [32, 33].

Bibliography

[1] V. Le Corvec, "Nonlinear 3d frame element with multi-axial coupling under consideration of local effects," PhD thesis, University of California, Berkeley, 2012.

[2] D. Addessi, S. Marfia, and E. Sacco, "A plastic nonlocal damage model," *Computer Methods in Applied Mechanics and Engineering*, vol. 191, pp. 1291–1310, 2002.

[3] B. De Saint Venant, *Memoire sur la torsion des prismes.* Mem. Savants etrangers, Paris, 1855.

[4] M. J. Boussinesq, *Application des potentiels.* Gauthier-Villars, Paris, 1885.

[5] E. Sternberg, "On Saint-Venant's principle," *Quarterly of Applied Mathematics*, vol. 11, pp. 393–402, 1954.

[6] L. C. Dell'Acqua, *Meccanica delle strutture 2, Le teorie strutturali e il metodo degli elementi finiti.* McGraw-Hill, 1994.

[7] A. Luongo and A. Paolone, *Scienza delle costruzioni: 2. Il problema di De Saint Venant.* CEA, 2005.

[8] S. Timoshenko and J. N. Goodier, *Theory of elasticity.* McGraw-Hill, 1951.

[9] K. J. Bathe, *Finite element method.* John Wiley & Sons, 2008.

[10] V. Ciampi and L. Carlesimo, "A nonlinear beam element for seismic analysis of structures," *Proceedings of the Eighth European Conferenceon Earthquake Engineering, Laboratorio Nacional de Engenharia Civil, Lisbon*, 1986.

[11] K. D. Hjelmstad and E. Taciroglu, "Mixed methods and flexibility approaches for nonlinear frame analysis," *Journal of Constructional Steel Research*, vol. 58, pp. 967–993, 2002.

[12] A. Saritas and O. Soydas, "Variational base and solution strategies for non-linear force-based beam finite elements," *International Journal of Non-Linear Mechanics*, vol. 47, no. 3, pp. 54–64, 2012.

[13] P. K. V. Nukala and D. W. White, "Variationally consistent state determination algorithms for nonlinear mixed beam finite elements," *Computer Methods in Applied Mechanics and Engineering*, vol. 193, no. 33-35, pp. 3647–3666, 2004.

[14] R. L. Taylor, F. C. Filippou, A. Saritas, and F. Auricchio, "A mixed finite element method for beam and frame problems," *Computational Mechanics*, vol. 31, pp. 192–203, 2003.

[15] E. Spacone, "Flexibility-based finite element models for the nonlinear static and dynamic analysis of concrete frame structures," Ph.D. dissertation, University of California, Berkeley, 1994.

[16] R. W. Clough, K. L. Benuska, and E. L. Wilson, "Inelastic earthquake response of tall buildings," in *Third World Conference on Earthquake Engineering, New Zealand*, 1965.

[17] R. W. Clough, "Effect of stiffness degradation on earthquake ductility requirements," *Structural Engineering Laboratory, University of California*, 1966.

[18] M. F. Giberson, "The response of nonlinear multi-story structures subjected to earthquake excitation," Ph.D. dissertation, California Institute of Technology, 1967.

[19] S. W. Liu, Y. P. Liu, and S. L. Chan, "Advanced analysis of hybrid steel and concrete frames. Part 2: Refined plastic hinge and advanced analysis," *Journal of Constructional Steel Research*, vol. 70, pp. 337–349, 2012.

[20] S. M. Kostic, F. C. Filippou, and B. Deretic-Stojanovic, "Generalized plasticity model for inelastic RCFT column response," *Computers & Structures*, vol. 168, pp. 56–67, 2016.

[21] P. L. Darvall and P. A. Mendis, "Elastic-plastic-softening analysis of plane frames," *Journal of Structural Engineering*, vol. 111, pp. 871–888, 1985.

[22] F. C. Filippou and A. Issa, "Nonlinear analysis of reinforced concrete frames under cyclic load reversals," *Earthquake Engineering Research Center, University of California*, vol. 88, 1988.

[23] M. H. Scott and G. L. Fenves, "Plastic hinge integration methods for force-based beam-column elements," *Journal of Structural Engineering*, vol. 132, pp. 244–252, 2006.

[24] F. L. Ribeiro, M. Barbosa, A. R.and Scott, and L. Neves, "Deterioration modeling of steel moment resisting frames using finite-length plastic hinge force-based beam-column elements," *Journal of Structural Engineering*, vol. 141, p. 04014112, 2014.

[25] E. Spacone, F. C. Filippou, and F. F. Taucer, "Fibre beam-column model for nonlinear analysis of R/C frames: Part 1. Formulation," *Earthquake Engineering & Structural Dynamics*, vol. 25, pp. 711–725, 1996.

[26] B. N. Alemdar and D. W. White, "Displacement, flexibility, and mixed beam-column finite element formulations for distributed plasticity analysis," *Journal of Structural Engineering*, vol. 131, pp. 1811–1819, 2005.

[27] A. Saritas and F. C. Filippou, "Numerical integration of a class of 3d plastic-damage concrete models and condensation of 3d stress-strain relations for use in beam finite elements," *Engineering Structures*, vol. 31, no. 10, pp. 2327–2336, 2009.

[28] H. R. Valipour and S. J. Foster, "Nonlinear reinforced concrete frame element with torsion," *Engineering Structures*, vol. 32, no. 4, pp. 988–1002, 2010.

[29] S. M. Kostic and F. C. Filippou, "Section discretization of fiber beam-column elements for cyclic inelastic response," *Journal of Structural Engineering*, vol. 138, no. May, pp. 592–601, 2012.

[30] J. W. Berman and M. Bruneau, "Experimental and analytical investigation of tubular links for eccentrically braced frames," *Engineering Structures*, vol. 29, no. 8, pp. 1929–1938, 2007.

[31] R. Alsafadie, M. Hjiaj, and J.-M. Battini, "Three-dimensional formulation of a mixed corotational thin-walled beam element incorporating shear and warping deformation," *Thin-Walled Structures*, vol. 49, no. 4, pp. 523–533, 2011.

[32] N. L. Rizzi, V. Varano, and S. Gabriele, "Initial postbuckling behavior of thin-walled frames under mode interaction," *Thin-Walled Structures*, vol. 68, pp. 124–134, 2013.

[33] A. Genoese, A. Genoese, A. Bilotta, and G. Garcea, "A geometrically exact beam model with non-uniform warping coherently derived from the Saint Venant rod," *Engineering Structures*, vol. 68, pp. 33–46, 2014.

[34] H.-X. Wan and M. Mahendran, "Bending and torsion of hollow flange channel beams," *Engineering Structures*, vol. 84, pp. 300–312, 2015.

[35] G. Ranzo, "Experimental and numerical studies on the seismic performance of beam-column RC structural members subjected to high shear," Ph.D. dissertation, Universitá di Roma, La Sapienza, 2000.

[36] Y. J. Lu, "Three-dimensional seismic analysis of reinforced concrete wall buildings at near-fault sites," Ph.D. dissertation, University of California, Berkeley, 2014.

[37] M. A. Haroun and H. M. Elsanadedy, "Behavior of cyclically loaded squat reinforced concrete bridge columns upgraded with advanced composite-material jackets," *Journal of Bridge Engineering*, vol. 10, pp. 741–748, 2005.

[38] T. T. C. Hsu, *Torsion of reinforced concrete*, 1984.

[39] S.-J. Zhou, "Finite beam element considering shear-lag effect in box girder," vol. 136, no. September, pp. 1115–1122, 2010.

[40] M. K. Ferradi and X. Cespedes, "A new beam element with transversal and warping eigenmodes," *Computers & Structures*, vol. 131, pp. 12–33, jan 2014.

[41] J. M. Bairán Garcia, "A non linear coupled model for the analysis of reinforced concrete sections under bending, shear, torsion and axial forces," Phd thesis, Universitat Politecnica de Catalunya, 2005.

[42] "Eurocode 2: Design of Concrete Structures," *British Standards Institution*, 2004.

[43] Z. P. Bazant and B. H. Oh, "Crack band theory for fracture of concrete," *Material and Structures*, vol. 93, pp. 155–177, 1983.

[44] T. J. Hughes, R. L. Taylor, and W. Kanoknukulchai, "A simple and efficient finite element for plate bending," *International Journal for Numerical Methods in Engineering*, vol. 11, pp. 1529–1543, 1977.

[45] O. Soydas and A. Saritas, "An accurate nonlinear 3d Timoshenko beam element based on Hu-Washizu functional," *International Journal of Mechanical Sciences*, vol. 74, pp. 1–14, 2013.

[46] O. C. Zienkiewicz and R. L. Taylor, *The finite element method for solid and structural mechanics*. Butterworth-Heinemann, 2005.

[47] A. Tessler and S. B. Dong, "On a hierarchy of conforming Timoshenko beam elements," *Computers & Structures*, vol. 14, pp. 335–344, 1981.

[48] D. Caillerie, P. Kotronis, and R. Cybulski, "A Timoshenko finite element straight beam with internal degrees of freedom," *International Journal for Numerical and Analytical Methods in Geomechanics*, vol. 39, pp. 1753–1773, 2015.

[49] J. M. Bairán and A. R. Marí, "Multiaxial-coupled analysis of RC cross-sections subjected to combined forces," *Engineering Structures*, vol. 29, no. 8, pp. 1722–1738, 2007.

[50] S. Mohr, J. M. Bairán, and A. R. Marí, "A frame element model for the analysis of reinforced concrete structures under shear and bending," *Engineering Structures*, vol. 32, no. 12, pp. 3936–3954, 2010.

[51] A. Saritas, "Mixed formulation frame element for shear critical steel and reinforced concrete members," Ph.D. dissertation, University of California Berkeley, 2006.

[52] J. N. Reddy, "A simple higher-order theory for laminated composite plates," *Journal of Applied Mechanics*, vol. 51, pp. 745–752, 1984.

[53] J. N. Gregori, M. F. Sosa, P. M.and Prada, and F. C. Filippou, "A 3D numerical model for reinforced and prestressed concrete elements subjected to combined axial, bending, shear and torsion loading," *Engineering Structures*, vol. 29, pp. 3404–3419, 2007.

[54] S. Capdevielle, S. Grange, and F. Dufour, "Introduction of warping in a nonlinear multifiber beam model in torsion for reinforced concrete structures," 2014.

[55] M. K. Ferradi, X. Cespedes, and M. Arquier, "A higher order beam finite element with warping eigenmodes," *Engineering Structures*, vol. 46, pp. 748–762, 2013.

[56] R. Vieira, F. Virtuoso, and E. Pereira, "A higher order thin-walled beam model including warping and shear modes," *International Journal of Mechanical Sciences*, vol. 66, pp. 67–82, 2013.

[57] R. F. Vieira, F. B. E. Virtuoso, and E. B. R. Pereira, "A higher order beam model for thin-walled structures with in-plane rigid cross-sections," *Engineering Structures*, vol. 84, pp. 1–18, 2015.

[58] I. C. Dikaros and E. J. Sapountzakis, "Generalized warping analysis of composite beams of an arbitrary cross section by BEM . I: Theoretical considerations and numerical implementation," *Journal of Engineering Mechanics*, pp. 1–14, 2014.

[59] E. J. Sapountzakis and I. C. Dikaros, "Advanced 3D beam element of arbitrary composite cross section including generalized warping effects," *International Journal for Numerical Methods in Engineering*, vol. 102, pp. 44–78, 2015.

[60] A. Genoese, A. Genoese, A. Bilotta, and G. Garcea, "A mixed beam model with nonuniform warpings derived from the Saint Venant rod," *Computers & Structures*, vol. 121, pp. 87–98, 2013.

[61] W. F. Chen and A. F. Saleeb, *Constitutive equations for engineering materials*. Elsevier, 1994.

[62] J. Lemaitre and J. L. Chaboche, *Mechanics of Solid Materials*. Cambridge University Press, 1994.

[63] J. C. Simo and T. J. R. Hughes, *Computational inelasticity*. Springer Science & Business Media, 2006.

[64] J. Mazars and G. Pijaudier-Cabot, "Continuum damage theory - Application to conrete," *Journal of Engineering Mechanics*, vol. 115, pp. 345–365, 1989.

[65] T. Gabet, Y. Malécot, and L. Daudeville, "Triaxial behaviour of concrete under high stresses : Influence of the loading path on compaction and limit states," vol. 38, pp. 403–412, 2008.

[66] H. B. Kupfer, H. K. Hilsdorf, and H. Rusch, "Behaviour of concrete under biaxial stresses," *ACI Journal*, vol. 66, no. 66, pp. 656–666, 1969.

[67] I. D. Karsan and J. O. Jirsa, "Behavior of concrete under compressive loadings," *Journal of the Structural Division*, 1969.

[68] T. Belytschko, J. Fish, and B. E. Engelman, "A finite element with embedded localization zones," *Computer Methods in Applied Mechanics and Engineering*, vol. 70, pp. 59–89, 1988.

[69] E. N. Dvorkin, A. M. Cuitino, and G. Gioia, "Finite elements with dispacement interpolated embedded localization lines insensitive to mesh size and distortions," *International Journal for Numerical Methods in Engineering*, vol. 30, pp. 541–564, 1990.

[70] A. A. Griffith, "The phenomena of rupture and flow in solids," *Philosophical transactions of the royal society of London*, vol. 221, pp. 163–198, 1921.

[71] A. Hillerborg, M. Modeer, and P. E. Petersson, "Analysis of crack formation and crack growth in concrete by means of fracture mechanics and finite elements," *Cement and Concrete Research*, vol. 6, pp. 773–782, 1921.

[72] R. De Borst, Crisfield, M.A., J. Remmers, and C. Verhoosel, *Nonlinear finite element analysis of solids and structures.* John Wiley & Sons, 2012.

[73] K. J. William, "Constitutive models for engineering materials," *Encyclopedia of Physical Science and Technology, Academic Press*, vol. 3, pp. 603–633, 2002.

[74] D. C. Kent and R. Park, "Flexural members with confined concrete," *Journal of the Structural Division*, 1971.

[75] J. B. Mander, M. J. N. Priestley, and R. Park, "Theoretical stress-strain model for confined concrete," *Journal of Structural Engineering*, vol. 114, pp. 1804–1826, 1988.

[76] F. J. Vecchio and M. P. Collins, "Response of reinforced concrete to in-plane shear and normal stresses," *Department of Civil Engineering, University of Toronto*, vol. 82, 1982.

[77] Z. P. Bazant and P. G. Gambarova, "Crack shear in concrete: crack band microplane model," *Journal of Structural Engineering*, vol. 110, pp. 2015–2035, 1984.

[78] J. Mazars, "A description of micro- and macroscale damage of concrete structures," *Engineering fracture Mechanics*, vol. 25, pp. 729–737, 1986.

[79] J. Lemaitre, "Coupled elasto-plasticity and damage constitutive equations," *Computer Methods in Applied Mechanics and Engineering*, vol. 51, pp. 31–49, 1985.

[80] J. Mazars, P. Kotronis, F. Ragueneau, and G. Casaux, "Using multifiber beams to account for shear and torsion," *Computer Methods in Applied Mechanics and Engineering*, vol. 195, no. 52, pp. 7264–7281, 2006.

[81] J. Mazars, F. Hamon, and S. Grange, "A new 3D damage model for concrete under monotonic, cyclic and dynamic loadings," *Materials and Structures*, 2014.

[82] J. Lee and G. L. Fenves, "Plastic-damage model for cyclic loading of concrete structures," *Journal of Engineering Mechanics*, vol. 124, no. 8, pp. 892–900, 1998.

[83] W.-F. Chen, *Plasticity in reinforced concrete*. J. Ross Publishing, 2007.

[84] D. C. Drucker and W. Prager, "Soil mechanics and plastic analysis for limit design," *Quarterly of Applied Mathematics*, no. 10, pp. 57–165, 1952.

[85] J. Lubliner, J. Oliver, S. Oller, and E. Onate, "A plastic-damage model for concrete," *International Journal of Solids and Structures*, vol. 25, pp. 299–326, 1989.

[86] C. Comi and U. Perego, "Fracture energy based bi-dissipative damage model for concrete," *International Journal of Solids and Structures*, vol. 38, no. 36-37, pp. 6427–6454, 2001.

[87] R. Faria, J. Oliver, and M. Cervera, "Modeling material failure in concrete structures under cyclic actions," *Journal of Structural Engineering*, vol. 130, no. December 2004, pp. 1997–2005, 2005.

[88] W. Prager, "A new method of analyzing stresses and strains in work-hardening plastic solids," *Journal of Applied Mechanics*, no. 23, pp. 493–496, 1956.

[89] M. Rezaiee-Pajand, M. Sharifian, and M. Sharifian, "Accurate and approximate integrations of Drucker-Prager plasticity with linear isotropic and kinematic hardening," *European Journal of Mechanics, A/Solids*, vol. 30, no. 3, pp. 345–361, 2011.

[90] E. Öztekin, S. Pul, and M. Hüsem, "Experimental determination of Drucker-Prager yield criterion parameters for normal and high strength concretes under triaxial compression," *Construction and Building Materials*, vol. 112, pp. 725–732, 2016.

[91] Q. S. Zheng and J. Betten, "On damage effective stress and quivalence hypothesis," *International Journal of Damage Mechanics*, vol. 5, pp. 219–240, 1996.

[92] J. C. Simo and J. W. Ju, "Strain- and stress-based continuum damage model - I. Formulation," *International Journal of Solids and Structures*, vol. 23, pp. 821–840, 1987.

[93] J. H. P. De Vree, W. A. M. Brekelmans, and M. A. J. Van Gils, "Comparison of nonlocal approaches in continuum damage mechanics," *Computers & Structures*, vol. 55, pp. 581–588, 1995.

[94] P. Di Re, D. Addessi, and F. C. Filippou, "3D beam-column finite element under non-uniform shear stress distribution due to shear and torsion," in *ECCOMAS Congress 2016, VII European Congress on Computational Methods in Applied Sciences and Engineering, Crete Island, Greece*, 2016.

[95] A. Neuenhofer and F. C. Filippou, "Evaluation of nonlinear frame finite-element models," *Journal of Structural Engineering*, vol. 123, no. 7, pp. 958–966, 1997.

[96] D. Addessi and V. Ciampi, "A regularized force-based beam element with a damage - plastic section constitutive law," *International Journal for Numerichal Methods in Engeneering*, vol. 70, no. October 2006, pp. 610–629, 2007.

[97] F. C. Filippou, *Nonlinear structural analysis, CE 221 Lecture notes.* University of California, Berkeley, 2015.

[98] G. R. Cowper, "The shear coefficient in Timoshenko' s beam theory," *Journal of applied mechanics*, 1966.

[99] K. P. V. V. Nukala and D. W. White, "A mixed finite element for three-dimensional nonlinear analysis of steel frames," vol. 193, pp. 2507–2545, 2004.

[100] V. Vlasov, *Thin-walled elastic beams.* National Technical Information Service, 1984.

[101] G. Strang, *Linear algebra and its application.* Thomson, Brooks Cole, 2006.

[102] R. Peerlings, M. Geers, R. De Borst, and W. Brekelmans, "A critical comparison of nonlocal and gradient-enhanced softening continua," *International Journal of solids and Structures*, vol. 38, pp. 7723–7746, 2001.

[103] M. H. Scott and O. M. Hamutc, "Numerically consistent regularization of force-based frame elements," *International Journal for Numerichal Methods in Engeneering*, vol. 76, no. June, pp. 1612–1631, 2008.

[104] G. Pijaudier-Cabot and Z. Bazant, "Nonlocal damage theory," *Journal of Engineering Mechanics*, vol. 113, pp. 1512–1533, 1987.

[105] E. Kroner, "Elasticity theory of materials with longrange cohesive forces," *International Journal of Solids and Structures*, vol. 3, pp. 731–742, 1968.

[106] I. A. Kunin, "The thoery of elastic media with microstructure and the theory of dislocations," *Mechanics of Generalized Continua*, pp. 321–328, 1968.

[107] A. Dazio, K. Beyer, and H. Bachmann, "Quasi-static cyclic tests and plastic hinge analysis of RC structural walls," *Engineering Structures*, vol. 31, no. 7, pp. 1556–1571, 2009.

[108] P. Pegon, C. Plumier, A. Pinto, J. Molina, P. Gonzalez, A. Colombo, P. Tognoli, O. Hubert, and D. Tirelli, "U-shaped walls: description of the experimental set-up," Tech. Rep., 2000.

[109] P. Pegon, C. Plumier, A. Pinto, J. Molina, P. Gonzalez, and P. Tognoli, "U-shaped walls: quasi-static bi-axial test in the X and Y directions - Test report," Tech. Rep., 2000.

[110] K. Beyer, a. Dazio, and M. J. N. Priestley, "Quasi-Static Cyclic Tests of Two U-Shaped Reinforced Concrete Walls," *Journal of Earthquake Engineering*, vol. 12, no. 7, pp. 1023–1053, 2008.

[111] K. J. Bathe and E. N. Dvorkin, "Short communication a four-node plate bending element based on Mindlin/Reissner plate theory and a mixed interpolation," *Internarional Journal for Numerical Methods in Engineering*, vol. 21, pp. 367–383, 1985.

[112] F. C. Filippou and M. Constantinides, "Fedeaslab getting started guide and simulation examples," NEESgrid, Tech. Rep., 2004.

[113] E. Spacone, F. C. Filippou, and F. F. Taucer, "Fibre beam-column model for non-linear analysis of R/C frames: part II. Applications," *Earthquake Engineering & Structural Dynamics*, vol. 25, no. January, pp. 727–742, 1996.

[114] M. Capurso, "Infuenza delle componenti di scorrimento nella deformazione delle travi di parete sottile con sezione aperta," *Giornale del Genio Civile*, vol. 122, pp. 127–144, 1984.

[115] A. Tralli, "A simple hybrid model for torsion and fexure of thin-walled beams," *Computers & Structures*, vol. 22, pp. 649–658, 1986.

[116] S. Y. Back and K. M. Will, "A shear-flexible element with warping for thin-walled open beams," *International Journal for Numerical Methods in Engineering*, vol. 1191, no. 43, pp. 1173–1191, 1998.

[117] R. L. Taylor, "FEAP - A Finite Element Analysis Program," 2013.

[118] K. D. Hjelmstad and E. P. Popov, "Cyclic behavior and design of link beams," *Journal of Structural Engineering*, vol. 109, no. 10, pp. 2387–2403, 1983.

[119] F. Auricchio and R. Taylor, "Two material models for cyclic plasticity: Nonlinear kinematic hardening and generalized plasticity," *International Journal of Plasticity*, vol. 11, no. 1, pp. 65–98, 1995.

[120] M. Jourawsky, *Sur la resistance d'un corps prismatiques e d'une piece composee en bois ou en tole de fer a une force perpendiculaire a leur longeur.* Annale des Ponts et Chaussees, 1856.

[121] C. G. Karayannis and C. E. Chalioris, "Experimental validation of smeared analysis for plain concrete in torsion," *Journal of Mechanics of Material and Structures*, vol. 126, pp. 646–653, 2000.

[122] C. E. Chalioris, "Torsional strengthening of rectangular and flanged beams using carbon fibre-reinforced-polymers - Experimental study," *Construction and Building Materials*, vol. 22, no. 1, pp. 21–29, 2008.

[123] D. Addessi and P. Di Re, "A 3D mixed frame element with multi-axial coupling for thin-walled structures with damage," *Frattura ed Integrità strutturale*, vol. 29, pp. 178–195, 2014.

[124] S. Chen, B. Diao, Q. Guo, S. Cheng, and Y. Ye, "Experiments and calculation of U-shaped thin-walled RC members under pure torsion," *Engineering Structures*, vol. 106, pp. 1–14, 2016.

[125] F. C. Filippou, E. P. Popov, and V. V. Bertero, "Modeling of R/C joints under cyclic excitations," *Journal of Structural Engineering*, vol. 109, pp. 2666–2684, 1983.

[126] R. J. Knops and P. Villaggio, "Recovery of stresses in a beam from those in a cone," *Journal of Elasticity*, vol. 2126, pp. 65–75, 1999.

[127] K. Yoon and P.-S. Lee, "Modeling the warping displacements for discontinuously varying arbitrary cross-section beams," *Computers & Structures*, vol. 131, pp. 56–69, 2014.